Development and Evaluation of Extracorporeal Gas Exchangers for Multi-Function Use in Respiratory Failure

by

David J. Skoog

A dissertation submitted in partial fulfillment
of the requirements for the degree of
Doctor of Philosophy
(Biomedical Engineering)
in the University of Michigan
2016

Doctoral Committee:

Associate Professor Keith Cook, Carnegie Mellon University, Co-Chair
Professor Joseph Bull, Co-Chair
Associate Professor Nikolaos Chronis
Professor Shuichi Takayama

Acknowledgements

This research and dissertation could not have been completed without the guidance and assistance of many people at the University of Michigan, Carnegie Mellon University, and Columbia University. I would like to thank my qualifying exam and dissertation committee members for their guidance through the years; Dr. Bull, Dr. Chronis, Dr. Takayama, Dr. Mazumder, Dr. Khanafer, and Dr. Cook. I owe a great deal of thanks to my advisor, Dr. Keith Cook, who provided over five years of guidance and support that helped me to advance my research, academic, and career goals.

I would like to thank all of the undergraduate students, graduate students, and laboratory technicians at the University of Michigan ALS and ECMO laboratories and the Carnegie Mellon University CPBE laboratory who spent numerous hours manufacturing devices, assisting with experiments, and caring for animals used in *in vivo* experiments. Our clinical collaborators, computational collaborator, and surgical fellows provided a level of skill and dedication that allowed these studies to be successful. Thank you Dr. Demos, Dr. Scipione, Dr. Khanafer, Dr. Demarest, and Dr. Bacchetta.

Lastly, I would like to thank all of my family and friends who supported me throughout graduate school.

Table of Contents

List of Figures

List of Tables

List of Appendices

Abstract

In the U.S., there are 400,000 respiratory failure deaths. Conventional treatment for acute respiratory failure employs lung damaging mechanical ventilation. The only long term treatment for chronic respiratory failure is lung transplantation. However, only 1800 transplants are performed each year due to donor shortages, resulting in the need for a destination therapy. Extracorporeal gas exchangers have been used as an alternative to mechanical ventilation in acute respiratory failure and as a bridge to transplantation in chronic respiratory failure. Blood is diverted to an extracorporeal gas exchanger, where oxygen is added and carbon dioxide is removed before returning the blood to the patient. Current gas exchangers are limited by their high resistance and low biocompatibility that lead to patient complications and device clot formation. This dissertation discusses three gas exchangers; the compliant thoracic artificial lung (cTAL), the compact cardiopulmonary support device (CCSD), and the pulmonary assist device (PAD).

Fourteen day *in vivo* studies evaluated the cTAL's long term performance and biocompatibility. The uncoated cTAL was capable of 14 days of support without a resistance increase or clot formation. In the future, the cTAL will be coated with anti-coagulant coatings and tested *in vivo* for 2 months. Individual components of the CCSD were designed and when tested, met design goals. However, enclosure pressures of negative 197 mmHg at flowrates of 4 L/min were encountered in CCSD system testing, causing gas embolus formation. The risk of gas embolus resulted in the discontinuation of CCSD development. The PAD was designed for long term use as a bridge to transplantation and destination therapy. Computational simulations were used to design the PAD with a theoretical resistance of 1.50 mmHg/(L/min) and a 98.3 percent

blood outlet oxyhemoglobin saturation at blood flowrates of 1.25 L/min. *In vitro* testing of the PAD yielded lower gas exchange performance (88.4 percent saturation) and higher resistance (3.47 mmHg/(L/min)). However, the gas exchange performance was skewed negatively by two devices with fabrication defects. PADs without defects were closer to the gas exchange goal. Future computational models will be improved, and the PAD will be redesigned for lower resistance and higher gas exchange.

Chapter 1: Background

In the United States, there are approximately 400,000 deaths from lung disease of various forms.(1) Respiratory diseases can be largely divided into acute respiratory failure (ARF) and chronic respiratory failure (CRF). A particulary severe form of ARF, acute respiratory distress syndrome (ARDS), affects approximately 190,000 people a year in the U.S. with a 27-40% mortality rate.(1, 2) Chronic respiratory failure, including chronic obstructive pulmonary disease(COPD), idiopathic pulmonary fibrosis (IPF), and cystic fibrosis (CF), affects over 12.1 million Americans with over 127,000 dying per year (largely from COPD).(1) Although there has been a great deal of research focusing on developing new treatment techniques, respiratory disease still is an unresolved problem that necessitates work in new treatments including improved gas exchange devices.

1.1. Respiratory Failure and Conventional Treatment

1.1.1 Respiratory Failure

Due to a variety of causes, the respiratory system can fail to adequately oxygenate and/or remove carbon dioxide from the blood. There are two methods for specifying the type of respiratory failure; based on the gas exchange inadequacies and based on the time progression of the disease. Type 1 Hypoxemic respiratory failure, is classified by an arterial partial pressure of oxygen, PaO_2, less than 60 mmHg.(3, 4) Type 2 Hypercapnic respiratory failure is classified by an arterial partial pressure of carbon dioxide, $PaCO_2$, greater than 50 mmHg.(3, 4) Respiratory failure can be Type 1, Type 2, or often a combination of the two.(3, 4) In terms of time frame, respiratory failure can be either further classified as acute respiratory failure (ARF) or chronic respiratory

failure (CRF).(3) Additionally, CRF patients can experience a sudden worsening of their disease, known as an acute exacerbation or acute on chronic respiratory failure.(3, 5) The stimulus of acute exacerbations varies, but they are often caused by a bacterial infection.(5)

1.1.2 Acute Respiratory Failure

Diseases and Conventional Therapy:

Acute respiratory failure (ARF) is a complex disease state encompassing many underlying conditions that cause a degradation in gas exchange. One particularly severe form of ARF is acute respiratory distress syndrome or ARDS. Patients with ARDS typically are in a state of extreme inflammation and pulmonary edema that can cause large decreases in lung compliance and gas exchange efficiency.(3) Like ARF in general, ARDS is usually a result of an underlying condition such as sepsis, aspiration, trauma, pneumonia, etc.(3, 6, 7) ARDS with sepsis as the underlying cause is associated with the highest incidence of mortality. (8)

The most recent consensus definition of ARDS, the Berlin Definition, breaks down ARDS into three designations according to severity of oxygen deficiency.(2) In general, according to this definition ARDS must develop within one week of a known clinical insult or new or worsening symptoms.(2) Additionally, the patient must have bilateral opacities in chest imaging that is not fully explained by effusions, lobar/lung collapse, or nodules.(2) Lastly the edema experienced by a patient must not be fully explained by cardiac failure or fluid overload.(2) The first designation of ARDS is "Mild" ARDS where the ratio of PaO_2 and fraction of inspired air composed of oxygen (FiO_2), PaO_2/FiO_2, is between 200 mmHg and 300 mmHg with a positive end-expiratory pressure (PEEP) or continuous positive airway pressure (CPAP) greater than or equal to 5 cmH_2O.(2) "Moderate" ARDS is defined when a patient has a PaO_2/FiO_2 ratio between 100 mmHg and 200 mmHg with a PEEP greater than or equal to 5 cmH_2O.(2) Lastly, "Severe" ARDS is defined when

the PaO_2/FiO_2 ratio is less than or equal to 100 mmHg with a PEEP greater than or equal to 5 cmH_2O.(2, 6) Mortality rates for mild, moderate, and severe ARDS are 27%, 32%, and 45%, respectively.(2)

Since ARDS is usually coupled with an underlying condition, treatment of the two disease states must be done in tandem. Treatment of the ARDS symptoms is performed as a temporary support for the respiratory needs of the patient while the underlying condition is treated.(6) It is not until the underlying condition is cured that the ARDS can resolve.(6) The first and least injurious treatment of ARDS is administration of supplemental oxygen without intubation using either an oxygen mask or nasal cannulas.(4) Although lung injury can ensue from oxygen toxicity at levels greater than 50%, supplemental oxygen can in some cases be sufficient to resolve the hypoxemia induced by ARDS.(6)

If administration of noninvasive ventilation is not sufficient, the patient can be intubated and treated with mechanical ventilation.(6) Mechanical ventilation is a technique where a patient is intubated endotracheally and gas is forced into and out of the lungs of a patient using a mechanical ventilator. The ventilator takes over the work of breathing from the body and allows for very controlled ventilation with adjustment of respiratory rate, tidal volume, peak inspiratory pressure (PIP), inspiratory to expiratory ratio, PEEP to prevent alveolar collapse, and fraction of inspired oxygen (FiO2) to name a few.

Ventilator Induced Lung Injury

Invasive mechanical ventilation is able to provide adequate oxygenation and CO_2 removal for many patients, but this comes at a cost. Injury can result from mechanical ventilation and is commonly known as ventilator induced lung injury or VILI. In addition to oxygen toxicity, the ventilator has the potential to induce barotrauma, an injury to the native lungs induced by over-

pressurization.(9, 10) ARDS patients are inundated with large amounts of pulmonary edema dispersed throughout the lung, decreasing the lung volume and changing the distribution of compliance within the lung. As the ventilator forces large tidal volumes of gas through the decreased volume, decreased compliance lung, high pressures are built up and the alveoli of the lung are damaged.(9)

Another suspected form of injury induced by mechanical ventilation is related to inflammation in the lungs and is known as biotrauma. There have been studies that show that even at low tidal volumes and pressures, mechanical ventilation induces release of inflammatory mediators in the lung.(9) Barotrauma of the lungs as well as cellular damage from repeated opening and collapsing of alveoli can induce the release of inflammatory mediators.(11) It has been theorized that the local inflammatory mediators in the lung arising from mechanical ventilation can spill over into the systemic circulation and contribute and may contribute to the development of multiple system organ failure in ARDS patients.(11-13) In addition to these forms of VILI, mechanical ventilation is plagued by ventilator associated infections, and patent sedation during many ventilation modes can result in patient weakening or deconditioning.(6, 14, 15)

Better understanding of these problems have led to changes in the way ARDS patients are treated. One of the most impactful is the utilization of lung protective ventilation strategies that focus less on maintaining normal blood gases and more on protecting the lung from barotrauma.(9) In these strategies, the tidal volume is limited to a maximum of 6 mL/kg body weight and ventilator plateau pressures are limited to less than 28-30 cmH_2O with the application of PEEP. These low tidal volume ventilator strategies have lowered the ARDS mortality rate(9). When safe ventilator settings have reached their limit, the physician can resort to a technique of permissive hypercapnia.(6) During permissive hypercapnia the patient is allowed to remain hypercapnic while

the pH imbalance is corrected using sodium bicarbonate.(6) Additionally, a conservative fluid management technique for reducing the level of pulmonary edema has increased lung function and reduced the number of days patients remain on a ventilator during ARDS.(16) Lastly, there have been studies coupling mechanical ventilation with other extracorporeal respiratory support techniques that have found that lowering tidal volumes below 6 mL/kg body further improves patient outcomes.(17-19) This suggests that VILI is still present when protective ventilation measures are employed. (17)

1.1.3 Chronic Respiratory Failure:

Diseases and Conventional Therapy:

Chronic respiratory failure (CRF) is characterized by a gradual decline in respiratory function marked by more rapid, transient acute exacerbations. A majority of CRF is caused by three diseases; chronic obstructive pulmonary disease (COPD), cystic fibrosis (CF), and idiopathic pulmonary fibrosis (IPF). Although there are some medical treatments that can temporarily alleviate symptoms, the is only cure for CRF diseases lung transplantation.(1, 20)

COPD includes two disease states, chronic bronchitis and emphysema, that sometimes overlap.(5) The American Lung Association defines chronic obstructive pulmonary disease as "the presence of a mucus-producing cough most days of the month, three months of a year for two years in a row without other underlying disease to explain the cough."(1) Due to blockage of airways with mucous, a patient with chronic bronchitis has decreased ventilation and typically cannot support their oxygen requirements, resulting in hypoxemia.(5) On the other hand, emphysema is a destruction of the alveoli, which leads to a decrease in lung elasticity.(5) Emphysema patients are typically able to maintain normal oxygen saturations for a period of time since ventilation and perfusion are decreased simultaneously.(5)However, over time they become

hypercapnic.(5) The chronic disease is slow to progress, but acute exacerbations lead to periods in a severe disease state that can lead to patient mortality. The first onset of a disease exacerbation that leads to ARF is an indicator for poor patient lifespan with a mortality rate of two thirds after two years.(5) During these exacerbations, the symptoms of the chronic disease are increased often to a point that requires hospitalization of the patient due to hypercapnia and hypoxemia. The stimuli for exacerbations can vary, but often they result from a bacterial infection of the lungs.(5)

Treatment of an acute exacerbation begins with relatively simple medical interventions such as inhaled β-agonist drugs to decrease obstruction and broad spectrum antibiotics for any underlying bacterial infection.(5) The progression of treatments of acute exacerbations of COPD is very similar to that for ARDS, with initial administration of supplemental oxygen, then CPAP, and, if the patient degrades even further, eventual intubation and mechanical ventilation.(6)

Treatment of the chronic state of COPD is accomplished largely with pharmacologic agents to reduce the symptoms, but eventually the disease will progress and create the need for lung transplantation. The most common treatment for the chronic disease state of COPD is using an inhaled anticholineric, such as ipratropium bromide, as a bronchodilator.(5) Chronic hypoxemia related to COPD can also be treated using naturally breathed supplemental oxygenation.(5) The quality of life of the patient can also be improved with respiratory rehabilitation sessions,(1) but over time the patients become tethered to supplemental oxygen until they expire.

Cystic fibrosis is an inherited disease that leads to an excess of thick mucus in the lungs, resulting in obstructed airways and airway inflammation.(1) This disease affects many organs including the lungs of a patient from a fairly young age(1), with patient mortality typically occurring by a median age of 37(21). Medical treatment of CF depends on a combination of therapies. Since respiratory infections are fairly common in CF patients (1), patients are often

treated with chronic antibiotics.(22) Ibuprofen treatment is also used in young patients to decrease lung inflammation and damage.(22) Dornase alpha is often administered to patients to degrade the DNA material in the mucous excretions, resulting in an improvement in lung function.(22, 23) In addition to drug administration, physical methodologies for loosening and clearing mucous from the lung have been developed, including handheld and vest worn vibration devices.(24)

According to the American Thoracic Society idiopathic pulmonary fibrosis (IPF) is "a specific form of chronic, progressive fibrosing interstitial pneumonia of unknown cause, occurring primarily in older adults, limited to the lungs, and associated with the histopathologic and/or radiologic pattern of usual interstitial pneumonia."(20) This fatal disease progresses slowly in most patients, but there is a fairly wide range of deterioration rates in the patient populations with a very small 5-10% of patients who have an acute exacerbation each year.(20, 25-29) Although corticosteroids can prove useful in acute exacerbations of the disease, there are no effective pharmacologic treatments for the chronic disease state.(20) The quality of life of patients can be improved with pulmonary rehabilitation and administration of naturally inhaled oxygen can treat hypoxemia in IPF patients, but the only final long term treatment for IPF is lung transplantation.(20, 30) Lung transplantation in these patients is hindered by the extremely varied nature of IPF disease progression which makes it very difficult to predict when a patient will need a lung transplant.(30) As a result transplantation, some clinicians recommend transplantation of a patient in the mild to moderate stages of the disease before the disease progresses to an untransplantable state.(30)

When chronic lung disease advances to its latest stages the patient will need a lung transplant to recover from the disease. Prior to 2005, patients were selected for a lung transplant largely based on how long they were waiting on the lung transplant list. This system favored

patients who were entered into the system in early disease states rather than patients who needed the transplant most urgently, leading to a high waitlist mortality.(31) In 2005 the lung allocation score (LAS) system for distributing donor lungs was implemented.(31) The LAS system is based on a weighting of urgency and chance of survival rather than time on the waitlist.(31, 32) As can be seen in **Figure 1.1** for patients with COPD, CF, IPH, and idiopathic pulmonary hypertension, the waitlist mortality has decreased since the implementation of the LAS.(31) However, the severity and unpredictability of IPF leads to a higher post-transplant mortality of these patients.

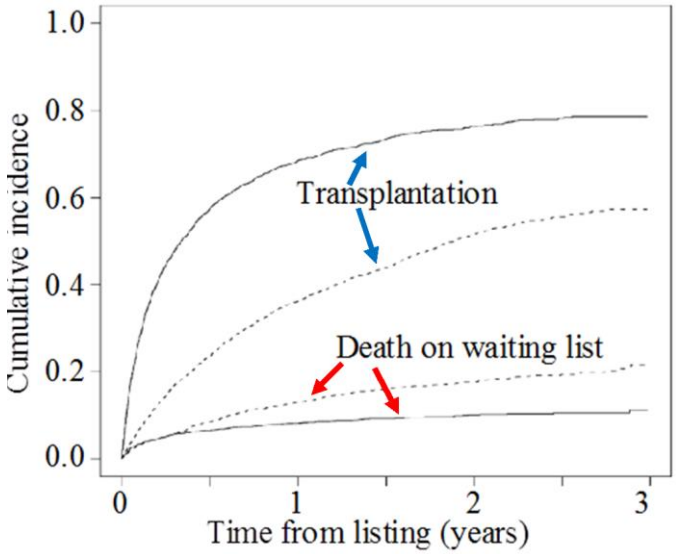

Figure 1.1: Cumulative instance curves of patients transplanted or died on waiting list; pre-LAS (dashed) and post-LAS (solid)). (31)

1.1.4 Pulmonary Hypertension

Pulmonary hypertension (PH) is a disease state that can be caused by respiratory diseases or exist as a primary vascular disease.(33) A normal mean pulmonary artery pressure (mPAP) in a healthy patient is 14 mmHg, however when a patient develops pulmonary hypertension their mPAP is equal or greater than 25 mmHg.(33) The increased pulmonary artery pressure will overload the right heart, eventually leading to heart failure. Edema occurs as a result of increased pulmonary pressures, and can exacerbate other conditions.(33) Pulmonary hypertension results from a single or multiple known or unknown disorders, with unknown causes being described as idiopathic pulmonary hypertension (IPH).(33) The underlying causes of PH are used to designate

the type of pulmonary hypertension on two levels. In the first level, pulmonary hypertension is described according to the location of the underlying condition as being either pre-capillary or post-capillary hypertension. Precapillary and post capillary hypertension are judged based on the pulmonary artery wedge pressure (PAWP) as an estimate of left atrial pressure. Pre-capillary PH occurs when the PAWP is less than or equal to 15 mmHg, and post-capillary PH occurs when the PAWP is greater than 15 mmHg.(33)

Pulmonary hypertension is further classified into 5 groups, Group 1-5. (**Table 1.1**) (33) Group 1 PH is a pre-capillary hypertension known as pulmonary arterial hypertension (PAH) where hypertension can result from a multitude of underlying conditions that increase the pressure in the arterial side of the pulmonary system including pulmonary venous occlusive disease.(33) Group 2 PH is a post-capillary pulmonary hypertension due to an underlying left heart condition such as a valvular disease.(33) A valvular disorder of the left heart or left ventricle causes an elevated left atrial pressure.(34) As a result, the upstream pulmonary venous pressure becomes increased.(34) Further upstream the pulmonary artery pressure becomes elevated from the back pressure of the pulmonary veins, leading to pulmonary hypertension.(34) Group 3 PH is a pre-capillary pulmonary hypertension due to underlying respiratory diseases such as COPD.(33) Group 4 PH is a pre-capillary PH due to pulmonary artery remodeling as a result of major vessel

Table 1.1: Definitions of pulmonary hypertension in to pre and post capillary, and into groups 1-5.

Definition	Characteristics[a]	Clinical group(s)[b]
PH	PAPm ≥25 mmHg	All
Pre-capillary PH	PAPm ≥25 mmHg PAWP ≤15 mmHg	1. Pulmonary arterial hypertension 3. PH due to lung diseases 4. Chronic thromboembolic PH 5. PH with unclear and/or multifactorial mechanisms
Post-capillary PH	PAPm ≥25 mmHg PAWP >15 mmHg	2. PH due to left heart disease 5. PH with unclear and/or multifactorial mechanisms
Isolated post-capillary PH (Ipc-PH)	DPG <7 mmHg and/or PVR ≤3 WU[c]	
Combined post-capillary and pre-capillary PH (Cpc-PH)	DPG ≥7 mmHg and/or PVR >3 WU[c]	

thromboembolism.(33) Group 5 PH can be a pre-capillary and/or post capillary PH from either unknown causes or a combination of causes from other groups.(33) Treatment for pulmonary hypertension varies according to the group and disease severity with treatments ranging from lung transplantation to drug therapy to left heart repair.(33)

1.2 Extracorporeal Gas Exchange

In acute and chronic respiratory failure, there are extracorporeal gas exchange devices that have been developed to address shortcomings in traditional treatment methods. These extracorporeal gas exchange devices function by diverting blood to a gas exchanger where carbon dioxide is removed from the blood and oxygen is added. In ARF, there is a point where mechanical ventilation is either not satisfactory in supporting the patient's respiratory needs, or the ventilator must be used with injurious settings to accomplish support. In these situations, extracorporeal gas exchangers have the potential to be used either in conjunction with mechanical ventilation or in a standalone mode.(10) In chronic respiratory insufficiency, artificial lungs are sometimes used as a bridge to lung transplantation.(35-38)

In the United States there are currently approximately 1800 patients a year who receive lung transplants for chronic respiratory failure, however 350 patients die on the waiting list each year while searching for a suitable donor.(39) Patients on the lung transplant list are typically in very advanced disease states and often require mechanical ventilation. However, mechanical ventilation is a contraindication to lung transplant due to lower long term survival rates post-transplant (61% vs. 71% 2 year survival with without mechanical ventilation) resulting from a possible combination of ventilator induced lung injury, ventilator associated infection, and muscular weakening of the patient.(14, 15, 40-42) In order to extend the amount of time a patient can stay on a waitlist and improve the patient's health and chances of surviving pre and post

transplant, extracorporeal gas exchange devices are being developed as a bridge to lung transplantation.(35-38) In addition to patients who will be bridged to lung transplantation, there are millions of patients with chronic respiratory failure who will never receive a lung transplant due to the mismatch between donor lung numbers and patients in need of a lung transplant. These patients have no alternatives and extracorporeal gas exchangers may be a suitable alternative in the coming years.(43)

1.2.1 Extracorporeal Gas Exchanger Function

Modern extracorporeal gas exchangers all function with the same premise of pulling blood high in carbon dioxide and low in oxygen from the body, using concentration gradients with a sweep gas supply to exchange gas with the blood, and finally returning it to the patient's body.(44) Once inside a gas exchanger, the patient's blood flows through a bank of hollow fibers with blood flowing on the outside of each fiber. (**Figure 1.2**) Concurrently a sweep gas typically composed of pure oxygen is pumped through the inside of each fiber.(44) A concentration gradient exists between the carbon dioxide and oxygen in the blood on the outside of a fiber and the pure oxygen flowing through the inside of a fiber. The wall of this fiber is permeable to both oxygen and carbon dioxide diffusion, but not blood. As a result the blood and the gas are largely separated by a physical barrier with only diffusion of oxygen into the blood and carbon dioxide out of the blood through the fiber wall. (**Figure 1.2**) The blood exiting the fiber bank is increased in its oxygen content and reduced in its carbon dioxide content as a result of the gas exchange. The sweep gas exiting the fiber follows the opposite

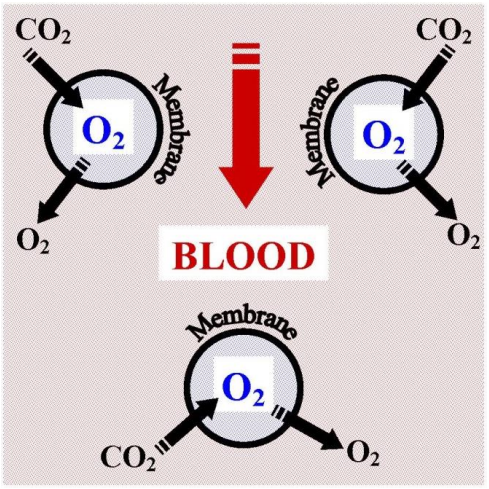

Figure 1.2: A schematic section of a gas exchanger hollow fiber bank with blood in red and sweep gas in blue.

pattern.

Extracorporeal gas exchangers functioning in this manner can be effective at providing gas exchange support for a patient with respiratory failure. However, the functioning of a gas exchanger can be severly impaired by clot formation and plasma leakage.(44-46) The foreign surface of the device activates platelets and when procoagulant molecules build up in regions of stasis and recirculation clot forms.(46) This clot formation shed from the device to create an embolus and/or stay within the gas exchanger and cover the fiber. When significant portions of fiber are covered with thrombus formations, the gas exchange suffers and the resistance increases. The gas exchange capabilities can also be impaired by plasma leakage through certain fiber materials, such as microporous polypropylene.(45) Plasma from the blood crosses the wall of the fiber into lumen where gas flows. This clogs up the inside of the fibers and leads to a reduction in gas exchange performance.(45)

1.2.2 Extracorporeal Attachment Modes

Attachment Mode

Extracorporeal gas exchangers can be attached to the vasculature at any combination of locations where enough blood flow can attained for adequate gas exchange. The most common attachment modes include veno-arterial access (VA), veno-venous access (VV), hybrid veno-arterio-venous access (VAV), hybrid veno-veno-arterial access (VVA), and arterio-venous access (AV). Each attachment mode has different capabilities in terms of gas exchange, blood flowrates, etc.

Veno-arterial access involves the pumping of systemic venous blood into the gas exchanger circuit and then back into the systemic arterial system (**Figure 1.3**).(47, 48) As the blood moves from the low pressure venous system to the high pressure arterial system, a blood pump is needed.

The pumping of blood from the venous to the arterial system in this attachment mode has the advantage of providing both cardiac and respiratory support for a patient.(47) However, the pump can cause a large amount of platelet activation and blood damage as it must pump at relatively high RPMs to generate the pressure head necessary to pump into the high pressure arteries.(47) As the drainage blood is systemic venous blood, it is high in carbon dioxide and low in oxygen, so respiratory support can be attained for both oxygen and carbon dioxide.

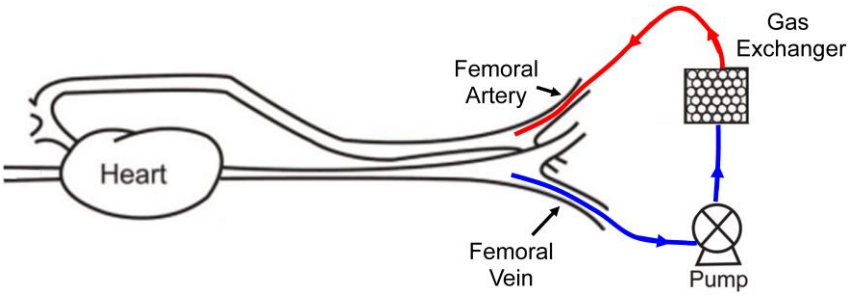

Figure 1.3: Two site VA attachment. Adapted from (48)

Veno-venous access involves the pumping of systemic venous blood through the gas exchanger circuit and back to the systemic venous system.(47) (**Figure 1.4**) (49) Since the blood is being withdrawn and returned to the same low pressure system, this attachment mode also requires a pump. Although the pump can cause blood damage and platelet activation, it is typically lower than during VA support as the pump can operate at lower RPMs. . The lower pressures in a VV system also typically result in fewer complications in comparison to VA systems.(47) As with VA attachment, VV attachment modes can provide both carbon dioxide and oxygen gas exchange support. However, since VV access pumps to and from the venous system no cardiac support is attained, somewhat

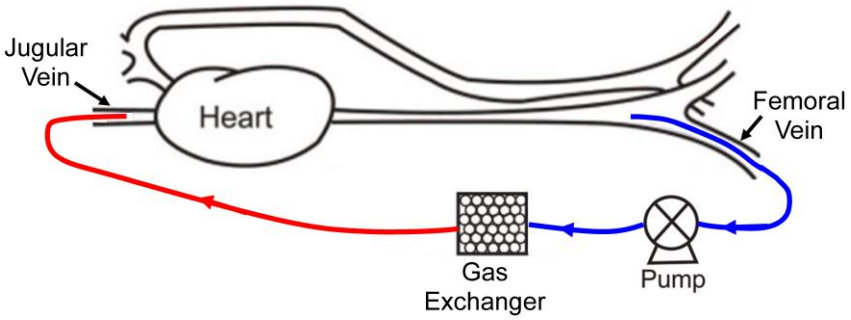

Figure 1.4: Two site VV attachment. Adapted from (48)

limiting the patient population.(47, 50) VV access also has the disadvantage of decreased gas exchange efficiency arising from some portion of the oxygenated blood from the reinfusion location being pulled back into the drainage location before it can enter into the systemic arterial system.(51, 52) As will be discussed in subsequent sections there have been efforts to reduce recirculation of oxygenated blood, but it still remains a concern in VV attachment modes.(51, 52)

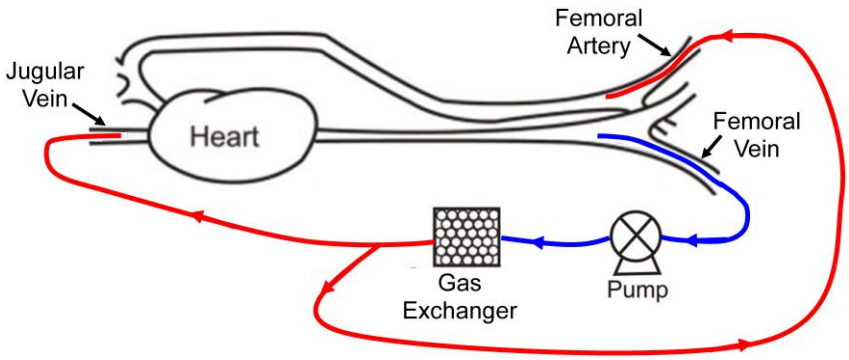

Figure 1.5: Hybrid VVA or VAV attachment. Adapted from (48)

Hybrid VVA and VAV attachment modes are essentially the same circuits with systemic venous blood drained from the body and reinfused back into the systemic arterial and systemic venous systems.(**Figure 1.5**) (50) However, the order in which the vasculature was attached to the circuit varies between VVA and VAV attachment modes. In a VAV mode, the patient is originally supported in a VA attachment mode, but is switched to a VAV mode when a venous reinfusion access point is added to provide increased oxygenation to the upper body.(50) In a VVA mode, the patient is typically originally supported in a VV mode, but subsequently requires some cardiac support, so an arterial reinfusion point is added.(50) As these hybrid systems drain from the low pressure systemic venous system, they require a pump and are able to provide both carbon dioxide removal and oxygenation. These attachment modes are more complex, but in some patients VVA and VAV modes are needed to adjust for changing physiology where a patient needs increased cardiac or respiratory support.(50)

Arterio-venous attachment modes passively drains blood from the arterial system and

returns it to the venous system. These AV systems can be attached as either purely pulmonary (**Figure 1.6**) or more typically purely systemic circuits (**Figure 1.7**).(44, 53) As the blood travels from the high pressure arterial system to the low pressure venous system a blood pump is not required to maintain flow.(44, 53) This reduces the size and complexity of the system and eliminates the blood damage caused by the pump. However, the entire circuit must maintain a relatively low resistance and a patient must be able to maintain adequate blood pressures to maintain proper flowrates through the devices.

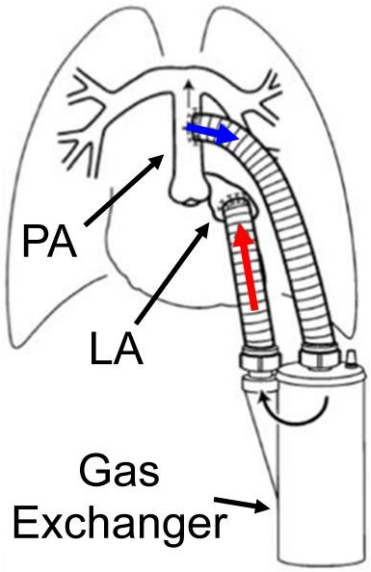

Figure 1.6: Pulmonary AV Attachment. Adapted from (44)

The systemic AV attachment mode has been used extensively for its simplicity, however it can only provide carbon dioxide removal and not significant oxygen transfer.(53-55) The attachment is predominantly limited because less than 20% of the cardiac output can be diverted through the device.(54-57) . Furthermore, the arterial drainage blood is already relatively high in oxygen content and thus a lesser amount can be transferred to it.(54, 56) The systemic AV shunt can also lead to hemodynamic instability.(58) The pulmonary AV attachment, typically pulmonary artery to left atrium, does have the ability to provide oxygen and carbon dioxide support since the pulmonary arterial blood is equivalent to systemic venous blood. Additionally, the pulmonary AV attachment mode has been used to provide a parallel, low resistance pathway around the

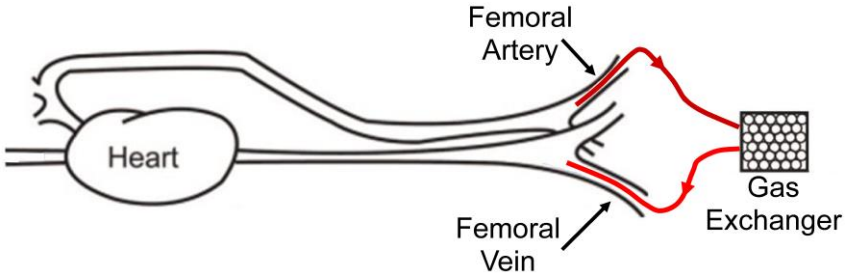

Figure 1.7: Systemic AV attachment. Adapted from (48)

Table 1.2: Attributes and capabilities of extracorporeal attachment modes.

Attachment Mode	O_2 Support	CO_2 Support	Cardiac Support	Pumpless	Ambulation Possible	Invasive	Right Heart Unloading
VA	Full	Full	Full	No	Yes	No	No
VV	Full	Full	No	No	Yes	No	No
VAV/VVA	Full	Full	Partial	No	Yes	No	No
Systemic AV	No	Full	No	Yes	No	No	No
Pulmonary AV	Full	Full	No	Yes	Yes	Yes	Yes

native lungs in patients with pre- capillary pulmonary hypertension.(55, 59-62) This low resistance parallel pathway lowers the total system resistance and unloads an overworked right heart. However, pulmonary AV attachment modes typically require a highly invasive thoracotomy to attach to the pulmonary vasculature.(62)

The attachment modes discussed have a range of capabilities, disadvantages, and advantages that dictate their use in different situations as seen in **Table 1.2**. Additionally, the attachment modes have an impact on the design and choice of other circuit components. In pumpless attachment modes, the gas exchanger circuit--including gas exchanger and attachment connections--must be of low resistance to maintain adequate blood flow. However, pumped attachment modes can also benefit from low resistance gas exchange circuits as the blood pumps can be used with settings less injurious to blood. Pumpless attachment modes can also be outfitted with pumps to increase and/or provide more controlled blood flow through the gas exchange circuit. Overall, each attachment mode can be used with a variety of circuit components depending on patient needs.

Vascular Access Connections

There are three primary types of attachment apparati that can be used for connecting to a patients vasculature: the cannula, the graft, and the combination graft-cannula. All have their positive and negative traits. The cannula is essentially a tapered tube with various blood flow ports

(**Figure 1.8**) that is inserted into a cut in the vasculature and secured with simple suture techniques.(63) These cannulas can be inserted very quickly with minimal surgical trauma. Early cannula designs were primarily single lumen cannulas requiring at a minimum two cannulas, one for drainage of blood and one for reinfusion of blood.(51) Depending on location sites for these cannulas, they can suffer from recirculation where oxygenated blood from the reinfusion cannula is pulled back into the drainage cannula before entering the systemic circulation.(51) This results in inefficient gas exchange and perfusion of the body.(51) Today, a range of cannulas are available, including a dual lumen cannula that allows for the application of a single cannula for both drainage and reinfusion with a port configuration designed for minimal recirculation.(51) The two largest drawbacks to cannula usage is the high fluid resistance through each cannula, and the fact that the cannula takes up a majority of the flow cross-section of a vessel possibly resulting in impaired blood flow to or from the vessel upstream of the cannulation site.(63, 64) Impaired blood flow upstream of a cannula can lead to ischemia or increased pressures upstream in areas such as the brain.(64)

Figure 1.8: Two venous drainage cannulas.

Synthetic grafts are typically polyester or PTFE fabric tubes that are used most commonly for vascular repair and replacement. However, they have been used in animal models of extracorporeal gas exchange by interfacing the graft with a piece of blood conduit tubing.(**Figure 1.9**)(65-68) The vasculature can be cut on its side and the synthetic graft can be sutured to the vasculature with its bore over the opening to form an end-to-side anastomosis. The tubing section

of the graft assembly can then be attached to an extracorporeal circuit. The grafting method results in a much lower resistance attachment than a cannula and it does not obstruct the flow of the vasculature.(65-68) However, this process is more invasive than cannulation and the graft assemblies are not readily available on the commercial market.

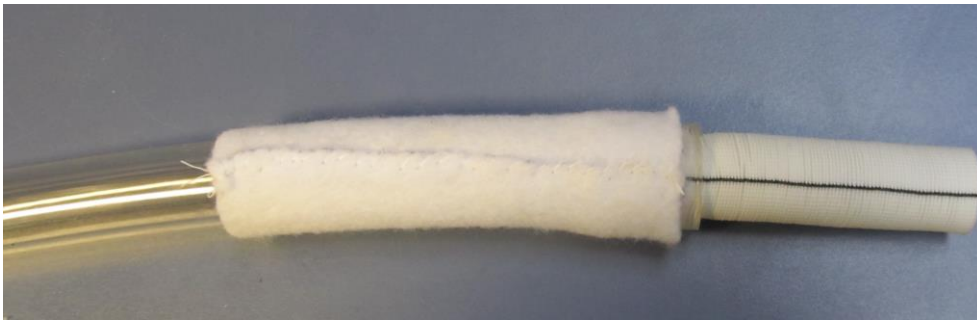

Figure 1.9: A 18mm synthetic graft assembly.

A third combination method has been recently developed that combines a more commercially available cannula with a section of synthetic graft material.(64, 69) In this configuration the vessel is cut on its side and a section of synthetic graft material is sutured with its bore over the cut. A cannula is then fed into the graft until the tip is extended to the opening of the vasculature and the cannula is sutured to the graft.(64, 69) All of the components of this graft cannula assembly are commercially available and this configuration avoids blocking of the vasculature with the cannula.(64, 69) However, the surgical attachment and detachment of the assembly is more involved than cannula placement and it still utilizes a high resistance cannula.(64, 69)

The choice of attachment mode comes down to the balance of expected duration of treatment, surgical trauma, speed of deployment, resistance of the attachment, potential complications, and commercial availability. For instance, in a patient treated with ARDS the duration of treatment is relatively short, so the usage of a cannula that is simple to introduce and remove is a better option than a more invasive graft. **Table 1.3** shows the tradeoff's between each

Table 1.3: Tradeoffs between vascular access connections.

Access Connection	Fast Deployment	Simple Removal	Commercially Available	Low Resistance	Invasive	Blocks Vasculature
Cannula	Yes	Yes	Yes	No	No	Yes
Graft	No	No	No	Yes	Yes	No
Combination Graft Cannula	No	No	Components Are	No	Intermediate	No

attachment mode. Today a vast majority of extracorporeal gas exchange circuits utilize cannulas for attachment, however in the future this may shift as new technologies emerge.

1.2.3 Perfusion Modes

Blood flow exiting the heart into the arterial system is highly pulsatile. As the blood travels through the compliant arterial blood vessels, it is damped out and largely steady once it reaches the venous system. Since the advent of cardiopulmonary bypass, there has been debate over whether extracorporeal gas exchange circuits should mimic the pulsatility of the heart when blood is reinfused to the arterial system. In the 1950's, in studies by Wesolowski, it was concluded that steady blood flow was sufficient to maintain adequate perfusion of the organs.(70, 71) This was welcomed by many, as reliable pulsatile flow blood pumps were not available at the time.(72) With the exception of pumpless systemic AV systems, commercial gas exchanger circuits in clinical use employ steady flow perfusion. However, over the years there have been studies in steady flow systems such as cardiopulmonary bypass that suggest poor perfusion of the renal system(73, 74), the myocardium(75), and the cerebral vasculature(76, 77). As a result there has been continued study of whether there is a benefit from maintaining pulsatile flow in VA attachment modes.(78-83)

Shepard, et al. mathematically described the increased perfusion capabilities of pulsatile perfusion in terms of energy equivalent pressure according to **Equation 1.1**.(84)

$$EEP = \frac{\int f(t) * p(t) dt}{\int f(t) dt} \quad (1.1)$$

Where EEP is the energy equivalent pressure, f(t) is the blood flowrate with time, p(t) is the blood pressure with time, and t is time.(84) In steady flow, f(t) and p(t) become constants and the energy equivalent pressure is equal to the mean arterial blood pressure. However, in physiologic pulsatile flow from the heart the integration yields an EEP approximately 10% greater than with steady flow.(85) The higher energy equivalent pressure delivered to the blood results in a stronger driving pressure that can in theory perfuse more distant capillary beds.(86) Recently, short 3 hour *in vivo* experiments involving a piglet model of extracorporeal membrane oxygenation (ECMO, described in **Section 1.3.1**) have provided further evidence that pulsatile flow results in increased perfusion.(78) In these experiments the test subjects were supported on steady and pulsatile flow, and near infrared spectroscopy was used to measure perfusion of the kidneys.(78) After an hour of ECMO the pulsatile group showed higher levels of local saturation in the frontal lobes of the kidneys than the steady flow group.(78)

These recent short term studies and past mathematical descriptions of pulsatile flow yield positive results in terms of perfusion. However, additional studies are needed to confirm its benefit, and long term tests are needed to study whether the higher shear stresses seen during systole in the gas exchanger, stasis in the gas exchanger during diastole, cannulas, and vasculature have deleterious effects. Pump technologies have improved and a new ECMO pump has been produced in Europe that is capable of reproducing physiologic pulsatile flows in a reliable manner.(79)

1.2.4 Desired Attributes of Acute and Chronic Extracorporeal Gas Exchange Systems

The requirements of gas exchange systems vary depending on the timeframe that they will be used. In an acute setting, the gas exchanger only needs to last one to two weeks and the main focus is on providing enough gas exchange for a patient to be supported on minimal ventilator

settings or without a ventilator entirely.

In a patient being treated for chronic respiratory failure the requirements of the gas exchanger and system are much more stringent. When bridging a patient to lung transplantation, the gas exchanger would ideally be able to last for up to a month or two and limit blood damage and activation. When patients require multiple blood transfusions due to blood trauma, immune system reactions can result that endanger the patient.(44) Additionally, there have been recent studies showing that patients being bridged to lung transplantation benefit from being able to perform physical therapy and walking while being bridged.(36, 87-89) As a result, many patients may benefit by a gas exchanger and associated system that is compact enough for ambulation.

In patients with chronic respiratory disease who will not receive a donor organ, a destination therapy gas exchange system has the potential to extend and improve the lives of many patients in a manner similar to ventricular assist device use as a destination therapy for chronic cardiac failure patients.(51) A destination therapy system must be extremely compact so as to allow full ambulation of a patient outside of a hospital. Also the device longevity will need to be at least 2 to 3 months, with periodic replacement to allow for treatment over a period of years. It also must induce little biochemical response from the body and avoid damaging the blood of the patient as repeat transfusions will not be an option for a patient supported for an extended period of time outside of a hospital. A summary of the requirements for a gas exchanger for ARF patients, CRF bridge to lung transplant patients, and CRF destination therapy patients can be seen in **Table**

Table 1.4: Desired attributes for a gas exchange system for ARF, CRF bridge to lung transplant, and CRF destination therapy patients.

	Treatment Duration	Device Longevity	Abulation	Compact	Gas Exchange Support
ARF	2-4 weeks	2-4 weeks	No	No	Full
CRF Bridge	1-2 months	1-2 months	Yes	Yes	Full
CRF Destination	years	2-3 months	Yes, high level	Yes, highly	Partial

1.4.

1.3 Current Extracorporeal Gas Exchange Systems

1.3.1 Extracorporeal Membrane Oxygenation

The first extracorporeal gas exchange system to be used for extended period of time outside of the operating room was extracorporeal membrane oxygenation (ECMO). ECMO is a complex system similar to cardiopulmonary bypass that pulls blood from the body, performs gas exchange on the blood, and returns it to the body at flowrates often greater than 4 L/min in adults.(47, 90) A basic ECMO circuit consists of a drainage cannula to pull blood from the body, tubing, a sealed reservoir, a blood pump, a gas exchanger, a heat exchanger to maintain body temperature at a predefined level, a reinfusion cannula to return blood to the body, monitoring equipment, and other possible small components, such as bubble traps.(47) Cannulas and/or combination graft cannulas are currently used today as vascular connections in ECMO circuits.

ECMO is very flexible in its configuration with VV, VA, VAV, and VVA attachment modes utilized with either single lumen or dual lumen cannulas. Early success of ECMO mostly occurred in in neonatal and pediatric patients, but recently has been successfully used in adult patients for both ARF and CRF. The use of ECMO over conventional mechanical ventilation has been a matter of argument for decades. However, several recent findings have led to expanded ECMO use. First, during the H1N1 flu pandemic, ECMO was successfully used to treat severely ill patients that were likely to die without ECMO support.(91) Second, the CESAR trial compared use of ECMO and mechanical ventilation for ARDS patients, showing a benefit of ECMO treatment in patients.(92) This study was later criticized for having a control group where doctors were allowed to treat as they normally would and thus some did not follow ARDSnet recommendation for lung protective mechanical ventilation.(93)

The used of ECMO as a bridge to lung transplantation has seen renewed practice since the LAS system for donor lungs shortened waitlist times in 2005. Despite ECMO patients often being in a more severe clinical state, several groups of researchers saw similar or better long term mortality rates for ECMO bridged patients as ventilator bridged or non-bridged patients.(38, 94-97) Graft rejection is more prevalent in the ECMO patients than mechanical ventilator patients, since there are a large number of transfusions given to ECMO patients and ECMO induces a systemic immune response.(94)

Despite recent positive results, ECMO is not a perfect treatment option. The ECMO system is very complex and expensive, necessitating a very large team to monitor and adjust the system.(92) The large number of blood contacting components and the pump used to drive the blood cause blood damage, clotting, and systemic immune system activation that can lead to damage of organs.(47) Multiple red blood cell (RBC) and platelet transfusions are needed to keep up with blood damage and consumption by the system, which can lead to patient deterioration.(98-100) Although there is large variation between ECMO centers and patients(99), the median daily RBC and platelet transfusion requirements 0.16-2 units and 0-3 units, respectively.(98) Larger physiologic complications include limb ischemia in VA ECMO (94) and intracranial hemorrhage(45, 52, 93). When used in ECMO, the oxygenators have a lifespan limited to approximately two to three weeks even with anti-thrombogenic coatings.(101-104) This limited device lifespan limits ECMO's use to bridge to transplantation rather than destination therapy. As a bridge to transplantation, ECMO can benefit those patients eligible for lung transplantation. However, it does not expand the pool of patients treated since the limiting factor to the number of patients treated is the shortage of donor organs.

Awake and Ambulatory ECMO

New strategies for ECMO used in bridging patients to lung transplantation include awake and ambulatory ECMO. In traditional ECMO, the patient is typically sedated and laying down in bed, which leads to muscular deconditioning that can reduce the chances of survival pre and post transplant. In awake ECMO the patient is not sedated without ventilator support, allowing them to sit up in bed and perform tasks such as eating. When a single dual lumen cannula is utilized, the patients can ambulate and perform physical therapy in what is known as ambulatory ECMO.(88) (**Figure 1.10**) Several studies comparing ambulatory ECMO bridged patients to non-bridged patients showed equal or improved outcomes in the sicker ambulatory ECMO bridged patients.(38, 95, 97)

Figure 1.10: A patient walking while being treated with ambulatory ECMO. (38)

1.3.2 Extracorporeal Carbon Dioxide Removal

Carbon dioxide removal systems are used to reduce ventilator settings or remove the need for a ventilator by providing full or partial carbon dioxide removal for patients with largely hypercapnic respiratory failure.(105) However, they typically provide low oxygen exchange due to low blood flowrates and/or drainage of systemic arterial blood.(105) These carbon dioxide removal systems include arterio-venous carbon dioxide removal ($AVCO_2R$) systems and modified VV ECMO ($VVCO_2R$) systems.(105)

Aterio-Venous Carbon Dioxide Removal

One of the most commonly used carbon dioxide removal systems is $AVCO_2R$.(106-110)

$AVCO_2R$ systems consist of a systemic arterial drainage cannula, a low resistance gas exchanger, and a systemic venous reinfusion cannula.(106-110) The pressure gradient of the AV cannulation, typically from the femoral artery to femoral vein (**Figure 1.11**), induces blood flows of 1-2.5 L/min through a low resistance gas exchanger.(106, 109) This system has been successfully utilized in clinical trials to reduce the ventilator settings in patients with ARDS.(106-110) In CRF patients there have been several successful studies using the Novalung iLA in an $AVCO_2R$ configuration to bridge a small number of patients to lung transplantation while either reducing ventilator settings (n=12, 83% survived to transplant, 80% post transplant 1 year survival) or removing the patient from the ventilator (n=2, 100% survival to transplant).(111, 112) However, $AVCO_2R$ is not without its complications. One of the major risks of $AVCO_2R$ is limb ischemia for the cannulated limbs, as the peripheral arterial supply is shunted towards the gas exchanger.(106, 108) This systemic AV shunt also only allows for very minimal oxygenation (112) and can lead to hemodynamic instability. (58) The pumpless circuit avoids some blood damage, but an arterial to venous pressure gradient of at least 60-80 mmHg is needed to maintain effective flow through the circuit, so patients with poor cardiac function cannot be treated effectively with $AVCO_2R$.(106) The longevity of the Novalung ILA is also very short with the devices needing to be changed out

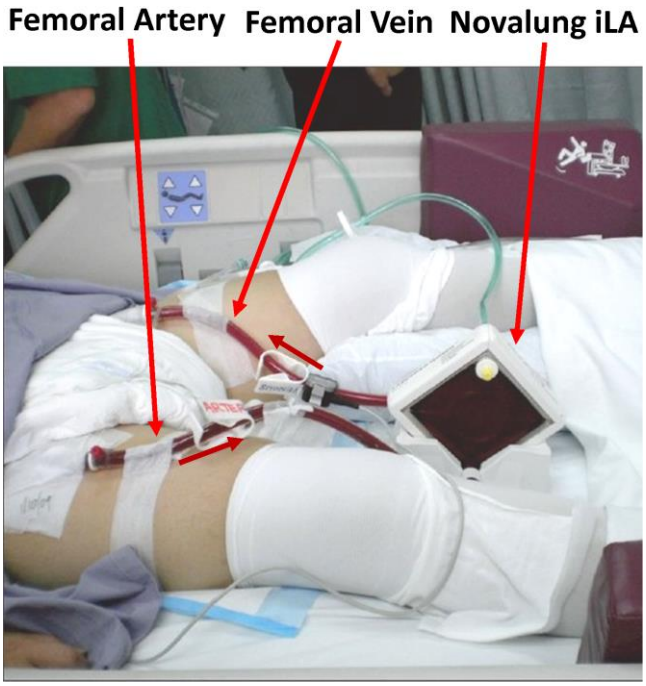

Figure 1.11: A Novalung iLA gas exchanger used in a femoral artery to femoral vein $AVCO_2R$ configuration. (42)

an average of every 10 days due to clot formation despite antithrombogenic coatings.(112) Laslty, the femoral cannulation typically used prevents any ambulation of a patient. As a result of these issues, the patient population who could use AVCO2R is limited.

Veno-Venous Carbon Dioxide Removal

$VVCO_2R$ is a method of CO2 removal that spun off from VV ECMO that removes carbon dioxide from the blood using lower blood flow rates than traditional ECMO.(105) $VVCO_2R$ cannulation sites are the same as VV ECMO, but the circuit can vary in its complexity.(105) One of the simplest systems the iLA Activve system, which uses a console that combines a Novalung iLA gas exchanger and a centrifugal blood pump into one unit.(105, 113, 114) This system is a simplified ECMO system that can be used with flowrates as low as 0.5 L/min for removing CO_2 and as high as 4.5 L/min for ECMO.(105, 113) In a larger study of an early VVCO2R system that utilized flow rates of 2 L/min, similar complications to traditional VV ECMO were found; bleeding, clotting, and blood product consumption.(115)

An ultralow flowrate version of VVCO2R is known as respiratory dialysis has been gaining some adoption.(105, 116-119) Respiratory dialysis utilizes a dual lumen cannula that drains from the superior vena cava and reinfuses blood into the right atrium accessed through either the femoral or jugular vein.(116-119) The Hemolung gas exchanger used in respiratory dialysis combines a centrifugal pump and gas exchanger into a single unit (**Figure 1.12**).(116-119) The mixing induced by the pumping portion of

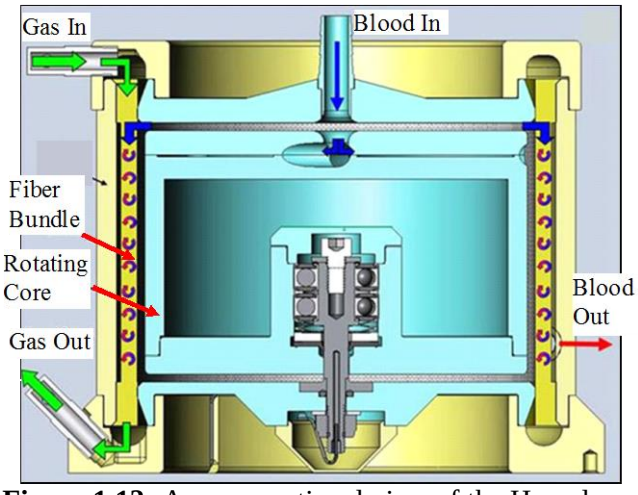

Figure 1.12: A cross-sectional view of the Hemolung gas exchanger-pump used in respiratory dialysis $VVCO_2R$. (116)

the device enhances gas exchange, allowing for the lower flowrates on the order of 400-600 mL/min.(116-119) A preliminary clinical trial in acute exacerbation of COPD showed promise with most patients either being removed from ventilation, avoiding ventilation, or having a reduction in ventilator settings.(118) However, the low blood flow rate results in very little oxygenation of the blood in comparison to other $VVCO_2R$ systems.

1.3.3 Thoracic Artificial Lungs

A thoracic artificial lung (TAL) is a pumpless pulmonary gas exchange circuit consisting of a pulmonary arterial drainage (typically pulmonary artery), a gas exchanger, and a pulmonary venous (right atrium) or arterial (pulmonary artery) reinfusion. In a pulmonary artery to left atrium (PA-LA) configuration the gas exchanger is placed in parallel to the natural lungs in a pulmonary AV attachment, while the pulmonary artery to pulmonary artery (PA-PA) configuration places the gas exchanger in series.(**Figure 1.13**) Both configurations allow for oxygenation and carbon dioxide removal while the pumping through the gas exchanger is driven by the pumping of the right heart. An in series (PA-PA) connection has a high total resistance, but it has the benefit of retaining the lungs natural embolus filtration function and metabolic functions.(44, 120, 121) In parallel configurations have very low resistance and can unload the right

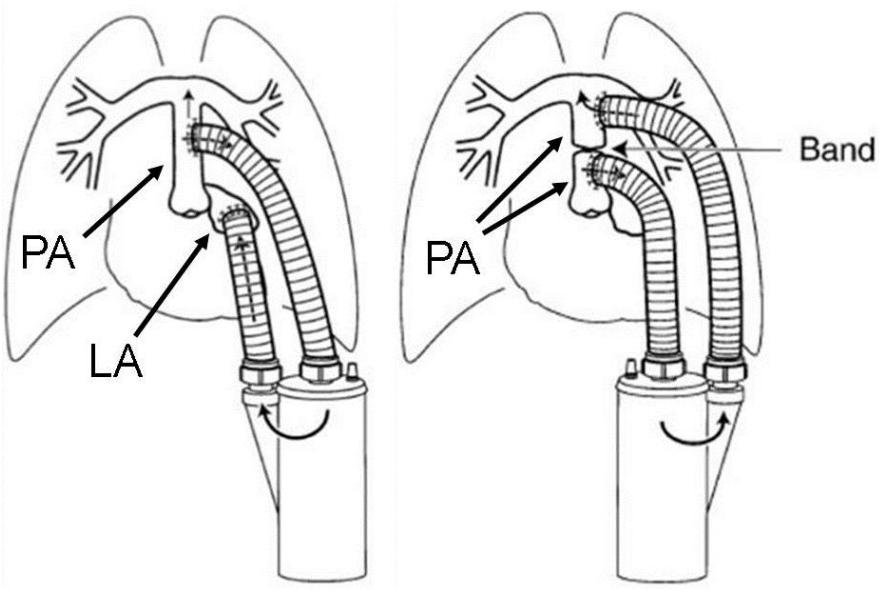

Figure 1.13: *Left:* A TAL in a PA-LA configuration. *Right:* A TAL in a PA-PA configuration. (44)

heart in cases of pulmonary hypertension, however there is some risk for embolus migration to the arterial side of circulation and a reduction in the metabolic functions of the native lungs.(44, 120, 121) In either configuration, the gas exchanger circuit must have a low resistance often necessitating the use of a large bore synthetic graft assembly and an ultra-low resistance gas exchanger. (65, 66, 68, 122-126)

TALs have advantages and disadvantages in their use. The simple, compact pumpless circuit allows for a patient to ambulate during treatment and avoids a blood damaging pump. Moreover, the blood flowrate and therefore gas exchange is controlled by the patient's own physiology. Additionally, the central grafting or cannulation attachment mode eliminates the risk of limb ischemia posed in peripheral cannulation. However, this central attachment requires a highly invasive thoracotomy for attachment and removal of the system, effectively eliminating its use as an ARF treatment. TALs are also in their infancy on comparison to other extracorporeal gas exchange systems.

Commercially available gas exchangers such as the Novalung have been used in a TAL configuration for a very limited number of cases. They were fairly successful in these small number of patients with 10 of the 11 patients surviving to transplantation.(59, 61, 62, 127) However they were hampered by a relatively high resistance, low gas exchange, and a device longevity that required replacement every two to three weeks despite anti-thrombogenic coatings.

There are some specifically designed thoracic artificial lungs (TAL) that are being tested in animals as a long term bridge to lung transplantation.(65, 66, 68, 122, 124-126) The MC3 Biolung has shown promise in animal studies with a low resistance of 1.8 mmHg/(L/min) and a device longevity of approximately 9.5 days without anti-thrombogenic coatings. The cTAL discussed in later chapters is also being developed as long term TAL with an ultra-low benchtop

resistance of 0.5 mmHg/(L/min). However, none of these experimental devices are currently available on the commercial market. TALs may one day be successful bridge to lung transplant or destination therapy device due to their simple circuit, but commercially available gas exchangers with an extended longevity and low resistance will be needed first.

1.4 Experimental Gas Exchangers

Three gas exchangers were studied for this work and will be discussed in the following chapters; the compact cardiopulmonary support device (CCSD), the compliant thoracic artificial lung (cTAL), and the pulmonary assist device (PAD). (**Table 1.5**) The compact pulmonary support device is a gas exchanger that is designed to provide cardiac and full respiratory support as a replacement for VA ECMO. The CCSD integrates a pulsatile blood pump, compliant housing gas exchanger, and heat exchanger into a single unit, allowing for patient ambulation and a reduction in blood contacting surface area. The compliant thoracic artificial lung is a TAL designed with a compliant housing that dampens out flow pulses from the right heart to reduce blood flow impedance and unload the right heart. The cTAL allows for a high level of patient mobility, and can provide full respiratory support for patient. The pulmonary assist device is a compact, modular gas exchanger system designed to provide partial respiratory support. Each PAD gas exchange module is composed of a solid housing, and is very compact to allow for a high level of patient

Table 1.5: A summary of the attributes of the gas exchangers that were designed and tested as discussed in subsequent chapters.

Device	Housing Type	Pumping	Attachment Mode	Attachment Connection	Blood Conduit Dia. (in)	Frontal Area (cm^2)	Surf. Area (m^2)	Bridge to Trans.	Destin. Therapy
CCSD	Compliant	Yes	VA, VV	Cannula	5/8	130	1.8	Yes	No
cTAL	Compliant	No	PA-LA	Graft	5/8	130	2.4	Yes	Yes
PAD	Solid	No	VA, VV, VVA,VAV, PA-LA	Cannula, Graft-Cannula, Graft	3/8	35	0.4	Yes	Yes

ambulation. When paired with a ventricular assist device quality pump, one or two gas exchange modules can be attached in a variety of pumped configurations. Additionally, the low resistance of the PAD will allow it to function in a pumpless TAL PA-LA configurations. A summary of the basic attributes of all gas exchangers discussed in future chapters can be seen in **Table 1.5**.

1.5 References

1. Association AL. Lung disease data: 2008. Focus: Clean Air and Lung Disease Retrieved from http://www lungusa org. 2008.
2. The ADTF. Acute respiratory distress syndrome: The berlin definition. JAMA. 2012;307(23):2526-33. doi: 10.1001/jama.2012.5669.
3. Bshesh KK, Alasnag M. Acute Respiratory Failure. Textbook of Clinical Pediatrics: Springer; 2012. p. 2519-23.
4. Burt CC, Arrowsmith JE. Respiratory failure. Surgery (Oxford). 2009;27(11):475-9.
5. Pitman AP, Systrom D. Chronic Obstructive Pulmonary. Medicine. 2004:105.
6. Vender RL, Pitman AP, Systrom D. Acute Respiratory Failure. Medicine. 2004:129.
7. Zapol W, Frikker M, Pontoppidan H, Wilson R, Lynch K. The adult respiratory distress syndrome at Massachusetts General Hospital: Etiology, progression, and survival rates 1978-1988. Lung biology in health and disease. 1991;50:367-80.
8. EISNER MD, THOMPSON T, HUDSON LD, LUCE JM, HAYDEN D, SCHOENFELD D, et al. Efficacy of low tidal volume ventilation in patients with different clinical risk factors for acute lung injury and the acute respiratory distress syndrome. American journal of respiratory and critical care medicine. 2001;164(2):231-6.
9. Ventilation with Lower Tidal Volumes as Compared with Traditional Tidal Volumes for Acute Lung Injury and the Acute Respiratory Distress Syndrome. New England Journal of Medicine. 2000;342(18):1301-8. doi: doi:10.1056/NEJM200005043421801. PubMed PMID: 10793162.
10. Koh Y. Update in acute respiratory distress syndrome. J Intensive Care. 2014;2(2):1-6.
11. Plötz FB, Slutsky AS, van Vught AJ, Heijnen CJ. Ventilator-induced lung injury and multiple system organ failure: a critical review of facts and hypotheses. Intensive Care Med. 2004;30(10):1865-72.
12. Slutsky AS, Tremblay LN. Multiple system organ failure is mechanical ventilation a contributing factor? American Journal of Respiratory and Critical Care Medicine. 1998;157(6):1721-5.
13. Dreyfuss D, Saumon G. From ventilator-induced lung injury to multiple organ dysfunction? Intensive Care Med. 1998;24(2):102-4. doi: 10.1007/s001340050529.
14. Palmer LB. Ventilator-associated infection. Current opinion in pulmonary medicine. 2009;15(3):230-5.
15. Chastre J, Fagon J-Y. Ventilator-associated pneumonia. American journal of respiratory and critical care medicine. 2002;165(7):867-903.
16. Comparison of Two Fluid-Management Strategies in Acute Lung Injury. New England Journal of Medicine. 2006;354(24):2564-75. doi: doi:10.1056/NEJMoa062200. PubMed PMID: 16714767.
17. Marhong J, Munshi L, Detsky M, Telesnicki T, Fan E. Mechanical ventilation during extracorporeal life support (ECLS): a systematic review. Intensive Care Med. 2015;41(6):994-1003. doi: 10.1007/s00134-015-3716-2.
18. Kolla S, Awad SS, Rich PB, Schreiner RJ, Hirschl RB, Bartlett RH. Extracorporeal life support for 100 adult patients with severe respiratory failure. Annals of surgery. 1997;226(4):544.
19. Schmidt M, Pellegrino V, Combes A, Scheinkestel C, Cooper DJ, Hodgson C. Mechanical ventilation during extracorporeal membrane oxygenation. Crit Care. 2014;18(1):203.
20. Raghu G, Collard HR, Egan JJ, Martinez FJ, Behr J, Brown KK, et al. An official ATS/ERS/JRS/ALAT statement: idiopathic pulmonary fibrosis: evidence-based guidelines for diagnosis and management. American Journal of Respiratory and Critical Care Medicine. 2011;183(6):788-824.
21. Cystic Fibrosis Foundation. Patient Registry 2006 Annual Report.
22. Mogayzel PJ, Naureckas ET, Robinson KA, Mueller G, Hadjiliadis D, Hoag JB, et al. Cystic Fibrosis Pulmonary Guidelines. American Journal of Respiratory and Critical Care Medicine. 2013;187(7):680-9. doi: 10.1164/rccm.201207-1160OE.

23. Flume PA, O'Sullivan BP, Robinson KA, Goss CH, Mogayzel PJ, Willey-Courand DB, et al. Cystic Fibrosis Pulmonary Guidelines. American Journal of Respiratory and Critical Care Medicine. 2007;176(10):957-69. doi: 10.1164/rccm.200705-664OC.
24. Schraufnagel DE, Kell B. Breathing in America: diseases, progress, and hope: American Thoracic Society; 2010.
25. King TE, Behr J, Brown KK, du Bois RM, Lancaster L, de Andrade JA, et al. BUILD-1: A Randomized Placebo-controlled Trial of Bosentan in Idiopathic Pulmonary Fibrosis. American Journal of Respiratory and Critical Care Medicine. 2008;177(1):75-81. doi: 10.1164/rccm.200705-732OC.
26. Raghu G. Idiopathic pulmonary fibrosis. A rational clinical approach. CHEST Journal. 1987;92(1):148-54.
27. Selman M, Carrillo G, Estrada A, Mejia M, Becerril C, Cisneros J, et al. Accelerated variant of idiopathic pulmonary fibrosis: clinical behavior and gene expression pattern. PLoS One. 2007;2(5):e482.
28. Collard HR, Moore BB, Flaherty KR, Brown KK, Kaner RJ, King TE, et al. Acute exacerbations of idiopathic pulmonary fibrosis. American journal of respiratory and critical care medicine. 2007;176(7):636-43.
29. Azuma A, Nukiwa T, Tsuboi E, Suga M, Abe S, Nakata K, et al. Double-blind, placebo-controlled trial of pirfenidone in patients with idiopathic pulmonary fibrosis. American journal of respiratory and critical care medicine. 2005;171(9):1040-7.
30. Perlman DM, Loor G, Kim HJ, Tomic R. Considerations for Lung Transplantation in Patients With Idiopathic Pulmonary Fibrosis. Clinical Pulmonary Medicine. 2015;22(2):68-73.
31. Chen H, Shiboski SC, Golden JA, Gould MK, Hays SR, Hoopes CW, et al. Impact of the lung allocation score on lung transplantation for pulmonary arterial hypertension. American journal of respiratory and critical care medicine. 2009;180(5):468-74.
32. Egan TM, Murray S, Bustami R, Shearon T, McCullough KP, Edwards L, et al. Development of the new lung allocation system in the United States. American journal of transplantation. 2006;6(5p2):1212-27.
33. Galiè N, Humbert M, Vachiery J-L, Gibbs S, Lang I, Torbicki A, et al. 2015 ESC/ERS Guidelines for the diagnosis and treatment of pulmonary hypertension. European Heart Journal. 2015:ehv317.
34. Soto F. Pulmonary Venous Hypertension: A Pulmonologist's Perspective. Advances in PH Journal. 2011;10(1). Epub Spring 2011.
35. Chiumello D, Coppola S, Froio S, Colombo A, Del Sorbo L. Extracorporeal life support as bridge to lung transplantation: a systematic review. Critical Care. 2015;19(1):19.
36. Lehr CJ, Zaas DW, Cheifetz IM, Turner DA. Ambulatory extracorporeal membrane oxygenation as a bridge to lung transplantation: Walking while waiting. Chest. 2015;147(5):1213-8. doi: 10.1378/chest.14-2188.
37. Inci I, Klinzing S, Schneiter D, Schuepbach RA, Kestenholz P, Hillinger S, et al. Outcome of Extracorporeal Membrane Oxygenation as a Bridge To Lung Transplantation: An Institutional Experience and Literature Review. Transplantation. 2015;99(8):1667-71.
38. Biscotti M, Sonett J, Bacchetta M. ECMO as bridge to lung transplant. Thoracic surgery clinics. 2015;25(1):17-25.
39. Valapour M, Paulson K, Smith JM, Hertz MI, Skeans MA, Heubner BM, et al. OPTN/SRTR 2011 Annual Data Report: Lung. American Journal of Transplantation. 2013;13:149-77. doi: 10.1111/ajt.12024.
40. Schweickert WD, Hall J. ICU-acquired weakness. CHEST Journal. 2007;131(5):1541-9.
41. Levine S, Nguyen T, Taylor N, Friscia ME, Budak MT, Rothenberg P, et al. Rapid disuse atrophy of diaphragm fibers in mechanically ventilated humans. New England Journal of Medicine. 2008;358(13):1327-35.

42. Singer J, Blanc P, Hoopes C, Golden J, Koff J, Leard L, et al. The Impact of Pretransplant Mechanical Ventilation on Short-and Long-Term Survival After Lung Transplantation. American Journal of Transplantation. 2011;11(10):2197-204.
43. Abrams D, Brodie D. Extracorporeal respiratory support: on the road to an artificial lung. Minerva Med. 2014.
44. Zwischenberger JB, Anderson CM, Cook KE, Lick SD, Mockros LF, Bartlett RH. Development of an implantable artificial lung: Challenges and progress. ASAIO journal. 2001;47(4):316-20.
45. Pesenti A, Zanella A, Patroniti N. Extracorporeal gas exchange. Current opinion in critical care. 2009;15(1):52-8. Epub 2009/01/31. doi: 10.1097/MCC.0b013e3283220e1f. PubMed PMID: 19179870.
46. Gartner MJ, Wilhelm CR, Gage KL, Fabrizio MC, Wagner WR. Modeling Flow Effects on Thrombotic Deposition in a Membrane Oxygenator. Artificial Organs. 2000;24(1):29-36. doi: 10.1046/j.1525-1594.2000.06384.x.
47. Van Meurs K, aZwischenberger JB, Extracorporeal Life Support O. ECMO: extracorporeal c ardiopulmonary support in critical care. [Ann Arbor, Mich.]: Extracorporeal Life Support Organization; 2005. xxiii, 625 p. p.
48. Gravlee GP. Cardiopulmonary bypass: principles and practice. Philadelphia: Lippincott Williams & Wilkins; 2000. xvi, 768 p. p.
49. Agerstrand CL, Bacchetta MD, Brodie D. ECMO for Adult Respiratory Failure: Current Use and Evolving Applications. ASAIO Journal. 2014;60(3):255-62. doi: 10.1097/mat.0000000000000062. PubMed PMID: 00002480-201405000-00001.
50. Biscotti M, Vail E, PhD, KEC, Kachulis B, Rosenzweig EB, et al. Hybrid Configurations via Percutaneous Access for Extracorporeal Membrane Oxygenation: A Single-Center Experience2014.
51. Abrams D, Bacchetta M, Brodie D. Recirculation in Venovenous Extracorporeal Membrane Oxygenation. ASAIO Journal. 2015;61(2):115-21. doi: 10.1097/mat.0000000000000179. PubMed PMID: 00002480-201503000-00001.
52. Bermudez CA, Rocha RV, Sappington PL, Toyoda Y, Murray HN, Boujoukos AJ. Initial Experience With Single Cannulation for Venovenous Extracorporeal Oxygenation in Adults. The Annals of Thoracic Surgery. 2010;90(3):991-5. doi: http://dx.doi.org/10.1016/j.athoracsur.2010.06.017.
53. Lynch J, Zwischenberger J. Support Therapy for Lung Failure. In: Ferguson MK, editor. Difficult Decisions in Thoracic Surgery: Springer London; 2011. p. 187-94.
54. BRUNSTON RLJ, TAO W. Organ Blood Flow During Arteriovenous Carbon Dioxide Removal. ASAIO Journal. 1997;43(5):M825. PubMed PMID: 00002480-199709000-00099.
55. Cypel M, Keshavjee S. Extracorporeal life support as a bridge to lung transplantation. Clinics in chest medicine. 2011;32(2):245.
56. Lynch JE, Hayes Jr D, Zwischenberger JB. Extracorporeal CO2 Removal in ARDS. Critical Care Clinics. 2011;27(3):609-25. doi: http://dx.doi.org/10.1016/j.ccc.2011.05.002.
57. Ronco JJ, Belzberg A, Phang PT, Walley KR, Dodek PM, Russell JA. No differences in hemodynamics, ventricular function, and oxygen delivery in septic and nonseptic patients with the adult respiratory distress syndrome. Critical care medicine. 1994;22(5):777-82.
58. Flörchinger B, Philipp A, Klose A, Hilker M, Kobuch R, Rupprecht L, et al. Pumpless Extracorporeal Lung Assist: A 10-Year Institutional Experience. The Annals of thoracic surgery. 2008;86(2):410-7.
59. Camboni D, Philipp A, Arlt M, Pfeiffer M, Hilker M, Schmid C. First Experience With a Paracorporeal Artificial Lung In Humans. ASAIO Journal. 2009;55(3):304-6 10.1097/MAT.0b013e31819740a0.
60. Fischer S, Hoeper MM, Tomaszek S, Simon A, Gottlieb J, Welte T, et al. Bridge to lung transplantation with the extracorporeal membrane ventilator Novalung in the veno-venous mode: the initial Hannover experience. ASAIO Journal. 2007;53(2):168-70.

61. Strueber M, Hoeper MM, Fischer S, Cypel M, Warnecke G, Gottlieb J, et al. Bridge to Thoracic Organ Transplantation in Patients with Pulmonary Arterial Hypertension Using a Pumpless Lung Assist Device. American Journal of Transplantation. 2009;9(4):853-7. doi: 10.1111/j.1600-6143.2009.02549.x.
62. de Perrot M, Granton JT, McRae K, Cypel M, Pierre A, Waddell TK, et al. Impact of extracorporeal life support on outcome in patients with idiopathic pulmonary arterial hypertension awaiting lung transplantation. The Journal of Heart and Lung Transplantation. 2011;30(9):997-1002.
63. Kohler K, Valchanov K, Nias G, Vuylsteke A. ECMO cannula review. Perfusion. 2013;28(2):114-24.
64. Javidfar J, Brodie D, Costa J, Miller J, Jurrado J, LaVelle M, et al. Subclavian Artery Cannulation for Venoarterial Extracorporeal Membrane Oxygenation. ASAIO Journal. 2012;58(5):494-8. doi: 10.1097/MAT.0b013e318268ea15. PubMed PMID: 00002480-201209000-00008.
65. Schewe RE, Scipione CN, Koch KL, Cook KE. In-parallel attachment of a low-resistance compliant thoracic artificial lung under rest and simulated exercise. The Annals of thoracic surgery. 2012.
66. Scipione CN, Schewe RE, Koch KL, Shaffer AW, Iyengar A, Cook KE. Use of a low-resistance compliant thoracic artificial lung in the pulmonary artery to pulmonary artery configuration. The Journal of thoracic and cardiovascular surgery. 2013.
67. Sato H, Griffith GW, Hall CM, Toomasian JM, Hirschl RB, Bartlett RH, et al. Seven-day artificial lung testing in an in-parallel configuration. The Annals of thoracic surgery. 2007;84(3):988-94.
68. Sato H, Hall CM, Lafayette NG, Pohlmann JR, Padiyar N, Toomasian JM, et al. Thirty-Day In-Parallel Artificial Lung Testing in Sheep. The Annals of Thoracic Surgery. 2007;84(4):1136-43. doi: http://dx.doi.org/10.1016/j.athoracsur.2007.05.051.
69. Biscotti M, Bacchetta M. The "Sport Model": Extracorporeal Membrane Oxygenation Using the Subclavian Artery. The Annals of thoracic surgery. 2014;98(4):1487-9.
70. Wesolowski S, Fisher J, Welch C. Perfusion of the pulmonary circulation by nonpulsatile flow. Surgery. 1953;33(3):370.
71. Wesolowski SA. The role of the pulse in maintenance of the systemic circulation during heart-lung by-pass. ASAIO Journal. 1955;1:84&hyhen.
72. Hickey PR, Buckley MJ, Philbin DM. Pulsatile and Nonpulsatile Cardiopulmonary Bypass: Review of a Counterproductive Controversy. The Annals of Thoracic Surgery. 1983;36(6):720-37. doi: http://dx.doi.org/10.1016/S0003-4975(10)60286-X.
73. Wenstone R, Campbell J, Booker P, McKay R. Renal function after cardiopulmonary bypass in children: comparison of dopamine with dobutamine. British journal of anaesthesia. 1991;67(5):591-4.
74. Alkan T, Akçevin A, Ündar A, Türkoglu H, Paker T, Aytaç A. Benefits of Pulsatile Perfusion on Vital Organ Recovery During and After Pediatric Open Heart Surgery. ASAIO Journal. 2007;53(6):651-4. doi: 10.1097/MAT.0b013e31814fb506. PubMed PMID: 00002480-200711000-00001.
75. Ündar A, Masai T, Yang S-Q, Eichstaedt HC, McGarry MC, Vaughn WK, et al. Pulsatile Perfusion Improves Regional Myocardial Blood Flow during and after Hypothermic Cardiopulmonary Bypass in a Neonatal Piglet Model. ASAIO Journal. 2002;48(1):90-5. PubMed PMID: 00002480-200201000-00017.
76. Jonas RA, Newburger JW, Volpe JJ. Brain injury and pediatric cardiac surgery. Boston, Mass.: Butterworth Heinemann; 1996. xvi, 416 p. p.
77. Wang W, Bai SY, Zhang HB, Bai J, Zhang SJ, Zhu DM. Pulsatile flow improves cerebral blood flow in pediatric cardiopulmonary bypass. Artificial organs. 2010;34(11):874-8.
78. Itoh H, Ichiba S, Ujike Y, Douguchi T, Obata H, Inamori S, et al. Effect of the Pulsatile Extracorporeal Membrane Oxygenation on Hemodynamic Energy and Systemic Microcirculation in a Piglet Model of Acute Cardiac Failure. Artificial Organs. 2015:n/a-n/a. doi: 10.1111/aor.12588.

79. Cremers B, Link A, Werner C, Gorhan H, Simundic I, Matheis G, et al. Pulsatile Venoarterial Perfusion Using a Novel Synchronized Cardiac Assist Device Augments Coronary Artery Blood Flow During Ventricular Fibrillation. Artificial Organs. 2015;39(1):77-82. doi: 10.1111/aor.12413.
80. Stang K, Borchardt R, Neumann B, Kurz J, Stoppelkamp S, Greiner TO, et al. First In Vivo Results of a Novel Pediatric Oxygenator with an Integrated Pulsatile Pump. ASAIO Journal. 2015;61(5):574-82.
81. Krawiec C, Wang S, Kunselman AR, Ündar A. Impact of Pulsatile Flow on Hemodynamic Energy in a Medos Deltastream DP3 Pediatric Extracorporeal Life Support System. Artificial Organs. 2014;38(1):19-27. doi: 10.1111/aor.12117.
82. Wang S, Kunselman AR, Clark JB, Ündar A. In Vitro Hemodynamic Evaluation of a Novel Pulsatile Extracorporeal Life Support System: Impact of Perfusion Modes and Circuit Components on Energy Loss. Artificial Organs. 2015;39(1):59-66. doi: 10.1111/aor.12430.
83. Wang S, Izer JM, Clark JB, Patel S, Pauliks L, Kunselman AR, et al. In Vivo Hemodynamic Performance Evaluation of Novel Electrocardiogram-Synchronized Pulsatile and Nonpulsatile Extracorporeal Life Support Systems in an Adult Swine Model. Artificial Organs. 2015;39(7):E90-E101. doi: 10.1111/aor.12482.
84. Shepard RB, Simpson DC, Sharp JF. ENergy equivalent pressure. Archives of Surgery. 1966;93(5):730-40. doi: 10.1001/archsurg.1966.01330050034005.
85. Wright G. Hemodynamic analysis could resolve the pulsatile blood flow controversy. The Annals of Thoracic Surgery. 1994;58(4):1199-204. doi: http://dx.doi.org/10.1016/0003-4975(94)90498-7.
86. Ji B, Ündar A. An Evaluation of the Benefits of Pulsatile versus Nonpulsatile Perfusion during Cardiopulmonary Bypass Procedures in Pediatric and Adult Cardiac Patients. ASAIO Journal. 2006;52(4):357-61. doi: 10.1097/01.mat.0000225266.80021.9b. PubMed PMID: 00002480-200607000-00001.
87. Hoopes C. Ambulatory Extracorporeal Membrane Oxygenation. Operative Techniques in Thoracic and Cardiovascular Surgery. 2014;19(2):129-37. doi: http://dx.doi.org/10.1053/j.optechstcvs.2014.09.002.
88. Polastri M, Loforte A, Dell'Amore A, Nava S. Physiotherapy for Patients on Awake Extracorporeal Membrane Oxygenation: A Systematic Review. Physiotherapy Research International. 2015:n/a-n/a. doi: 10.1002/pri.1644.
89. Javidfar J, Brodie D, Iribarne A, Jurado J, LaVelle M, Brenner K, et al. Extracorporeal membrane oxygenation as a bridge to lung transplantation and recovery. The Journal of Thoracic and Cardiovascular Surgery. 2012;144(3):716-21. doi: http://dx.doi.org/10.1016/j.jtcvs.2012.05.040.
90. Allen S, Holena D, McCunn M, Kohl B, Sarani B. A review of the fundamental principles and evidence base in the use of extracorporeal membrane oxygenation (ECMO) in critically ill adult patients. Journal of Intensive Care Medicine. 2011;26(1):13-26.
91. Patroniti N, Zangrillo A, Pappalardo F, Peris A, Cianchi G, Braschi A, et al. The Italian ECMO network experience during the 2009 influenza A(H1N1) pandemic: preparation for severe respiratory emergency outbreaks. Intensive Care Med. 2011;37(9):1447-57. doi: 10.1007/s00134-011-2301-6.
92. Peek GJ, Mugford M, Tiruvoipati R, Wilson A, Allen E, Thalanany MM, et al. Efficacy and economic assessment of conventional ventilatory support versus extracorporeal membrane oxygenation for severe adult respiratory failure (CESAR): a multicentre randomised controlled trial. Lancet (London, England). 2009;374(9698):1351-63.
93. Turner DA, Cheifetz IM. Extracorporeal Membrane Oxygenation for Adult Respiratory Failure. Respiratory care. 2013;58(6):1038-52.

94. Toyoda Y, Bhama JK, Shigemura N, Zaldonis D, Pilewski J, Crespo M, et al. Efficacy of extracorporeal membrane oxygenation as a bridge to lung transplantation. The Journal of Thoracic and Cardiovascular Surgery. 2013;145(4):1065-71. doi: http://dx.doi.org/10.1016/j.jtcvs.2012.12.067.
95. Hoopes CW, Kukreja J, Golden J, Davenport DL, Diaz-Guzman E, Zwischenberger JB. Extracorporeal membrane oxygenation as a bridge to pulmonary transplantation. The Journal of Thoracic and Cardiovascular Surgery. 2013;145(3):862-8. doi: http://dx.doi.org/10.1016/j.jtcvs.2012.12.022.
96. Bermudez CA, Rocha RV, Zaldonis D, Bhama JK, Crespo MM, Shigemura N, et al. Extracorporeal Membrane Oxygenation as a Bridge to Lung Transplant: Midterm Outcomes. The Annals of Thoracic Surgery. 2011;92(4):1226-32. doi: http://dx.doi.org/10.1016/j.athoracsur.2011.04.122.
97. Fuehner T, Kuehn C, Hadem J, Wiesner O, Gottlieb J, Tudorache I, et al. Extracorporeal membrane oxygenation in awake patients as bridge to lung transplantation. American journal of respiratory and critical care medicine. 2012;185(7).
98. Ang A, Teo D, Lim C, Leou K, Tien S, Koh M. Blood transfusion requirements and independent predictors of increased transfusion requirements among adult patients on extracorporeal membrane oxygenation–a single centre experience. Vox sanguinis. 2009;96(1):34-43.
99. Ang AL. Predictors of increased transfusion requirements and optimizing transfusional support in patients on Extracorporeal membrane oxygenation (ECMO). ISBT Science Series. 2012;7(1):89-91. doi: 10.1111/j.1751-2824.2012.01552.x.
100. Khoshbin E, Roberts N, Harvey C, Machin D, Killer H, Peek GJ, et al. Poly-Methyl Pentene Oxygenators Have Improved Gas Exchange Capability and Reduced Transfusion Requirements in Adult Extracorporeal Membrane Oxygenation. ASAIO Journal. 2005;51(3):281-7.
101. Lehle K, Philipp A, Gleich O, Holzamer A, Müller T, Bein T, et al. Efficiency in Extracorporeal Membrane Oxygenation-Cellular Deposits on Polymethypentene Membranes Increase Resistance to Blood Flow and Reduce Gas Exchange Capacity. ASAIO Journal. 2008;54(6):612-7.
102. Haneya A, Philipp A, Mueller T, Lubnow M, Pfeifer M, Zink W, et al. Extracorporeal Circulatory Systems as a Bridge to Lung Transplantation at Remote Transplant Centers. The Annals of Thoracic Surgery. 2011;91(1):250-5. doi: http://dx.doi.org/10.1016/j.athoracsur.2010.09.005.
103. Maul TM, editor. ECMO Anticoagulation: It's Still the Biggest Challenge. ASAIO 61st Annual Conference; 2015; Chicago, IL: American Society of Artificial Internal Organs,.
104. Santambrogio L, Nosotti M, Palleschi A, Tosi D, Mendogni P, Lissoni A, et al. Use of Venovenous Extracorporeal Membrane Oxygenation as a Bridge to Urgent Lung Transplantation in a Case of Acute Respiratory Failure. Transplantation Proceedings. 2009;41(4):1345-6. doi: http://dx.doi.org/10.1016/j.transproceed.2009.02.065.
105. Cove ME, MacLaren G, Federspiel WJ, Kellum JA. Bench to bedside review: Extracorporeal carbon dioxide removal, past present and future.
106. Bein T, Weber F, Philipp A, Prasser C, Pfeifer M, Schmid F-X, et al. A new pumpless extracorporeal interventional lung assist in critical hypoxemia/hypercapnia*. Critical care medicine. 2006;34(5):1372-7.
107. Bein T, Zimmermann M, Hergeth K, Ramming M, Rupprecht L, Schlitt H, et al. Pumpless extracorporeal removal of carbon dioxide combined with ventilation using low tidal volume and high positive end-expiratory pressure in a patient with severe acute respiratory distress syndrome. Anaesthesia. 2009;64(2):195-8.
108. Zimmermann M, Bein T, Arlt M, Philipp A, Rupprecht L, Mueller T, et al. Pumpless extracorporeal interventional lung assist in patients with acute respiratory distress syndrome: a prospective pilot study. Crit Care. 2009;13(1):R10.
109. Johnson P, Fröhlich S, Westbrook A. Use of extracorporeal membrane lung assist device (Novalung) in H1N1 patients. Journal of cardiac surgery. 2011;26(4):449-52.

110. Iglesias M, Martinez E, Badia JR, Macchiarini P. Extrapulmonary ventilation for unresponsive severe acute respiratory distress syndrome after pulmonary resection. The Annals of thoracic surgery. 2008;85(1):237-44.
111. Fischer S, Simon AR, Welte T, Hoeper MM, Meyer A, Tessmann R, et al. Bridge to lung transplantation with the novel pumpless interventional lung assist device NovaLung. The Journal of Thoracic and Cardiovascular Surgery. 2006;131(3):719-23. doi: http://dx.doi.org/10.1016/j.jtcvs.2005.10.050.
112. Bartosik W, Egan JJ, Wood AE. The Novalung interventional lung assist as bridge to lung transplantation for self-ventilating patients – initial experience. Interactive CardioVascular and Thoracic Surgery. 2011;13(2):198-200. doi: 10.1510/icvts.2011.266346.
113. Baker A, Richardson D, Craig G. Extracorporeal carbon dioxide removal (ECCO2 R) in respiratory failure: an overview, and where next? 2C04 3A13.
114. iLA Activve. Available from: http://www.novalung.com/userfiles/EN-002-2011-05%20iLA%20activve%20product%20information.pdf.
115. Morris A, Wallace C, Menlove R, Clemmer T, Orme Jr J, Weaver L, et al. Randomized clinical trial of pressure-controlled inverse ratio ventilation and extracorporeal CO2 removal for adult respiratory distress syndrome. American Journal of Respiratory and Critical Care Medicine. 1994;149(2):295-305.
116. Batchinsky AI, Jordan BS, Regn D, Necsoiu C, Federspiel W, Morris M, et al. Veno-venous Extracorporeal CO 2 Removal: Can We Reduce Dependence on Mechanical Ventilation During En-route Care?
117. Batchinsky AI, Jordan BS, Regn D, Necsoiu C, Federspiel WJ, Morris MJ, et al. Respiratory dialysis: Reduction in dependence on mechanical ventilation by venovenous extracorporeal CO2 removal*. Critical care medicine. 2011;39(6):1382.
118. Burki NK, Mani RK, Herth FJ, Schmidt W, Teschler H, Bonin F, et al. A Novel Extracorporeal CO2 Removal SystemExtracorporeal CO2 Removal in COPDResults of a Pilot Study of Hypercapnic Respiratory Failure in Patients With COPD. CHEST Journal. 2013;143(3):678-86.
119. Wearden P, Federspiel W, Morley S, Rosenberg M, Bieniek P, Lund L, et al. Respiratory dialysis with an active-mixing extracorporeal carbon dioxide removal system in a chronic sheep study. Intensive Care Med. 2012;38(10):1705-11. doi: 10.1007/s00134-012-2651-8.
120. Boschetti F, Perlman CE, Cook KE, Mockros LF. Hemodynamic effects of attachment modes and device design of a thoracic artificial lung. ASAIO journal. 2000;46(1):42-8.
121. Perlman CE, Cook KE, Seipelt R, Mavroudis C, Backer CL, Mockros LF. In vivo hemodynamic responses to thoracic artificial lung attachment. ASAIO journal. 2005;51(4):412-25.
122. Akay B, Reoma JL, Camboni D, Pohlmann JR, Albert JM, Kawatra A, et al. In-parallel artificial lung attachment at high flows in normal and pulmonary hypertension models. The Annals of thoracic surgery. 2010;90(1):259-65.
123. Cook KE, Makarewicz AJ, Backer CL, Mockros LF, Przybylo H, Crawford SE, et al. Testing of an intrathoracic artificial lung in a pig model. Asaio Journal. 1996;42(5):M604-8.
124. Kuo AS, Sato H, Reoma JL, Cook KE. The relationship between pulmonary system impedance and right ventricular function in normal sheep. Cardiovascular Engineering. 2009;9(4):153-60.
125. Sato H, McGillicuddy JW, Griffith GW, Cosnowski AM, Chambers SD, Hirschl RB, et al. Effect of artificial lung compliance on in vivo pulmonary system hemodynamics. ASAIO journal. 2006;52(3):248-56.
126. Chambers S, Merz S, Mcgillicuddy J, Bartlett R, editors. Development of the MC3 BioLung™. Engineering in Medicine and Biology, 2002 24th Annual Conference and the Annual Fall Meeting of the Biomedical Engineering Society EMBS/BMES Conference, 2002 Proceedings of the Second Joint; 2002: IEEE.

127. Schmid C, Philipp A, Hilker M, Arlt M, Trabold B, Pfeiffer M, et al. Bridge to lung transplantation through a pulmonary artery to left atrial oxygenator circuit. The Annals of thoracic surgery. 2008;85(4):1202-5.

Chapter 2: Compact Cardiopulmonary Support Device

2.1 Introduction

Extracorporeal membrane oxygenation (ECMO) is a treatment where blood is pumped from the large vessels of the body through a circuit that removes carbon dioxide from the blood, adds oxygen to the blood, and returns the blood to the large vessels of the body. A large ECMO circuit (**Figure 2.1**) (1) consists of a centrifugal or roller pump, heat exchanger, gas exchanger, cannulas for the vessels, a blood reservoir, tubing, and monitoring equipment. ECMO systems are large with multiple devices with large resistances. This leads to excessive heat loss, large amounts of blood damage, limited ambulation, and a high level of required monitoring. Moreover, current ECMO systems employ steady blood flow. As discussed in Chapter 1, this steady blood flow regime is a deviation from the physiologic pulsatile flow regime, and there have been studies that suggest that poor organ perfusion results.(2-7)

Figure 2.1: A large pediatric ECMO circuit. (1)

Thoracic artificial lungs (TAL) have been proposed as replacements for ECMO, but they typically require a highly invasive thoracotomy.(8-11) As a result of a large surgical trauma to the

patient when a TAL is employed, it is not an option for patients who only require short term support. The compact cardiopulmonary assist device (CCSD) has been designed as a more compact replacement for ECMO that also produces a more physiologically similar pulsatile flow regime. The CCSD combines the heat exchanger, pump, and gas exchanger into one unit that is able to support a patient's gas exchange needs while theoretically providing better end organ perfusion when used in a VA attachment mode.(12, 13) The combining of multiple components into a single component should reduce heat exchange requirements, enhance patient mobility, reduce shear induced blood trauma, and reduce the level of monitoring required. Early prototype CCSD systems failed to produce blood flowrates adequate for supporting a patient. This study focuses on designing an improved CCSD system capable of delivering flowrates of at least 4 L/min to a patient.

2.2 Methods

2.2.1 CCSD System Description

The CCSD system is composed of 6 components (**Figure 2.2**); the gas exchange unit, the gas exchange enclosure, a pulsatile blood pump (Harvard Apparatus, Holliston, MA), a fluid warmer, and tubing for blood and saline. The CCSD contains two fluid systems separated by the flexible wall of the gas exchanger; the saline system and the blood system. Blood flows from the patient's large blood vessel(s) through a cannula, through a one way inlet valve in the gas exchanger, through the fiber bundle of gas exchanger where gas exchange occurs, through a one way outlet valve, back through a cannula, and into the patient's large blood vessel(s). The CCSD system functions in a cycle very similar to the cardiac cycle as seen in **Figure 2.3**. Saline is pumped from a pulsatile pump through a fluid warmer and into the CCSD rigid outer enclosure. As saline is pumped into the rigid enclosure, the pressure builds up inside the enclosure, and in turn the

blood inside the gas exchanger is also pressurized through the flexible wall of the gas exchanger. (**Figure 2.3 B**) Once the enclosure pressure exceeds the opening pressure of the gas exchanger's blood outlet valve, the housing of the gas exchanger compresses towards the fiber bundle and blood is pumped to the patient's venous or arterial vasculature.(**Figure 2.3 C**) At the end of systole the pressure gradient between the enclosure and the blood outside the outlet valve is equalized, and the blood outlet valve closes into its natural position.(**Figure 2.3 D**) As the pump cycles back, saline is pumped out of the rigid enclosure creating a negative pressure in the enclosure and on the blood inside the gas exchanger.(**Figure 2.3 E**) Once the enclosure pressure drops below the blood inlet valve opening pressure, the inlet valve opens. The housing of the gas exchanger

Figure 2.2: *Top:* The original prototype CCSD enclosure and gas exchanger assembly. *Middle:* The original prototype CCSD external ball valves. *Bottom:* The original prototype CCSD Harvard pulsatile pump.

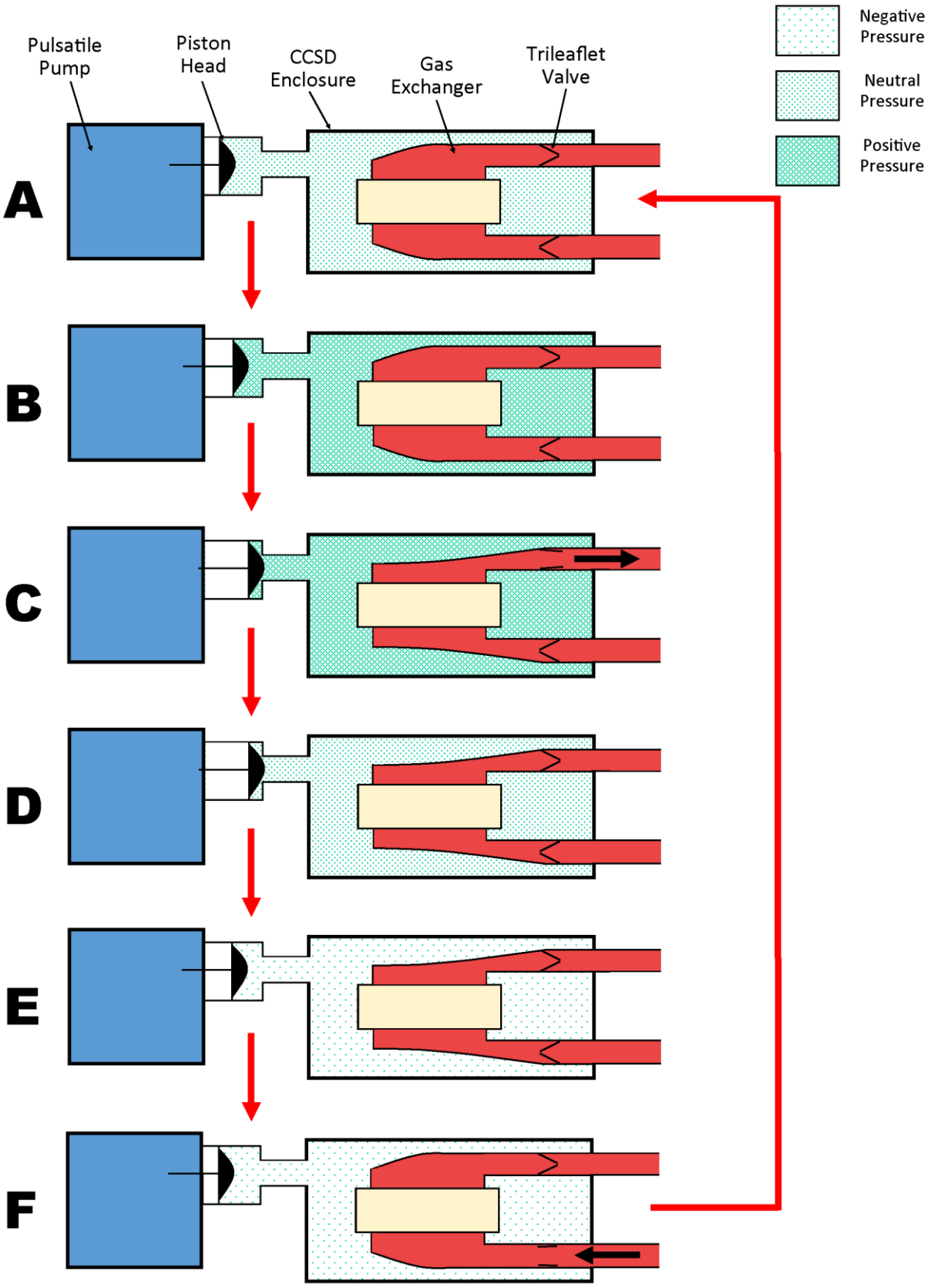

Figure 2.3: Pumping cycle of the CCSD.

expands away from the fiber bundle and pulls venous blood from the patient. (**Figure 2.3 F**) At the end of diastole, the enclosure pressure is equalized and the blood inlet valve closes back to its natural position to start the cycle again.(**Figure 2.3 A**) Since the saline entering the outer enclosure is warmed, heat is also added to the blood through the wall of the gas exchanger housing. This process repeats and cyclically draws blood from the patient, exchanges gasses with the blood, heats the blood, and pumps the blood back to the patient.

Early CCSD Prototype Shortcomings

Early prototype CCSD systems failed to produce adequate blood flowrates with cannula attachment due to excessive flexure of the CCSD enclosure and poor valve performance. The original prototype system shown in **Figure 2.2** employed external ball valves designed for non-medical applications (**Figure 2.2 Middle**) and a thin walled enclosure susceptible to stroke loss from flexure of the housing at high positive and negative pressures. Additionally, the blood conduit connectors attached to the enclosure had a tendency to leak during operation. An improved CCSD system was designed and tested to improve on these shortcomings as well as integrate more biocompatible valves into the gas exchange device itself. The development of the improved CCSD system is described in the following sections. The design and testing of the CCSD was broken down into three main sections; design of a more rigid housing with integrated blood conduit connections, design of integrated biocompatible valves, and testing of the overall CCSD system.

2.2.2 CCSD Enclosure Design and FEA Modeling

Based upon estimates from testing of the first generation CCSD system, the outer rigid enclosure of the device may experience pressures as high as 300 mmHg and as low as -200 mmHg. Flexing of the housing during pumping of the pulsatile saline pump leads to a loss in stroke volume and reduces pumping efficiency of the system. An enclosure flexure stroke loss of 10 mL as the

pump cycled from -200 mmHg to 300 mmHg was chosen as the maximum acceptable stroke loss when designing the enclosure. An initial enclosure design was drafted in Solidworks (Dassault Systems, Velizy-Villacoublay Cedexx, France) and was composed of two halves that bolt together encapsulate the gas exchanger. In order to accommodate the blood inlet and outlet ports, the two halves of the housing were unequal in thickness. The thicker half referred to as the "large half" included integrated blood inlet, blood outlet, gas inlet, and gas outlet ports.(**Figure 2.4**) The thinner half referred to as the "small half" included a saline port.(**Figure 2.5**) CAD models of this initial enclosure design were produced with wall thicknesses of 0.5, 0.75, 1, and 1.25 inches.

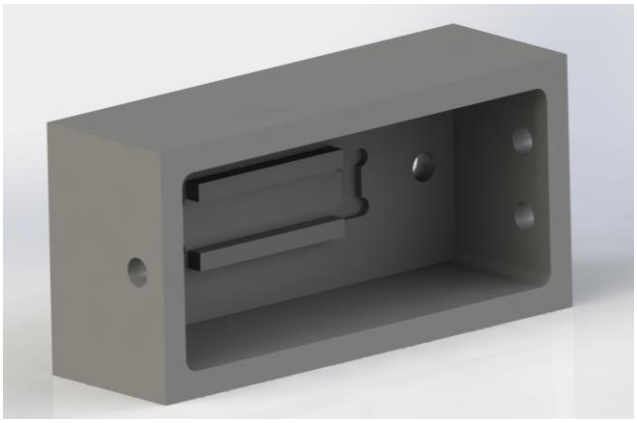

Figure 2.4: Large half of CCSD enclosure used in finite element modeling.

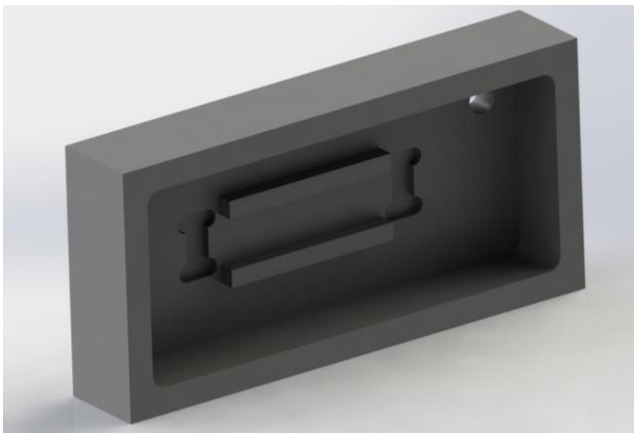

Figure 2.5: Small half of CCSD enclosure used in finite element modeling.

Ansys Mechanical finite element solver and Ansys Results modules (ANSYS Inc., Canonsburg, PA) were used to estimate the stroke volume loss due to enclosure flexure for enclosure designs with different wall thicknesses. The large half and small half of each enclosure were modeled separately and the volume stroke loss for each half were summed to yield a total volume loss for the enclosure. In order to capture the volume loss over one pressure cycle, the

maximum positive and negative pressures of 300 mmHg and -200 mmHg were modeled for the entire enclosure and the results were summed to yield a total stroke volume loss.

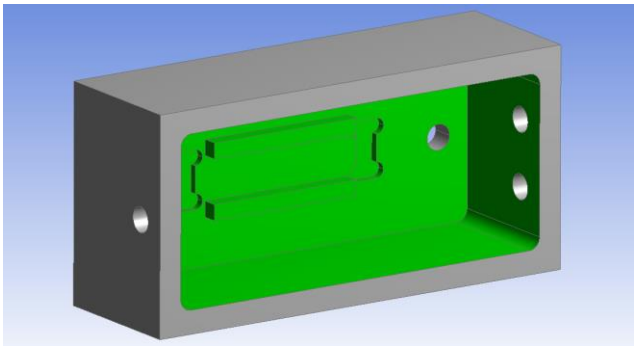

Figure 2.6: Inside faces of the large half of CCSD Enclosure.

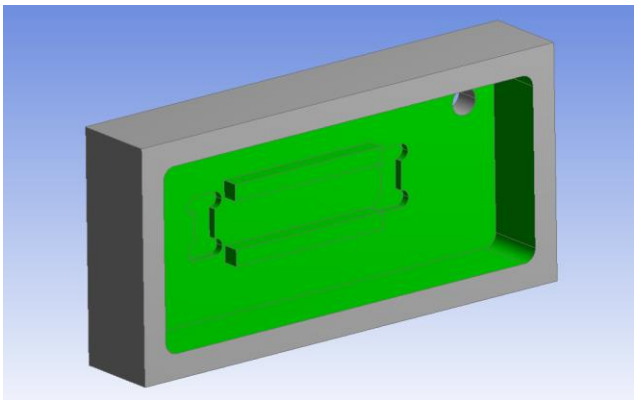

Figure 2.7: Inside faces of the small half of CCSD Enclosure.

Geometry and Meshing

The Solidworks part file was converted to an .igs file and was imported into the Ansys Static Structural module. The Ansys Meshing program was used to create a free mesh that discretized the geometry finite element analysis. A global grid spacing was specified for the entire body, and a refined face grid spacing was imposed for all small and/or curved faces. A named selection of "inside faces" was created on all inside surfaces of the enclosure for later load creation.(**Figures 2.6 & 2.7**) In order to perform a grid independence study, a refined mesh was also created with spacings half the size of the original grid spacings. The original and refined grid spacings are listed in **Table 2.1**, and sample meshes can be seen in **Figures 2.8** and **2.9**. The total stroke volume loss was calculated for the two grid

Table 2.1: The grid spacings used in FEA modeling.

Grid	Global Spacing (mm)	Refinement Region Spacing (mm)
1	5.08	1.27
2	2.54	0.635

spacings and compared to confirm that further refinement the mesh results in minimal changes in the results. Mesh was classified as "grid independent" if the results varied by less than 5%. The grid dependence study was performed for the enclosure design with a wall thickness of 0.5 inches since the most deflection will be observed in this case and will require the most refined grid.

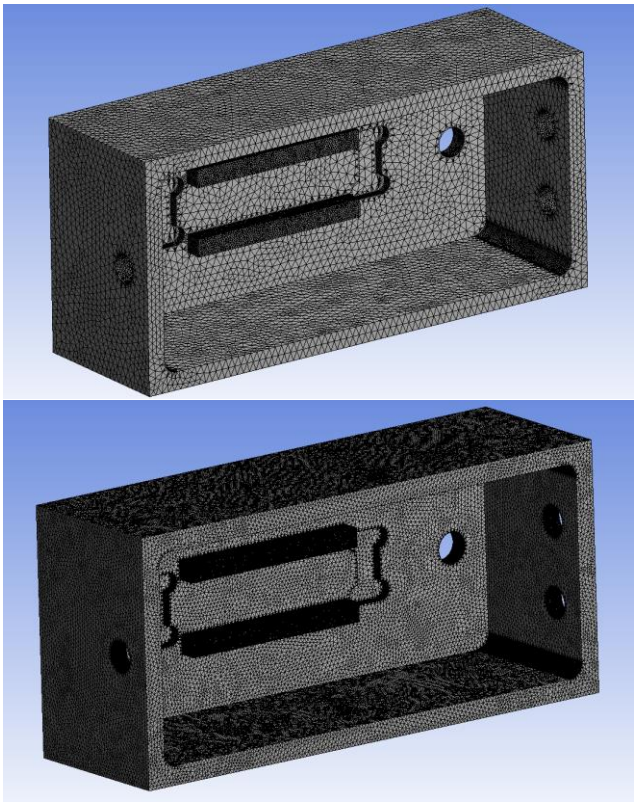

Figure 2.8: Meshes of the large half of the enclosure. *Top:* Course Grid. *Bottom:* Fine Grid

Finite Element Analysis

The Ansys Static Structural module was utilized to setup the finite element solver. The finite element analysis was performed using cell cast acrylic and Type 1 PVC. The Cell cast Acrylic was modeled using a density of 1185 $\frac{kg}{m^3}$, a poisson's ratio of 0.37, and a Young's modulus of 3.05 GPa. Type 1 PVC was modeled using a density of 1400 $\frac{kg}{m^3}$, a poisson's ratio of 0.41, and a Young's modulus of 2.90 GPa. Load and boundary conditions were imposed to simulate pressurization of the enclosure at the systolic and diastolic pressures of 300 mmHg and negative 200 mmHg, respectively. The part was fixed in three dimensional space by imposing two sets of boundary conditions. The back outside corners of the enclosure were fixed in the x and y directions since they will experience minimal deformations in those directions during pressurization.(**Figure 2.10**) The sealing face was fixed in the z direction since the clamping of the two halves of the enclosure together will only allow for very little deformation in this direction

since the clamping bolts will take the load of pressurization in the z direction at this face.(**Figure 2.11**) The Ansys Mechanical finite element solver was run and results were output for post processing.

Post Processing

The Ansys Results module was utilized to estimate the total stroke volume loss due to enclosure flexure. Clip planes were used to reduce the deformed surface mesh to the inside faces of each enclosure half as seen in **Figures 2.12** and **2.13**. Clipping of the mesh resulted in extra surfaces near inlet/outlet port holes. However any mesh displacement on these holes will be offset to some extent by the lack of mesh on the face of port holes, and will provide sufficiently accurate results for the purpose of choosing a proper wall thickness for the enclosure design. The area weighted integral of mesh deformation was calculated over the clipped surface mesh to yield an estimate of the change in volume of the inside of each enclosure half. The summation of the volume change of each

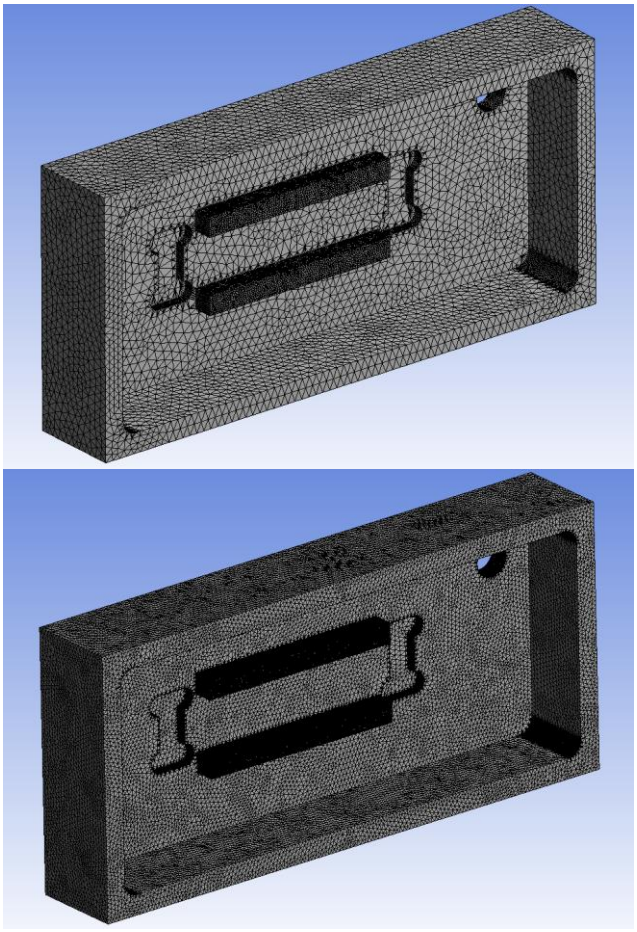

Figure 2.9: Meshes of the Small half of the enclosure. *Top:* Course Grid. *Bottom:* Fine Grid

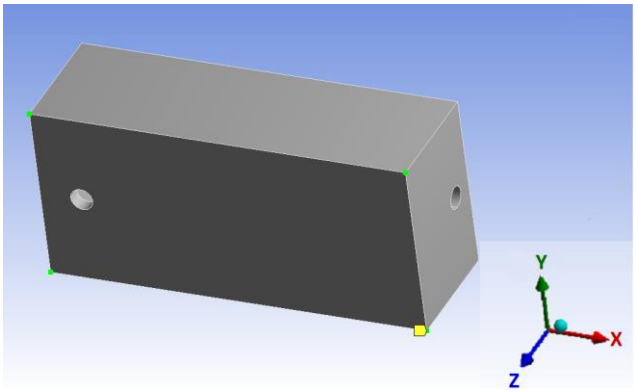

Figure 2.10: Constrained corners of the large enclosure half.

enclosure half yielded the total volume change for the enclosure at the given pressure. This procedure was performed at the diastolic pressure of negative 200 mmHg and the systolic pressure of positive 300 mmHg. The absolute value of change in enclosure volume for systolic and diastolic cases were summed to yield the total stroke volume loss due to enclosure flexure at a given wall thickness.

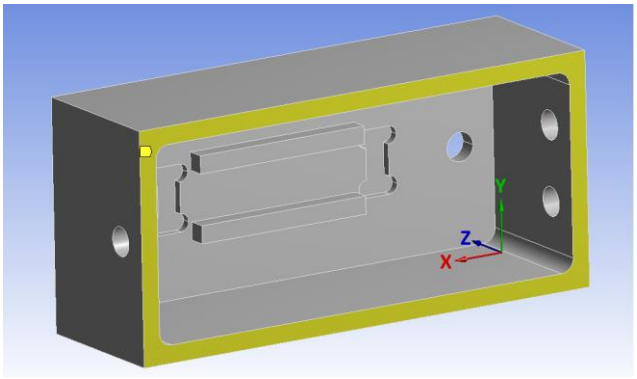

Figure 2.11: Constrained face of the large enclosure half.

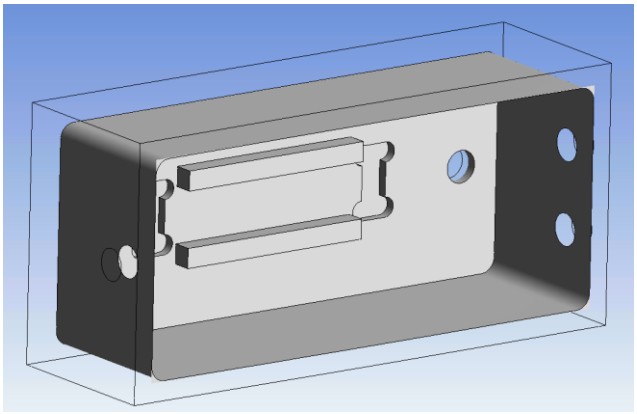

Figure 2.12: Clipped surfaces used in post processing for the large enclosure half.

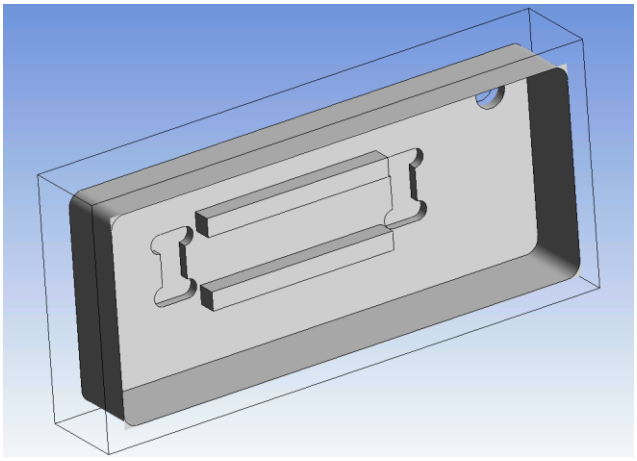

Figure 2.13: Clipped surfaces used in post processing for the small enclosure half.

Final Design FEA

After finding an appropriate wall thickness through the use of finite element analysis a final enclosure design was produced in Solidworks. As can be seen in **Figures 2.14** and **2.15**, the final design integrated the device holding/ anti-shunting region of the enclosure into the wall to increase wall thickness without adding material costs and to reduce machining costs. Prior to machining, the above finite element analysis methods were utilized to produce a final estimate of total stroke volume loss.

2.2.3 CCSD Enclosure Benchtop Testing

After fabrication of the CCSD enclosure it was tested for total stroke volume loss. All ports were clamped off with the exception of the two de-airing/pressure monitoring luer lock ports. The enclosure was bolted together and de-aired through the two luer lock ports. A syringe pump () filled with saline was attached to one enclosure luer port, and a Transpac IV pressure transducer (ICU Medical Inc, San Clemente, CA) was attached to the other luer lock port. A Biopac MP150 data acquisition system (Biopac Systems Inc, Goleta, CA) was used to record pressure inside the enclosure in real time. A syringe pump (New Era Pump Systems Inc, Farmingdale, NY) was used to inject fluid volume into the enclosure in small increments resulting in incremental pressure increases in the enclosure. Once a pressure of positive 300 mmHg was obtained the volume injected into the enclosure was recorded. This procedure was repeated with the syringe pump withdrawing fluid from the enclosure rather than injecting in order to obtain a negative pressure of 200 mmHg. **Equation 2.1** was utilized to correct for small deviations from the target pressures.

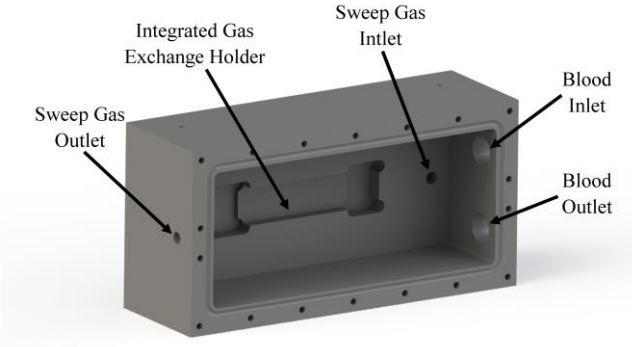

Figure 2.14: Large Half of the final CCSD enclosure design.

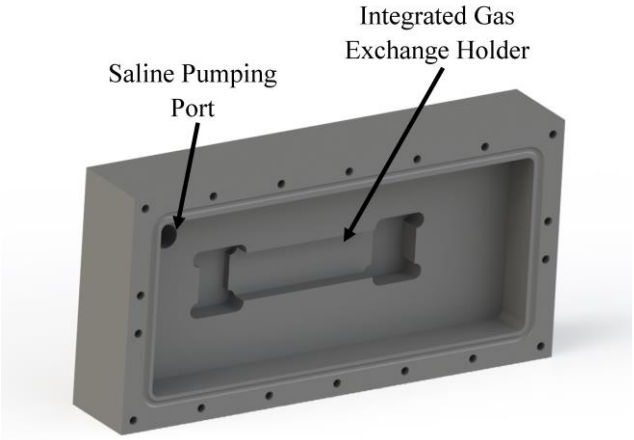

Figure 2.15: Large Half of the final CCSD enclosure design.

$$V_{cor} = V_{inj} * \frac{P_{tar}}{P_{inj}}, \tag{2.1}$$

where V_{cor} is the corrected volume injected, V_{inj} is the actual volume injected during the experiment, P_{tar} is the target pressure for the experiment, and P_{inj} is the actual pressure attained during the experiment. For example, an actual pressure and injected volume of 279.2 mmHg and 2.60 mL, respectively, the corrected volume was 2.62 mL. The corrected volume injected to increase the pressure to 300 mmHg and the corrected volume withdrawn to decrease the pressure to negative 200 mmHg were summed to yield a total stroke volume loss due to enclosure flexure. The enclosure was disassembled, reassembled, and tested three times (n=3).

2.2.4 CCSD Valve Description and Fabrication

The first feasibility prototype of the CCSD used external ball valves located outside of the CCSD enclosure to maintain uni-directional flow. However, these valves are designed for non-medical use and would likely cause damage to the blood and result in thrombus and subsequent emboli shedding in the valve. Additionally, these external valves add to system complexity and bulk. As a result, more biocompatible valves were desired that would integrate into the gas exchange unit's blood inlet and outlet conduits. In order to allow efficient pumping and blood damage these valves needed to have a resistance below 1 mmHg/(L/min) and a regurgitant fraction below 10%.

The flexible housing of the gas exchanger was composed of Biospan polyurethane (DSM, Exton, PA), and the valves were fabricated from the same material. A tri-leaflet design was chosen to partially mimic the mitral valve of the heart. Previous attempts of fabricating polymeric trileaflet heart valves have been largely unsuccessful because they utilized either single sheets of polymer folded and sutured into a mitral valve like configuration or individual pieces of polymer sutured onto a ring to form valve leaflets. Repeated cycling of sutured polymers eventually leads to tearing at or near the sutures.

The valve ring and leaflet for the CCSD valve are molded as a single piece of polyurethane to enhance durability of the valve. A detailed description of the fabrication process can be seen in **Appendix A**. A basic description of the valve fabrication process are as follows. A Teflon mold of the valve is dipped into Biospan polyurethane and placed on a rotisserie for drying. After at least 2 hours of drying, the valve is re-dipped and dried multiple times to attain the desired valve leaflet thickness. The seams between the leaves are then cut to form three separate leaves. The valve is then epoxied into either the CCSD blood inlet or outlet conduit for CCSD system testing or into a separate Biospan tube for *in vitro* valve testing. The outside of the valve is reinforced with a polycarbonate or PVC tube to prevent valve collapse during application of negative pressures.

2.2.5 CCSD Valve Benchtop Testing

Prior to testing the CCSD system with integrated Biospan trileaflet valves, valves of different diameters and leaflet thicknesses were tested for optimal resistance and regurgitation characteristics. Valves were fabricated with diameters of 0.688, 1, 1.125, and 1.25 inches and leaflet thicknesses of approximately 0.040 and 0.060 inches. The 0.688 inch diameter was also manufactured with a leaflet thickness of 0.020 inches. Each of these valves was tested in a test circuit consisting of a pulsatile pump, an industrial ball valve, a valve to be tested, and a reservoir.(**Figure 2.16**) The circuit was filled with glycerol having a viscosity of 3.0 cP to simulate blood. Transpac IV pressure transducers were attached immediately before and after the valve to measure pressure drop, and a 5/8 inch PXL tubing flow probe (Transonic Systems Inc, Ithaca, NY) was placed upstream of the valve to measure volume flow rate. Pressure and flow data was acquired using a Biopac MP150 data acquisition system.

After circuit assembly the valves were tested at a variety of flowrates, pump cycle rates,

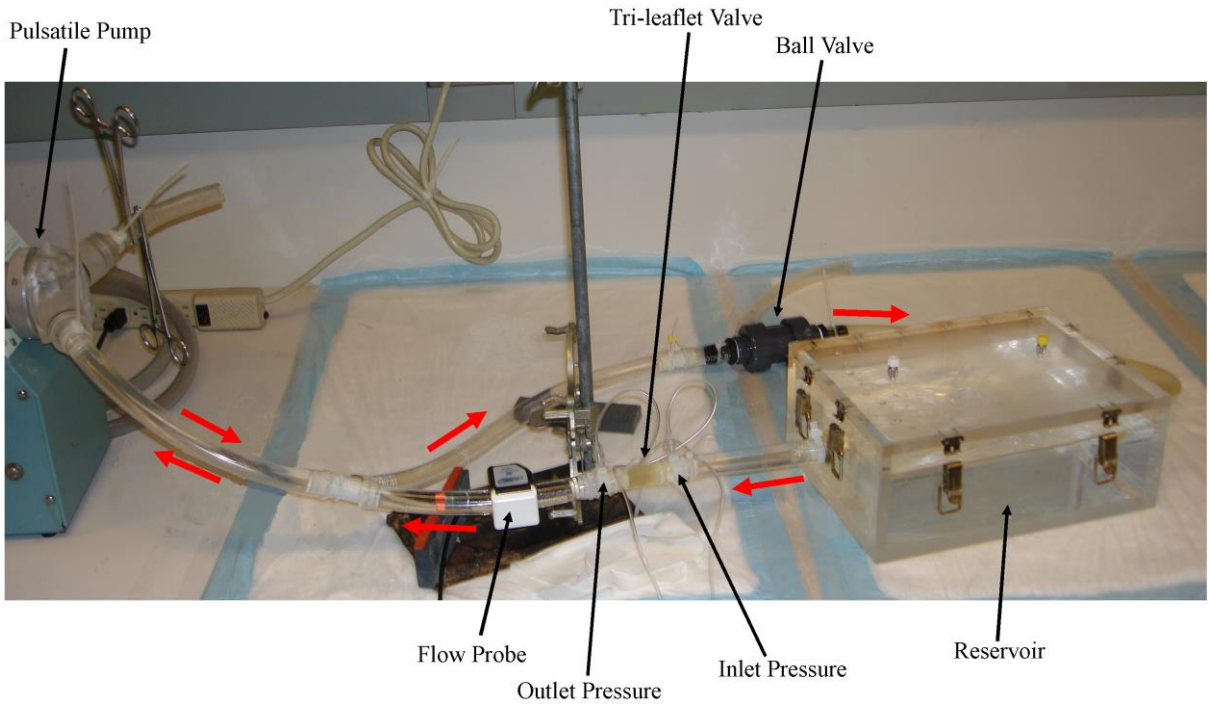

Figure 2.16: CCSD valve *in vitro* testing circuit.

and systolic to diastolic ratios by altering the settings on the Harvard pulsatile pump. Each valve design was tested with three valves (n=3) at flowrates of 3 and 5 L/min, pump cycle rates of 80 and 100 bpm, and a % systolic time of 33%. Data from the flow probe and pressure transducers were analyzed to yield resistance through the valve and regurgitant fraction of the valve. Raw data from five cycles of the pump were manually segregated from the data set and used in subsequent calculations. Resistance of the valve was calculated using **Equation 2.2**.

$$Res = \frac{P_{post} - P_{post}}{\dot{Q_f}} \tag{2.2}$$

Where Res is the valve resistance, P_{post} is the time averaged post valve pressure during forward flow, P_{pre} is the time averaged pre valve pressure during forward flow, and Q_f is the time averaged flowrate during forward flow. Regurgitant fraction of the valve was calculated from **Equation 2.3**.

$$RF = \frac{\dot{Q_r}}{\dot{Q_t}} \tag{2.3}$$

Where RF is the regurgitant fraction, $\dot{Q}_r$ is the time averaged reversed flowrate, and $\dot{Q}_t$ is the time averaged flowrate for all flow directions.

2.2.6 CCSD System In vitro Fluid Dynamics Testing

After finalizing the valve size of the CCSD system, the gas exchange device was fabricated and the system was assembled for initial *in vitro* fluid dynamics testing to characterize the regurgitant fraction of the system, pumping flowrate capabilities, and enclosure pressures. The *in vitro* testing of the CCSD was performed in three stages. In the first stage the first prototyped CCSD systems utilizing 0.040" leaflet thickness valves were tested for regurgitant fraction and enclosure driving pressures. In the second stage of the testing the CCSD was fabricated with thicker 0.060" leaflet valves and tested with the same end goals as stage 1 since the 0.040" leaflet valves were not sufficiently stiff.

In the third stage of testing, multiple priming methods were employed with the goal of reducing the magnitude of negative pressures inside the enclosure during pumping of the CCSD. These priming methods were performed to pre-stretch the housing of the CCSD gas exchanger and increase the amount of time in the unfurling stage of the housing. As the housing of the CCSD and similar cTAL gas exchangers are filled with fluid their expansion undergoes two phases; unfurling and stretching. In the unfurling stage where the housing is expanding with little stretching, the housing is very

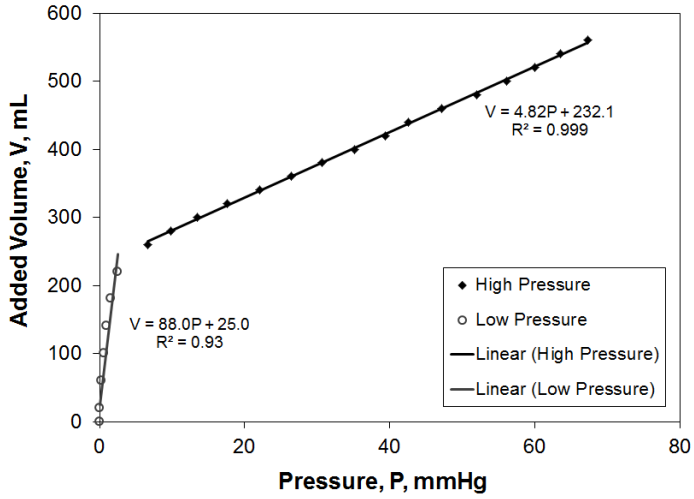

Figure 2.17: Compliance of the cTAL with high pressure representing the stretching phase and low pressure representing the unfurling stage. (8)

compliant with large changes in volume occurring with little change in pressure.(**Figure 2.17**) (9) However, once the housing unfurls completely it enters the stretching phase where any increases in volume are due to low compliance housing stretching and are in turn accompanied by large changes in pressure.(**Figure 2.17**) (9) In the altered priming methods maximizing the time in the unfurling stage has the potential to reduce the amount of work performed by the pump to pull fluid into the gas exchanger housing, thereby reducing negative enclosure pressures.

CCSD System Fabrication

The gas exchanger was fabricated using methods described in **Appendix B**. A basic outline of the process are as follows. The flexible housing of the gas exchanger was dip cast in Biospan polyurethane in a series of layers to build up a wall thickness. A fiber bundle composed of Membrana 300 micron outside diameter microporous polypropylene fibers (Membrana GmbH, Wuppertal, Germany) was wound around a polycarbonate core. The bundle and housing were centrifuge potted together using polyurethane. The potted section was partially sliced off to open the lumen of the gas exchange fibers, and acrylic gas caps were attached to serve as gas distribution manifolds. The trileaflet valves were epoxied into the inside of the blood inlet and outlet conduits. A stiff reinforcement tube was epoxied onto the outside of the blood inlet and outlet conduits to prevent valve performance losses from crushing of the conduits. The gas exchanger was inserted into the rigid acrylic enclosure and all tubing was secured to the enclosure's integrated connectors with zip ties. Outside of the enclosure, the blood inlet and outlet conduits were gradually stepped down in diameter until the final tubing size of 3/8 inch inner diameter tubing was attained.

CCSD System In vitro Experimental Setup

The *in vitro* testing setup (**Figure 2.18**) consisted of the CCSD assembly, a Harvard pulsatile pump for controlling CCSD pumping, a glycerol reservoir, and optional cannulas (32/40

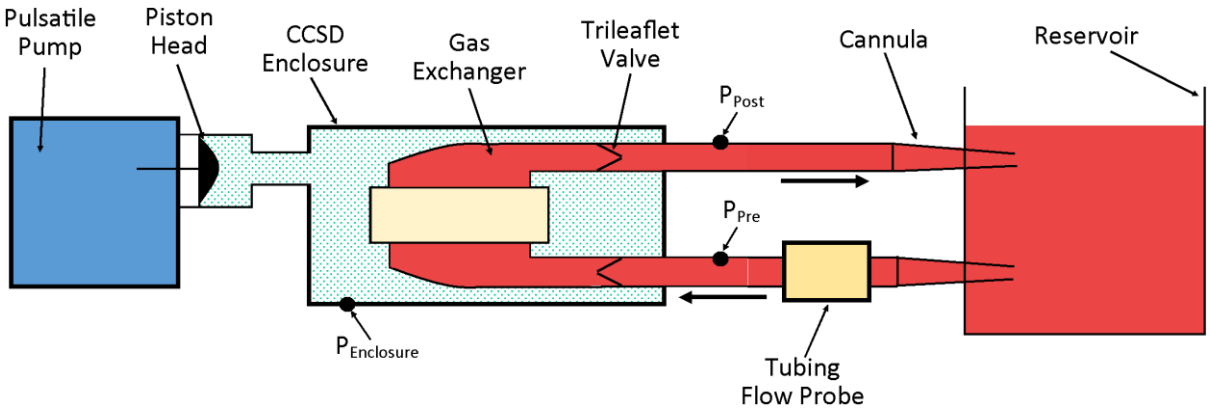

Figure 2.18: The CCSD system *in vitro* testing circuit.

Fr). Initial tests of the CCSD system in Stage 1 did not utilize cannulas with cannulas being added in later experiments to simulate *in vivo* tests. The gas exchange unit and blood conduits were primed with a 3.0 cP glycerol solution to simulate blood, and the enclosure and pulsatile pump were primed with water as the pumping fluid medium. Pressure transducers were connected on the enclosure pressure port to measure enclosure pressure, and immediately before and after the CCSD gas exchanger to measure inlet and outlet conduit pressures. A 5/8 inch PXL tubing flow probe was attached downstream of the gas exchanger to measure flowrate and regurgitant fraction. All data was recorded with a MP150 Biopac data acquisition system and analyzed in Microsoft Excel (Microsoft, Redmond, WA). The pulsatile pump was used to control the pumping rate, systolic to diastolic ratio, and volume flowrate. The reservoir was placed at different levels to simulate different positioning of the device relative to the patient. The controls on the pulsatile pump were adjusted to attain the target flow conditions. If significant amounts of air were pulled into the system as flowrate increased, the device was de-aired in preparation for the next test condition. Regurgitant fraction was calculated from **Equation 2.3**.

CCSD System Priming

During priming of the CCSD, in the stage 1 and stage 2 *in vitro* testing of the CCSD system, the CCSD was primed as follows. First the gas exchanger unit was placed into the CCSD enclosure

with the blood conduits facing vertically and filled with glycerol up until the first step down in tubing size. Gas bubbles were removed from the device and the tubing was clamped before returning the device to the horizontal position. The enclosure was then sealed and the pump head was returned to its fully retracted position. The enclosure, pump tubing, and pump head were filled with water and de-aired. The second tubing connection of the pulsatile pump was unused, so tubing was attached and clamped off to prevent any flow through this connection. The remaining blood conduit tubing was filled with glycerol, inserted to the glycerol reservoir, and the blood conduit tubing clamps were removed.

In stage 3 *in vitro* testing of the CCSD system, six priming methods were employed in an attempt to increase the amount of time in the housing unfurling stage and reduce the magnitude of internal negative pressures in the CCSD enclosure. Of these 6 methods, the method resulting in the lowest magnitudes of negative enclosure pressure is presented. The gas exchanger was placed with the blood conduits facing vertically and filled with glycerol up until the first step down in tubing size. Gas bubbles were removed from the device and the tubing was clamped before returning the device to the horizontal position. The enclosure was then sealed in preparation for enclosure priming. The stroke volume setting of the pulsatile pump was set to its 100% position and the piston head was retracted to its fully retracted position. A hand pump sphygmomanometer

Table 2.2: The testing conditions for Stage 1 *in vitro* CCSD pumping experiments.

Test Condition	Flowrate (L/min)	Pulse Rate (bpm)	Percent Systolic Time (%)	Reservior Raised? (Y/N)	Cannulas (Y/N)
1	2	80	33%	N	N
2	2	100	33%	N	N
3	4	80	33%	N	N
4	4	100	33%	N	N
5	2	80	33%	Y	N
6	2	100	33%	Y	N
7	4	80	33%	Y	N

(Welch Allyn, Skaneateles, NY) was attached to the blood inlet conduit and was used to pressurize the gas exchanger to 20 mmHg. The enclosure and pump head were primed with water and de-aired before removing the sphygmomanometer. The remaining blood conduit tubing and cannulas were primed with glycerol and inserted into the glycerol reservoir. Lastly, the blood conduits were then unclamped to complete priming.

CCSD System In vitro Test Conditions

During Stage 1, the CCSD system with 0.040" leaflet valves was tested without cannulas at the conditions listed in **Table 2.2**. When the glycerol reservoir was in its raised position the reservoir was raised so that the surface level of the glycerol was 30.2 inches higher than the center of the gas exchanger to simulate use with the CCSD on a low cart bedside to a patient. When the reservoir was not in its raised position the glycerol surface was 3.7 inches higher than the center of the gas exchanger to simulate the system used at bed level. During Stage 2, the CCSD system

Table 2.3: The testing conditions for Stage 2 *in vitro* CCSD pumping experiments.

Test Condition	Flowrate (L/min)	Pulse Rate (bpm)	Percent Systolic Time (%)	Reservior Raised? (Y/N)	Cannulas (Y/N)
1	2	80	33%	Y	N
2	2	100	33%	Y	N
3	4	100	33%	Y	N
4	4	Maximum	33%	Y	N
5	2	80	33%	Y	Y
6	2	100	33%	Y	Y
7	4	100	33%	Y	Y
8	4	Maximum	33%	Y	Y
9	2	80	50%	Y	Y
10	2	100	50%	Y	Y
11	4	100	50%	Y	Y
12	4	Maximum	50%	Y	Y
13	2	80	33%	N	Y
14	2	100	33%	N	Y
15	4	100	33%	N	Y
16	4	Maximum	33%	N	Y

Table 2.4: The testing conditions for Stage 3 *in vitro* CCSD pumping experiments.

Test Condition	Priming Pressure (mmHg)	Flowrate (L/min)	Pulse Rate (bpm)	Percent Systolic Time (%)	Reservior Raised? (Y/N)	Cannulas (Y/N)
1	20	2	80	33%	N	Y
2	20	2	100	33%	N	Y
3	20	4	100	33%	N	Y
4	20	4	Maximum	33%	N	Y

with 0.060" leaflet valves was tested with and without cannulas at the conditions listed in **Table 2.3**. During Stage 3, the CCSD system with 0.060" leaftlet valves and an altered priming method was tested with cannulas at the conditions listed in **Table 2.4**.

2.3 Results

2.3.1 CCSD Enclosure Modeling

The CCSD enclosure was modeled using finite element analysis to determine the wall thickness necessary to reduce stroke volume losses due to enclosure flexure to below 10 mL. A sample band plot of mesh deformation (**Figure 2.19**) shows that the largest areas of enclosure deformation occurred at the sealing edges of the long sidewalls of the large enclosure half. A plot of total stroke volume as a function of wall thickness for acrylic and PVC enclosures can be seen in **Figure 2.20**. As the wall thickness increases above 1 inch, the volume losses reduce exponentially to a point were further increases in wall thickness yield only small changes in stroke volume loss. The stiffer acrylic enclosure yielded slightly lower total stroke volume losses when compared to the PVC enclosures. The final enclosure design had a side wall thickness of 1.125 inches and was machined from acrylic. The final enclosure design yielded a total stroke volume loss of 5.84 mL predicted by finite element analysis.

2.3.2 CCSD Enclosure Benchtop Testing

Benchtop testing of the final machined enclosure was performed to attain the actual

physical losses of volume during CCSD operation. The volume loss due to enclosure flexure for systole, diastole, and the entire stroke can be seen in **Table 2.5**. The total stroke volume loss due to enclosure flexure for the final machined enclosure was 4.707 ± 0.257 mL.

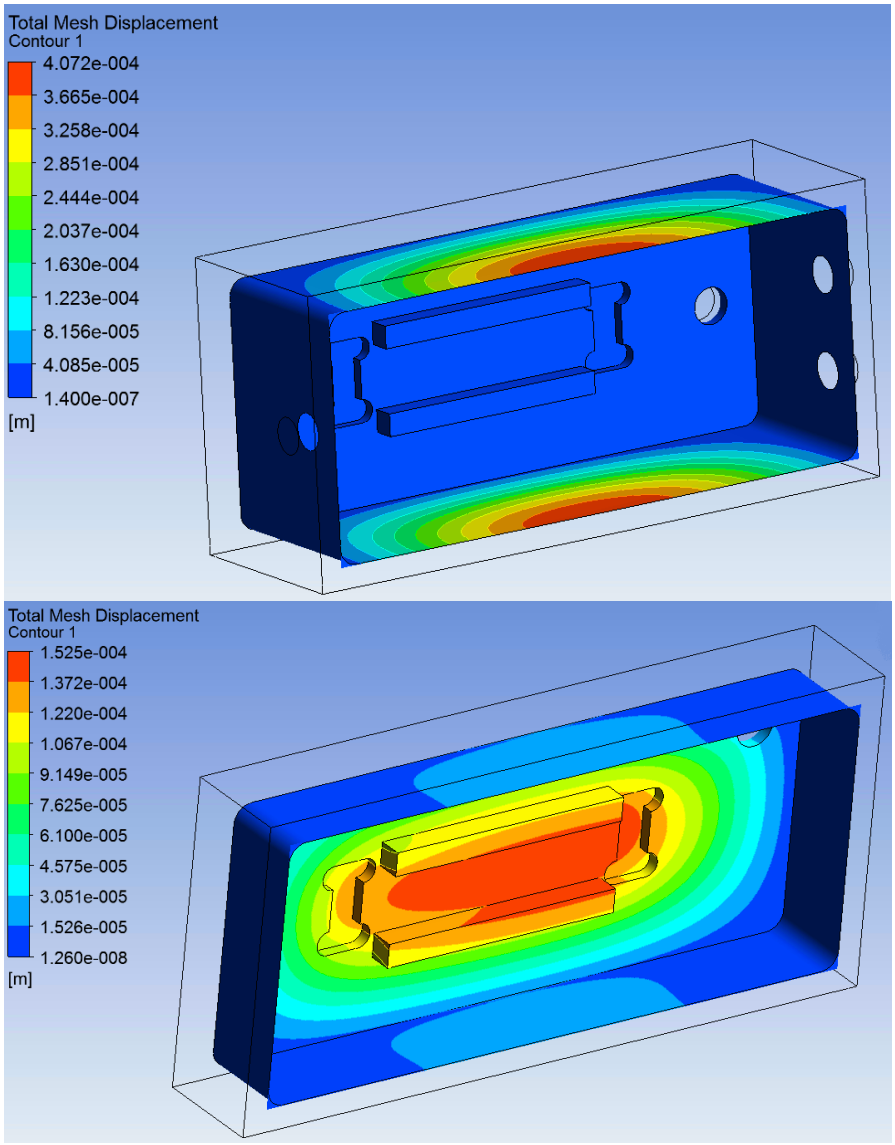

Figure 2.19: Displacement band plots. *Top:* Large enclosure half. *Bottom:* Small enclosure half.

2.3.3 CCSD Valve Benchtop Testing

The CCSD valves were tested in a benchtop system to characterize the regurgitation and resistance of valves with diameters ranging from 0.688 to 1.25 inches and leaflet thicknesses ranging from 0.020 to 0.060 inches. The only diameter valve tested with a leaflet thickness of 0.020 inches was the 0.688 diameter valve since it was not robust enough to prevent complete valve leaflet reversal and subsequent large regurgitant fractions. When valve leaflet reversal occurred cavitation occurred at the valve and gas bubbles were generated in the

glycerol solution. The valves were fabricated and tested in the following order: 0.688 inch diameter, 1 inch diameter, 1.25 inch diameter and 1.125 inch diameter. The valve resistance as a function of valve diameter for flowrates of 3 and 5 L/min can be seen in **Figures 2.21** and **2.22**, respectively, for pulse rates of 80 and 100 bpm, and leaflet thicknesses of 0.040 and 0.060 inches. The regurgitant fraction as a function of valve diameter for flowrates of 3 and 5 L/min can be seen in **Figures 2.23** and **2.24**, respectively, for pulse rates of 80 and 100 bpm, and leaflet thicknesses of 0.040 and 0.060 inches.

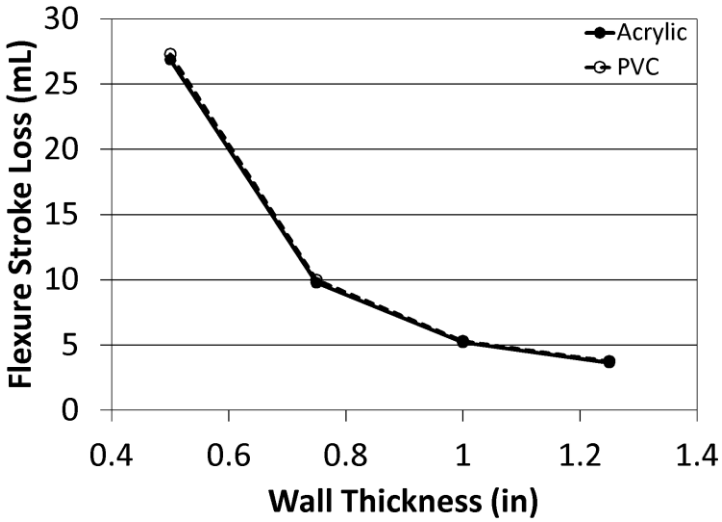

Figure 2.20: Total flexural stroke loss for pvc and acrylic enclosures as a function of wall thickness.

2.3.4 CCSD System In Vitro Fluid Dynamics Testing

The attained flowrate, attained pulse rate, regurgitant fraction, peak positive enclosure pressure and peak negative enclosure pressure are summarized in **Table 2.6** for all stage 1 *in vitro* testing conditions using a valve leaflet thickness of 0.040." In general magnitudes of peak pressure increased with increasing flowrate and pulse rate, and regurgitant fraction increased with increasing flowrate. Raising the reservoir raised the magnitude of the peak positive enclosure

Table 2.5: Flexural stroke volume losses during *in vitro* testing of the final enclosure design.

Run	Positive Volume Loss (mL)	Negative Volume Loss (mL)	Total Volume Loss (mL)
1	2.49	1.99	4.48
2	2.69	2.09	4.78
3	2.52	2.01	4.53
4	2.62	2.41	5.04
Ave	2.58	2.13	4.71

pressure but lowered the magnitude of the peak negative pressure. High regurgitant fractions and large magnitude enclosure pressure magnitudes were seen at all test conditions with 2 L/min glycerol flow rates. As the stroke volume was adjusted upwards to move from 2 L/min to 4 L/min of glycerol flowrate, complete valve reversal occurred resulting in high regurgitant fractions, a drop in flowrate, and cavitation around the valves. The high regurgitant fractions and high magnitude peak pressures are evident in **Figures 2.25** and **2.26** for the 2 L/min, 80 bpm and the 4 L/min, 100 bpm non-raised reservoir cases, respectively.

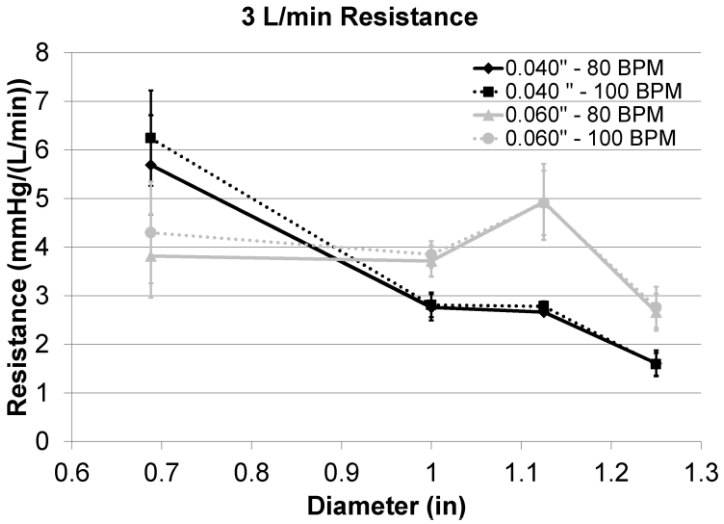

Figure 2.21: CCSD valve *in vitro* testing resistance results at 3 L/min glycerol flowrate.

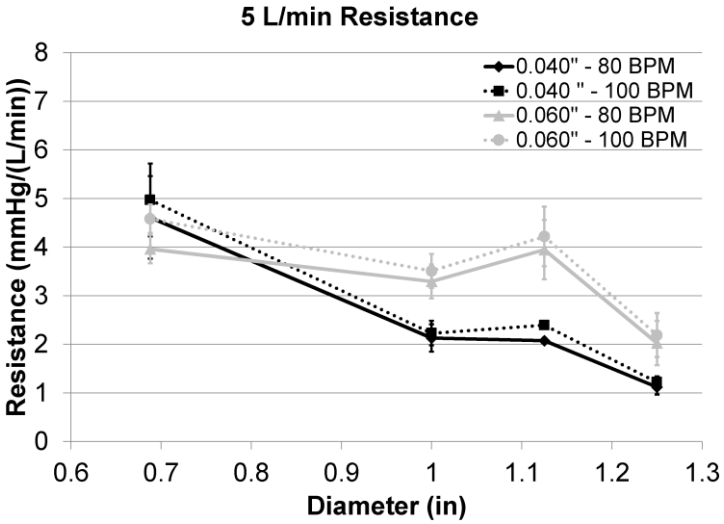

Figure 2.22: CCSD valve *in vitro* testing resistance fraction results at 5 L/min glycerol flowrate.

In Stage 2 of the *in vitro* testing of the CCSD system, the gas exchangers were built with thicker valves that had a leaflet thickness of 0.060 inches. The attained flowrate, attained pulse rate, regurgitant fraction, peak positive enclosure pressure and peak negative enclosure pressure are summarized in **Table 2.7** for all stage 2 *in vitro* testing conditions The first round of tests

utilizing no cannulas, a raised reservoir, and a % systolic time of 33% were successful in attaining flowrates of 4 L/min without significant valve reversal. As can be seen in **Tables 2.6** and **2.7**, the thicker valved stage 2 CCSD outperformed the thinner valved counterpart from stage 1 testing in all areas. For comparison to the stage 1 CCSD with thinner leaflet valves seen in **Figure 2.26**, pressure and volume flowrate graphs for the stage 2, non-raised, no cannula, 4 L/min, 100 bpm case can be seen in **Figure 2.27**. However, upon increasing glycerol flowrates up to 4 L/min, large amounts of gas were pulled from the gas side into the glycerol side of the gas exchanger. Concurrently, the gas caps of the CCSD filled with glycerol. Despite this, all target flowrates and pulse rates were attained for all tests at 4 L/min flowrate.

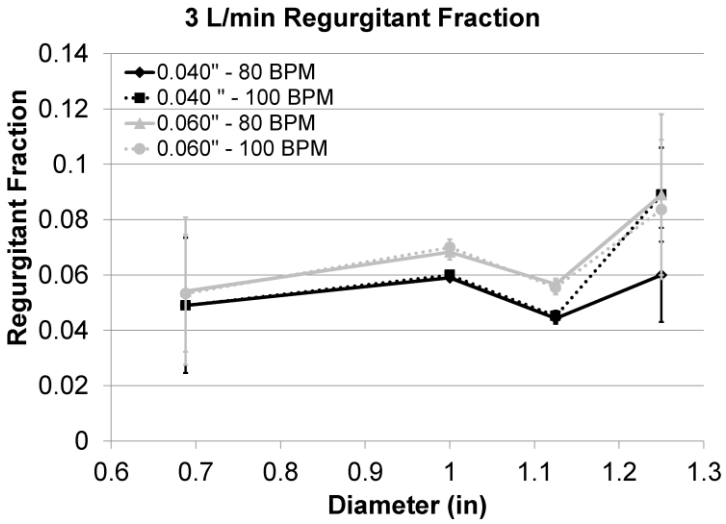

Figure 2.23: CCSD valve *in vitro* testing regurgitant fraction results at 3 L/min glycerol flowrate.

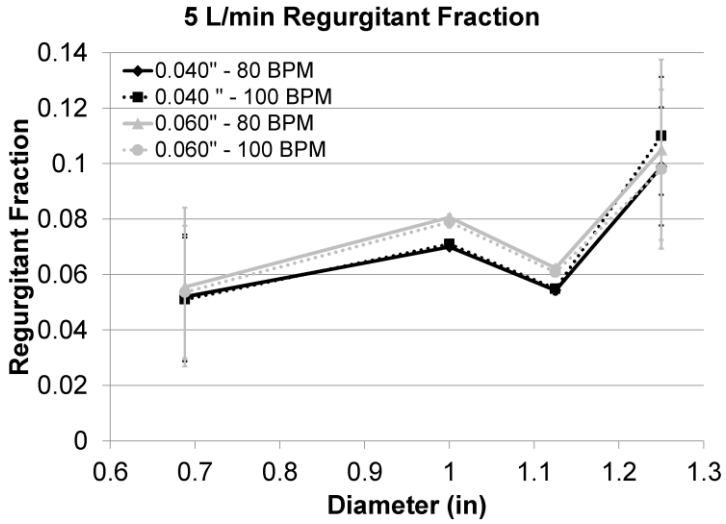

Figure 2.24: CCSD valve *in vitro* testing regurgitant fraction results at 5 L/min glycerol flowrate.

After making a comparison between results with CCSD devices using 0.040" and 0.060" thick valves using no cannulas, cannulas were added to simulate *in vivo* use of the entire CCSD system. As can be seen in **Table 2.9**, the regurgitant fraction increased with increasing flowrate

Table 2.6: Stage 1 in vitro CCSD pumping test results.

Test Condition	Target Flow (L/min)	Target Pulse Rate (bpm)	Systolic to Diastolic Ratio (%)	Reservior Raised (Y/N)	Cannulas (Y/N)	Flow (L/min)	Pulse Rate (bpm)	Regurg. Fraction	Peak Positive Pressure (mmHg)	Peak Negative Pressure (mmHg)
1	2	80	33%	N	N	2.05	80.2	0.137	137	-194
2	2	100	33%	N	N	2.07	99.7	0.248	156	-216
3	4	80	33%	N	N	1.32	78.9	0.648	189	-262
4	4	100	33%	N	N	1.20	97.9	1.075	268	-290
5	2	80	33%	Y	N	2.04	80.2	0.126	187	-140
6	2	100	33%	Y	N	2.04	100.1	0.237	201	-148
7	4	80	33%	Y	N	1.32	79.6	0.654	228	-228

and increasing pulse rate. The magnitudes of peak negative and peak positive enclosure pressures increased with increasing flowrate. When comparing the 33% to 50% systolic time cases, the latter had higher regurgitant fractions, higher peak enclosure pressure, and lower magnitude peak negative enclosure pressures at equivalent testing conditions. As with stage 2 cases with no cannulas, the all of the stage 2 cases with cannulas had a pulling of air from the gas side of the system to the blood side of the system when increasing to 4 L/min glycerol flowrate.

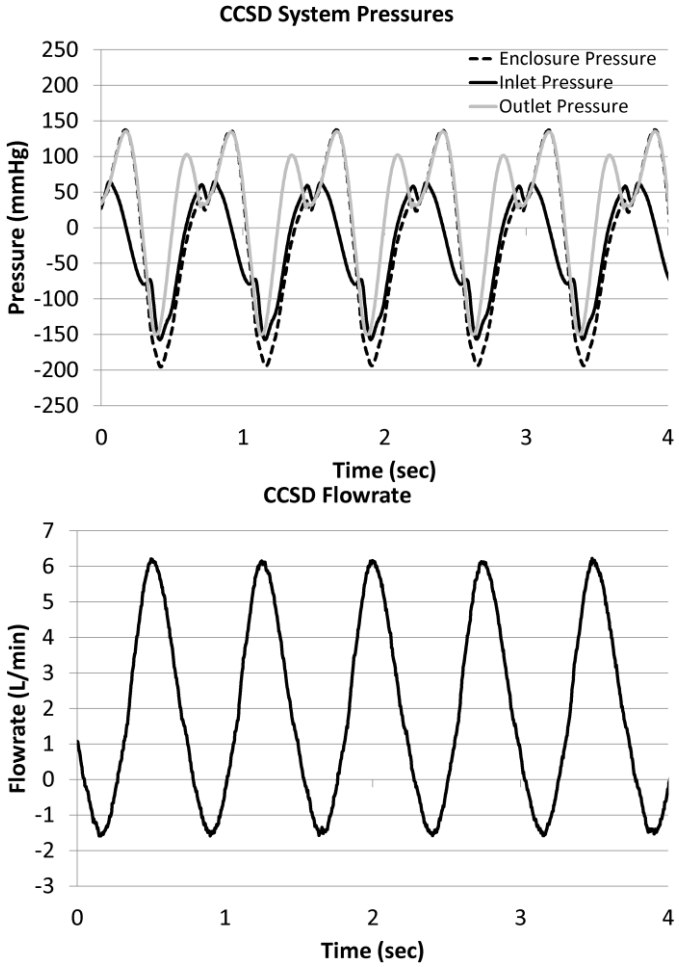

Figure 2.25: *In vitro* traces for stage 1, 2 L/min, 80 bpm test. *Top:* Pressures. *Bottom:* Flowrate.

In stage 3 *in vitro* testing of the CCSD system, six priming methods

were explored to reduce the magnitude of negative pressures exerted on the gas exchanger. The prime condition with the lowest magnitude negative pressures is presented. The regurgitant fraction, attained flowrate, attained pulse rate, peak positive systolic pressure, and peak negative diastolic pressure for the stage 3 tests are listed in **Table 2.8**. In general, the regurgitant fraction, peak positive enclosure pressure, and magnitude of peak negative pressure increased with increasing flowrate. When comparing the results from this stage 3 prime condition (Test Conditions 1-4) to the equivalent stage 2 results from **Table 2.7** (Test Conditions 13-16), it is evident that the magnitudes of peak negative and positive pressures are lower for the stage 3 priming method. Additionally the regurgitant fraction is lower for all stage 3 test conditions with the exception of the 4 L/min, maximum pulse rate case. As with stage 2 testing, in stage 3 testing air was pulled to the blood side of the device and glycerol was pulled to the air side of the device when increasing from 2 L/min to 4 L/min glycerol flowrate.

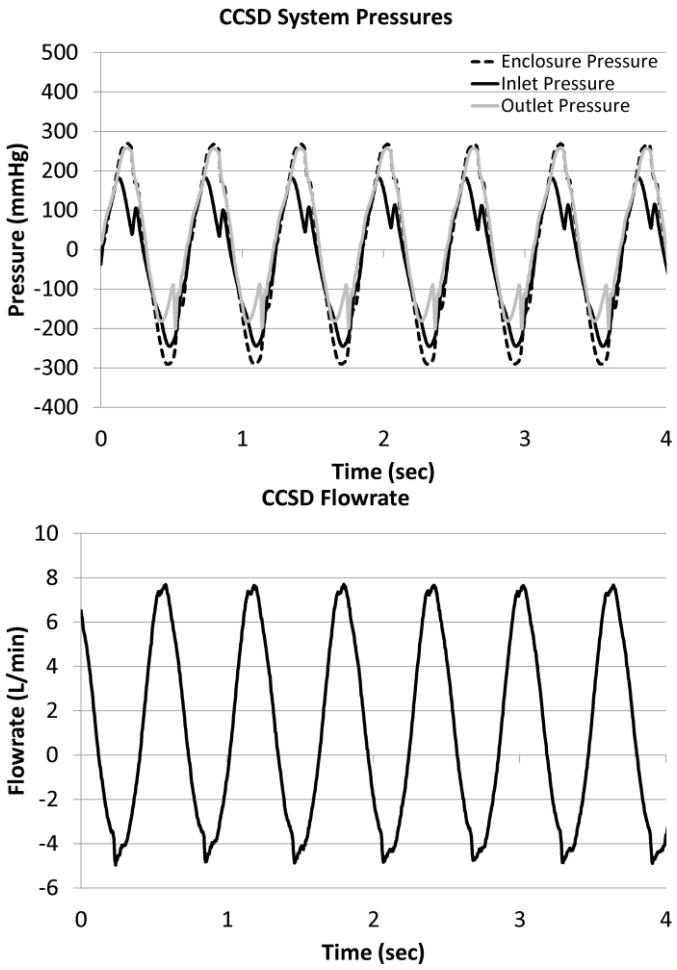

Figure 2.26: *In vitro* traces for stage 1, 4 L/min, 100 bpm test. *Top:* Pressures. *Bottom:* Flowrate.

2.4 Discussion

2.4.1 CCSD Enclosure

Table 2.7: Stage 2 *in vitro* CCSD pumping test results.

Test Condition	Target Flow (L/min)	Target Pulse Rate (bpm)	Percent Systolic Time (%)	Reservior Raised (Y/N)	Cannulas (Y/N)	Flow (L/min)	Pulse Rate (bpm)	Regurg. Fraction	Peak Positive Pressure (mmHg)	Peak Negative Pressure (mmHg)
1	2	80	33%	Y	N	2.05	80.5	0.061	133	-79
2	2	100	33%	Y	N	2.09	100.1	0.107	107	-69
3	4	100	33%	Y	N	4.17	100.0	0.115	217	-143
4	4	Max	33%	Y	N	4.17	103.9	0.128	222	-141
5	2	80	33%	Y	Y	2.11	80.2	0.082	144	-111
6	2	100	33%	Y	Y	2.13	100.0	0.135	136	-109
7	4	100	33%	Y	Y	4.17	100.0	0.157	279	-246
8	4	Max	33%	Y	Y	4.20	102.6	0.170	285	-247
9	2	80	50%	Y	Y	2.05	80.3	0.102	148	-61
10	2	100	50%	Y	Y	2.11	99.7	0.167	178	-72
11	4	100	50%	Y	Y	4.17	99.5	0.179	333	-193
12	4	Max	50%	Y	Y	4.17	99.6	0.188	337	-201
13	2	80	33%	N	Y	2.01	80.6	0.036	116	-118
14	2	100	33%	N	Y	2.04	99.6	0.060	82	-107
15	4	100	33%	N	Y	4.08	100.1	0.080	168	-264
16	4	Max	33%	N	Y	4.13	105.9	0.106	224	-235

The early CCSD prototype suffered from inefficiencies caused by flexing of the enclosure that acts as a pressurization chamber. A new CCSD enclosure was designed to reduce stroke volume losses to less than 10 mL when the enclosure is cycled from -200 mmHg to 300 mmHg. Finite element analysis of an initial design with varying wall thicknesses yielded **Figure 2.20**, where the plot shows the stroke volume loss as a function of wall thickness for acrylic and PVC enclosures. As the wall thickness increases there is an exponential decrease in stroke volume. Above a wall thickness of 1 inch the benefit of adding more thickness is minimal in terms of stroke volume, so a final wall thickness of 0.125 inches was chosen. The final enclosure included a more integrated gas exchanger holder that reduced machining costs and thickened the back wall of the enclosure. Finite element analysis estimates of the stroke volume loss was fairly close to the actual benchtop testing of the device where the finite element analysis yielded a stroke volume loss of 5.84 mL and the benchtop testing yielded a stroke volume loss of 4.71 mL. The newly designed

enclosure allowed the second generation CCSD system to operate more efficiently than the first generation.

2.4.2 CCSD Valves

The first generation CCSD device utilized external ball valves designed for industrial applications. These valves add components and prime volume to system, and likely would not have had the biocompatibility necessary for long term use with blood. In order to reduce separate components and prime volume, it was desired that the valves be integrated into the blood inlet and outlet conduits of the CCSD gas exchanger. In an attempt to create a more biocompatible valve than a tilting disc or bi-leaflet mechanical valve, a polymeric trileaflet valve was designed. This trileaflet valve was fabricated in a single piece since other

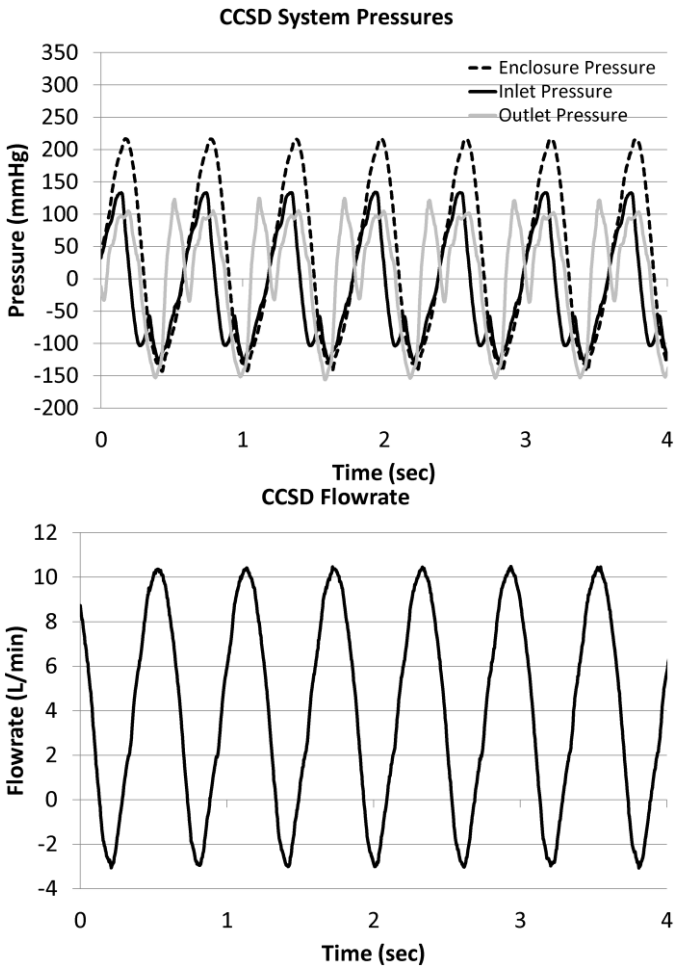

Figure 2.27: *In vitro* traces for stage 2, 4 L/min, 100 bpm test. *Top:* Pressures. *Bottom:* Flowrate.

Table 2.8: Stage 3 *in vitro* CCSD pumping test results.

Test Condition	Target Flow (L/min)	Target Pulse Rate (bpm)	Percent Systolic Time (%)	Reservior Raised (Y/N)	Cannulas (Y/N)	Flow (L/min)	Pulse Rate (bpm)	Regurg. Fraction	Peak Positive Pressure (mmHg)	Peak Negative Pressure (mmHg)
1	2	80	33%	N	Y	2.05	79.5	0.073	103	-105
2	2	100	33%	N	Y	2.04	100.1	0.087	50	-90
3	4	100	33%	N	Y	4.12	104.3	0.101	191	-197
4	4	Max	33%	N	Y	4.12	107.4	0.100	187	-195

attempts of creating polymeric valves failed at seams created when fabricating the part from multiple components. The biospan polyurethane that was used for the construction of the gas exchanger housing proved to be durable in the limited time windows when the valve was used in the *in vitro* testing. Further accelerated longevity testing would be needed to confirm the safety of these single piece polymeric valves.

Valves with diameters ranging from 0.688 inches to 1.25 inches and leaflet thicknesses ranging from 0.020 inches to 0.060 inches were fabricated and tested for optimal resistance and regurgitant fraction characteristics. It was desired that the valves have a regurgitant fraction less than 0.10 and a resistance less than 2 mmHg/(L/min) per valve at flowrates up to 5 L/min. Resistance tended to decrease with increasing valve diameter and increase with increasing valve thickness. Counterintuitively, as the stroke volume was decreased by raising pulse rate, there was a non-significant trend for the resistance of the valves to be slightly higher. This may have been due to the larger amount of time spent with the valve open in relation to the time spent in the opening/closing phase of valve cycling for the larger stroke volume cases. This would yield smaller energy losses due to valve opening and closing for a given amount of fluid traveling through the valve. Regurgitant fraction followed the opposite course, where the regurgitant fraction tended to increase with increasing valve diameter and decrease with increasing leaflet thickness.

Also apparent when inspecting the graphs of resistance and regurgitant fraction is deviation from the linear trends for the 1.125 inch diameter valves when increasing valve diameter. The error bars resulting from the 1.125 inch diameter valves tended to be smaller than the other valve diameters at a leaflet thickness of 0.040 inches. These deviations can be attributed to the fact that the 1.125 inch valve was the last valve size to be fabricated and tested. The valves were all hand dipped and during the course of manufacturing the different sized valves, the processed slowly

evolved to create more uniform valves. The 1.125 inch valves were not only more uniform, but slightly stiffer, resulting in elevated resistances and decreased regurgitant fractions.

The 1.125 inch diameter, 0.040 inch leaflet thickness valve was chosen to be used in the CCSD gas exchanger for its balance of regurgitant fraction and valve resistance. The regurgitant fraction was well within the target of less than 0.10, and the resistance was only slightly higher than the target of 2 mmHg/(L/min) per valve. However, when the valves were used in the full CCSD system, the valves exhibited large reguritant fractions from valve reversal. This indicates that the valve *in vitro* testing circuit was not an accurate representation of the forces the valves would encounter in the CCSD system. An improvement of the *in vitro* valve testing system would be to use two polymeric valves in the system rather than a ball valve and polymeric valve. Additionally, a resistance element, such as a Hoffman clamp, could be added upstream of the inlet valve and downstream of the outlet valve being tested in order to simulate the resistance of the tubing and cannulas of the CCSD system. Ultimately a 1.125 inch diameter, 0.060 inch leaflet thickness valve was utilized in the final CCSD system to reduce regurgitant fractions. These valves performed well, although their resistance exceeds the original target. Computational fluid structure interaction simulations, *in vitro* flow visualization studies, and/or *in vivo* biocompatibility studies would be needed to confirm biocompatibility of the valves.

2.4.3 CCSD System Pumping

During stage 1 *in vitro* testing of the CCSD system with 0.040 inch leaflet thickness valves and no cannulas there were significant problems with valve regurgitation. At 2 L/min of flowrate the system was yielding regurgitant fractions between 0.126 and 0.248. Additionally, peak pressure magnitudes were higher than expected for these cases. When increasing the stroke volume to attain the 4 L/min flowrate condition the regurgitation increased greatly until complete valve

reversal was visually seen. Once valve reversal occurred, the flowrate dropped significantly and the target flowrate of 4 L/min was not able to be attained for both pulse rates. Additionally, cavitation occurred at the valves during reversal and gas built up inside the gas exchanger housing. The addition of high resistance cannulas to the system would have diminished the performance of the system. As a result, gas exchangers with a thicker 0.060 inch leaflet valve were manufactured for the second stage of CCSD system *in vitro* testing.

For comparison to stage 1 testing, stage 2 testing was started first without cannulas, with a raised reservoir, and % systolic time ratio of 33%. In stage 2 testing the regurgitant fractions and peak pressure magnitudes were lower at all flow conditions compared. However, as the stroke volume was increased to accommodate 4 L/min of flow, large amounts of gas was pulled into the blood side of the gas exchanger despite no gas being flowed through the gas side of the gas exchanger. This occurred with all devices tested at all flow conditions targeted at 4 L/min of flow including % systolic times of 33% and 50%, and pulse rates of 100 bpm and the maximum pulse rate produced by the pump. Upon de-priming the CCSD enclosure and removing the gas exchanger it was observed that the gas caps of the device and the gas lines were filled with large amounts of glycerol solution. This indicates a blowout in the potting material, gas and glycerol leakage across the porous wall of the hollow fibers, and/or hollow fiber rupture that allow gas to travel to the blood side the gas exchanger and glycerol to travel from the blood side to the gas side of the gas exchanger. All conditions occur as a result of the high magnitude negative pressures generated within the CCSD enclosure and gas exchanger. Additionally, high magnitude positive pressures can lead to blowout of the potting material.

When comparing the same test conditions in Stage 2 with a raised reservoir for 33% and 50% systolic times, it can be seen that there were increases in the magnitude of peak positive

pressures and decreases in the magnitude of peak negative pressures when switching to % systolic time of 50%. At 4 L/min and 100 bpm, the peak positive pressure was increased by 54 mmHg and the peak negative pressure was reduced by 53 mmHg. At 4 L/min and the maximum pulse rate, the peak positive pressure was increased by 52 mmHg and the peak negative pressure was reduced by 46 mmHg. However, gas leakage was seen at all test conditions, and peak negative pressures were around negative 200 mmHg.

The stage 3 testing focused on reducing the peak negative pressure magnitudes in the gas exchanger, by attempting to improve the priming method of the gas exchanger. Since the housing is much more compliant in its unfurling stage rather than in its pure stretching stage, the pre-stretching could reduce negative pressures by allowing the gas exchanger to operate more in the unfurling stage rather than in the stretching phase. At 4 L/min, 100 bpm and 4 L/min with the maximum pulse rate the improved priming method reduced the peak negative pressures by 67 mmHg and 40 mmHg, respectively. However, there was still air pulled into the blood side of the gas exchanger and the enclosure pressures still ranged close to negative 200 mmHg. Based on Stage 2 testing, a % systolic time of 50% would likely reduce the magnitude of negative peak pressures, but not to a large enough extent as to yield a device safe from air embolism.

After testing the CCSD system during stage 3 the project was abandoned for safety concerns and a reduced benefit in comparison to ECMO. In the past five years, ECMO has improved to a point where circuits have been miniaturized and patients are starting to ambulate while being treated with ECMO. As a result, one of the major advantages of the CCSD system where the patient could ambulate to some extent while receiving therapy has been eliminated. Additionally, these smaller ECMO circuits won't lose as much heat as their predecessors and safe fiber based heat exchangers are integrated into ECMO gas exchangers. With the improvement of

ECMO technologies, the only real advantage of the CCSD is the pulsatility of the flow regime. However, the theoretical improved perfusion will only be seen if the device is used in a veno-arterial configuration. In recent years treatments have shifted more from veno-arterial treatment to veno-venous treatment, which results in a smaller potential patient pool for the CCSD. Lastly, there are safety concerns with air embolism. The risk of air embolism stemming from gas pulled from the fiber during diastole could be reduced by applying a negative pressure on the gas outlet, but this increases the pressure gradient between the blood and gas phase during systole, increasing the risk of rupturing the potting material. Additionally, these tests were performed with some of the largest cannulas available in order to reduce cannula resistance. In actual clinical use, the device would likely be paired with smaller single lumen or dual lumen cannulas for many patients. This would result in larger resistances, larger magnitude enclosure pressures, and more air embolism risk.

Overall the enhanced risk and small cohort of patients that could be treated with the technology outweighs the benefits of pulsatile perfusion and the system should not be pursued further. However, the one piece polymeric valves could be viable replacements for more traditional mechanical heart valves. The benefits of pulsatile perfusion may also be integrated into ECMO by utilizing varying rotational speeds in ECMO pumps(14-16) or pump replacement with piston pumps similar to pulsatile flow ventricular assist devices Both of these methods of inducing pulsatility to the flow regime eliminate negative pressures on the fiber bundle of the exchanger thereby reducing air embolism risk.

2.5 References

1. ECMO circuit.
2. Wenstone R, Campbell J, Booker P, McKay R. Renal function after cardiopulmonary bypass in children: comparison of dopamine with dobutamine. British journal of anaesthesia. 1991;67(5):591-4.
3. Alkan T, Akçevin A, Ündar A, Türkoglu H, Paker T, Aytaç A. Benefits of Pulsatile Perfusion on Vital Organ Recovery During and After Pediatric Open Heart Surgery. ASAIO Journal. 2007;53(6):651-4. doi: 10.1097/MAT.0b013e31814fb506. PubMed PMID: 00002480-200711000-00001.
4. Ündar A, Masai T, Yang S-Q, Eichstaedt HC, McGarry MC, Vaughn WK, et al. Pulsatile Perfusion Improves Regional Myocardial Blood Flow during and after Hypothermic Cardiopulmonary Bypass in a Neonatal Piglet Model. ASAIO Journal. 2002;48(1):90-5. PubMed PMID: 00002480-200201000-00017.
5. Jonas RA, Newburger JW, Volpe JJ. Brain injury and pediatric cardiac surgery. Boston, Mass.: Butterworth Heinemann; 1996. xvi, 416 p. p.
6. Wang W, Bai SY, Zhang HB, Bai J, Zhang SJ, Zhu DM. Pulsatile flow improves cerebral blood flow in pediatric cardiopulmonary bypass. Artificial organs. 2010;34(11):874-8.
7. Itoh H, Ichiba S, Ujike Y, Douguchi T, Obata H, Inamori S, et al. Effect of the Pulsatile Extracorporeal Membrane Oxygenation on Hemodynamic Energy and Systemic Microcirculation in a Piglet Model of Acute Cardiac Failure. Artificial Organs. 2015:n/a-n/a. doi: 10.1111/aor.12588.
8. Schewe RE, Scipione CN, Koch KL, Cook KE. In-parallel attachment of a low-resistance compliant thoracic artificial lung under rest and simulated exercise. The Annals of thoracic surgery. 2012.
9. Scipione CN, Schewe RE, Koch KL, Shaffer AW, Iyengar A, Cook KE. Use of a low-resistance compliant thoracic artificial lung in the pulmonary artery to pulmonary artery configuration. The Journal of thoracic and cardiovascular surgery. 2013.
10. Sato H, Griffith GW, Hall CM, Toomasian JM, Hirschl RB, Bartlett RH, et al. Seven-day artificial lung testing in an in-parallel configuration. The Annals of thoracic surgery. 2007;84(3):988-94.
11. Sato H, Hall CM, Lafayette NG, Pohlmann JR, Padiyar N, Toomasian JM, et al. Thirty-Day In-Parallel Artificial Lung Testing in Sheep. The Annals of Thoracic Surgery. 2007;84(4):1136-43. doi: http://dx.doi.org/10.1016/j.athoracsur.2007.05.051.
12. Shepard RB, Simpson DC, Sharp JF. ENergy equivalent pressure. Archives of Surgery. 1966;93(5):730-40. doi: 10.1001/archsurg.1966.01330050034005.
13. Wright G. Hemodynamic analysis could resolve the pulsatile blood flow controversy. The Annals of Thoracic Surgery. 1994;58(4):1199-204. doi: http://dx.doi.org/10.1016/0003-4975(94)90498-7.
14. Cremers B, Link A, Werner C, Gorhan H, Simundic I, Matheis G, et al. Pulsatile Venoarterial Perfusion Using a Novel Synchronized Cardiac Assist Device Augments Coronary Artery Blood Flow During Ventricular Fibrillation. Artificial Organs. 2015;39(1):77-82. doi: 10.1111/aor.12413.
15. Krawiec C, Wang S, Kunselman AR, Ündar A. Impact of Pulsatile Flow on Hemodynamic Energy in a Medos Deltastream DP3 Pediatric Extracorporeal Life Support System. Artificial Organs. 2014;38(1):19-27. doi: 10.1111/aor.12117.

16. Wang S, Izer JM, Clark JB, Patel S, Pauliks L, Kunselman AR, et al. In Vivo Hemodynamic Performance Evaluation of Novel Electrocardiogram-Synchronized Pulsatile and Nonpulsatile Extracorporeal Life Support Systems in an Adult Swine Model. Artificial Organs. 2015;39(7):E90-E101. doi: 10.1111/aor.12482.

Chapter 3: Compliant Thoracic Artificial Lung

3.1 Introduction

Each year in the United States approximately 127,000 people die from chronic respiratory disease including COPD, IPF, and CF.(1) The only long term cure for these patients is lung transplantation, although only about 1800 lung transplants are performed each year due to donor organ shortages.(2) Extracorporeal membrane oxygenation (ECMO) can be used as a bridge to lung transplantation for some patients. However as discussed in **Chapter 1**, ECMO offers limited patient ambulation (3-6) and biocompatibility issues lead to patient deterioration over time.(4, 7-13) Chief amongst these is significant blood damage and activation that necessitates blood product transfusion.(7-9) Additionally, the number of patients bridged to transplantation using any method is limited by the scarcity of donor lungs. The compliant Thoracic Artificial Lung (cTAL) is thus needed as a possible bridge to transplantation or destination therapy.

The cTAL has an advantage over ECMO as a bridge to transplantation and destination therapy due to its simple, pumpless system and low resistance. The cTAL should produce lower blood damage and be more portable than an ECMO system since it does not utilize a pump to maintain blood flow.(14, 15) Additionally, the cTAL in particular has a very low resistance, which should reduce the shear on the blood leading to less blood damage and clot inducing platelet activation.(15)

Past studies of the compliant Thoracic Artificial Lung (cTAL) have characterized the impedance and gas exchange capabilities in an *in vitro* setting, and the cTAL's effects on physiology in acute *in vivo* experiments.(14-16) The cTAL has excellent gas exchange capabilities,

with the rated flow exceeding 7 L/min of blood flow.(15) The cTAL has the lowest impedance and in turn resistance attributes of current artificial lungs.(15) The resistance of the cTAL is approximately 0.5 mmHg/(L/min), which is less than half the resistance of the next lowest resistance gas exchanger, the MC3 Biolung.(15, 17, 18) Furthermore, the zeroth order impedance modulus decreases with stroke volume and the first order impedance modulus has minimal increases with stroke volume in pulsatile flow.(15) The favorable resistance and impedance moduli are attributable to the cTAL's gradual tapering blood inlet and outlet manifolds, the large frontal area of the device, and the compliant housing.(15) This housing design maximizes spatial and temporal uniformity of blood flow through the fiber bundle in an effort to reduce the blood flow resistance, improve gas exchange efficiency, and limit coagulation.(15)

When attached in a PA-LA configuration in parallel with the native lungs the low 0.5 mmHg/(L/min) resistance of the cTAL has the ability to unload the right heart in patients with pulmonary hypertension.(14) Short term *in vivo* studies have also shown that minimal degradations in the cardiac function occur with up to 90% of the cardiac output delivered to the cTAL, even under simulated exercise conditions.(14) The present study aims to assess the cTAL's efficacy as a bridge to lung transplantation and destination therapy device by testing the long term function and biocompatibility of the uncoated cTAL for 14 day periods. In particular, this study seeks to examine if the device can maintain the gas exchange and resistance characteristics demonstrated during short-term *in vitro* and *in vivo* studies while maintaining normal animal physiology.

3.2 Methods

3.2.1 cTAL System Description

The cTAL is a hollow-fiber membrane artificial lung with a compliant housing previously described by Schewe et al.(14-16) As can be seen in **Figure 3.1**, the device consists of a compliant

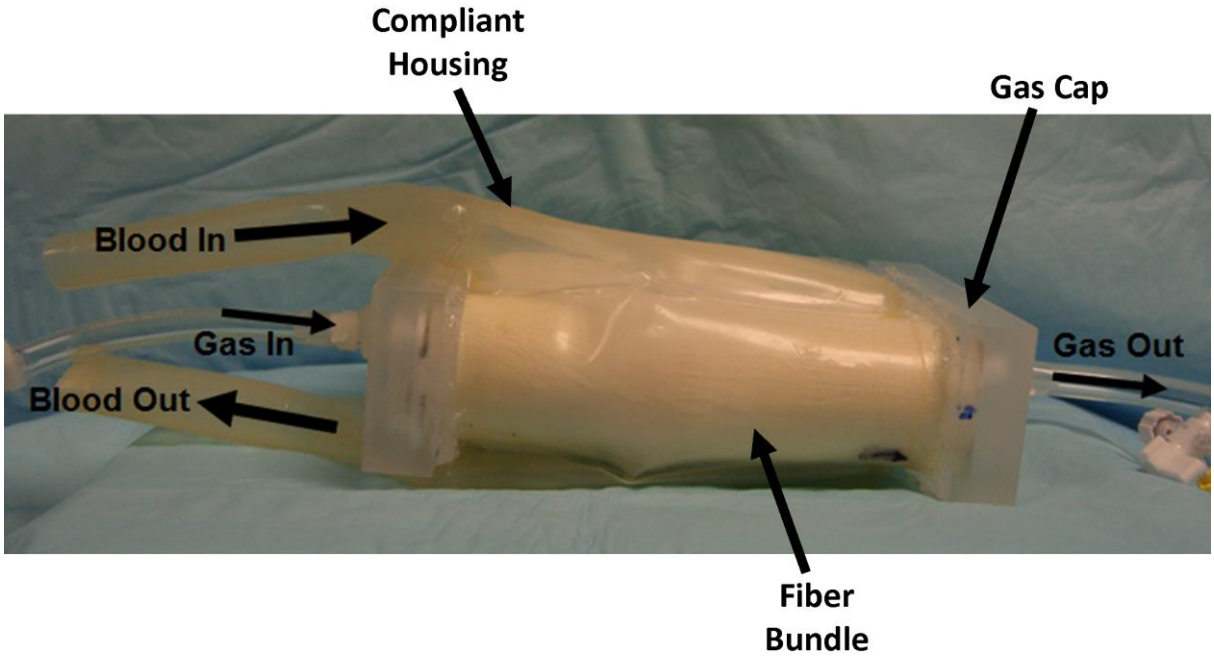

Figure 3.1: An assembled cTAL consisting of a compliant housing, fiber bundle, and gas caps. Adapted from (19)

housing with tapering blood inlet and outlet manifolds, a gas exchange fiber bundle potted into the compliant housing, and acrylic gas caps used to distribute the sweep gas to the hollow fibers.(19) The gas exchange membrane has 2.4 m^2 of surface area consisting of microporous polypropylene fibers (Membrana, Charlotte, NC). The compliant housing is fabricated from Biospan polyurethane (DSM PTG, Berkeley, CA). In addition to the gas exchanger, a cage was manufactured to protect the cTAL's compliant housing and eliminate any shunt flow that could occur around the fiber bundle while allowing for housing expansion and contraction. The first version, used in Sheep 1 (**Figure 3.2**), clamped the sides of the cTAL fiber bundle with high pressure. The second version, used in all subsequent sheep, held the cTAL with minimal pressure placed on the fiber bundle. **(Figure 3.3**) These holders were very large so as to provide flexibility to adaptation in research use. However, the commercial holder would be a more compact and durable two piece molded housing. In order to divert pulmonary blood flow to and from the cTAL, custom blood inflow and outflow conduits where manufactured. These conduits (**Figure 3.4)**

consisted of six inches of 5/8" ID tygon tubing bonded to 18 mm dacron vascular grafts (Maquet Getinge, Wayne, NJ, or Terumo Cardiovascular, Ann Arbor, MI) using previously published methods (see **Appendix C** for full detail).(20)

3.2.2 Surgery

The cTAL was attached to five sheep weighing 60-65 kg. All sheep received humane care in compliance with the Guide for the Care and Use of Laboratory Animals, and all methods were approved by the University of Michigan Committee for the Use and Care of Animals. Sheep were given transdermal fentanyl (100 µg/hour) 24 hours prior to surgery, and surgical anesthesia was induced with propofol (400-600 mg, IV). The sheep were intubated, mechanically ventilated, and a plane of anesthesia was maintained with 1-5% isoflurane. An

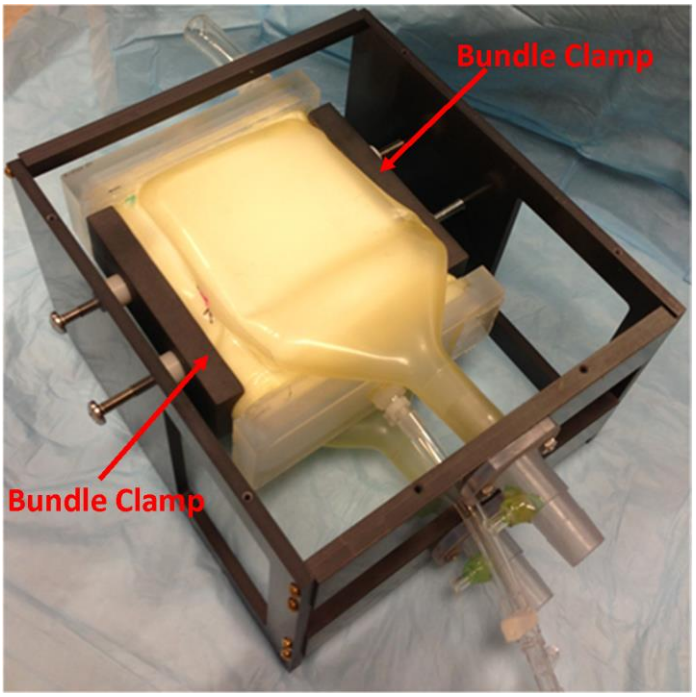

Figure 3.2: The cTAL bundle clamped in the first generation device holder.

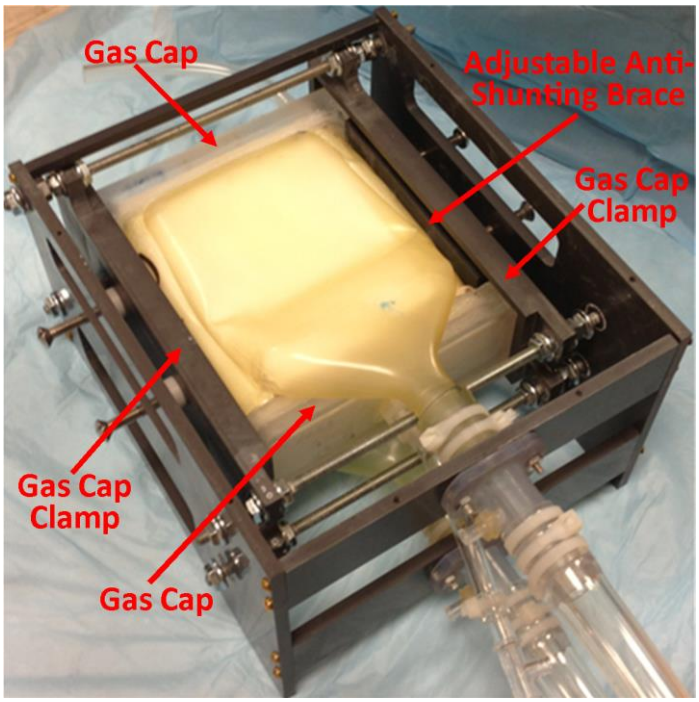

Figure 3.3: The cTAL gas caps clamped in the second generation device holder.

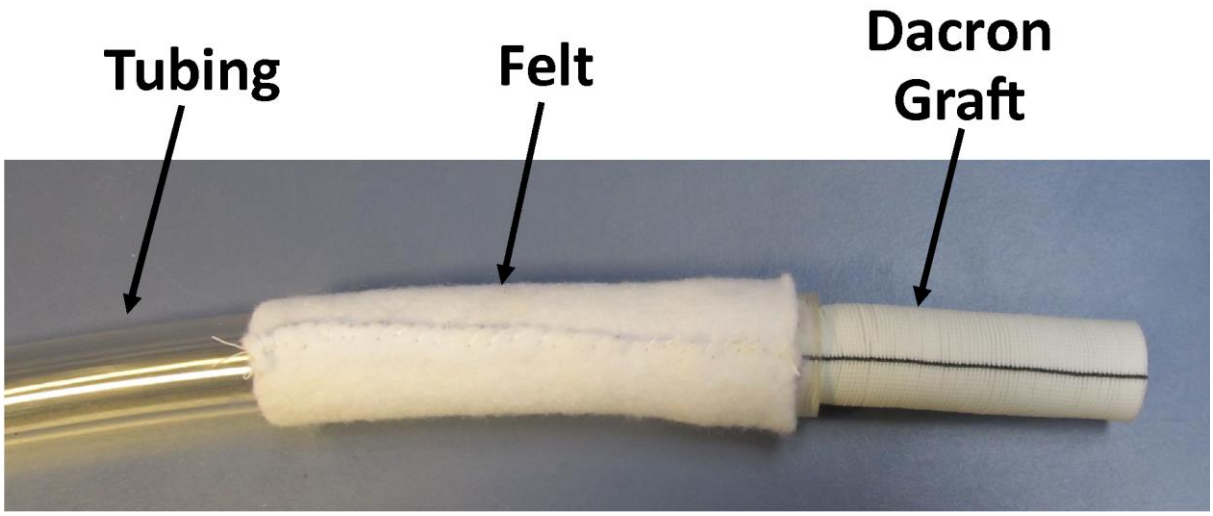

Figure 3.4: The graft used to attach the cTAL to the vasculature.

orogastric tube was placed to prevent abdominal distension. A carotid arterial line was placed for monitoring mean arterial pressure (MAP), heart rate (HR), and arterial pO_2, pCO_2, pH, and hemoglobin (Hb). A venous line was placed in the jugular vein for monitoring central venous pressure and administering fluids and medications.

A left thoracotomy was performed. Nafcillin (1000 mg, IV), gentamicin (120 mg, IV), heparin (5000-8000 Units, IV) buprenorphine (0.6 mg) and flunixin (60 mg, IV) were administered. The outlet and inlet graft conduits were attached to the LA and PA, respectively, via end-to-side anastomoses and tunneled through the sixth intercostal space. A flow probe (Transonic, Ithaca, NY) was placed around the main trunk of the PA, proximal to the conduit, to measure cardiac output and its cable was tunneled through the sheep's back. Ventral and dorsal chest tubes (n=4) or a single ventral chest tube (n=1, Sheep 1) were placed. Initially, the inlet and outlet grafts were connected via 5/8" PVC tubing to maintain graft patency while awaiting sheep recovery and cTAL attachment. A tubing flow probe (Transonic, Ithaca NY) was placed on this shunt and blood flow was limited to 1 L/min using a Hoffman clamp. A heparin drip was supplied to the distal end of the inlet conduit with the goal of maintaining a systemic activated clotting time

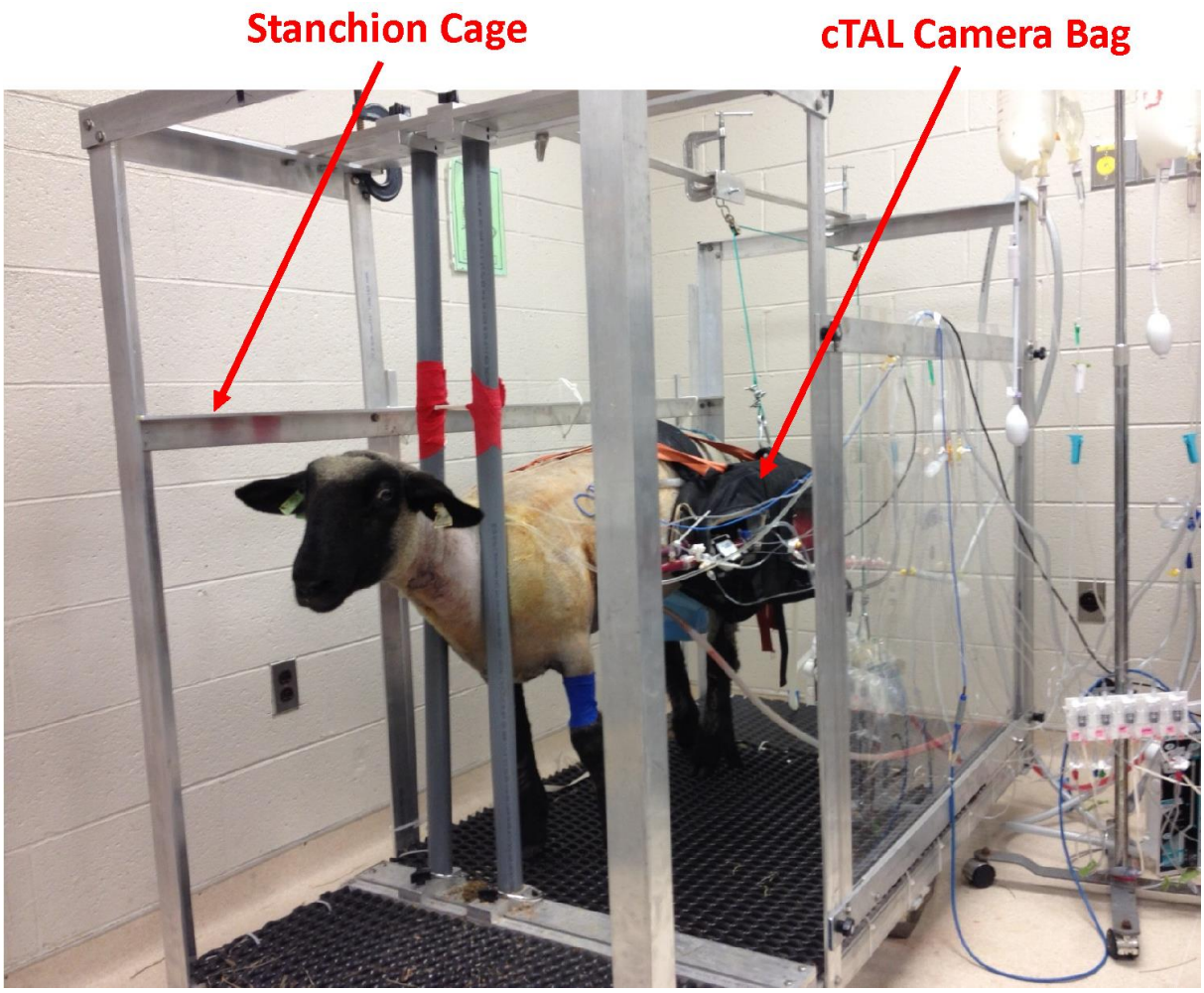

Figure 3.5: A sheep in a custom stanchion cage during a 14 day cTAL experiment.

(ACT) between 200-280 s. The sheep was then recovered according to previous methods and moved to a custom-built cage (**Figure 3.5**) that allowed all activity except turning around.(17) In Sheep 2-4 the cTAL was attached the morning following surgery. In Sheep 1 the cTAL was attached 6 hours after surgery, and in Sheep 5 the cTAL was attached 2 mornings after the surgery due to limited surgical staff availability. The sheep were awake, and ate and drank freely during the 14 days of cTAL support.

3.2.3 cTAL Attachment

Prior to attachment the cTAL was primed with 1.3 L of lactated Ringer's solution, 50 mL albumin (25% solution), 6000 units heparin, and 500 mg methylprednisolone. Heparin (5000-8000

Units) and methylprednisolone (500 mg) were also administered intravenously immediately prior to attachment to prevent clotting and inflammatory reactions to device attachment, respectively. The inlet and outlet conduits of the cTAL were clamped, the cTAL as was then inserted into its protective holder, and these were inserted into a camera bag customized to hold the cTAL onto the sheep while providing an additional layer of protection.(**Figure 3.5**) After cTAL preparation, the shunt tube was removed and the cTAL was attached using sterile technique without sedation. A sweep gas of 100% O_2 was attached to the cTAL gas inlet at a rate of 5 L/min, a vacuum was established at the gas outlet to maintain gas inlet pressure between negative 15-30 mmHg, and blood flow was initiated through the device. The vacuum was applied to the gas outlet of the device to prevent air embolism that results from bulk flow of sweep gas through the porous polypropylene fibers when sweep gas pressures exceed blood pressures inside the device. Due to the excessive CO_2 transfer in the cTAL, CO_2 (6.9+/-0.3%) was blended into the sweep gas to maintain normal arterial pCO_2 and respiratory rate.

3.2.4 Animal Management

All animals were administered nafcillin (500 mg IV) every six hours and gentamicin (120 mg IV) every eight hours for three days or as needed. Pain management was accomplished through buprenorphine (0.6 mg, IM) every four to six hours and flunixin (60 mg, IV) every twelve hours or toradol (60 mg, IM or IV) every six hours. Analgesic dosages and schedules were adjusted as needed. In order to reduce the effects of pulmonary edema and hemodilution, Furosemide (40 mg, IV) was administered every 12 hours from device attachment to day 7 and day 9 for Sheep 4 and 5, respectively. Heparin was administered as a continuous infusion to maintain a targeted systemic ACT between 200-280 sec. Fluids and electrolytes were administered as needed to maintain normal physiology. Animals had access to food and water ad libitum. Sheep 2 received 10 mg of

Diazapam during an episode of restlessness. After the episode subsided, the sheep was administered with 12 mg of Fumazenil to reverse the effects of the Diazapam. Sheep 2 also was administered several doses of atropine and epinephrine as rescue medications during acute bradycardic arrhythmias. Lastly, sheep 4 received a transfusion on day 6 to correct a low hemoglobin, but lysed the transfusion over the following days due to a lack of blood type matching.

If elevated body temperature (>104°F) was observed a bacterial culture was submitted for analysis. After 14 days, animals were euthanized using sodium pentobarbital (16 mL, IV), and necropsied. The pulmonary artery, left atrium, and detached inlet and outlet grafts were inspected for gross thrombus formation. The heart, kidneys, and liver were inspected for signs of gross infarct. The lungs were visually inspected for atelectasis and pulmonary edema.

3.2.5 Data Collection and Analysis

Arterial Hb, pO_2, and pCO_2 were measured using a blood gas analyzer (Radiometer, West Lake, OH) every one to six hours as needed. ACT was measured using a whole blood coagulation system (Hemochron, Edison, NJ) every one to six hours as needed. Blood chemistry panels including aspartate aminotransferase (AST), alanine transaminase (ALT), blood urea nitrogen (BUN), and creatinine were run upon intake into animal housing and approximately every other day following surgery. White blood cell (WBC) and platelet counts (Plt) were run upon intake into animal housing and approximately every other day following. No blood chemistry panels, WBC counts, or platelet counts were performed on the weekend due to closure of diagnostic facilities on the weekend. In order to account for hemodilution and blood loss, the WBC and Plt counts were normalized to the pre-device hemoglobin for each individual sheep according to **Equation 1.1**

$$X_{norm} = X * \frac{Hb_{PD}}{Hb} \tag{1.1}$$

where X_{norm} is the normalized value, X is the measured value at any given time, Hb is the

hemoglobin at that same time, and Hb_{PD} is the pre-device hemoglobin. MAP was recorded hourly from the patient monitor (Marquette Electronics, Milwaukee, WI). The HR was recorded daily with a Biopac MP150 data acquisition system (Biopac Systems, Goleta, CA) (Sheep 2-5) or hourly with the patient monitor (Sheep 1). The cTAL flowrate was recorded hourly from the ultrasonic flow meter (Transonic, Ithaca, NY). The cTAL oxygen transfer rate (V_{O2}) was calculated from inlet and outlet blood gas measurements and cTAL flow rate twice a day using **Equation 1.2**

$$V_{O_2} = \dot{Q} * ((P_{O2_{Out}} - P_{O2_{In}}) + 1.34 * Hb * (S_{O2_{Out}} - S_{O2_{In}})) \quad (1.2)$$

where $\dot{Q}$ is the blood flowrate through the device, P_{O2Out} is the partial pressure of oxygen in the outlet blood sample, P_{O2In} is the partial pressure of oxygen in the inlet blood sample, 1.34 is the amount of oxygen that can be dissolved in 1 gram of hemoglobin with units mL_{O2}/g_{hb}, Hb is the hemoglobin level, S_{O2Out} is the hemoglobin oxygen saturation in the outlet blood sample, and S_{O2In} is the hemoglobin oxygen saturation in the inlet blood sample. The device blood flow resistance was calculated in the standard fashion from inlet and outlet blood pressures and cTAL flow rate recorded with the Biopac MP150 data acquisition system according to **Equation 1.3**

$$R = \frac{P_{In} - P_{Out}}{\dot{Q}} \quad (1.3)$$

where R is the cTAL resistance, P_{In} is the cTAL inlet blood pressure, P_{Out} is the cTAL outlet blood pressure, and $\dot{Q}$ is the cTAL blood flowrate.

Data represented as "pre-device" (PD) has been averaged from data taken over the six hours leading up to device attachment, and data represented as "baseline" (BL) is averaged over the six hours following device attachment. All other data is averaged over 24 hour periods after device attachment. The one exception to this are the clinical veterinary labs (AST, ALT, BUN, Creatinine, WBC, and Plt). These baseline samples were measured at intake and averaged over 3 day periods

after device attachment. Exceptions are; Sheep 2 had no intake labs and due to complications and animal unrest post attachment Sheep 4 had a BL V_{O2} taken at 7 hours post device attachment. Statistical comparisons utilized data from baseline (BL) through fourteen days. Comparisons were performed with SPSS (SPSS, Chicago, IL) using a linear mixed model with the sheep number as the subject variable and time as the fixed, repeated measure variable. Post-hoc analysis using a Bonferroni-corrected confidence interval was employed to compare all variables to baseline data to examine changes with time.

3.3 Results

Three of the five sheep survived the entire 14 day experiment, and no device exchanges were performed. Sheep 2 was euthanized on day 6 due to a bradycardic arrhythmia that was evident prior to device attachment but worsened thereafter. Sheep 2 also developed a rear limb palsy following administration of Diazapam and a long period of sitting on the rear limb, although this did not contribute to early euthanasia. Sheep 5 was euthanized on day 11 after a blood conduit tubing connection failed.

3.3.1 Sheep Physiology:

General animal physiology was largely normal and unchanged throughout the experiment. The MAP was 84±12.8 mmHg prior to attachment, 90±8.4 mmHg at baseline, and averaged 103±0.8 mmHg thereafter (**Figure 3.6**), with no statistically significant

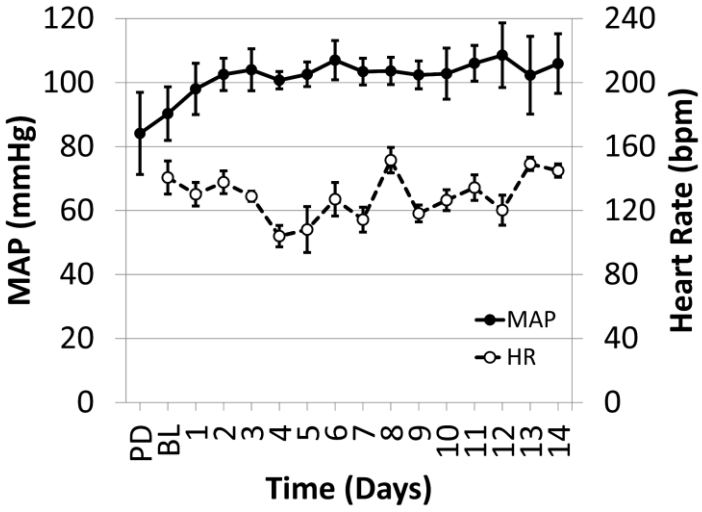

Figure 3.6: The mean arterial pressure and heart rate as a function of experimental time.

comparisons to baseline (p=0.24). The HR was 141±17.3 bpm prior to attachment, 130±10.1 bpm at baseline, and averaged 124±5.0 bpm thereafter (**Figure 3.6**), with no statistically significant comparisons to baseline (p=0.37). Arterial PCO_2 was 33±1.0 mmHg prior to cTAL attachment, 32±0.8 mmHg at baseline, and averaged 40±0.4 mmHg thereafter (**Figure 3.7**). The PCO_2 was statistically higher than baseline on Day 6 (p=0.02). Arterial PO_2 was 65±4 mmHg prior to cTAL attachment due to the presence of the shunt, 138±13 mmHg at baseline, and averaged 130±1.1 mmHg thereafter (**Figure 3.7**). Pre-device PO_2 was significantly lower than BL (p=0.01), but PO_2 was not statistically different from baseline thereafter (p=0.99).

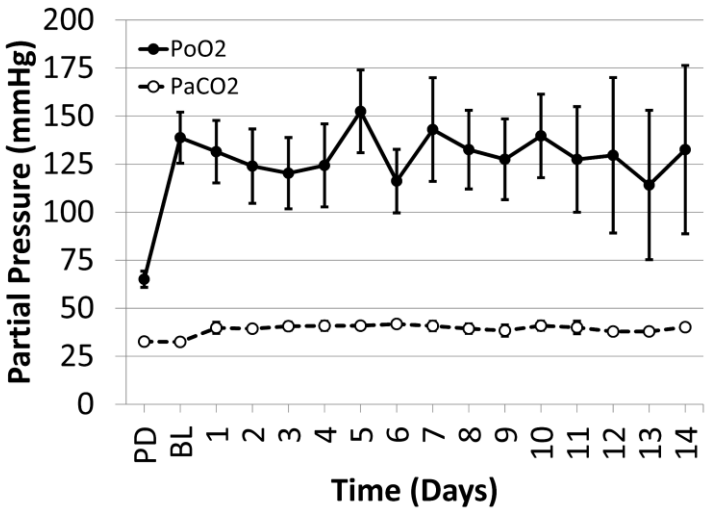

Figure 3.7: The arterial oxygen and carbon dioxide partial pressures as a function of experimental time.

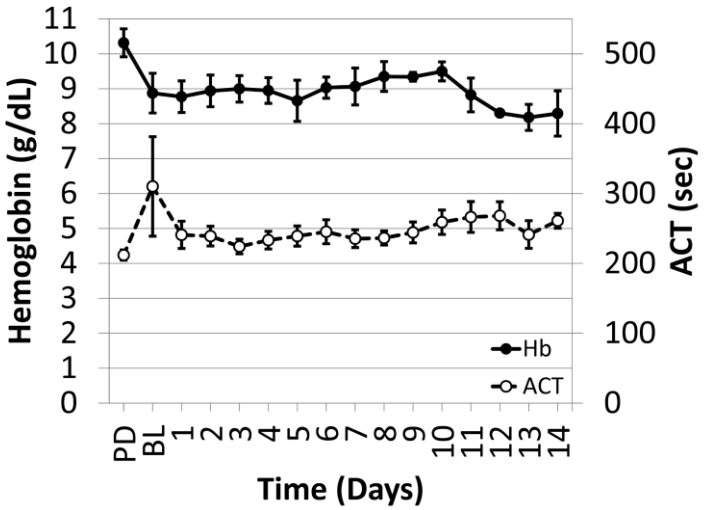

Figure 3.8: The blood hemoglobin level and activated clotting time as a function of experimental time.

3.3.2 Hematology

Neither ACT, normalized WBC, nor normalized platelet counts (p=0.99, p=0.27, and

p=0.75, respectively) varied significantly from baseline. The hemoglobin was 10.3±0.4 g/dL prior to cTAL attachment, 8.9±0.6 g/dL at baseline, and averaged 9.0±0.1 g/dL thereafter (**Figure 3.8**). The drop in hemoglobin from pre-device attachment to baseline was the only statistically significant comparison to baseline (p=0.01). The ACT was 211±7.3 sec prior to cTAL attachment, 310±71 sec at baseline, and averaged 238±2.1 g/dL thereafter (**Figure 3.8**). The normalized WBC count was 6.2±0.5 k/μL at baseline, trended upward throughout the experiment with an average of 6.8±0.6 k/μL over the course of the entire experiment with the count reaching a mamximum of 12.9±2.68 k/μL in the day 13-14 period (**Figure 3.9**). Despite this, WBC counts did not vary significantly from baseline (p=0.27). Bacterial cultures were analyzed from Sheep 3, 4, and 5 due to elevated body temperatures 5 days before surgery, Day 8, and Day 9, respectively. All culture results were negative for both aerobic and anaerobic bacterial growth. Normalized platelet counts were 281±36

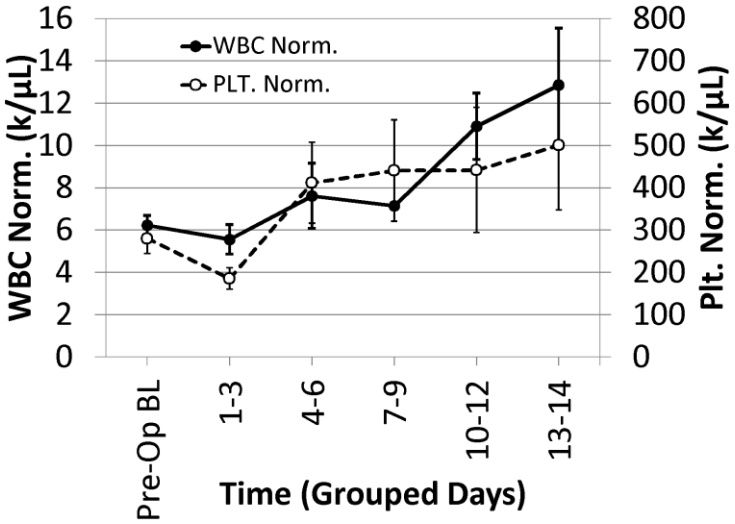

Figure 3.9: The hemoglobin normalized white blood cell and platelet counts function of experimental time.

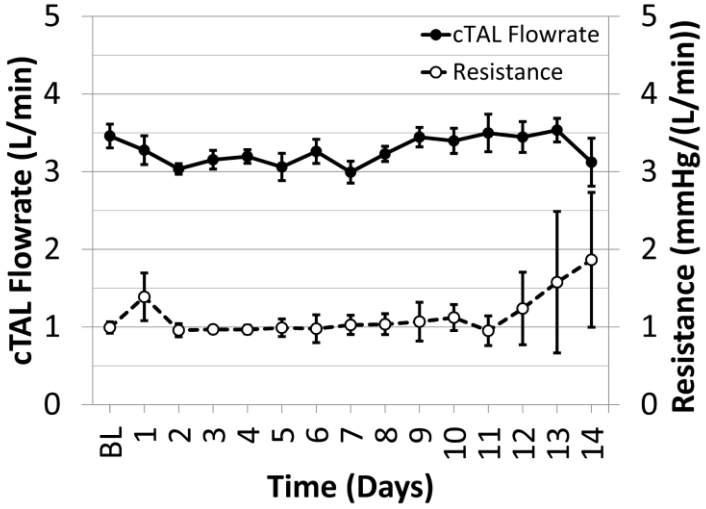

Figure 3.10: The cTAL flowrate and resistance as a function of experimental time.

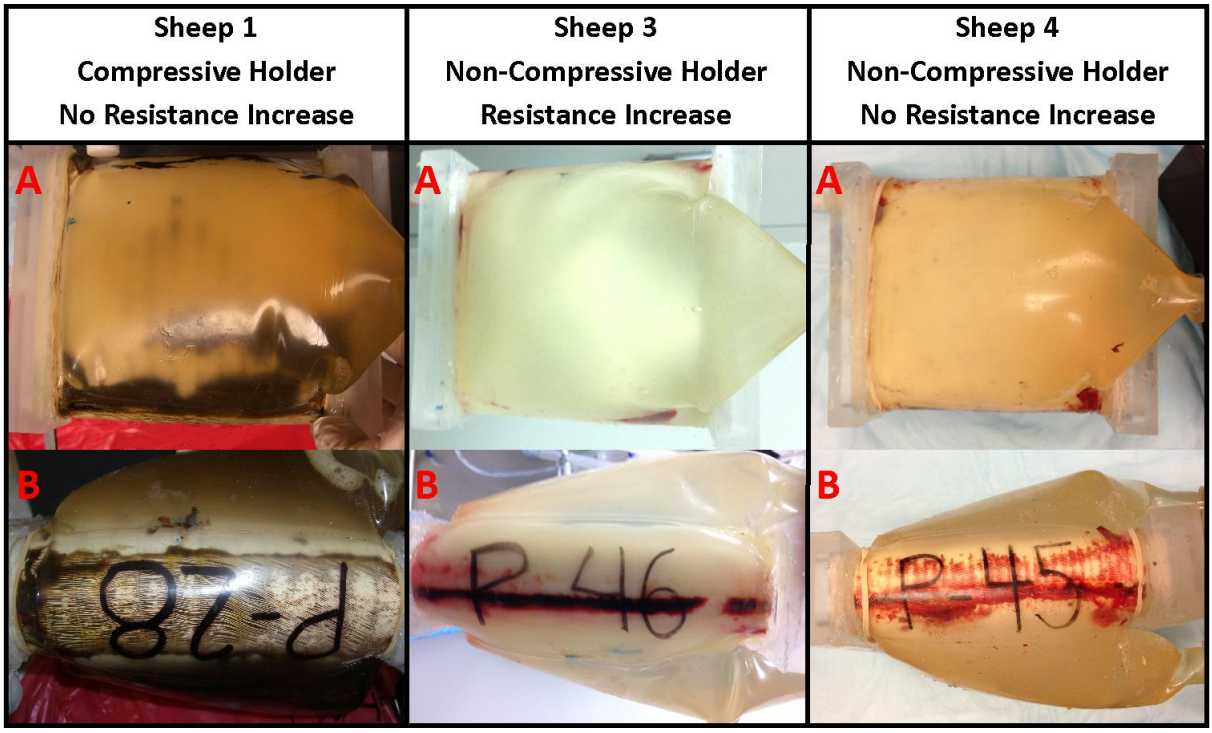

Figure 3.11: The clot formation in the cTAL's removed from all sheep surviving 14 days. *A:* The top views of the fiber bundles. *B:* The side views of the fiber bundles.

k/µL at baseline, dropped to 185±25 k/µL after device attachment, and averaged 346±81 k/µ thereafter (**Figure 3.9**).

3.3.3 Device Function

The cTAL functioned without any statistically significant changes in device flowrate, resistance, and VO_2 when comparing to baseline($p=0.68$, $p=0.99$, and $p=0.27$, respectively). Blood flow through the cTAL was 3.46±0.15 L/min at baseline and averaged 3.18±0.05 L/min throughout the experiment (**Figure 3.10**). cTAL resistance had a baseline of 0.99±0.07 mmHg/L/min and averaged 1.04±0.05 mmHg/L/min over the course of the experiment (**Figure 3.10**). In sheep 3, the cTAL resistance increased over days 12- 14 despite minimal visual thrombus formation in this device (**Figure 3.11**), possibly due to a faulty stop-cock with significant thrombus formation or a failed pressure transducer. Additionally, this cTAL did not have substantial decrease in flowrate with an average of 3.48 L/min for days 1-11 and 3.40 L/min days 12-14, suggesting faulty

resistance measurement over this period. cTAL VO_2 was 206±27 mL/min at baseline and averaged 180±8 mL/min over the course of the experiment (**Figure 3.12**). At approximately day 7, plasma leakage was observed in the gas outlet of the cTAL for most of the sheep. However, periodic increases in gas flow rates to clear plasma preserved gas exchange.

Devices that were attached to 14 day survivors had varying amounts of thrombus formation depending on which device holder was employed (**Figure 3.11**). The device from Sheep 1 employed the first generation holder and had gross thrombus formation on the sides of the device where the holder clamped on the fiber bundle. The devices from sheep 3 and sheep 4 employed the second generation

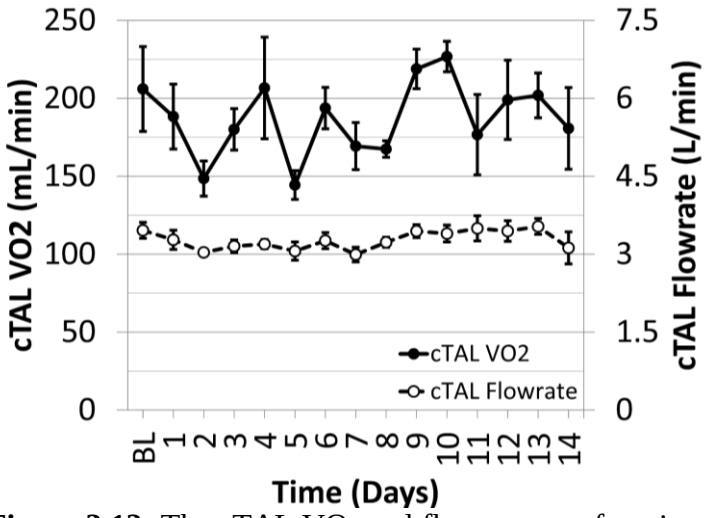

Figure 3.12: The cTAL VO_2 and flowrate as a function of experimental time.

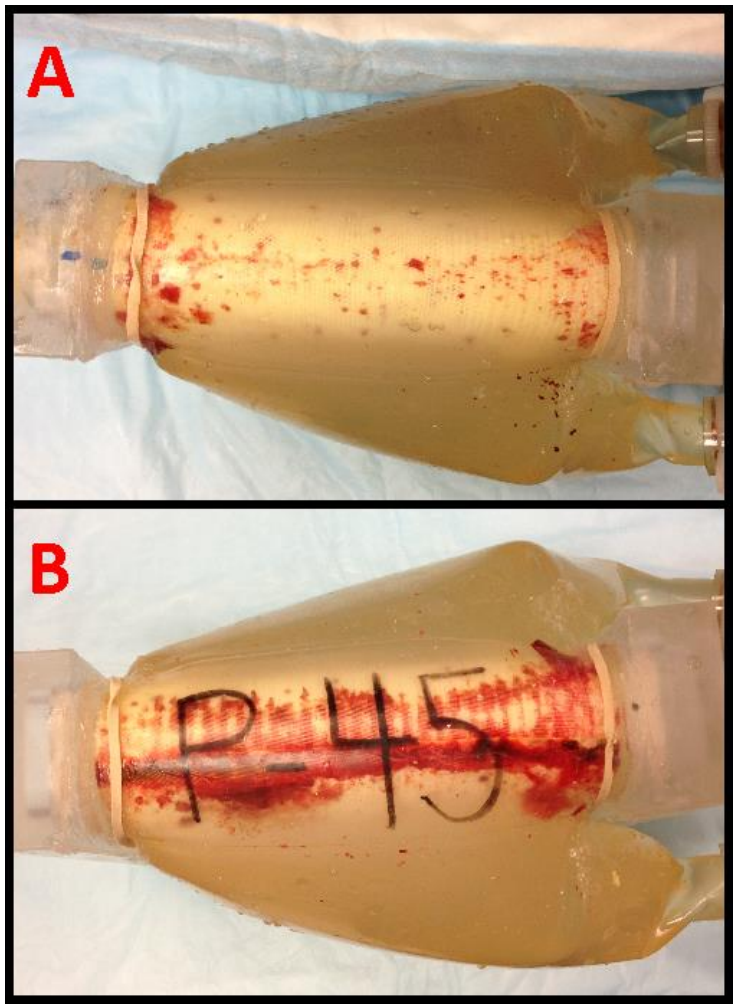

Figure 3.13: The cTAL removed from Sheep 4 after 14 days. *A:* Non-taped side. *B:* Taped side.

device holder and had very little thrombus formation. The majority of the bundles were clear of significant thrombus formation, with a small section of thrombus at device corners and thrombus formation on the side of the cTAL bundle stemming from a section of double sided tape used during device fabrication (**Figure 3.11 B and Figure 3.12 B**). The effect of the tape on thrombus formation can be seen in **Figure 3.13** showing the thrombus formation in the non-taped and taped sides of the fiber bundle from Sheep 4.

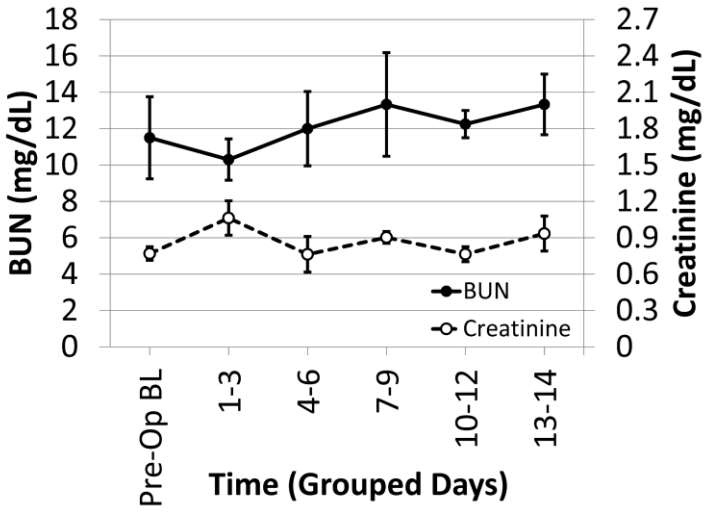

Figure 3.14: The kidney function markers BUN and creatinine as a function of experimental time.

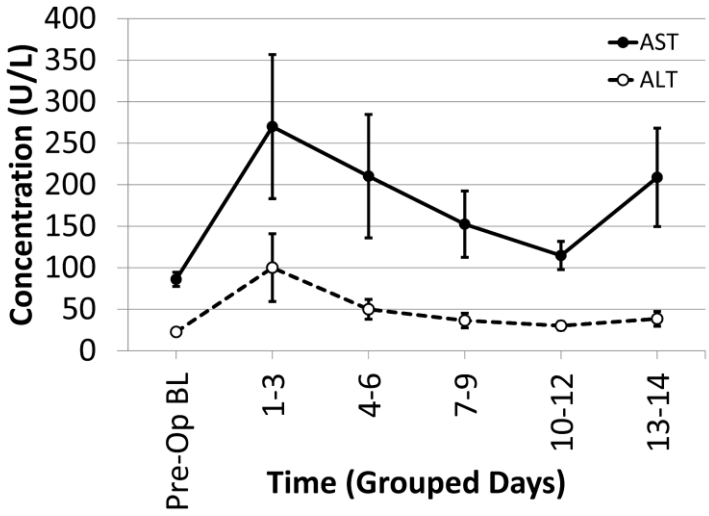

Figure 3.15: The liver function markers ALT and AST as a function of experimental time.

3.3.4 Organ Function

Neither BUN, creatinine, ALT nor AST varied significantly from baseline ($p=0.99$, $p=0.36$, $p=0.27$, and $p=0.51$, respectively). The baseline BUN and creatinine were 11.5±2.3 mg/dL and 0.77±0.06 mg/dL, respectively and averaged 11.9±0.9 mg/dL and 0.91±0.09 mg/dL, respectively thereafter (**Figure 3.14**). Liver enzymes increased immediately after surgery, but fell thereafter and stayed within normal ranges. However, at day 13-14 there was

a non-significant increase in the AST due to reduced sheep numbers coupled with an increase in one sheep. Of the sheep that were euthanized early the AST levels prior to euthanization were undetectable and 73 prior to euthanication for Sheep 2 and 5, respectively. The baseline ALT and AST were 23±3.6 U/L and 86±8.5 U/L, respectively and averaged 62±19.3 U/L and 211±34 U/L, respectively thereafter (**Figure 3.15**). Sheep 2 had an elevated AST of 450 prior to euthanization.

3.3.5 Necropsy

Gross inspections of the organs during necropsy were largely unremarkable with the exception of the lungs. The lungs of the sheep typically exhibited pulmonary edema throughout the lung, and atelectasis in the upper lobes and in the areas around the chest tubes and blood conduits. Also noted during the necropsy were visual signs of infection around the graft site of Sheep 4 due to inadequate tissue in-growth to seal the chest wall.

3.4 Discussion

The purpose of these studies was to determine if an uncoated cTAL could maintain the gas exchange and resistance characteristics demonstrated during short-term *in vitro* and *in vivo* studies while maintaining normal animal physiology for a period of 14 days. Overall, the cTAL demonstrated that it has the capability to be used for at least two weeks without any anticoagulant coatings, and likely longer with more sophisticated biomaterials approaches. The device maintained a low, constant resistance while supporting normal blood gases. Animal physiology was, in general, normal with initial changes due to the effect of surgery and a trend back towards normal values thereafter, with the exception of slightly elevated AST levels in one sheep, and atelectasis and edema in the lungs of the necropsied sheep.

Even though the cTAL doesn't utilize anti-coagulant coatings, there wasn't a significant increase in resistance over 14 days. There was a consistent upward spike in device resistance after

one day but resistance returned to baseline values thereafter. This likely reflects some initial, transient protein or cellular binding that then resolves. After 14 days, gross visual thrombus formation in the cTAL was minimal in all devices except the device attached to Sheep 1. In this sheep the device was primed and placed tightly within its holder, which led to stasis regions and clot formation on the sides of the fiber bundle. The remaining devices utilizing a less compressive holder had almost no gross thrombus formation in the entirety of the bundle with the exception of some thrombus formation stemming from a piece of tape used during device fabrication on the one side of the fiber bundle. Elimination of this tape is a minor alteration and should reduce the thrombus formation. Despite minimal clot formation, the resistance of the device attached to Sheep 3 apparently tripled over days 11-14. This was perplexing due to the minimal gross thrombus formation (**Figure 3.12**) and no reduction in the blood flow rate through the device. It is possible that the source of error was one of the stopcocks exhibiting back-bleeding and clotting or a faulty pressure transducer, but this is unknown.

Previous *in vitro* and acute *in vivo* experiments demonstrated a consistent resistance of approximately 0.5 mmHg/(L/min) (14-16), however the resistance started at 1 mmHg/(L/min) in this study. The higher resistance seen here may be due to different positioning of the device. In the short-term *in vivo* studies, the device was in its ideal positioning, sitting flat on the animal. In these long-term studies, the device was placed on its side at the animals flank. This can cause lower pressure and housing collapse in the superior regions of the device, and may limit blood flow through these regions. In theory, this could cause both increased resistance as well as stasis and coagulation in those regions. However, there was no noticeable difference in clot formation between the upper and lower regions of the device. Even when the device is poorly positioned on the animal, the resistance of the cTAL is lower than healthy normal lungs and the least resistive

commercially available device, the iLA membrane oxygenator with 6 mmHg/(L/min) resistance.(21, 22)

Overall, the cTAL proved more biocompatible than similar devices. The uncoated MC3 Biolung on average failed from clot formation within 7 days(18), while the anticoagulant coated iLA membrane oxygenator in a PA-LA configuration lasts 14-21 days before replacement is required.(23-26) The uncoated cTAL would have functioned well beyond 14 days, and the application of anti-thrombogenic coatings could potentially extend the functional lifespan into the range of a few months.

Gas exchange through the cTAL was maintained over 14 days despite some problems with plasma leakage. This is true, in part, because the cTAL's rated flow exceeds 7 L/min, and blood flow rates averaged 3.46 L/min. Thus, a considerable decrement of performance would have been necessary to see reduced gas exchange. When performance did degrade to a point of reduced gas exchange, the plasma was cleared from the fibers by increasing the sweep gas flowrate to 10 L/min for a period of time. Plasma leakage was observed because the cTAL was constructed with porous polypropylene fibers. Polypropylene fibers were used since nonporous polymethylpentene fibers offer limited choices of fiber diameters, and it was believed prior to this study that plasma leakage was not a problem in sheep. For clinical prototypes, PDMS coated polypropylene fibers or solid silicone fibers will be necessary.(27-30)

Animal physiology was largely normal over the course of the experiment. The heart rate, MAP, and arterial blood gasses normalized after device attachment. The kidneys of the animals were functioning normally throughout the experiment with only slight fluctuations in BUN and creatinine. The liver enzyme values showed some dysfunction post surgery, but the values trended back down to normal levels throughout the experiment. One exception was a non-significant

increase in the AST level on the last two day period of the experiment. This was largely the effect of the euthanization of two sheep (Sheep 2 and 5) with lower AST concentrations and an AST increase in one animal (Sheep 3). Sheep 2, that encountered limb palsy, was administered with Diazepam, Fumazenil, atropine, and epinephrine, and was euthanized on Day 5 due to a bradycardic arrhythmia. In the 24 hours prior to ethanization this sheep showed liver dysfunction with elevated ALT and an undetectable AST. Gross inspection of the organs at necropsy revealed no signs of major infarct or other deraignment with the exception of atelectasis and edema throughout the lungs. The atelectasis and edema likely resulted from a low respiratory drive brought on by too much carbon dioxide removal in the system.

Hematologically, the physiology was affected by the hemodilution of device attachment, but hematological values stayed consistent or rebounded the longer the cTAL was attached. Following device attachment and initial hemodilution, hemoglobin levels remained relatviely consistent with some non-significant decrease with time, and platelet counts trended back to normal. However, increased experimental repetitions may have yielded a statistically significant decrease in hemoglobin levels in part due to the large number of blood samples taken over the course of the experiment. The overall white blood cell count did not vary significantly over the course of the experiment. The WBC count for Sheep 1 and 3 increased steadily throughout the experiment indicating possible infection. However, Sheep 3, 4, and 5 were all cultured for bacteria and had negative cultures. The effects of hemodilution were offset by the minimal blood product consumption by the device, evidenced by the stable hemoglobin and normal platelet countsin the later course of the experiment. In clinical use, patients treated with the cTAL may need an initial transfusion of packed red blood cells after device attachment, but should not need any further transfusions over the remainder of the treatment with the cTAL. This is in contrast to ECMO where

reported blood product median daily transfusions can range from 0.16 to 2 units per day for red blood cell transfusions and from 0 to 3 units per day for platelet transfusions.(8, 31) These transfusion requirements can be particularly high for patients with significant pulmonary hypertension or other conditions that necessitate the utilization of the higher operating pressure VA ECMO configuration.(9) The prime volume of the cTAL and resulting hemodilution can be reduced by shrinking the overall size of the device. This is feasible since the cTAL is currently overdesigned in terms of gas exchange, and the fiber bundle frontal area and path length could both be reduced simultaneously to maintain low resistance.

The ultimate goal for the cTAL will be its use as a long term bridge to lung transplantation and destination therapy. In order to progress the cTAL towards this goal, the device will be reduced in size and prime volume, utilize a solid walled fiber to reduce plasma leakage and air embolism risk, and anticoagulant coatings will be applied to all surfaces of the device. The cTAL's superior fluid dynamic design coupled with these coatings could allow the functional lifetime of a single device to be on the order of months. Utilizing periodic device replacement, cTAL treatment could be used for years in a patient as a destination therapy. The lack of blood damage and need for continuing blood transfusions further indicates the cTAL's potential use as a destination therapy.

The 14 day long term efficacy experiments of the uncoated cTAL demonstrated the device's ability to support a patient for a period of weeks without major thrombus formation and subsequent device failure. The cTAL was able to maintain gas exchange performance despite the incidence of plasma leakage. During the period of cTAL attachment there were no major physiological derangements and the device consumed very little in terms of blood products. Even without anti-coagulant coatings, the cTAL could have functioned beyond the current 14 day experimental time, and continued improvements of the device including these coatings would

allow it to serve as a destination therapy.

3.5 References

1. Association AL. Lung disease data: 2008. Focus: Clean Air and Lung Disease Retrieved from http://www lungusa org. 2008.
2. Valapour M, Paulson K, Smith JM, Hertz MI, Skeans MA, Heubner BM, et al. OPTN/SRTR 2011 Annual Data Report: Lung. American Journal of Transplantation. 2013;13:149-77. doi: 10.1111/ajt.12024.
3. Hayes Jr D, Kukreja J, Tobias JD, Ballard HO, Hoopes CW. Ambulatory venovenous extracorporeal respiratory support as a bridge for cystic fibrosis patients to emergent lung transplantation. Journal of Cystic Fibrosis. 2012;11(1):40-5.
4. Bermudez CA, Rocha RV, Sappington PL, Toyoda Y, Murray HN, Boujoukos AJ. Initial Experience With Single Cannulation for Venovenous Extracorporeal Oxygenation in Adults. The Annals of Thoracic Surgery. 2010;90(3):991-5. doi: http://dx.doi.org/10.1016/j.athoracsur.2010.06.017.
5. angi AA, Mason DP, Yun JJ, Murthy SC, Pettersson GB. Bridge to lung transplantation using short-term ambulatory extracorporeal membrane oxygenation. The Journal of thoracic and cardiovascular surgery. 2010;140(3):713-5.
6. Garcia JP, Iacono A, Kon ZN, Griffith BP. Ambulatory extracorporeal membrane oxygenation: a new approach for bridge-to-lung transplantation. The Journal of thoracic and cardiovascular surgery. 2010;139(6):e137-e9.
7. Cheung P-Y, Sawicki G, Salas E, Etches PC, Schulz R, Radomski MW. The mechanisms of platelet dysfunction during extracorporeal membrane oxygenation in critically ill neonates. Critical care medicine. 2000;28(7):2584-90.
8. Ang A, Teo D, Lim C, Leou K, Tien S, Koh M. Blood transfusion requirements and independent predictors of increased transfusion requirements among adult patients on extracorporeal membrane oxygenation–a single centre experience. Vox sanguinis. 2009;96(1):34-43.
9. Shafii AE, Mason DP, Brown CR, Vakil N, Johnston DR, McCurry KR, et al. Growing experience with extracorporeal membrane oxygenation as a bridge to lung transplantation. ASAIO Journal. 2012;58(5):526-9.
10. Van Meurs K, aZwischenberger JB, Extracorporeal Life Support O. ECMO: extracorporeal cardiopulmonary support in critical care. [Ann Arbor, Mich.]: Extracorporeal Life Support Organization; 2005. xxiii, 625 p. p.
11. Turner DA, Cheifetz IM. Extracorporeal Membrane Oxygenation for Adult Respiratory Failure. Respiratory care. 2013;58(6):1038-52.
12. Toyoda Y, Bhama JK, Shigemura N, Zaldonis D, Pilewski J, Crespo M, et al. Efficacy of extracorporeal membrane oxygenation as a bridge to lung transplantation. The Journal of Thoracic and Cardiovascular Surgery. 2013;145(4):1065-71. doi: http://dx.doi.org/10.1016/j.jtcvs.2012.12.067.
13. Pesenti A, Zanella A, Patroniti N. Extracorporeal gas exchange. Current opinion in critical care. 2009;15(1):52-8. Epub 2009/01/31. doi: 10.1097/MCC.0b013e3283220e1f. PubMed PMID: 19179870.
14. Schewe RE, Scipione CN, Koch KL, Cook KE. In-parallel attachment of a low-resistance compliant thoracic artificial lung under rest and simulated exercise. The Annals of thoracic surgery. 2012.
15. Schewe RE, Khanafer KM, Arab A, Mitchell JA, Skoog DJ, Cook KE. Design and In

Vitro Assessment of an Improved, Low-Resistance Compliant Thoracic Artificial Lung. ASAIO Journal. 2012;58(6):583-9.
16. Scipione CN, Schewe RE, Koch KL, Shaffer AW, Iyengar A, Cook KE. Use of a low-resistance compliant thoracic artificial lung in the pulmonary artery to pulmonary artery configuration. The Journal of thoracic and cardiovascular surgery. 2013.
17. Sato H, Hall CM, Lafayette NG, Pohlmann JR, Padiyar N, Toomasian JM, et al. Thirty-Day In-Parallel Artificial Lung Testing in Sheep. The Annals of Thoracic Surgery. 2007;84(4):1136-43. doi: http://dx.doi.org/10.1016/j.athoracsur.2007.05.051.
18. Sato H, Griffith GW, Hall CM, Toomasian JM, Hirschl RB, Bartlett RH, et al. Seven-day artificial lung testing in an in-parallel configuration. The Annals of thoracic surgery. 2007;84(3):988-94.
19. Schewe-Mott RE. Thoracic Artificial Lung Design: University of Michigan; 2012.
20. Akay B, Foucher JA, Camboni D, Koch KL, Kawatra A, Cook KE. Hemodynamic design requirements for in series thoracic artificial lung attachment in a model of pulmonary hypertension. ASAIO journal (American Society for Artificial Internal Organs: 1992). 2012;58(4):426.
21. Müller T, Lubnow M, Philipp A, Bein T, Jeron A, Luchner A, et al. Extracorporeal pumpless interventional lung assist in clinical practice: determinants of efficacy. European Respiratory Journal. 2009;33(3):551-8. doi: 10.1183/09031936.00123608.
22. Flörchinger B, Philipp A, Klose A, Hilker M, Kobuch R, Rupprecht L, et al. Pumpless Extracorporeal Lung Assist: A 10-Year Institutional Experience. The Annals of thoracic surgery. 2008;86(2):410-7.
23. de Perrot M, Granton JT, McRae K, Cypel M, Pierre A, Waddell TK, et al. Impact of extracorporeal life support on outcome in patients with idiopathic pulmonary arterial hypertension awaiting lung transplantation. The Journal of Heart and Lung Transplantation. 2011;30(9):997-1002.
24. Schmid C, Philipp A, Hilker M, Arlt M, Trabold B, Pfeiffer M, et al. Bridge to lung transplantation through a pulmonary artery to left atrial oxygenator circuit. The Annals of thoracic surgery. 2008;85(4):1202-5.
25. Strueber M, Hoeper MM, Fischer S, Cypel M, Warnecke G, Gottlieb J, et al. Bridge to Thoracic Organ Transplantation in Patients with Pulmonary Arterial Hypertension Using a Pumpless Lung Assist Device. American Journal of Transplantation. 2009;9(4):853-7. doi: 10.1111/j.1600-6143.2009.02549.x.
26. Camboni D, Philipp A, Arlt M, Pfeiffer M, Hilker M, Schmid C. First Experience With a Paracorporeal Artificial Lung In Humans. ASAIO Journal. 2009;55(3):304-6 10.1097/MAT.0b013e31819740a0.
27. Kawahito S, Motomura T, Glueck J, Nosé Y. Development of a new hollow fiber silicone membrane oxygenator for ECMO: The recent progress. Annals of thoracic and cardiovascular surgery. 2002;8(5):268-74.
28. Sato H, Odeleye ME, Chambers SD, Hirschl RB, Bartlett RH, Cook KE. Thoracic artificial lung (TAL) development: Determining the most suitable fiber for TAL. ASAIO Journal. 2005;51(2):51A.
29. LaFayette NG, Schewe RE, Montoya JP, Cook KE. Performance of a MedArray silicone hollow fiber oxygenator. ASAIO Journal. 2009;55(4):382-7.
30. Eash HJ, Jones HM, Hattler BG, Federspiel WJ. Evaluation of plasma resistant hollow fiber membranes for artificial lungs. ASAIO journal. 2004;50(5):491-7.

31. Javidfar J, Brodie D, Iribarne A, Jurado J, LaVelle M, Brenner K, et al. Extracorporeal membrane oxygenation as a bridge to lung transplantation and recovery. The Journal of thoracic and cardiovascular surgery. 2012;144(3):716-21.

Chapter 4: Pulmonary Assist Device Computational Modeling and Design

4.1 Introduction

In the United States there are over 12 million patients with chronic lung diseases that are fatal without lung transplantation.(1) However, there are less than 2,000 lung transplantations performed each year in the United States.(2) These transplants account for a fraction of a percent of patients who need treatment. The device described here, the pulmonary assist device (PAD), is designed both as a bridge to lung transplantation as well as a destination therapy device for the millions of patients who have no chance of receiving a donor lung.

Current gas exchangers are large devices with high resistances and large blood contacting surface areas. Modern adult gas exchangers for use in ECMO and $AVCO_2R$ have gas exchange surface areas that range from 1.1 m^2 to 2.5 m^2.(3, 4) While they are very efficient in gas exchange, their large blood contacting surface area and high resistances (lowest available, 5-6 mmHg/(L/min))(5, 6) have negative effects on biocompatibility.(7, 8) When used in pumped configurations the high resistance of the device leads to higher blood pump speeds and, in turn, blood damage and activation.(7) The higher pump speeds combined with large blood contacting surface areas also result in greater incidence of clot formation and a limitation of two to three weeks of device longevity despite anti-coagulant coatings and systemic heparinization(7, 9).

In addition to biocompatibility issues, current gas exchangers are limited in their long term use by their portability. These devices and their associated pumps and circuits are very large and confine patients to the ICU. Advances in ECMO miniaturization have allowed for limited ambulation, but these patients need a team to assist in their walking.(10-12) Thus, regular patient-

initiated exercise is not an option, and they are not able to return home or to regular patient rooms during treatment. As a result, there is a need for a smaller, more portable device and ECMO system.

4.1.1 Design Goals

As a long term support device, our goal is to design a PAD that is compact for ease of transportation in the hospital or at home and modular for flexibility to the needs of the patient. Modularity will allow for one or two module configurations as dictated by respiratory needs and/or the need for unloading of the heart in a pulmonary AV attachment. Additionally, the PAD was designed with the goal of achieving a clot free lifespan of months so that treatment can continue for years with preventative device change-outs. In order to satisfy these needs, the pulmonary assist device was designed to be used in one or two gas exchanger module configurations operating in either a pumped or pumpless manner with a variety of vascular attachment mode possibilities.

Design goals for gas exchange capabilities of the PAD were developed through discussion with our clinical collaborator, Dr. Matthew Bacchetta. He expressed that most patients can be effectively treated with partial oxygen exchange support. It was desired that the device be able to oxygenate venous blood to 95% saturation with a flowrate of 1.25 L/min through each module. This would allow for up to 2.5 L/min of blood flowrate when used in a two module configuration. The PAD was also designed to remove at least 50 mL/min of carbon dioxide per module with 5 L/min of sweep gas flowrate through each module. The Novalung has a resistance of 5-6 mmHg/(L/min),(5, 6) and was not able to provide sufficient unloading of the right heart in pulmonary hypertension patients.(13-16) The resistance of the PAD should have a resistance similar to that of a healthy natural lung when placed in a two module parallel configuration. A target single module resistance less than 2.5 mmHg/(L/min) would result in a parallel two module resistance of 1.25 mmHg. Lastly, the device must be small enough to be used with a patient in a

home setting, preferably worn on a belt.

The first stage of the design of the pulmonary assist device was devoted to determining a compact fiber bundle geometry meeting the gas exchange and resistance goals. This fiber bundle design was performed using semi-empirical computational methods that rely on data from similar, previously tested fiber bundles. These computational methods were performed in Matlab (The Mathworks Inc, Natick, MA) and outlined in the early part of the chapter.

The second stage of computational modeling focused on the design of the housing around the fiber bundle geometry chosen in the first stage of design. With an initial port configuration and bundle design, computational fluid dynamics simulations were performed for several housing geometries similar to the cTAL tested in the previous chapter with the goal of choosing an inlet and outlet configuration that is the most compact and avoids clot promoting regions of blood stasis and recirculation. In regions of blood stasis and recirculation, pro-coagulant molecules that are generated from blood contact with artificial surfaces are able to build up and induce clot formation within the gas exchanger. Clot formation leads to an increase in device resistance, reduced gas exchange, and increased risk of thromboembolism. No quantifiable rules exist for an acceptable degree of recirculation or minimum blood flow velocity. Thus, care will be taken to minimize recirculation and statis while not making dramatic changes to the overall device concept.

4.2 Methods

4.2.1 Computational Bundle Modeling

Custom Matlab code was written to choose the appropriately sized fiber bundle for the PAD. Design curves were created to characterize the bundle aspect ratio, oxygen exchange, and bundle resistance as a function of fiber surface area and bundle blood flow frontal area. Design curves of carbon dioxide exchange were produced as a function of surface area and sweep gas

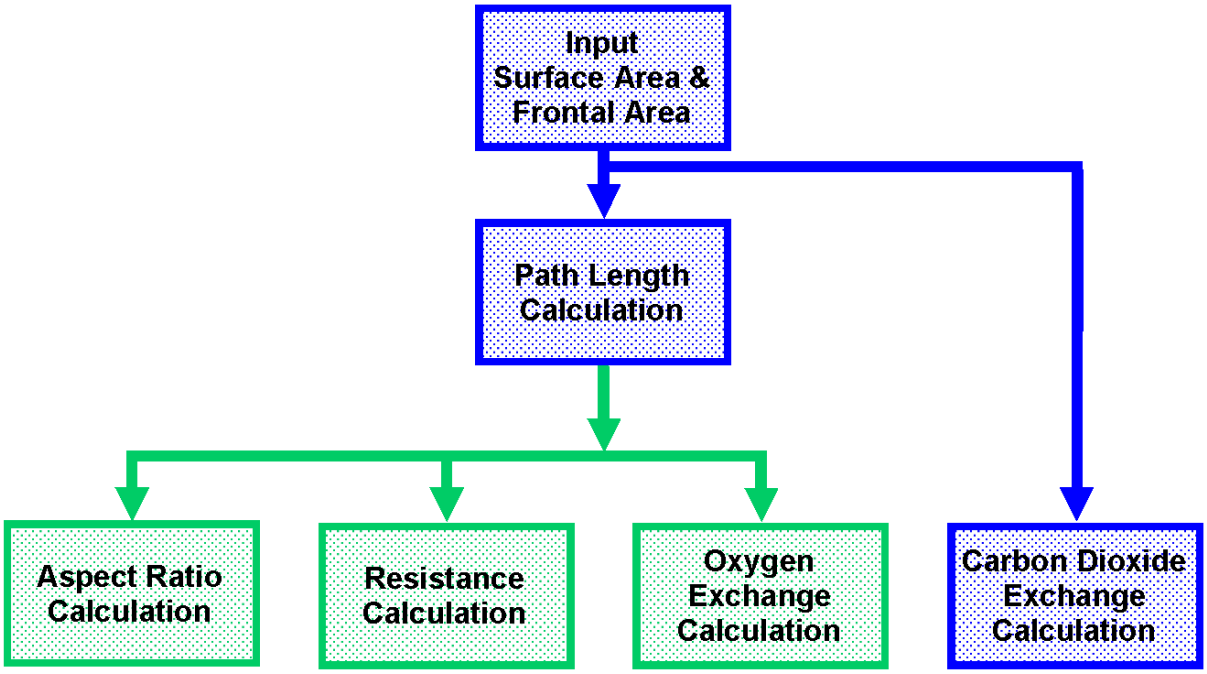

Figure 4.1: The flowchart of bundle design computational modeling in Matlab.

flowrate. A flowchart of the computational modeling procedure can be seen in **Figure 4.1**.

Bundle Dimensions and Aspect Ratio

Bundle dimensions (**Figure 4.2**) were calculated from a range of fiber bundle surface areas between 0.1 and 0.5 m^2 with a step size of 0.1 m^2, and bundle blood flow path frontal areas between 20 and 50 cm^2 with a step size of 0.1 cm^2. The rolling of a fiber bundle creates a radius at either end of the fiber bundle (**Figure 4.2.A**) that would affect overall surface area of the device and therefore gas exchange. However, the prediction of the exact size of a rolled fiber bundle is subject to variability and difficult to model accurately, so for the purposes of computational modeling of the bundle in Matlab, the bundle was modeled as a rectangular prism.(**Figure 4.2.B**)

With known frontal and surface areas, the bundle dimension of height or path length was calculated using fiber and fiber mat geometries and **Equation 4.1** as detailed in **Appendix D.**

$$PL = \frac{(\Phi_f + gap) * SA * \cos\theta}{\pi * \Phi_f * FA * spacing} \quad (4.1)$$

where PL is the bundle path length, Φ_f is the diameter of a single fiber, w is the width of the fiber bundle, gap is the distance between layers of fiber mat, spacing is the density of fiber packing in the fiber mat expressed as the number of fibers per unit length, and θ is the distortion angle that the angled fiber of the fiber mat makes with the axis across the width of the fiber bundle as shown in **Figure 4.3**. Since **Equation 4.1** only requires frontal area and none of the other Matlab analyses in subsequent sections require specific bundle width or length values, the frontal area of the bundle is assumed to be square for simplicity. However, the actual constructed bundle can be any ratio of width to length so long as it meets the frontal area and surface area specifications.

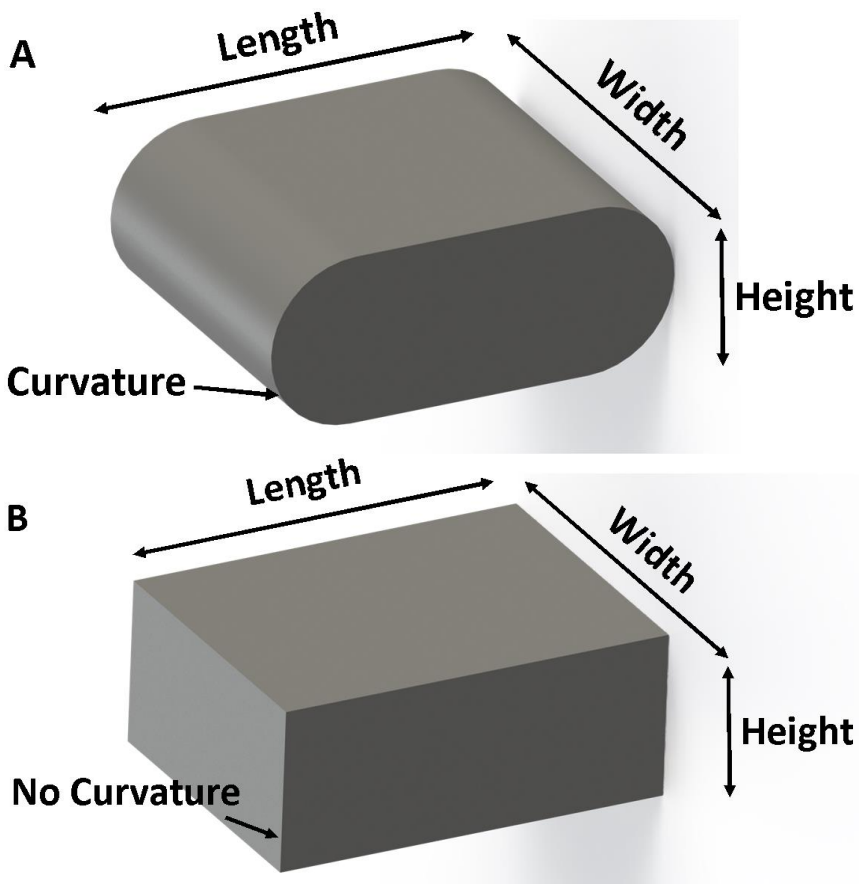

Figure 4.2: The dimensions of the fiber bundles for: *A* a curved fiber bundle. *B* a rectangular fiber bundle.

After the path lengths were known the bundle aspect ratio was calculated for each combination of frontal and surface area, according to **Equation 4.2**

$$AR = \frac{\sqrt{FA}}{PL} \tag{4.2}$$

in which AR is the aspect ratio and FA is the frontal area. The aspect ratio is important for the

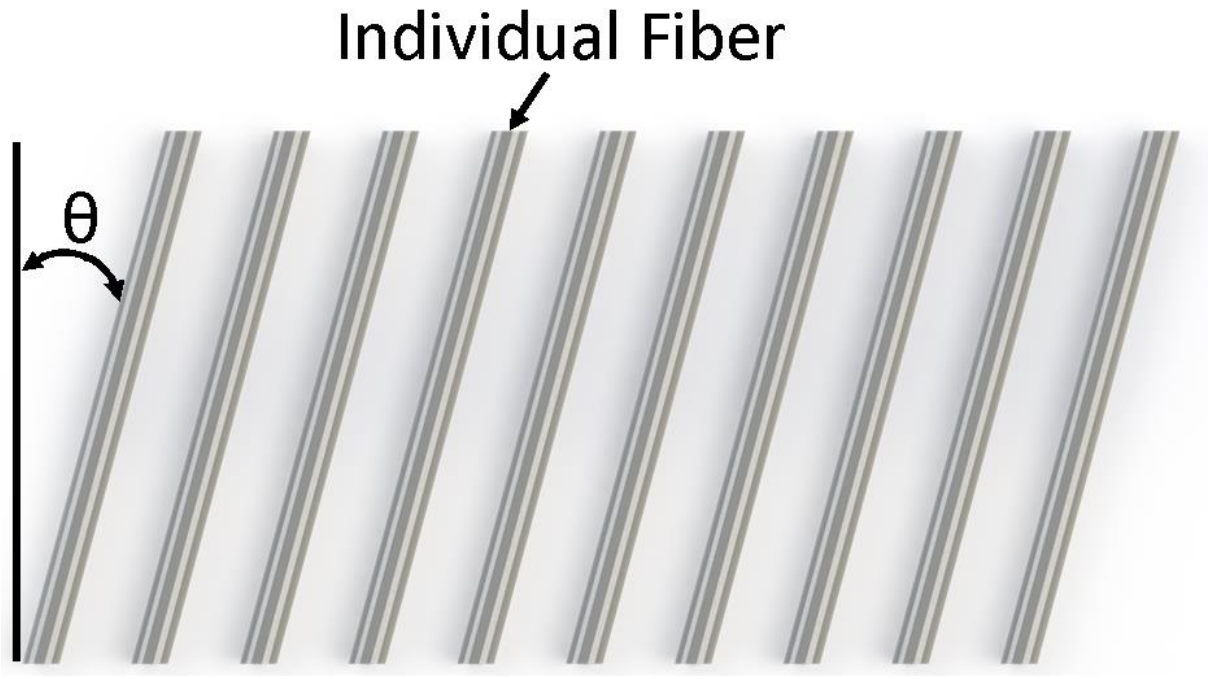

Figure 4.3: A single layer of fibers with the distortion angle labeled.

overall design for several reasons. First, although the modeling is performed on idealized, rectangular fiber bundles, the rolled bundles have curvature at the ends of the bundle that results in a variation of path length that can effect gas exchange and bundle resistance. Second, a bundle with low aspect ratio is difficult to manufacture since it is close to circular.

Bundle Resistance

Once the dimensions of the fiber bundle were output, the resistance of the bundle could be estimated using a Darcy law porous media model according to **Equation 4.3**

$$k_p = \frac{Q*\mu*PL}{FA*\Delta P} \tag{4.3}$$

where k_p is the permeability, μ is the dynamic viscosity, and ΔP is the pressure drop across the fiber bundle. A permeability of $2.81e^{-9}$ m^2 was obtained from experimental data from an early cTAL prototype with a similar fiber bundle to the PAD fiber bundle.(17) **Equation 4.3** was rearranged to yield **Equation 4.4**

$$\frac{\Delta P}{Q} = \frac{\mu * PL}{FA * k_p} \tag{4.4}$$

The left hand side of **Equation 4.4** is equal to the resistance of the fiber bundle, R, so **Equation 4.4** reduces to **Equation 4.5**

$$R = \frac{\mu * PL}{FA * k_p} \tag{4.5}$$

The dynamic viscosity of blood was calculated according to **Equation 4.6**

$$\mu = (2.205e - 5) * e^{\left[\frac{1965}{273.15+T} + (2.31 * H)\right]} \tag{4.6}$$

where μ is the dynamic viscosity of blood in Poise, T is the Temperature in degrees Celsius, and H is the fractional hematocrit.(18) The resistances were calculated and plotted for all frontal area and surface area combinations.

Oxygen Exchange Theory

Previous studies of gas exchangers have utilized heat exchange theory from shell and tube heat exchangers to model the oxygen exchange in medical gas exchangers.(18-21) The gas exchange fiber bundle of a medical gas exchanger is very similar to a crossflow shell and tube heat exchanger, but instead of transferring heat to a fluid it transfers oxygen to a fluid removes carbon dioxide from the fluid. However, the interactions of oxygen and carbon dioxide in the blood are much more complex than the interaction of heat with a fluid in a heat exchanger. When oxygen and carbon dioxide are exchanged with the blood, they are not merely dissolved. The oxygen both dissolves in the blood and chemically binds with hemoglobin. Carbon dioxide is dissolved in the blood and becomes sequestered as bicarbonate in the blood. Furthermore, carbon dioxide exchange is typically limited by the sweep gas flowrate, so heat exchanger theory typically isn't used for modeling. The exchange of oxygen is highly dependent on the blood flow in the gas exchanger

and can still be modeled using heat exchange theory, but with adaptations to account for uptake of oxygen by hemoglobin.(18-21)

The crossflow shell and tube heat exchanger heat exchange theory can be adapted to the oxygen exchange of a medical gas exchanger as described by previous studies. Dimensionless analysis of tube banks in both heat exchange theory adapted for mass transfer, and mass transfer theory yields a model of mass transfer in a fiber bundle described by the Reynolds number, the Stanton number, and the Schmidt number according to **Equations 4.7-4.9**

$$N_{St} = \frac{K_L}{v} \tag{4.7}$$

$$N_{Sc} = \frac{\mu}{\rho * D_{eff}} \tag{4.8}$$

$$f(N_{Re}) = N_{St} * {N_{Sc}}^{2/3} . \tag{4.9}$$

The N_{St} is the mass transfer Stanton number expressed as the ratio of mass flux to the mass flux capacity of the fluid flow. The N_{Sc} is the Schmidt number, which is the gas exchange equivalent of the Prandtl number. It is expressed as the ratio of momentum transport to diffusive transport in which K_L is the local mass transfer coefficient of oxygen from the gas exchange fiber, v is the velocity of the blood, D_{eff} is the effective diffusivity of oxygen in blood, μ is the dynamic viscosity of blood, and ρ is the density of blood.(18) Combining **Equations 4.7-4.9** yields **Equation 4.10**

$$f(N_{Re}) = \frac{K_L}{v} * \left(\frac{\mu}{\rho * D_{eff}}\right)^{2/3} \tag{4.10}$$

Low Reynolds numbers heat exchanger experiments yielded a power law relationship for the Reynolds number function leading to **Equation 4.11**

$$\Phi * {N_{Re}}^{-m} = \frac{K_L}{v} * \left(\frac{\mu}{\rho * D_{eff}}\right)^{2/3} \tag{4.11}$$

where m and Φ are dimensionless constants derived from experimental data for a given gas exchanger fiber mat and bundle. With further manipulation this equation becomes the basis for being able to predict the oxygen exchange performance of varying sized fiber bundles within a gas exchanger.(18) The m and Φ values were derived from experimental data and then fed back into this equation to predict the oxygen exchange for a differently sized fiber bundle. **Equation 4.12** gives the velocity of flow through the porous media composed of the fibers of the gas exchange fiber bundle

$$v = \frac{Q_b}{por * Af} \tag{4.12}$$

where Q_b is the bulk blood flowrate through the fiber bundle, por is the porosity of the fiber bundle, and A_f is the frontal area of the fiber bundle that the blood flows through. The porosity of the fiber bundle, which is the ratio of void volume to total volume around a fiber, can be solved using **Equation 4.13**

$$\text{por} = 1 - \frac{\pi * \Phi_f * spacing}{4} \tag{4.13}$$

Inserting **Equation 4.12** into **Equation 4.11** yields **Equation 4.14**.

$$\Phi * {N_{Re}}^{-m} = \frac{K_L * por * Af}{Q_b} * \left(\frac{\mu}{\rho * D_{eff}}\right)^{2/3} \tag{4.14}$$

With the goal of further refining **Equation 4.14**, the local mass transfer coefficient of oxygen in blood for the gas exchanger, K_L, is derived using a balance of the mass transfer rate between the gas exchanger and the uptake of oxygen by the blood. The local rate of mass transfer along an increment of the path length of the fiber bundle, $\dot{m}_{bundle}$, has been shown to follow **Equation 4.15** (18)

$$\dot{m}_{bundle} = K_L * dSA * (C_{O_{2f}} - C_{O_{2b}}) \tag{4.15}$$

where dSA is the incremental surface area contained in an incremental distance dx into the fiber bundle, C_{O2f} is the concentration of oxygen at the outer diameter of the fiber and C_{O2b} is the concentration of oxygen in the bulk flow of blood. The incremental surface area contained in dx can be restated as a function of dx using fiber geometry and **Equation 4.16**

$$dSA = \frac{4*(1-por)*A_f}{\Phi_f} * dx \tag{4.16}$$

where Φ_f is the outside diameter of the fiber and dx is the incremental distance into the fiber bundle perpendicular to the frontal area. The difference in concentration of oxygen in the blood at the fiber outer surface and the bulk flow can be related to the partial pressure of oxygen dissolved in the blood according to **Equation 4.17** (18)

$$C_{O_{2f}} - C_{O_{2b}} = k_{WB} * \left(P_{O_{2g}} - P_{O_{2b}}\right) \tag{4.17}$$

where k_{WB} is the solubility of oxygen in whole blood, P_{O2g} is the partial pressure of oxygen in the sweep gas, and P_{O2b} is the partial pressure of oxygen dissolved in the bulk flow of blood. **Equations 4.16** and **4.17** can be inserted into **Equation 4.15** to yield **Equation 4.18**

$$\dot{m}_{bundle} = K_L * \frac{4*(1-por)*A_f}{\Phi_f} * k_{WB} * (P_{O_{2g}} - P_{O_{2b}}) * dx \tag{4.18}$$

The mass transfer rate of oxygen taken up by the blood, $\dot{m}_{blood}$, can be calculated with **Equation 4.19**

$$\dot{m}_{blood} = \dot{m}_{blood_b} + \dot{m}_{blood_d} \tag{4.19}$$

where $\dot{m}_{bloodb}$ is the mass transfer rate of oxygen taken up by the blood in the form of oxygen bound to hemoglobin and $\dot{m}_{bloodd}$ is the mass transfer rate of oxygen taken up by the blood in the form of oxygen dissolved in the blood. $\dot{m}_{bloodb}$ has been shown previously to follow **Equation 4.20** (18)

$$\dot{m}_{blood_b} = Q_b * k_{WB} * \frac{dP_{O_2}}{dx} * dx \tag{4.20}$$

where P_{O2} is the partial pressure of oxygen dissolved in the blood and Q_b is the blood flowrate. $\dot{m}_{bloodb}$ has been shown previously to follow **Equation 4.21** (18)

$$\dot{m}_{blood_d} = Q_b * 1.34 * C_{hb} * \frac{dS}{dx} * dx \tag{4.21}$$

where 1.34 is the amount of oxygen that can be dissolved in 1 gram of hemoglobin with units mL_{O2}/g_{hb}, C_{hb} is the hemoglobin concentration in blood, and S is the oxyhemoglobin saturation. **Equations 4.20** and **4.21** can be inserted into **Equation 4.19** and rearranged to yield **Equation 4.22**

$$\dot{m}_{blood} = \left(1 + 1.34 * \frac{C_{hb}}{k_{WB}} * \frac{dS}{dP_{O_2}}\right) * k_{WB} * Q_b * \frac{dP_{O_2}}{dx} * dx \tag{4.22}$$

Since the amount of oxygen given off by the gas exchanger is equal to the amount of oxygen taken up by the blood, $\dot{m}_{bundle}$ is equal to $\dot{m}_{blood}$. The right hand sides of **Equations 4.18** and **4.22** can then be equated to create **Equation 4.23**

$$K_L * \frac{4 * (1 - por) * A_f}{\Phi_f} * k_{WB} * \left(P_{O_{2g}} - P_{O_{2b}}\right) * dx =$$

$$[1 + (1.34 * \frac{C_{hb}}{k_{WB}} * \frac{dS}{dP_{O_2}})] * k_{WB} * Q_b * \frac{dP_{O_2}}{dx} * dx \tag{4.23}$$

Simplifying **Equation 4.23** and solving for K_L yields **Equation 4.24**

$$K_L = \frac{Q_b * \Phi_f}{4 * (1 - por) * A_f} * \frac{1 + \lambda(P)}{P_g - P} * \frac{dP_{O_2}}{dx} \tag{4.24}$$

where $\lambda(P_{O2})$ is a sink term that takes into account oxygen uptake by hemoglobin with $\lambda(P)$ following **Equation 4.25**

$$\lambda\left(P_{O_2}\right) = 1.34 * \frac{C_{hb}}{k_{WB}} * \frac{dS}{dP_{O_2}} \quad (4.25)$$

where the oxyhemoglobin saturation, S, can be derived from **Equation 4.26**

$$S = \frac{(\frac{P_{O_2}}{P_{50}})^{n_{rbc}}}{1+(\frac{P_{O_2}}{P_{50}})^{n_{rbc}}} \quad (4.26)$$

where n_{rbc} is the Hill parameter which for bovine blood is equal to 2.85 and human blood is equal to 2.7, and P_{50} is the partial pressure of oxygen dissolved in blood in mmHg when the hemoglobin is 50% saturated.(18, 21) **Equation 4.26** can be differentiated and combined with **Equation 4.25** combined to yield **Equation 4.27**

$$\lambda\left(P_{O_2}\right) = 1.34 * \frac{C_{hb}}{k_{WB}} * \left(\frac{P_{O_2}}{P_{50}}\right)^{n_{rbc}-1} * \frac{n}{P_{50}} * \frac{1}{[1+\left(\frac{P_{O_2}}{P_{50}}\right)^{n_{rbc}}]^2} \quad (4.27)$$

P_{50} can be found using **Equations 4.28** and **4.29** for bovine and human blood, respectively (18)

$$P_{50_{bovine}} = 29.0 * 10^{\{[0.41*(7.4-pH)]-[0.024*(37-T)]\}} \quad (4.28)$$

$$P_{50_{human}} = 26.6 * 10^{\{[0.48*(7.4-pH)]-[0.024*(37-T)]\}} \quad (4.29)$$

where T is the temperature in degrees Celsius. The solubility of oxygen in whole blood, k_{WB}, can be calculated using **Equations 4.30-4.32**.(18, 21)

$$k_c = (4.658e-5) * 1.01^{(37-T)} \quad (4.30)$$

$$k_p = (2.855e-5) * 1.01^{(37-T)} \quad (4.31)$$

$$k_{WB} = (k_c * H) + [k_p * (1-H)] \quad (4.32)$$

where k_c is the solubility of oxygen in the cellular component of blood in $mL_{O2}/(mL_{blood}*mmHg)$,

k_c is the solubility of oxygen in the plasma component of blood in $mL_{O2}/(mL_{blood}*mmHg)$, k_{WB} is the solubility of oxygen in whole blood in $mL_{O2}/(mL_{blood}*mmHg)$, and H is the fractional hematocrit. The effective diffusivity that takes into account reactions between oxygen and hemoglobin can be found using **Equation 4.33** (18, 21)

$$D_{eff} = \frac{D_{WB}}{1+\lambda(P_{O_2})} \tag{4.33}$$

where D_{WB} is the diffusivity of oxygen in whole blood. The diffusivity of oxygen in whole blood can be calculated using **Equations 4.34-4.40**

$$D_c = (0.76e-5) * 1.025^{(T-25)} \tag{4.34}$$

$$D_p = (1.62e-5) * 1.025^{(T-25)} \tag{4.35}$$

$$N = \frac{k_c * D_c}{k_p * D_p} \tag{4.36}$$

$$\beta = \frac{(N-1)}{3} * \left\{\frac{2}{1+\left[(N-1)*\left(\frac{m_{rbc}}{2}\right)\right]} + \frac{1}{1+[(N-1)*(1-m_{rbc})]}\right\} \tag{4.37}$$

$$\chi = \frac{1-[N*(1-\beta)]}{N-1-\beta} \tag{4.38}$$

$$G = \frac{H*(N-1)}{N+\chi} \tag{4.39}$$

$$D_{WB} = \frac{D_p * k_p * [1+(G*\chi)]}{k_{WB}*(1-G)} \tag{4.40}$$

where D_c is the diffusivity of oxygen in the cellular component of blood in cm^2/sec, D_p is the diffusivity of oxygen in the plasma component of blood in cm^2/sec, D_{WB} is the diffusivity of oxygen in whole blood in cm^2/sec; N, β, G, and χ are intermediary constants included for ease of calculation, and m_{rbc} is the aspect of ratio of a red blood cell, assumed to be 0.283.(18, 21)

Equations 4.14, **4.24**, and **4.33** can be combined to form **Equation 4.41**

$$\Phi * {N_{Re}}^{-m} = \frac{\frac{Q_b * \Phi_f}{4*(1-por)*A_f} * \frac{1+\lambda(P)}{P_{O_{2g}} - P_{O_{2b}}} * \frac{dP_{O_2}}{dx} * por * Af}{Q_b} * \left(\frac{\mu}{\rho * \frac{D_{WB}}{1+\lambda(P)}}\right)^{2/3} \quad (4.41)$$

which can be simplified to **Equation 4.42**

$$\Phi * {N_{Re}}^{-m} = \frac{\Phi_f * por}{4*(1-por)} * \left(\frac{\mu}{\rho * D_{WB}}\right)^{2/3} * \frac{\left(1+\lambda\left(P_{O_2}\right)\right)^{5/3}}{(P_{O_{2g}} - P_{O_{2b}})} * \frac{dP_{O_2}}{dx} \quad (4.42)$$

However according to Vaslef, the right hand side of **Equation 4.42** does not take into account variation in the capacity of the blood entering the device to take up oxygen, so it is divided by the oxygen binding capacity term, (1+λ(P)), to yield **Equation 4.43** (18)

$$\Phi * {N_{Re}}^{-m} = \frac{\Phi_f * por}{4*(1-por)} * \left(\frac{\mu}{\rho * D_{WB}}\right)^{2/3} * \frac{\left(1+\lambda\left(P_{O_2}\right)\right)^{2/3}}{(P_{O_{2g}} - P_{O_{2b}})} * \frac{dP_{O_2}}{dx} \quad (4.43)$$

Oxygen Exchange Bundle Modeling

The above previously studied oxygen exchange theory was used to computationally produce oxygen exchange design curves for a variety of fiber bundle geometries using the venous blood conditions as follows; temperature = 37°C, hematocrit = 40%, hemoglobin concentration = 13.3 g/dL, oxygen saturation = 65%, and pH = 7.4. Gas exchange constants m=0.214 and Φ=0.82 from previous cTAL testing were used in oxygen modeling.(17) Bundle dimensions produced as described in previous sections were used in combination with **Equation 4.43** to predict PAD oxygen exchange. Since **Equation 4.43** represents local oxygen exchange in a small portion of the path length of the fiber bundle the equation was manipulated to model the entire fiber bundle. Rearranging **Equation 4.43** to solve for $\frac{dP}{dx}$ yields **Equation 4.44 (21)**

$$\frac{dP_{O_2}}{dx} = \Phi * N_{Re}{}^{-m} * \frac{4*(1-por)}{\Phi_f * por} * \left(\frac{\rho * D_{WB}}{\mu}\right)^{2/3} * \frac{(P_{O_{2g}} - P_{O_{2b}})}{\left(1+\lambda\left(P_{O_2}\right)\right)^{2/3}} \quad (4.44)$$

The Reynolds number for the fiber bundle is represented by **Equation 4.45**

$$N_{Re} = \frac{Q_b * \Phi_f * \rho}{(1-por) * A_f * \mu} \quad (4.45)$$

Equation 4.45 was inserted into **Equation 4.44** and **Equation 4.44** was simplified to yield **Equation 4.46**

$$\frac{dP_{O_2}}{dx} = \Phi * \left(\frac{Q_b * \Phi_f * \rho}{(1-por) * A_f * \mu}\right)^{-m} * \frac{4 * (1-por)}{\Phi_f * por} * \left(\frac{\rho * D_{WB}}{\mu}\right)^{2/3} * \frac{(P_{O_{2g}} - P_{O_{2b}})}{\left(1+\lambda\left(P_{O_2}\right)\right)^{2/3}} \quad (4.46)$$

A forward differencing numerical scheme was utilized to solve **Equation 4.46** for the change in partial pressure of oxygen in the blood from the bundle inlet to the bundle outlet, ΔP_{O2}, using **Equation 4.47**.

$$\Delta P_{O_2} = \Delta x * \Phi * \left(\frac{Q_b * \Phi_f * \rho}{(1-por) * A_f * \mu}\right)^{-m} * \frac{4*(1-por)}{\Phi_f * por} * \left(\frac{\rho * D_{WB}}{\mu}\right)^{2/3} * \frac{(P_{O_{2g}} - P_{O_{2b}}(x))}{\left(1+\lambda\left(P_{O_2}(x)\right)\right)^{2/3}} \quad (4.47)$$

Where Δx is a small change of the distance into the fiber bundle (1e-6 m) and PL is the path length of the fiber bundle. For the initial partial pressure of oxygen at the inlet of the bundle, the pressure was set to the partial pressure of oxygen in the inlet blood. In an iterative manner **Equation 4.47** was stepped by Δx and solved for ΔP_{O2}. At each step the output ΔP_{O2} was added to $P_{O2}(x)$ to

increase the starting partial pressure of oxygen in the blood as the forward differencing is marched through the fiber bundle path length. Once the upper x bound of the forward differencing corresponding to the outlet of the fiber bundle is reached, the partial pressure of oxygen was output as P_{O2Out}. P_{O2Out} was inserted into **Equation 4.26** to output the outlet hemoglobin oxygen saturation, S_{Out}. Lastly the rate of oxygen exchange, VO_2, was calculated and output using **Equation 4.48**

$$V_{O_2} = Q_b * \{[k_{WB} * (P_{O_{2In}} - P_{O_{2Out}})] + [1.34 * C_{hb} * (S_{Out} - S_{In})]\} \quad (4.48)$$

where P_{O2In} is the partial pressure of oxygen in the inlet blood, S_{in} is the oxyhemoglobin saturation in the inlet blood, and 1.34 is the amount of oxygen that can be dissolved in 1 gram of hemoglobin with units mL_{O2}/g_{hb}. VO_2 and S_{out} were plotted as a function of bundle frontal and surface area.

Carbon Dioxide Exchange

According to Federspiel, et al the amount of carbon dioxide exchanged by a gas exchanger can be modeled based on a gas transfer constant and the gas flowrate due to the fact that the concentration gradient of carbon dioxide and the blood is very low, ~40 mmHg.(22) This low concentration gradient means that any buildup of carbon dioxide on the gas side of a gas exchange fiber results in a reduced ability to remove additional CO_2. Additionally, carbon dioxide diffuses quickly in the blood due to its high solubility. Therefore, removal of CO_2 buildup on the gas side of a fiber is greatly affected by the sweep gas flowrate, and can be modeled with **Equation 4.49**

$$V_{CO_2} = K_{CO_2} * A_s * (\overline{P_{CO2_b}} - \overline{P_{CO2_g}}) \quad (4.49)$$

where V_{CO2} is the rate of carbon dioxide removal from the blood, K_{CO2} is the mass transfer coefficient of a gas exchanger, A_s is the surface area of a gas exchanger, $\overline{P}_{CO2b}$ is the average partial

pressure of carbon dioxide dissolved in the blood within the gas exchanger, and $\overline{P}_{CO2g}$ is the average partial pressure of carbon dioxide in the sweep gas within the gas exchanger.(22) $\overline{P}_{CO2g}$ can be approximated by using the average between the partial pressure of carbon dioxide entering the gas exchanger in the sweep gas and the partial pressure of carbon dioxide leaving the gas exchanger in the sweep gas according to **Equation 4.50** (22)

$$\overline{P_{CO2_g}} = \frac{P_{CO_{2o}} + P_{CO_{2i}}}{2} \tag{4.50}$$

In most instances, 100% oxygen is used as the inlet sweep gas, so P_{CO2i} will be equal to zero which reduces the equation down to **Equation 4.51**

$$\overline{P_{CO2_g}} = \frac{P_{CO_{2o}}}{2} \tag{4.51}$$

Substituting **Equation 4.51** into **Equation 4.49** yields **Equation 4.52**

$$V_{CO_2} = K_{CO_2} * A_s * (\overline{P_{CO2_b}} - \frac{P_{CO_{2o}}}{2}) \tag{4.52}$$

The carbon dioxide exchange from the sweep gas can also be calculated with a mass balance according to **Equation 4.53** (22)

$$V_{CO_2} = Q_g * \frac{P_{CO_{2o}} - P_{CO_{2i}}}{P_g} \tag{4.53}$$

Once again the inlet sweep gas is 100% oxygen so **Equation 4.53** will simplify to **Equation 4.54**

$$V_{CO_2} = Q_g * \frac{P_{CO_{2o}}}{P_g} \tag{4.54}$$

Since the rate of carbon dioxide to the sweep gas is equal to the rate of carbon dioxide transferred from the blood by the gas exchanger **Equations 4.52** and **4.54** can be set equal to one another yielding **Equation 4.55**

$$K_{CO_2} * A_s * (\overline{P_{CO2_b}} - \frac{P_{CO_{2O}}}{2}) = Q_g * \frac{P_{CO_{2O}}}{P_g} \quad (4.55)$$

Solving for P_{CO2o} and simplifying yields **Equation 4.56**

$$P_{CO_{2O}} = \frac{K_{CO_2} * A_s * P_g * \overline{P_{CO2_b}}}{Q_g + (\frac{1}{2} * K_{CO_2} * A_s * P_g)} \quad (4.56)$$

Substituting **Equation 4.56** back into **Equation 4.52** and simplifying yields **Equation 4.57**

$$V_{CO_2} = \frac{2 * K_{CO_2} * A_s * Q_g * \overline{P_{CO2_b}}}{(2 * Q_g) + (K_{CO_2} * A_s * P_g)} \quad (4.57)$$

Matlab code was generated to predict VCO2 from **Equation 4.57**. $\overline{P}_{CO2b}$ was assumed to be 40 mmHg for separate plots. Unpublished data from the early cTAL prototype in Cook et al, resulted in a K_{CO2} of 4.61 mL_{CO2}/(min*mmHg).(17) Equation 4.54 was used to calculate V_{CO2} at sweep gas flowrates from 0 to 5 L/min and a blood flowrate of 1.25 L/min. V_{CO2} was plotted as a function of sweep gas flowrate and device surface area. Refer to **Appendix E** for all Matlab code.

4.2.2 Computational Fluid Dynamics Modeling:

Computational Fluid Dynamics (CFD) was utilized to investigate the flow patterns and device resistance of the PAD. Drafting of the PAD fluid and fiber bundle domains was completed using Solidworks 2015 (Dassault Systems, Velizy-Villacoublay Cedexx, France). CFD modeling was performed using the ANSYS Workbench 14.5 package (ANSYS Inc., Canonsburg, PA).

Domain Drafting

The CAD for the PAD computational simulations consisted of three domains; the housing inlet fluid domain, the fiber bundle porous media domain, and the housing outlet fluid domain. (**Figure 4.4**) These domains were drafted as a multibody part and imported into ANSYS using a direct export from Solidworks. This automatically sews the shared faces of all of the domains, so that a conformal mesh was produced. The fiber bundle geometry includes an additional face at the

front and rear of the device where the fiber bundle curvature meets the housings.(**Figure 4.5**) These faces were created for three reasons: 1) the fiber bundle is compressed slightly when meeting up the housing to prevent shunting of blood around the fiber bundle, 2) the mesh is more difficult to refine without highly skewed elements at these bundle-housing interfaces if a tangential bundle geometry is used, and 3) where the fiber bundle meets the housing a single fiber contacts the housing and acts as a face. These faces were added and sized at 0.008 inches to approximate the thickness of a single fiber.

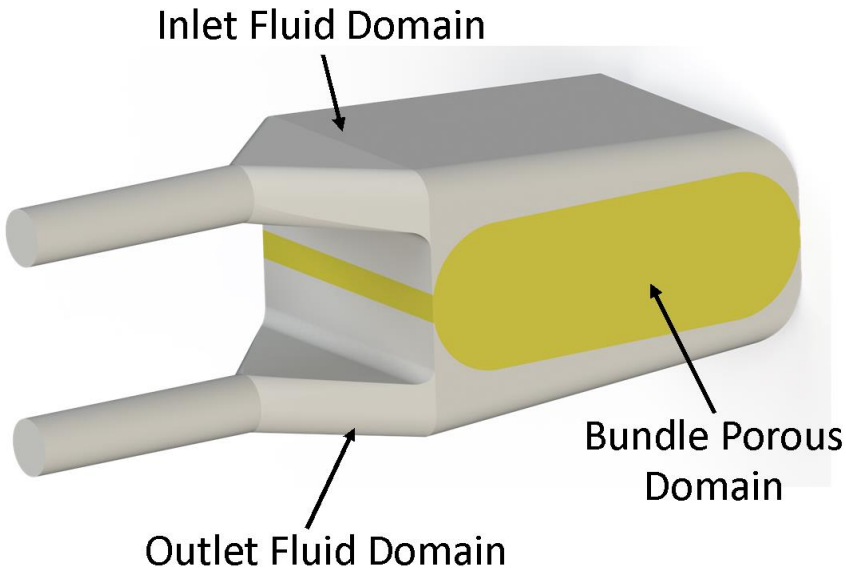

Figure 4.4: The domains modeled in the CFD analyses.

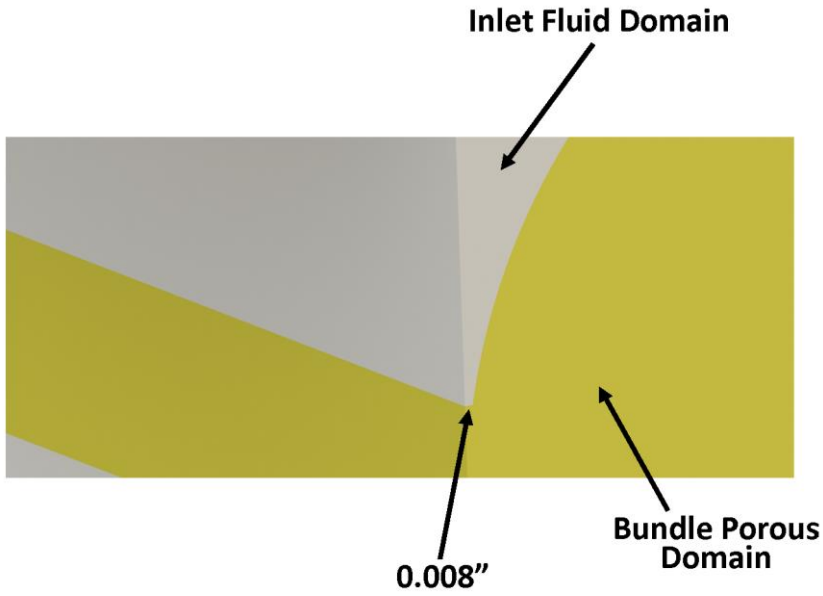

Figure 4.5: A zoomed in image of the domains modeled in the CFD analyses with one of the flat faces labeled that was added to the fiber bundle where the fiber bundle meets the housing.

Mesh Generation

After domain drafting an ANSYS workbench Fluent fluid flow analysis system was created. The ANSYS Meshing module was utilized to produce the finite volume discretized mesh using free meshing scheme with refinement zones where complex fluid dynamics were expected. The mesh was refined in the blood inlet region (**Figure 4.6**) and at the interface faces between the bundle and housing at the front and rear of the fiber bundle.(**Figure 4.7**) Mesh sizings were repeatedly halved during the grid dependence study. Mesh global settings and refinement settings for the grid dependence study are shown in **Table 4.1**. A

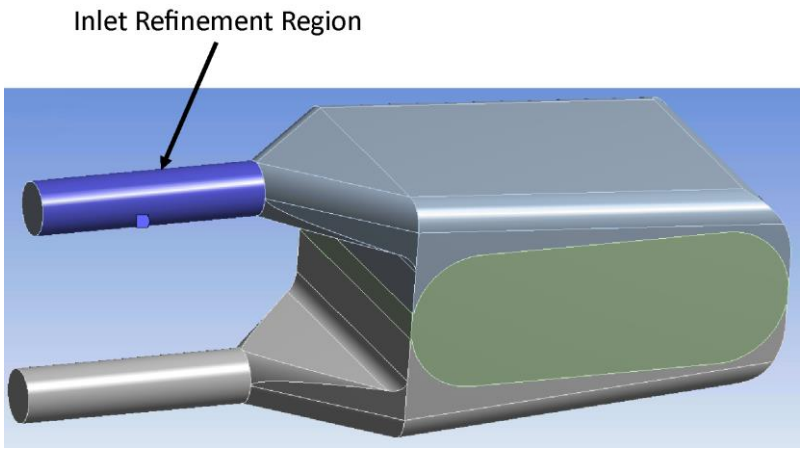

Figure 4.6: The inlet region of mesh refinement.

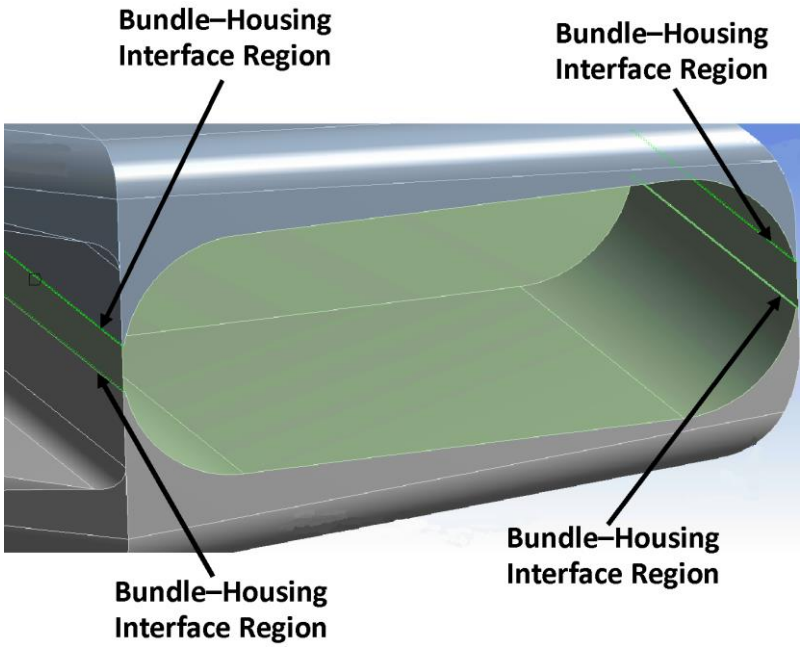

Figure 4.7: The bundle-housing interface area of mesh refinement.

Table 4.1: The mesh sizing settings for the grid dependence study of the PAD CFD.

	Global Min Element Size (m)	Global Max Element Size (m)	Global Max Face Size (m)	Global Curvature Normal Angle (˚)	Bundle-Housing Interface Element Size (m)	Inlet Conduit Element Size (m)
Mesh 1	6.0228E-05	1.2E-02	1.2E-02	34	2.032E-04	2.0E-03
Mesh 2	3.0114E-05	6.0E-03	6.0E-03	17	1.016E-04	1.0E-03
Mesh 3	1.5057E-05	3.0E-03	3.0E-03	8.5	5.080E-05	5.0E-04

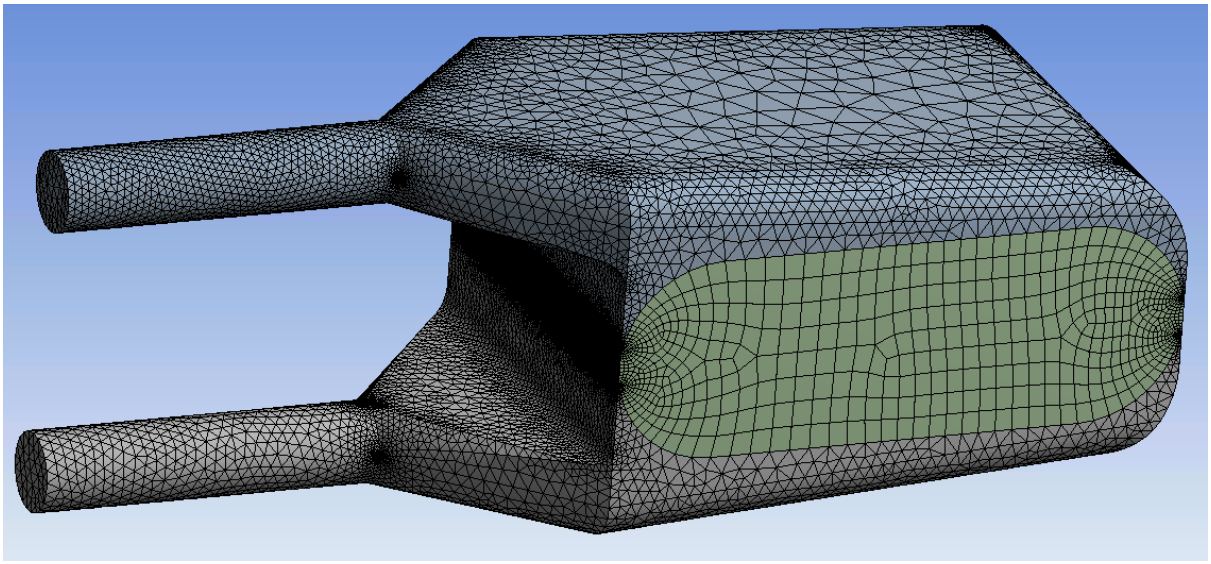

Figure 4.8: A mesh used in the CFD analysis of the PAD.

sample mesh can be seen in **Figure 4.8**.

Model Parameters

The housing inlet and outlet fluid domains were modeled as a Newtonian fluid with a density of 1040 kg/m^3 and a dynamic viscosity of 3.0 cP to simulate blood. However, blood is non-Newtonian so the computational model will vary to some degree from *in vivo* fluid dynamics. The bundle domain was modeled as a Darcy porous media. The Darcy porous media model in Ansys incorporates two input parameters; the bundle porosity and the viscous resistance coefficient, C_{Rvisc}. As discussed in the computational bundle design section, the porosity of the bundle was obtained using **Equation 4.15** coupled with fiber mat physical dimensions, diameter and spacing. The calculated permeability of a similar fiber mat, 2.81e-9 m^2, was converted to the viscous

Table 4.2: Blood flow characteristics as a function of blood flowrate and inlet dimensions.

Flowrate (L/min)	Inlet Diameter (in)	Inlet Velocity (m/sec)	Inlet Reynolds Number	Entrance Length (in)
0.75	3/8	0.175424	579	13.03
0.75	1/2	0.098676	434	13.03
1.25	3/8	0.292374	965	21.72
1.25	1/2	0.164460	724	21.72

resistance coefficient for input into the porous media definition in Ansys Fluent using **Equation 4.58**

$$C_{R_{visc}} = \frac{1}{k_p} \tag{4.58}$$

Boundary Conditions

The blood inlet was modeled with a uniform blood inlet velocity specified in **Table 4.2** to simulate a blood volume flowrate of 1.25 L/min for PAD's with inlet diameters of $^3/_8$ and $^1/_2$ inches and inlet/outlet tapering angles of 30 and 45 degrees.(**Figure 4.9**) The blood outlet was modeled as an outflow with a constant pressure of 8 mmHg to simulate a mean left atrial pressure if the device is attached in a pump controlled pulmonary artery to left atrium.(**Figure 4.10**) A no-slip boundary condition was imposed at all walls where the fluid meets the housing, including the regions within the fiber bundle.

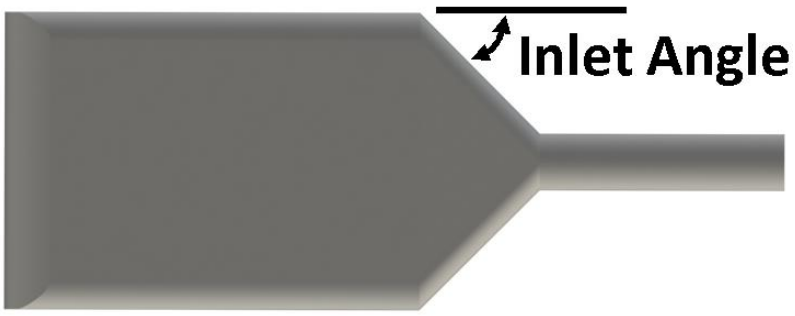

Figure 4.9: A top view of the PAD with inlet angle labeled.

Convergence Monitoring

Convergence monitors were imposed to iterate the computation until crucial output parameters converged. The solution was deemed to be "converged" if all monitored output parameters for a given iteration varied by

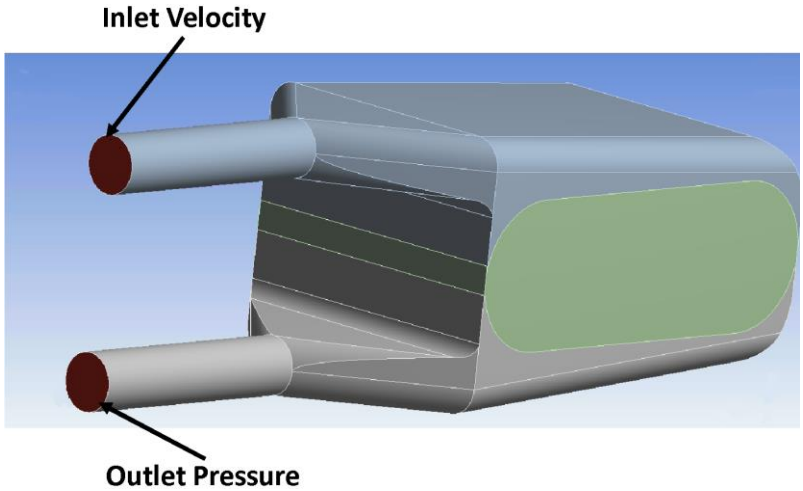

Figure 4.10: The inlet and outlet boundary condition locations used in the PAD CFD.

less than or equal to 0.2% from the previous 15 iterations. The first 20 iterations were ignored to eliminate false convergence from the imposed initialization. Area weighted averaged pressure and velocity at the inlet and outlet face of the fluid domain were monitored to ensure that a converged device flow resistance was achieved. The area weighted average velocity component in the y direction (front to back on the bundle) and the area weighted average velocity component in the z direction (along the pathlength of the bundle) were monitored on the top surface of the fiber bundle on the inlet half of the device since flow patterns will vary greatly in the inlet half of the device and were used for design comparisons.(**Figure 4.11**) The area averaged velocity component in the x-direction was not monitored since the flow patterns are largely symmetric in this direction.

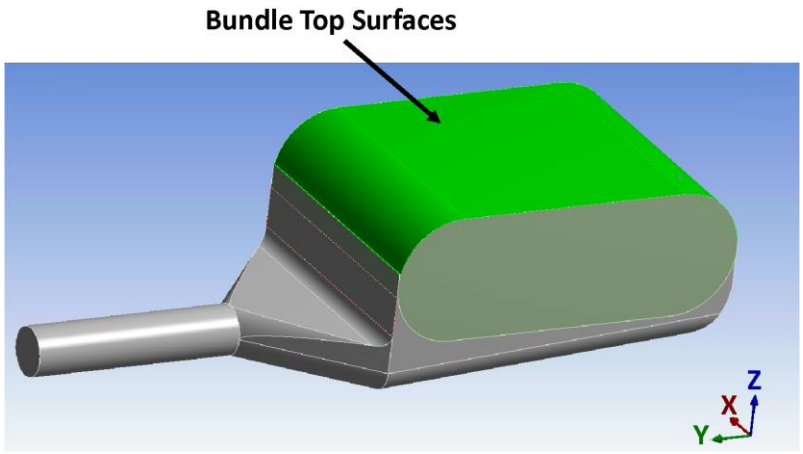

Figure 4.11: The top surfaces of the fiber bundle (highlighted in bright green) used in convergence monitoring of the PAD CFD.

Numerical Solver Scheme

Fluent's pressure based steady flow solver in double precision was utilized to calculate the finite volume solution of the fluid dynamics within the PAD. Peak Reynolds numbers dictated modeling in the laminar regime. (**Table 4.2**) The pressure-velocity coupling of the solver was set to "SIMPLE", the spatial discretization gradient was set to Least Squares Cell Based, the spatial discretization pressure was set to PRESTO!, and the special discretization Momentum was set to Second Order Upwind. Solution stability was maintained with the following under-relaxation

factors; Pressure = 0.3, Density = 1, Body Forces = 1, and Momentum = 0.5. The solution was initialized with a standard initialization outlet gauge pressure of 8 mmHg and outlet normal velocity equal to the velocity set at the inlet boundary condition.

Fluid Mechanics Post Processing

All post processing for the final mesh and grid dependence study was performed using Ansys CFD-Post. In order to assess the performance of the PAD, numerical data investigating gross properties and graphical data to visualize fluid flows were analyzed. Numerically, area weighted averages were taken of pressure and velocity at the blood inlet, blood outlet, bundle top surface, and bundle bottom surface. These were then used to calculate the overall device resistance and component resistances.

Contour and vector plots were produced on preexisting device surfaces as well as user defined surfaces at specific regions in the device. A contour plot of velocity was produced on the existing top surface of the fiber bundle. Two horizontal user defined planes parallel to the top surface of the fiber bundle (xy-plane) were created for velocity contour and vector plots at key

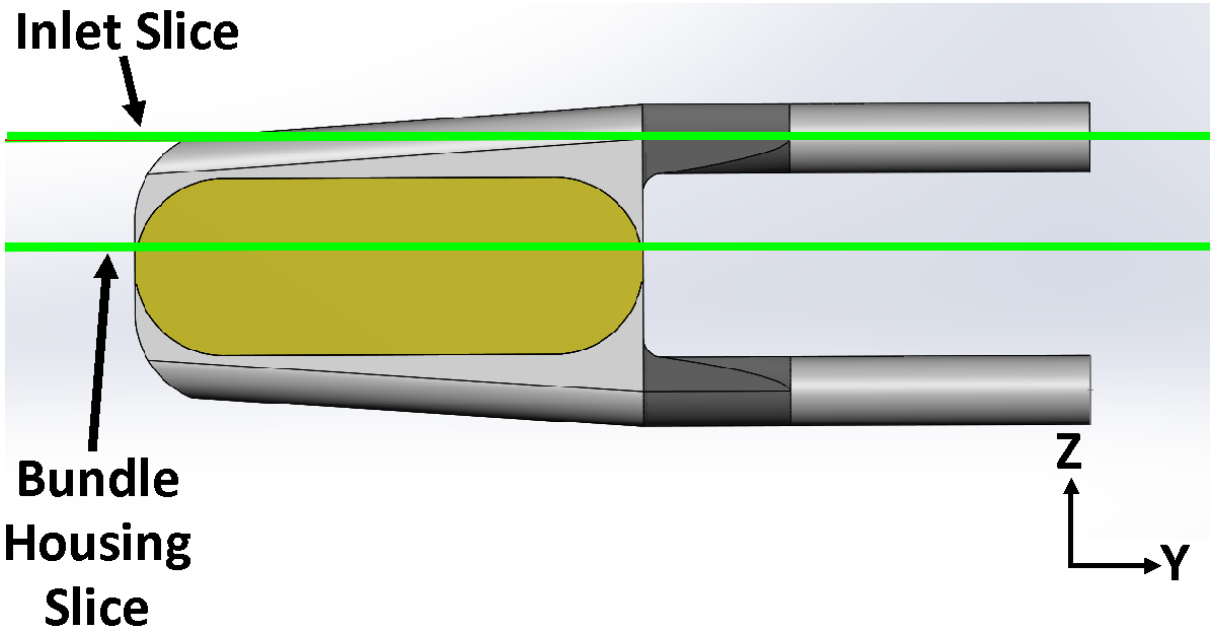

Figure 4.12: The horizontal domain slices used to create vector and contour plots.

locations in the inlet half of the fluid domain. The horizontal planes referred to as "bundle-housing slice," and "inlet slice" in the vertical direction (z-direction) align with the point where the fiber bundle first contacts the housing and the midpoint of the blood inlet conduit, respectively.(**Figure 4.12**) Two vertical user defined planes parallel to the side face of the fiber bundle (yz-plane) were created. The vertical planes referred to as "quarter slice" and "mid slice" in the horizontal direction across the width of the fiber bundle (x-direction) align with the point one quarter across the fiber bundle and with the point halfway across the fiber bundle, respectively.(**Figure 4.13**) All user defined surfaces were used for producing velocity vector plots. In addition to vector and contour plots, streamlines were produced from 1000 points on the inlet blood conduit face. All velocity contour plots were inspected for areas of stasis. Velocity vectors and streamlines were inspected for areas of recirculation.

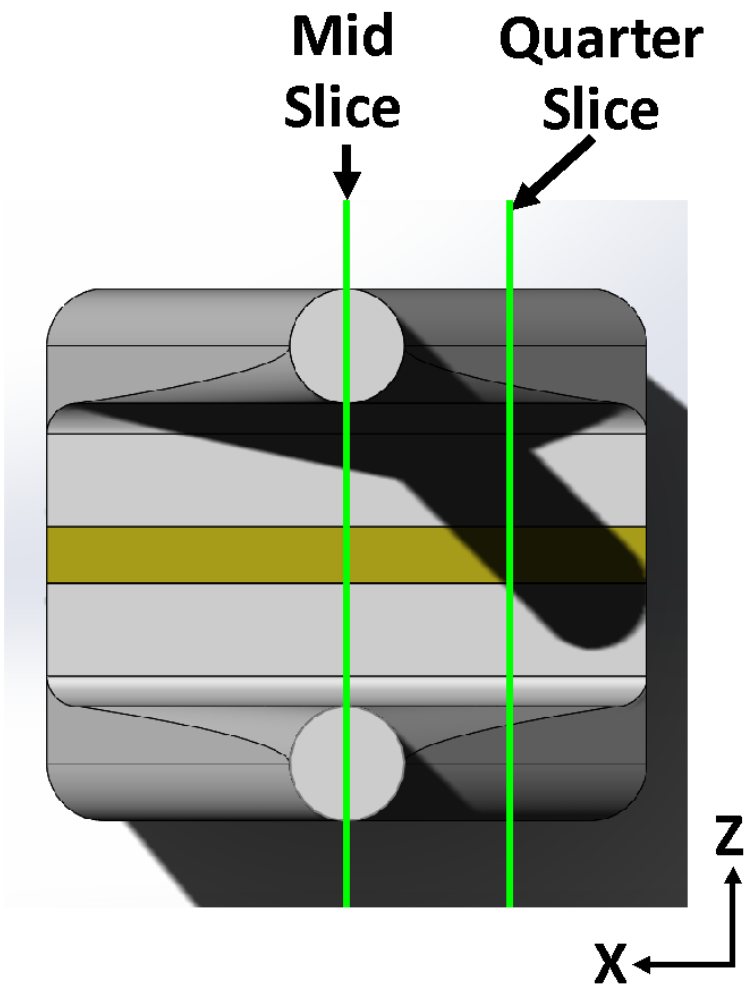

Figure 4.13: The vertical domain slices used to create vector and contour plots.

Grid Dependence Study

A grid dependence study was performed to ensure that the volume discretized grid spacing

was refined sufficiently to produce results that do not change significantly with further grid refinement. This was achieved by progressively halving the grid spacing until results varied by less than 5% between spacings. Area weighted averages of fluid inlet and outlet velocities and pressures and the calculated resistance were included in the grid dependence study. Area weighted averages of the velocity component in the y direction (front to back on the bundle) of velocity and velocity component in the z direction (side to side on the bundle) were calculated for the grid dependence study at the inlet slice and bundle-housing slice.

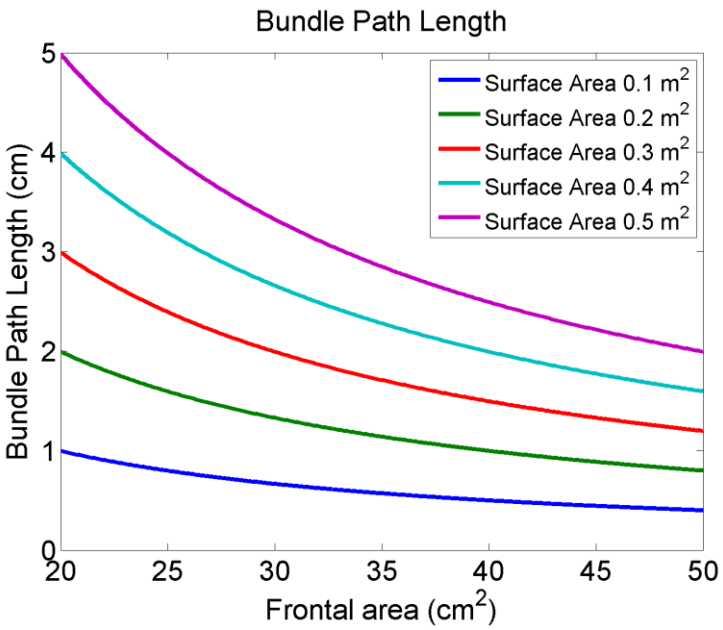

Figure 4.14: A plot of bundle path length as a function of frontal area for a range of bundle surface areas.

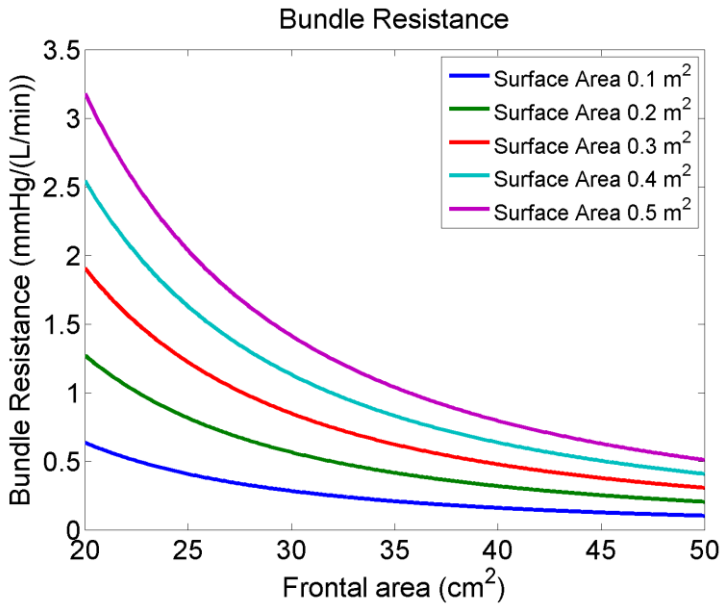

Figure 4.15: A plot of bundle resistance as a function of frontal area for a range of bundle surface areas.

4.3 Results

4.3.1 Computational Bundle Modeling

Bundle computational modeling was performed to design the PAD's bundle. As can be

seen in **Figure 4.14**, the path length of the bundles decreased as the frontal area was increased for a given surface area, and at a fixed frontal area the path length increased with increasing surface area. The resistance also decreased with increasing frontal area at a fixed surface area but to a greater extent than path length, as can be seen in **Figure 4.15**. The resistance also increased with increasing surface area at a fixed frontal area.

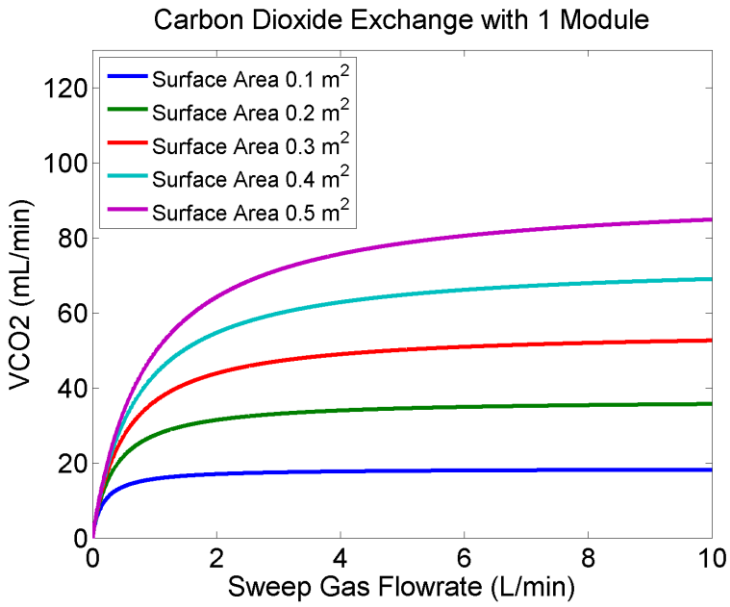

Figure 4.16: A plot of carbon dioxide exchange as a function of sweep gas flowrate for a range of bundle surface areas while utilizing a single PAD module.

The carbon dioxide removal by the PAD, VCO_2, can be seen in **Figure 4.16**. At all surface areas, the VCO_2 asymptotically increases towards a maximum as sweep gas flowrate is increased, and this asymptotic value increases with surface area. The oxygen exchange, VO_2, can be seen in **Figure 4.17**. Increasing the frontal area while keeping surface area fixed decreases the oxygen exchange, and increasing the surface area while keeping the frontal

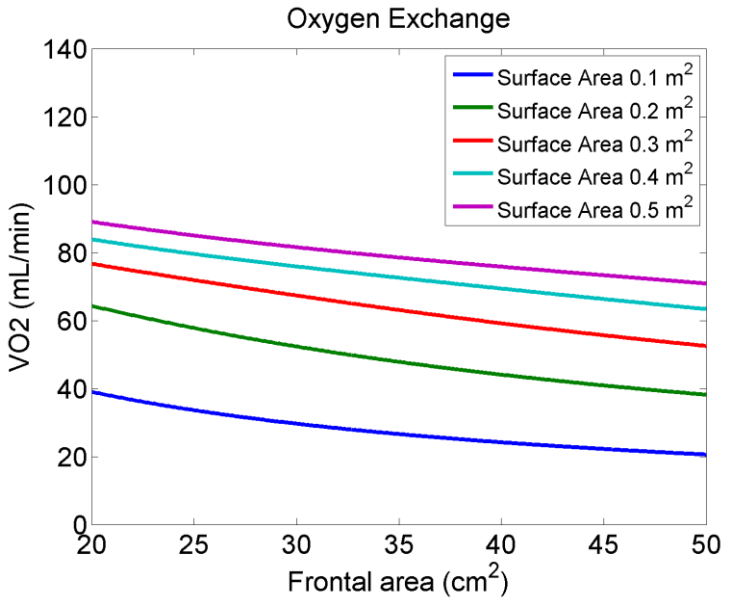

Figure 4.17: A plot of oxygen exchange as a function of frontal area for a range of bundle surface areas when the blood hemoglobin level is 12 g/dL.

area fixed increases the oxygen exchange. The outlet hemoglobin oxygen saturations can be seen in **Figure 4.18**. The general trend was for outlet saturations to decrease with increasing frontal area and increase with increasing surface area.

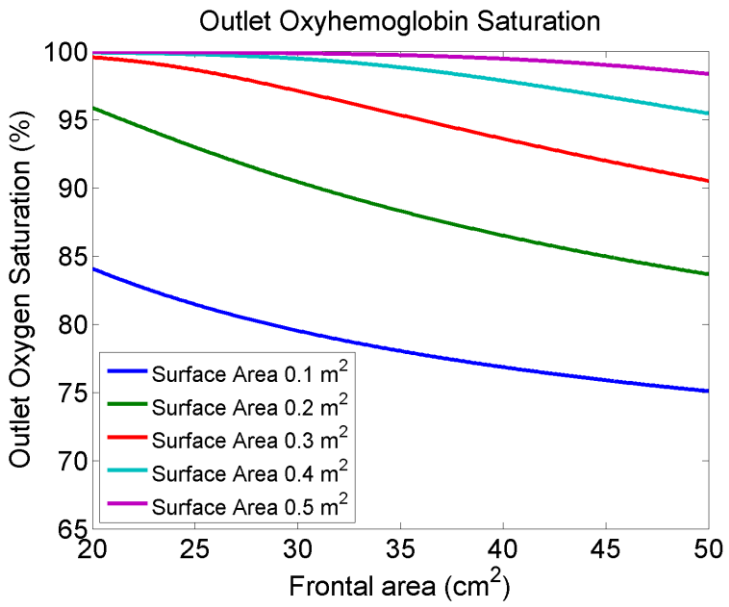

Figure 4.18: A plot of outlet oxygen saturation as a function of frontal area for a range of bundle surface areas when the blood hemoglobin level is 12 g/dL.

4.3.2 Computational Fluid Dynamics Modeling

The CFD simulation results were analyzed in both a quantitative and qualitative manner. From a quantitative standpoint, bundle resistance, inlet manifold resistance, outlet manifold resistance, and total resistance were organized into **Table 4.3** for all housing designs. As would be expected the bundle resistances were similar amongst all housing designs with bundle resistances ranging from 0.666 to 0.677 mmHg/(L/min). The resistances of the remaining components and in turn overall resistance varied between designs, most drastically between blood conduit diameters. The predicted resistances were dominated by the bundle resistance, followed by the outlet manifold resistance, and lastly the inlet manifold resistance.

Table 4.3: Blood flow characteristics as a function of blood flowrate and inlet dimensions.

Inlet Diameter	Taper	Overall Resistance (mmHg/(L/min)	Inlet Resistance (mmHg/(L/min))	Bundle Resistance (mmHg/(L/min))	Outlet Resistance (mmHg/(L/min))
0.375	45	1.498	0.286	0.666	0.546
0.5	45	0.963	0.094	0.677	0.193
0.375	30	1.494	0.273	0.667	0.554
0.5	30	0.963	0.094	0.677	0.192

In a qualitative manner, streamlines and velocity vector plots were inspected for areas of recirculation, and band plots of velocity were inspected for regions of stasis. When inspecting the streamlines for all of the housing geometries (**Figure 4.19**) the most distinguishing feature of the flow patterns was fluid jetting from the device inlet. This jetting effect resulted in fluid impacting the rear of the device and recirculating in two recirculations that spanned from the rear to the front of the device. These recirculations were also evident in the velocity vector plots of the inlet slice for all housing geometries.(**Figure 4.20**) When inspecting the velocity vectors of the vertical midslice, further small recirculations were evident in all housing geometries.(**Figure 4.21**) These recirculations reside at the rear and front of the fiber bundle on the inlet half of the device. The vertical quarter slices also exhibited the rear recirculations seen in the midslices.(**Figure 4.22**) The frontal recirculations reside further back on the bundle in the quarter slice in comparison to the mid slice. In all cases the fiber bundle evens out flow on the

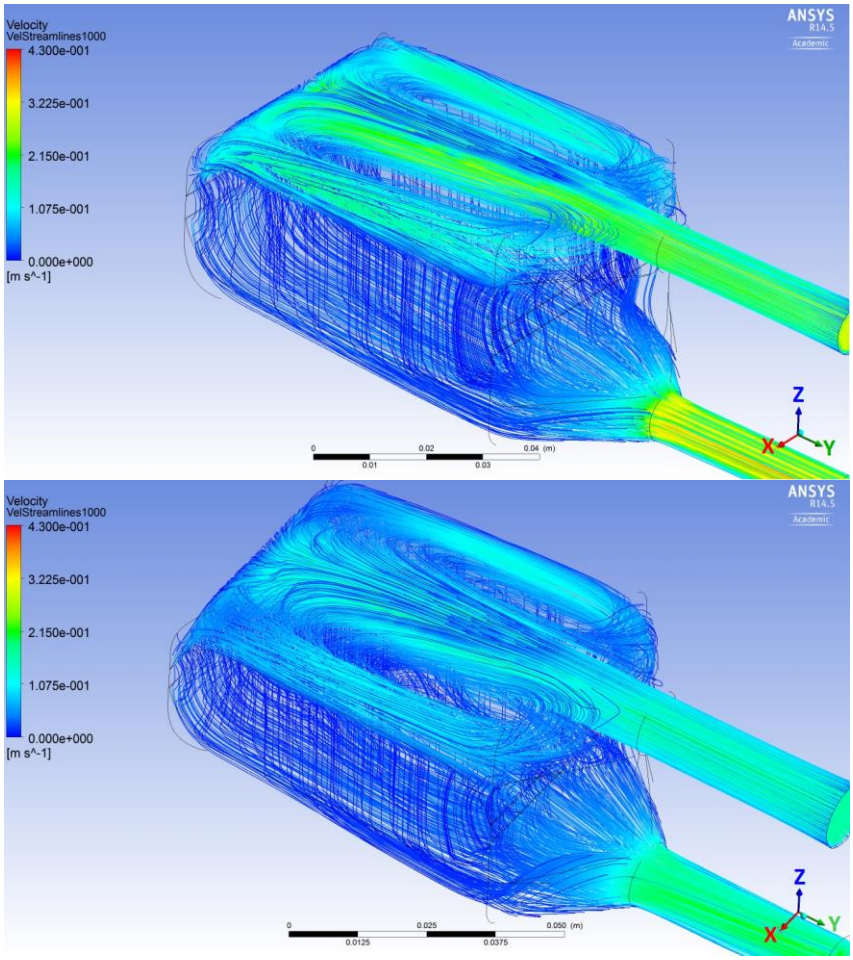

Figure 4.19: Streamline plots. *Top:* 0.375" conduit, 45˚ taper. *Bottom:* 0.5" conduit, 45˚ taper.

outlet half of the device.

When inspecting the band plots of velocity the main areas of stasis were at the center of the recirculations in the inlet half of the device for all designs.(**Figure 4.23**) Additionally, high velocities were evident in the center of the housing where the jetting fluid impacts the fiber bundle.

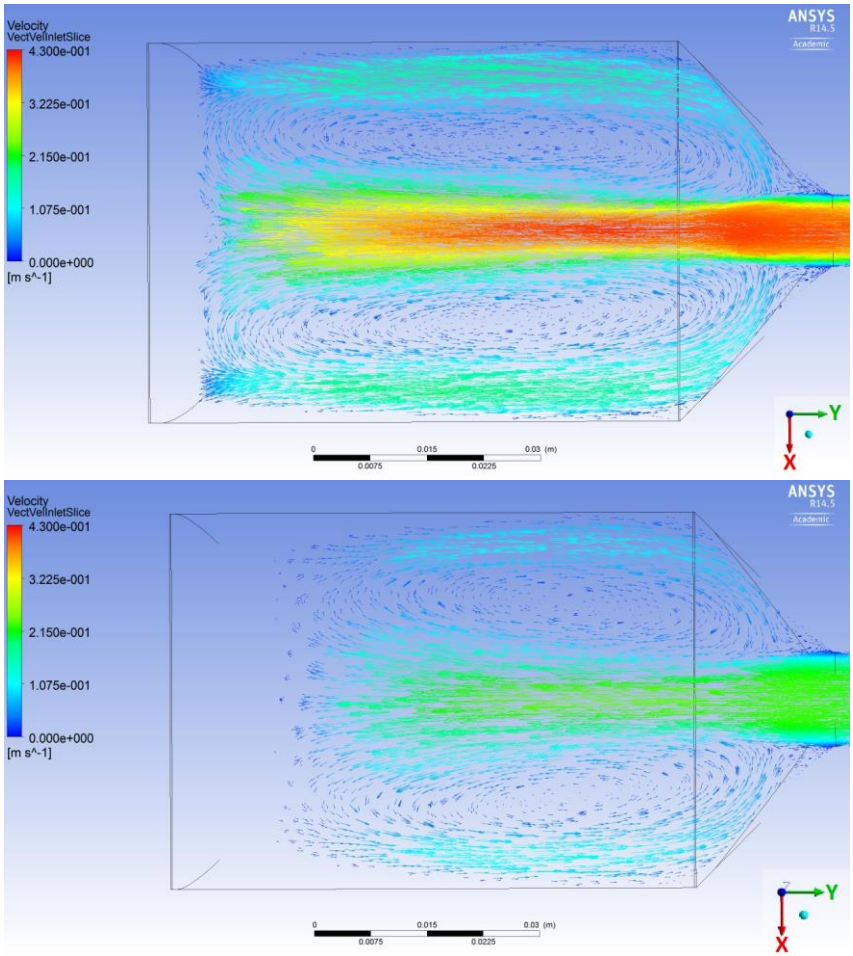

Figure 4.20: Velocity Vector plots, inlet slice. *Top:* 0.375" conduit, 45˚ taper. *Bottom:* 0.5" conduit, 45˚ taper.

4.4 Discussion

4.4.1 Computational Bundle Modeling

The bundle computational modeling was used to design the fiber bundle used in the pulmonary assist device. Due to the non-linearity between frontal area and bundle resistance additional functionality gains from reducing resistance through increased frontal area level off with frontal areas exceeding 35-40 cm^2 depending on bundle surface area. Increasing frontal area beyond these values would add to device size and prime volume, and decrease gas exchange. However, all predicted bundle resistances were close to five times lower than the overall device resistance goal.

In choosing a fiber bundle sizing based on oxygen exchange, a more stringent outlet saturation of 98% was chosen to allow for errors in the computational models. The gas exchange constants, m and Φ, used from an early cTAL prototype were expected to overestimate gas exchange since the outlet saturations produced during *in vitro* testing of this device never dropped to 98% or lower. The outlet hemoglobin saturations for the 0.1 and 0.2 m^2 surface area bundles are inadequate at all frontal areas modeled. The 0.3, 0.4, and 0.5 m^2 surface area bundles produce 98% saturations at frontal areas below 25.2, 36.3, and 48.2 cm^2, respectively.

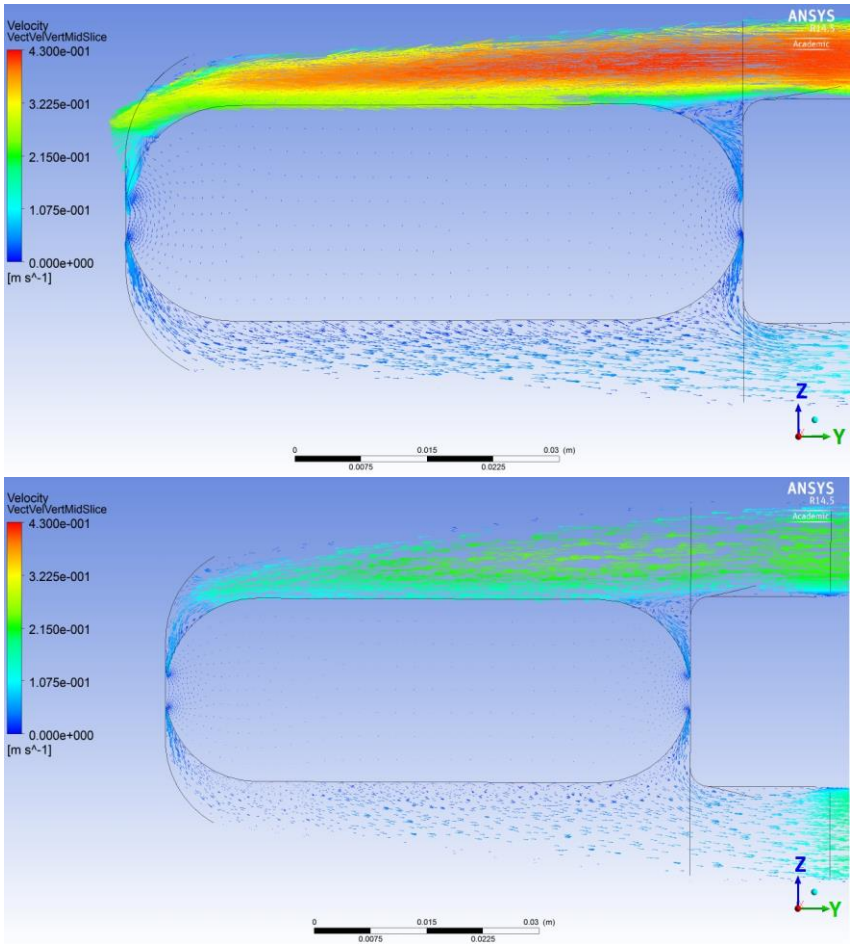

Figure 4.21: Velocity Vector plots, mid slice. *Top:* 0.375" conduit, 45˚ taper. *Bottom:* 0.5" conduit, 45˚ taper.

The carbon dioxide exchange for the PAD ranged from inadequate to more than adequate. The goal for CO_2 exchange was at least 50 mL/min of carbon dioxide exchange with up to 5 L/min of total sweep gas at a blood flowrate of 1.25 L/min/module. Any surface area above 0.3 m^2 would provide adequate CO_2 exchange for the PAD when increasing the sweep gas flowrate to 5 L/min. For surface areas 0.4 m^2 and above target carbon dioxide transfer could be achieved with sweep

gas flowrates of 1.5 L/min, reducing the demands on oxygen concentrators or oxygen tanks.

The aspect ratio of the bundle, which is essentially a measure of the amount of curvature in the rolled fiber bundle, was a minor decision making variable in comparison to gas exchange and resistance. However, it was desired to have a fiber bundle with an aspect ratio close to that of the previously tested cTAL (2.7) for ease of manufacture and to reduce the effect of the curved regions of the fiber bundle on gas exchange. Bundles with surface areas below 0.3 m^2 had aspect ratios at least that of the cTAL for all investigated frontal areas. However, for surface areas of 0.3 m^2 and greater, frontal areas in the 30-40 cm^2 range are needed to achieve aspect ratios as large as the cTAL.

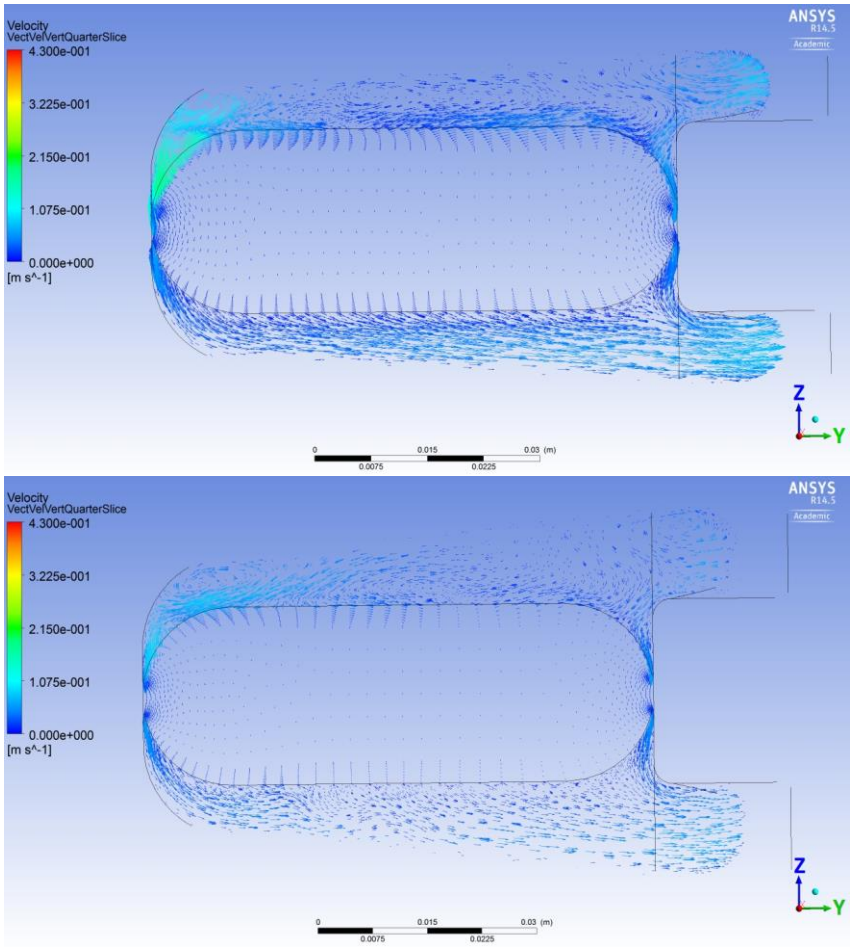

Figure 4.22: Velocity Vector plots, quarter slice. *Top:* 0.375" conduit, 45˚ taper. *Bottom:* 0.5" conduit, 45˚ taper.

In the final bundle design the bundle resistance, aspect ratio, carbon dioxide exchange, and oxygen exchange were taken into account. The carbon dioxide and oxygen exchange requirements of the PAD eliminate all devices with surface areas less than 0.3 m^2. At a surface area of 0.3 m^2

oxygen exchange requirements would dictate a frontal area less than 25.2 cm^2 while the resistance and aspect ratio requirements would dictate a frontal area in the 30-40 cm^2 range. Additionally, the carbon dioxide exchange capabilities of the 0.3 m^2 surface area device would be barely adequate. As a result, the PAD bundle surface areas were narrowed down to 0.4 and 0.5 m^2.

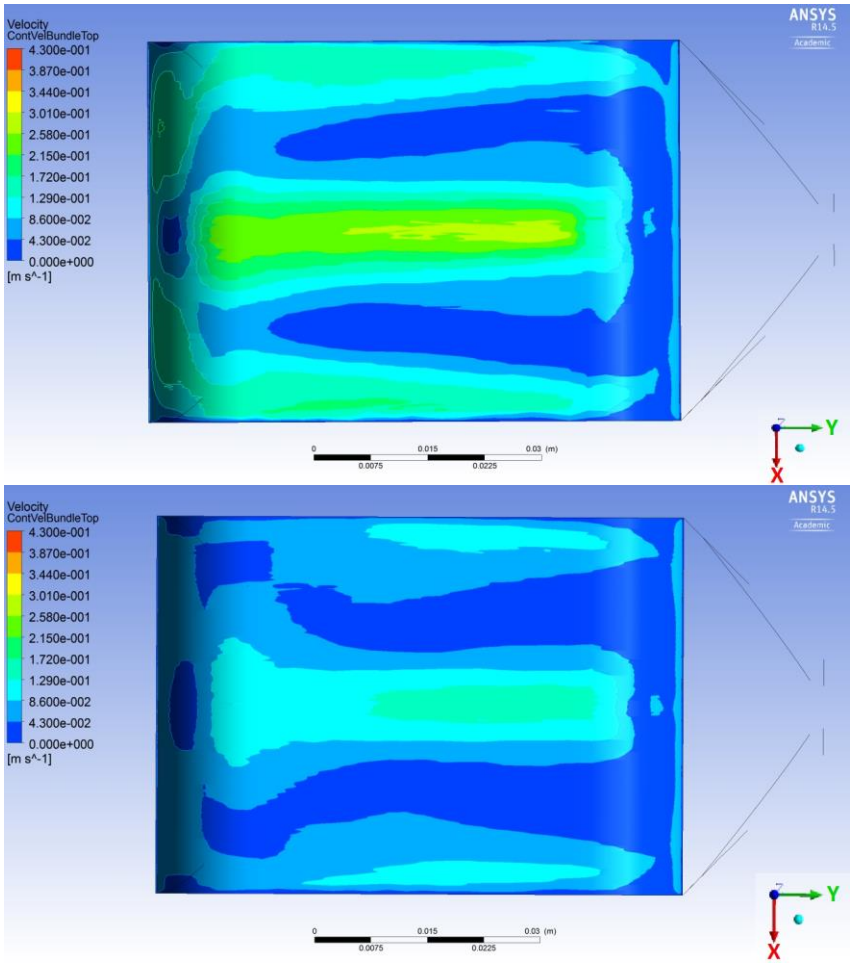

Figure 4.23: Velocity Band Plots, bundle top. *Top:* 0.375" conduit, 45˚ taper. *Bottom:* 0.5" conduit, 45˚ taper.

When investigating the gas exchange capabilities of the 0.4 m^2 device the carbon dioxide removal requirements should be met at low sweep gas flowrates and the oxygen exchange requirements would be met with a frontal area less than 36.3 cm^2. Using a cTAL aspect ratio the frontal area would be 35.9 cm^2 and the bundle resistance would be 0.79 mmHg/(L/min).

When investigating the gas exchange capabilities of the 0.5 m^2 device the carbon dioxide removal requirements should be met at low sweep gas flowrates and the oxygen exchange requirements would be met with a frontal area less than 48.2 cm^2 of frontal area. Using a cTAL

aspect ratio the frontal area would be 41.6 cm^2 and the bundle resistance would be 0.74 mmHg/(L/min).

Between these two surface areas, the smaller surface area should result in a lower resistance, increased aspect ratio, and reduced prime volume and physical size of the device at a given frontal area. Additionally, the smaller surface area device does not have as much surface area to react with the blood and induce clot formation. However, the gas exchange capabilities of the larger surface area device are greater at a given frontal area. When taking into account the aspect ratio of the two surface area bundles, the 0.5 m^2 device would need to be a little larger in all directions, but would have similar resistance to the 0.4 m^2 device at the aspect ratio of the cTAL. Ultimately, the 0.4 m^2 fiber bundle was chosen since it had a smaller volume and a smaller blood contacting surface area. A frontal area of 35 cm^2 was chosen since it should meet all design requirements.

The bundle with a surface area of 0.4 m^2 and frontal area of 35 cm^2 was further refined to increase the aspect ratio. The fiber bundle was increased in length from 5.9 cm to 7 cm increasing the aspect ratio from 2.6 to 3.1. The final fiber bundle design of 0.4 m^2 surface area and 5 cm wide by 7 cm long frontal area was used in subsequent CFD simulations and *in vitro* testing of the PAD.

4.4.2 Computational Fluid Dynamics Modeling

The computational simulations for all designs were distinguished by a low predicted resistance in all cases, but also large levels of recirculations due to jetting of the fluid from the blood inlet conduit. The areas of recirculation existed in all inlet designs, but were slightly less severe in the 0.5” inlet diameter cases. Additionally, the resistance was lower for the 0.5” inlet diameter cases. However, in both inlet diameters this level of recirculation will not be acceptable for the PAD to serve as a long term support device, as clot will inevitably form relatively quickly

in all of these devices. When comparing 45˚ and 30˚ designs of the same inlet diameter, there was little difference between designs.

The 0.5” conduit devices have the disadvantage that a majority of current oxygenators, cannulas, and pump heads are designed for use with 0.375” diameter tubing. As a result if a 0.5” diameter blood conduit were used, tubing sizes from cannulas and pump heads will need to be stepped up in size upstream of the device and then back down in size downstream of the device. This will result in more connection points where failure can occur, greater heat loss from the circuit, increased prime volume, increased system complexity, and increased bulk. Additionally, there would likely be market resistance to changing to a non-standard size ECMO tubing.

Since all of the housing designs suffered from large areas of recirculations, major design modifications will need to be made to the device for *in vivo* testing. Initial prototypes of the PAD were produced from these computational simulations to provide a baseline for gas exchange and future computational modeling. The 0.5” blood conduit device exhibited slightly improved resistance and flow patterns over the 0.375” blood conduit device, but the non-standard tubing size was a major disadvantage. Ultimately, the 0.375” blood conduit PAD was chosen since it utilizes a more standard 0.375” tubing size and will serve as a better baseline of comparison for the redesigned PAD.

4.5 References

1. Association AL. Lung disease data: 2008. Focus: Clean Air and Lung Disease Retrieved from http://www lungusa org. 2008.
2. Valapour M, Paulson K, Smith JM, Hertz MI, Skeans MA, Heubner BM, et al. OPTN/SRTR 2011 Annual Data Report: Lung. American Journal of Transplantation. 2013;13:149-77. doi: 10.1111/ajt.12024.
3. Anastasiadis K, Antonitsis P, Argiriadou H. MECC Equipment. Principles of Miniaturized ExtraCorporeal Circulation: Springer Berlin Heidelberg; 2013. p. 23-42.
4. Potkay JA. The promise of microfluidic artificial lungs. Lab on a Chip. 2014;14(21):4122-38.
5. Müller T, Lubnow M, Philipp A, Bein T, Jeron A, Luchner A, et al. Extracorporeal pumpless interventional lung assist in clinical practice: determinants of efficacy. European Respiratory Journal. 2009;33(3):551-8. doi: 10.1183/09031936.00123608.
6. Flörchinger B, Philipp A, Klose A, Hilker M, Kobuch R, Rupprecht L, et al. Pumpless Extracorporeal Lung Assist: A 10-Year Institutional Experience. The Annals of thoracic surgery. 2008;86(2):410-7.
7. Murphy DA, Hockings LE, Andrews RK, Aubron C, Gardiner EE, Pellegrino VA, et al. Extracorporeal Membrane Oxygenation—Hemostatic Complications. Transfusion Medicine Reviews. 2015;29(2):90-101. doi: http://dx.doi.org/10.1016/j.tmrv.2014.12.001.
8. Venema LH, Sharma AS, Simons AP, Bekers O, Weerwind PW. Contemporary Oxygenator Design Relative to Hemolysis. The Journal of Extra-corporeal Technology. 2014;46(3):212-6. PubMed PMID: PMC4566829.
9. Lehle K, Philipp A, Gleich O, Holzamer A, Müller T, Bein T, et al. Efficiency in Extracorporeal Membrane Oxygenation-Cellular Deposits on Polymethypentene Membranes Increase Resistance to Blood Flow and Reduce Gas Exchange Capacity. ASAIO Journal. 2008;54(6):612-7.
10. Hoopes CW, Kukreja J, Golden J, Davenport DL, Diaz-Guzman E, Zwischenberger JB. Extracorporeal membrane oxygenation as a bridge to pulmonary transplantation. The Journal of Thoracic and Cardiovascular Surgery. 2013;145(3):862-8. doi: http://dx.doi.org/10.1016/j.jtcvs.2012.12.022.
11. Fuehner T, Kuehn C, Hadem J, Wiesner O, Gottlieb J, Tudorache I, et al. Extracorporeal membrane oxygenation in awake patients as bridge to lung transplantation. American journal of respiratory and critical care medicine. 2012;185(7).
12. Biscotti M, Sonett J, Bacchetta M. ECMO as bridge to lung transplant. Thoracic surgery clinics. 2015;25(1):17-25.
13. Camboni D, Philipp A, Arlt M, Pfeiffer M, Hilker M, Schmid C. First Experience With a Paracorporeal Artificial Lung In Humans. ASAIO Journal. 2009;55(3):304-6 10.1097/MAT.0b013e31819740a0.
14. Strueber M, Hoeper MM, Fischer S, Cypel M, Warnecke G, Gottlieb J, et al. Bridge to Thoracic Organ Transplantation in Patients with Pulmonary Arterial Hypertension Using a Pumpless Lung Assist Device. American Journal of Transplantation. 2009;9(4):853-7. doi: 10.1111/j.1600-6143.2009.02549.x.
15. de Perrot M, Granton JT, McRae K, Cypel M, Pierre A, Waddell TK, et al. Impact of extracorporeal life support on outcome in patients with idiopathic pulmonary arterial hypertension awaiting lung transplantation. The Journal of Heart and Lung Transplantation. 2011;30(9):997-1002.

16. Schmid C, Philipp A, Hilker M, Arlt M, Trabold B, Pfeiffer M, et al. Bridge to lung transplantation through a pulmonary artery to left atrial oxygenator circuit. The Annals of thoracic surgery. 2008;85(4):1202-5.
17. Cook KE, Perlman CE, Seipelt R, Backer CL, Mavroudis C, Mockros LF. Hemodynamic and gas transfer properties of a compliant thoracic artificial lung. ASAIO journal. 2005;51(4):404-11.
18. Vaslef SN. Analysis and design of an intravascular lung assist device1990.
19. Vaslef SN, Mockros LF, Anderson RW, Leonard RJ. Use of a Mathematical Model to Predict Oxygen Transfer Rates in Hollow Fiber Membrane Oxygenators. ASAIO Journal. 1994;40(4):990-6.
20. Mockros L, Leonard R. Compact cross-flow tubular oxygenators. ASAIO Journal. 1985;31(1):628&hyhen.
21. Cook K. Design and testing of intrathoracic artificial lungs [master's thesis]. Northwestern University. 1996.
22. Federspiel WJ, Haulert BG. Sweep gas flowrate and C02 exchange in artificial lungs. Artificial organs. 1996;20(9):1050-2.

Chapter 5: Pulmonary Assist Device *In vitro* Testing

5.1 Introduction

The computational modeling of the PAD predicted a device with a resistance of 1.50 mmHg/(L/min), and 98% oxyhemoglobin saturation when processing 1.25 L/min of blood. *In vitro* testing was carried out to characterize the actual gas exchange and resistance performance of prototype devices. The *in vitro* resistance was compared to the resistance predicted by the computational modeling to validate or invalidate the computational fluid dynamics model. The *in vitro* gas exchange results were used to both compare to modeling results as well develop more effective dimensionless constants for that model. The gas exchange constants used in the modeling (1) are expected to be at least somewhat inaccurate in that they were derived from experiments where the gas exchanger was never challenged enough to produce accurate constants. In those experiments, the outlet oxygen saturation never dropped to 98%.(1) The PAD gas exchange experiments performed here were designed to challenge the device to a greater extent and thus should yield more accurate constants.

5.2 Methods

5.2.1 In vitro Test Device Prototyping

Five prototype PAD devices were fabricated for testing in *in vitro* gas exchange and resistance experiments. Detailed specifications on the fabrication process can be seen in the appendix. A basic outline of the fabrication process is outlined as follows. First a fiber bundle core was cut using a laser cutter (Trotec Laser, Inc, Canton, MI). Then the fiber was attached to the core using a small amount of Wacker Elastosil RT625 PDMS (Wacker Chemie AG, Germany) in

Table 5.1: The coating methods employed to prevent leakage during PAD testing.

Device #	External Coating	Internal Coating Housing Half #1	Internal Coating Housing Half #2
3	Epoxy	None	None
4	Epoxy	None	None
6	Epoxy	PVC	Silicone
7	Epoxy	Silicone	Silicone
8	Epoxy	Silicone	Silicone

a region where the fiber is not exposed to blood. The bundle was then rolled a given number of turns and measured until the final bundle dimensions were obtained. The loose end of the fiber was then attached to the main fiber bundle using a small amount of PDMS in a region where the fiber is not contacted by blood. The bundle was completed by painting a small amount of PDMS onto the ends of the fibers to secure the layers of the bundle to each other. A housing was fabricated from ABS using a 3-D printer. The porosity of the 3-D printed housings resulting in fluid leakage through the housing. Multiple coating methods on the inside and outside of the device housing were employed to eliminate the leakage. (**Table 5.1**) The external epoxy coating was applied by spreading marine grade epoxy on all surfaces not enclosed by the gas caps of the assembly. The internal PVC coating was applied by painting PVC dissolved in cyclohexanone on all internal surfaces not in contact with potting material. As the cyclohexanone evaporated, PVC was left behind on all coated surfaces. Internal silicone coating was applied by painting Med-6019 silicone (Nusil Technology LLC, Carpinteria, CA) onto all internal surfaces not in contact with potting material. The fiber bundle was inserted into the housing, and the housing was glued together with PDMS. The ends of the fiber bundle were encased in polyurethane ("potted") using a centrifuge separate the blood and gas space of the device. The potted region of the bundle was cut to expose the lumen of the fibers. The outside of the housing was coated with epoxy to further seal the housing, and gas caps were attached to the device using silicone RTV.

5.2.2 In vitro Gas Exchange Testing

The oxygen and carbon dioxide exchange capabilities of the pulmonary assist device were tested in an *in vitro* testing circuit seen in **Figure 5.1**. The circuit is composed of two main branches separated by tubing clamps: a conditioning recirculation circuit shown in blue and a device testing circuit shown in blue and red. Approximately 4 gallons of fresh bovine blood was anticoagulated immediately on collection with 180,000 units of heparin and 64 mg of sodium citrate dehydrate (Sigma Aldrich, St. Louis, MO). The conditioning circuit was primed with carbon dioxide for ease of bubble removal. The bovine blood was inserted into the feed reservoir common to both branches of the circuit and the reservoir was sealed. Blood was recirculated through the conditioning circuit with a centrifugal pump (Terumo Cardiovascular, Ann Arbor, MI or Medtronic, Minneapolis, MN) at flowrates ranging from 2.5 to 3 L/min per conditioning gas exchanger. The clamped off device testing circuit was primed first with carbon dioxide at a flowrate of 5 L/min for a minimum of 2 minutes, and then saline to ensure that the test device was free from air bubbles.

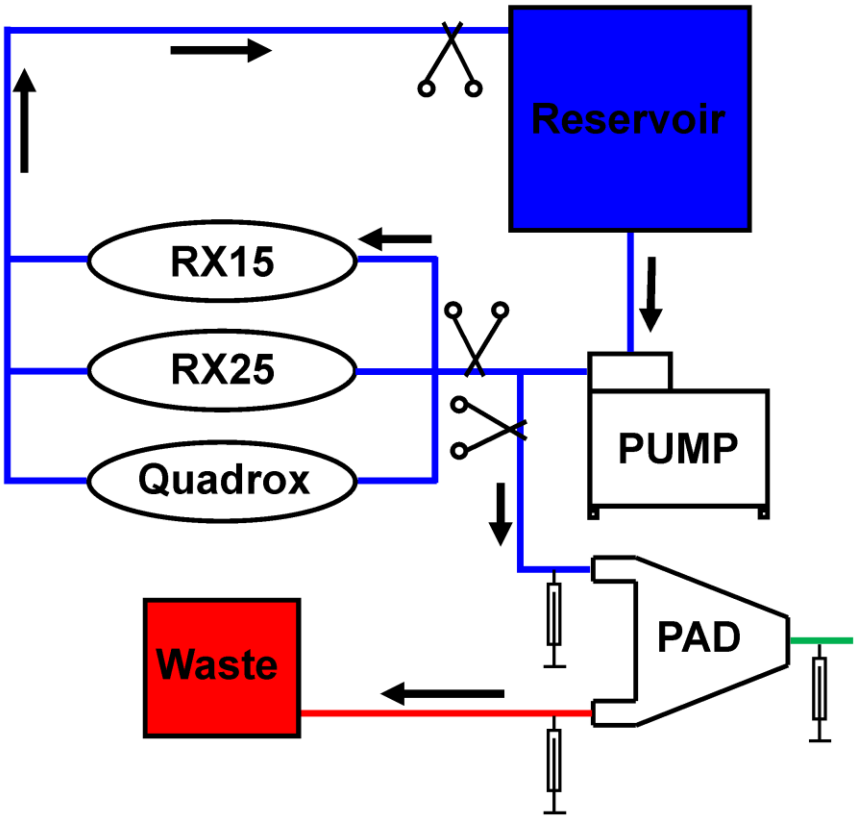

Figure 5.1: The *in vitro* gas exchange circuit comprised of a conditioning branch and a test branch separated by tubing clamps.

Blood Conditioning

Within the conditioning circuit, two to three gas exchangers (Terumo Cardiovascular, Ann Arbor, MI or Maquet, Germany) were used to continuously condition the blood gasses and blood temperature to AAMI specifications, as listed in **Table 5.2**. The sweep gas was balanced with a blend of nitrogen, oxygen, and carbon dioxide to condition the blood gasses. The hemoglobin was adjusted down to AAMI specifications by saline addition, and the base excess was adjusted by the addition of sodium bicarbonate. Blood gas samples were drawn and tested with a blood gas analyzer (Radiometer, Denmark) approximately every 10-30 minutes to obtain the status of the blood conditioning, and the temperature was monitored with a temperature probe (YSI, Yellow Springs, OH) and monitor (YSI, Yellow Springs, OH or Seabrook Medical Systems, Inc, Cincinnati, OH). Once the blood was conditioned to AAMI standards, a two point calibration was performed on the blood gas analyzer to ensure measurement accuracy, and a new blood gas sample was drawn and tested to confirm appropriate blood conditioning before commencing the experimental run.

Table 5.2: AAMI blood conditioning specifications.

Hemoglobin (g/dL)	12±1
pH	7.4±0.1
Base Excess (mmol/L)	0±5
pCO_2 (mmHg)	45±5
Oxygen Saturation (%)	65±5
Temperature (˚C)	37±2

PAD Testing

After the blood was conditioned, the pump was stopped, the conditioning circuit was clamped off, and the test circuit was unclamped. The pump was then restarted and blood was pumped through the PAD and into a waste reservoir. The blood supply reservoir contained a polyethylene expansion bag connected to an opening on the lid of the reservoir. This provided a barrier between the conditioned blood and the atmosphere to prevent gas exchange within the reservoir while limiting pressure changes in the reservoir. The pump flowrate was measured using

a 3/16" PXL tubing flow probe and associated TS410 flowmeter (Transonic, Ithaca, NY) and was set to the target blood flowrates (**Table 5.3**). Concurrently, sweep gas containing pure oxygen was supplied to the gas inlet of the PAD at a flowrate twice that of the target blood flowrate. One minute was allowed between the start of blood pump adjustment and sample taking to allow for full saline and blood clearance from the PAD. **Table 5.3** shows the target blood and sweep gas flowrates tested and the order in which they were tested. At each condition, blood samples were drawn in duplicate from the blood inlet and outlet of the PAD and analyzed in a blood gas analyzer. A sweep gas sample was also drawn in duplicate and analyzed with a blood gas analyzer to measure the carbon dioxide content for carbon dioxide exchange calculations. Following sampling, the pump was adjusted to the next flowrate with one minute between start of adjustment and the next round of sampling, and the process was repeated for all test conditions.

Table 5.3: The blood and gas flowrate conditions for PAD testing.

Test Condition	Blood Flowrate (L/min)	Sweep Gas Flowrate (L/min)
1	2.5	5
2	2	4
3	1.5	3
4	1	2
5	0.5	1

Gas Exchange Calculation

All duplicate blood and sweep gas samples were first averaged for calculation purposes. The outlet blood oxygen saturations were calculated from the pH and partial pressure of oxygen in the outlet blood according to **Equations 4.22** and **4.24**. The outlet saturation was then plotted as a function of blood flowrate. The oxygen transfer rate $\dot{V}_{O2}$ in mL/min was calculated using **Equations 4.45 and 4.26-4.28.** The volume rate of carbon dioxide exchange ($\dot{V}_{CO2}$) in mL/min was calculated from the sweep gas outlet sample using **Equation 5.1**

$$\dot{V_{CO_2}} = Q_g * C_{CO_2} \quad (5.1)$$

where Q_g is the sweep gas flowrate through the device in mL/min, C_{CO2} is the fractional concentration of carbon dioxide in the sweep gas outlet. The $\dot{V}_{O2}$ and $\dot{V}_{CO2}$ were graphed to assess gas exchange performance.

Experimental Oxygen Exchange Constants Calculation

The experimental data from the PAD testing was used to calculate new gas exchange constants, m and Φ, for future fiber bundle modeling. According to previous gas exchange theory for artificial lungs the gas exchange characteristics can be modeled locally using **Equation 4.39,** re-written below for convenience.(2-6)

$$\Phi * {N_{Re}}^{-m} = \frac{\Phi_{f*por}}{4*(1-por)} * \left(\frac{\mu}{\rho*D_{WB}}\right)^{2/3} * \frac{\left(1+\lambda\left(P_{O_2}\right)\right)^{2/3}}{\left(P_g-P_{O_2}\right)} * \frac{dP_{O_2}}{dx} \quad (4.39)$$

In the case of experimental data, the path length of the fiber and the inlet and outlet partial pressures of oxygen in the blood are known, but m and Φ as well as the distribution of the partial pressure change of oxygen within the fiber bundle are not known. The global solution to **Equation 4.39** can be obtained by integration yielding **Equation 5.2**.(6)

$$\Phi * {N_{Re}}^{-m} = \frac{\Phi_{f*por}}{4*(1-por)} * \left(\frac{\mu}{\rho*D_{WB}}\right)^{2/3} *$$

$$\frac{1}{PL} * \int_0^{PL} \frac{\left(1+\lambda\left(P_{O_2}\right)\right)^{2/3}}{\left(P_g-P_{O_2}\right)} * \frac{dP_{O_2}}{dx}\, dx \quad (5.2)$$

Which can be simplified and rearranged to form **Equation 5.3** that utilizes the known inlet and outlet partial pressures of oxygen from experimental data for the integration.(6)

$$\Phi * {N_{Re}}^{-m} = \frac{\Phi_f * por}{4 * (1 - por)} * \left(\frac{\mu}{\rho * D_{WB}}\right)^{2/3} *$$

$$\frac{1}{PL} * \int_{P_{O2_{In}}}^{P_{O2_{Out}}} \frac{\left(1+\lambda(P_{O_2})\right)^{2/3}}{(P_g - P_{O_2})} dP_{O_2} \quad (5.3)$$

The right hand side of **Equation 5.3** was calculated using a trapezoidal numerical integration with a 1 pascal step size for all flowrates tested with the PAD. The Reynolds number was calculated for all flowrates using **Equation 4.41**, re-written below for convenience.(3-6)

$$N_{Re} = \frac{Q_b * \Phi_f * \rho}{(1 - por) * A_f * \mu} \quad (4.41)$$

All data was combined into a single data set and a log-log plot with Reynolds number on the x-axis and the right hand side of **Equation 5.2** on the y-axis was then produced. A power law fit was performed on the data in excel, yielding values of m and Φ.

5.2.3 In Vitro Resistance Testing and Computational Model Validation:

The computational model validation testing was performed by comparing *in vitro* resistance measurements to the resistance predicted by the computational fluid dynamics. *In vitro* resistance testing was performed by measuring the pressure drop from the PAD blood inlet to the blood outlet while pumping at a known flowrate. The *in vitro* resistance test circuit can be seen in **Figure 5.2**. The flowrate provided by the pump was measured by a tubing flow probe and associated flow meter, and was recoded using a Biopac data acquisition system.(Biopac Systems, Inc, Goleta, CA) The pressure drop was recorded by placing tubing T-connectors upstream of the PAD blood inlet and downstream of the blood outlet to create pseudo-manometers. As the pressure increases in the blood conduits the fluid rises according to a gravitational pressure head equal to the pressure inside the blood conduits. The difference in fluid heights were measured with a

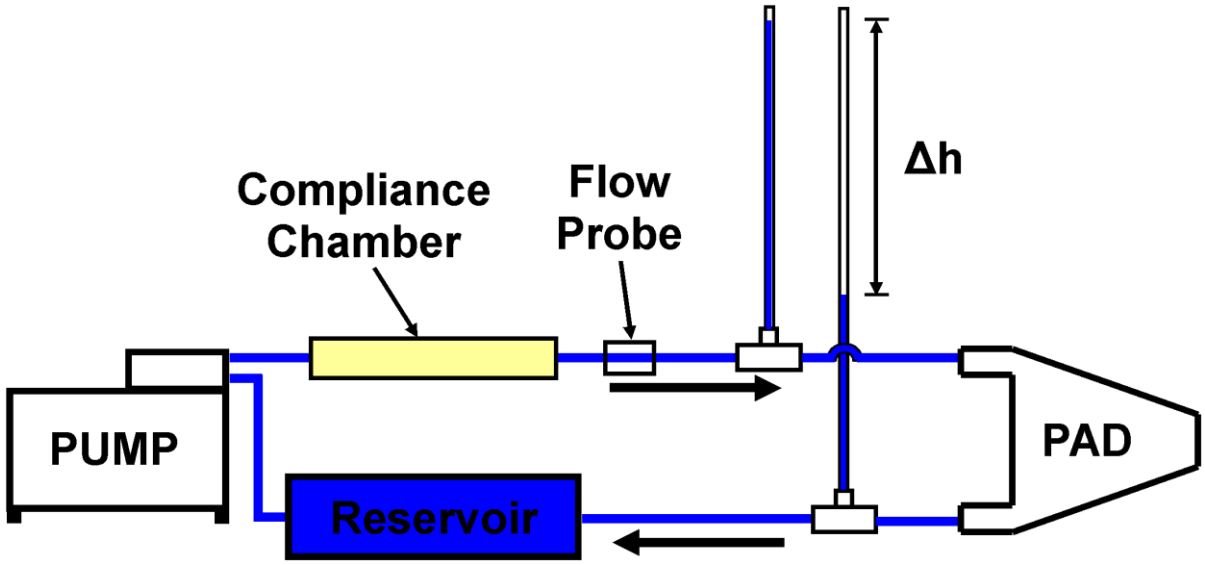

Figure 5.2: The *in vitro* resistance testing circuit with the fluid column height difference labeled with Δh.

caliper, and the pressure drop was calculated using **Equation 5.4**

$$\Delta P = \rho * g * \Delta h \tag{5.4}$$

where ΔP is the pressure drop from the blood inlet to blood outlet, ρ is the measured fluid density, g is the gravitational acceleration, and Δh is the height difference between fluid heights in the vertical fluid column tubes. The total resistance, R_t, for the PAD and tubing between the T-connectors and device was calculated from **Equation 5.5**

$$R_t = \frac{\Delta P}{Q} \tag{5.5}$$

where ΔP is the pressure drop from the inlet to outlet T connector and Q is the fluid flowrate through into the PAD. The resistance of the conduits between the T-connectors and the PAD, R_C, was calculated as laminar flow through a pipe according to **Equation 5.6**

$$R_c = \frac{128*(L_{in}+L_{out})*Q*\mu}{\pi*{D_c}^4} \tag{5.6}$$

where L_{in} is the distance between the inlet conduit and the inlet T-connector, L_{out} is the distance

between the outlet conduit and the outlet T-connector, Q is the fluid flowrate, μ is the dynamic viscosity, and D_c is the inside diameter of the blood conduits. Since the resistances of the PAD and conduits are in series with each other, the resistance of the PAD, R_{PAD}, was calculated as the blood conduit resistance subtracted from the total resistance in **Equation 5.7**

$$R_{PAD} = R_t - R_c \tag{5.7}$$

Combining **Equations 5.3-5.7** yielded the final equation for the resistance of the PAD, **Equation 5.8**

$$R_{PAD} = \frac{\rho * g * h}{Q} - \frac{128 * (L_{in} + L_{out}) * Q * \mu}{\pi * {D_c}^4} \tag{5.8}$$

This experiment was performed (n=4) using glycerol with a dynamic viscosity of 3.0 cP and a density of 1068 kg/m^3 to simulate blood by matching the Reynolds number of blood in the PAD within 3%. At a flowrate of 1.25 L/min, the Reynolds number of the glycerol in the fiber bundle and blood inlet conduit during *in vitro* testing were 1.59 and 992, respectively. At a flowrate of 1.25 L/min, the Reynolds number of blood in the fiber bundle and blood inlet conduit would be 1.55 and 965, respectively. The resistance was calculated at flowrates of 0.5, 0.75, 1, 1.25, 1.5, 1.75, and 2 L/min and were graphed as a function of flowrate. The flowrate of 1.25 L/min was used to compare to the computational model.

5.3 Results

5.3.1 In Vitro Gas Exchange Testing

There was a range in oxygen exchange capabilities between the individual prototypes tested as can be seen in **Figures 5.3** and **5.4**. The outlet hemoglobin oxygen saturation levels were relatively high among PADs 3, 4, and 6. PADs 7 and 8 had considerably lower outlet saturations. In all cases, the outlet saturations decreased with increasing blood flowrate. The amount of oxygen

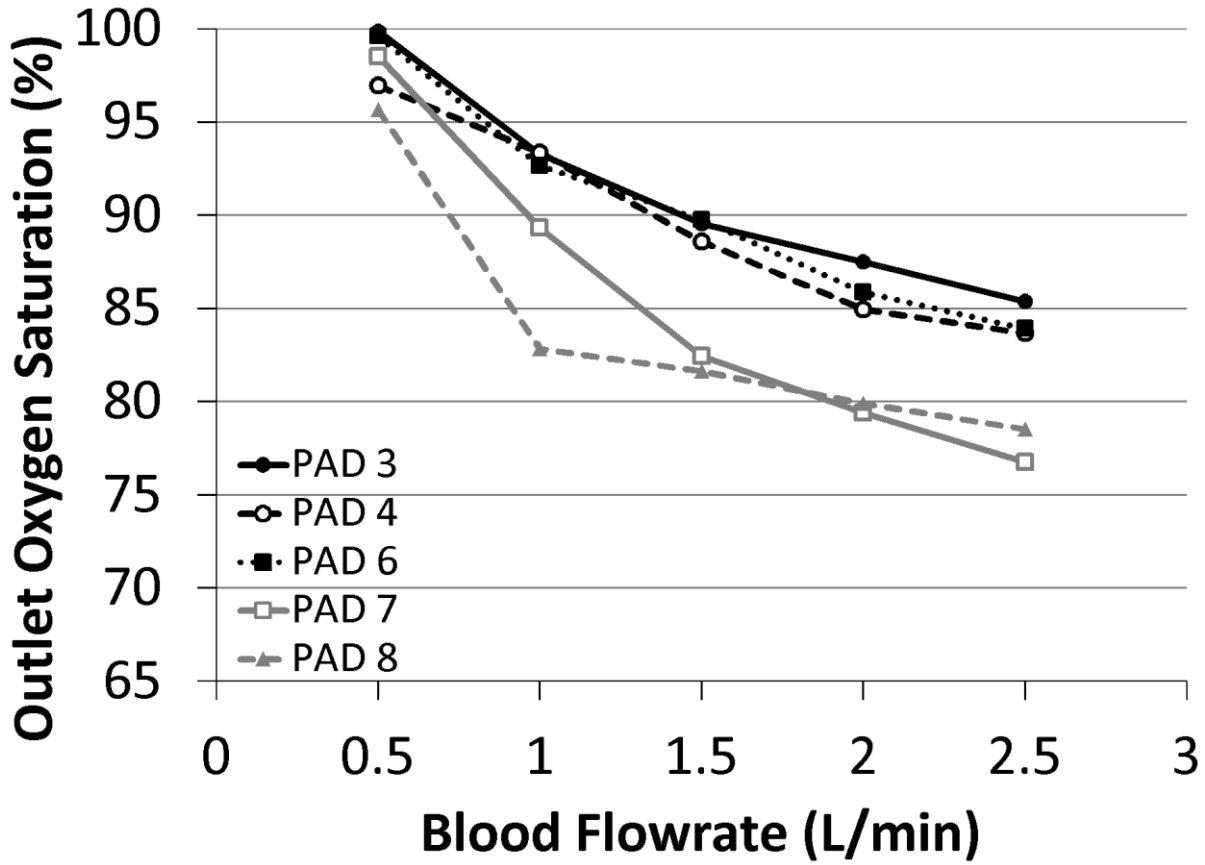

Figure 5.3: The outlet hemoglobin oxygen saturation as a function of blood flowrate.

exchanged, VO_2, also varied greatly between devices. The VO_2 for PADs 3 and 4 were higher than the other devices, exceeding 90 mL/min at a blood flowrate of 2.5 L/min. The VO_2 for PADs 7 and 8 was considerably lower, close to half the VO_2 of PADs 3 and 4. PAD 6 had VO2s in between the two other groups of devices. In all cases the VO_2 increased with increasing blood flowrate as would be expected.

As can be seen in **Figure 5.5**, the carbon dioxide exchange, VCO_2, followed similar patterns where the carbon dioxide exchange was highest for PADs 3 and 4, and lowest for PADs 7 and 8. Once again PAD 6 performed in between the two groups, but had only slightly better performance than PADs 7 and 8. The CO2 exchange increased with increasing sweep gas flowrate.

For future gas exchange modeling the oxygen exchange modeling constants, m and Φ, were

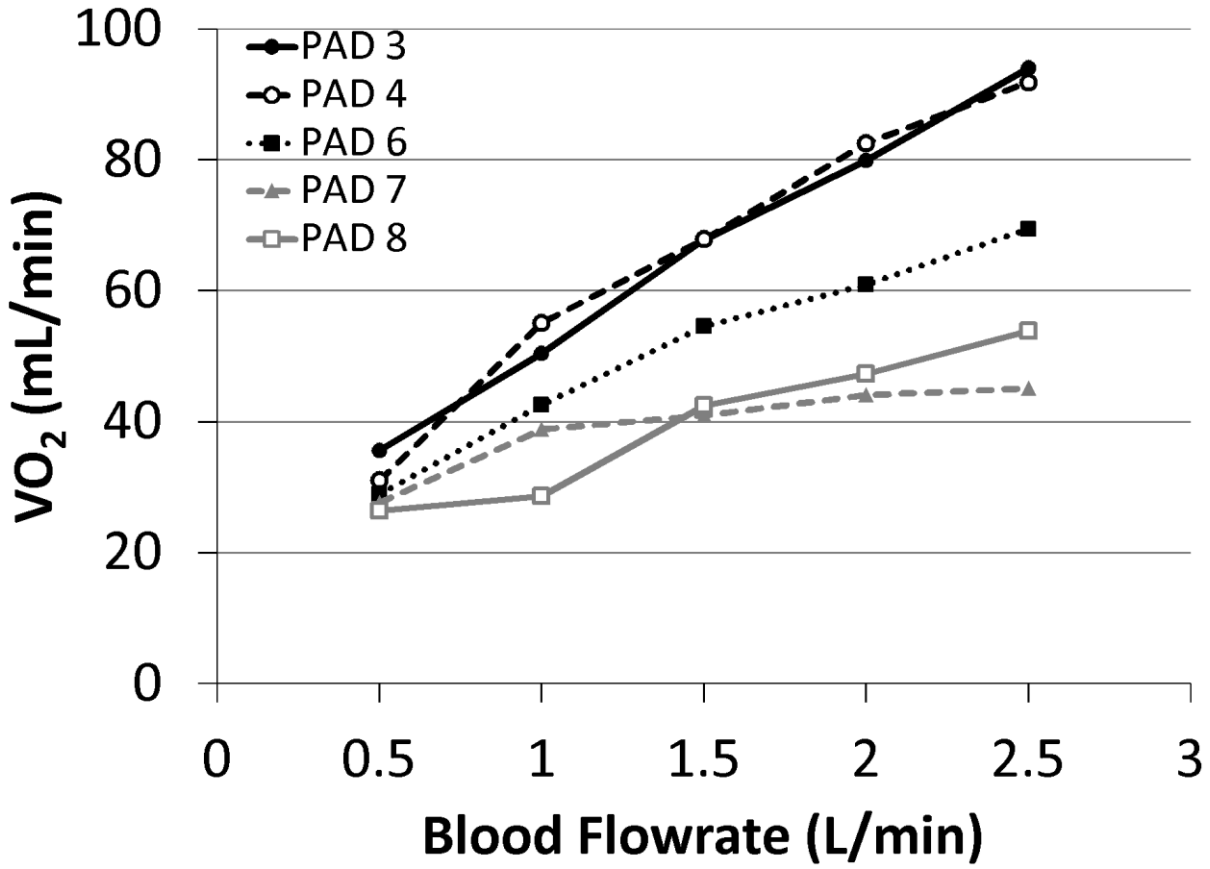

Figure 5.4: The oxygen exchange as a function of blood flowrate.

calculated for all PADs grouped together, and for PADs 3, 4, and 6 grouped together. The log-log graph of the right hand sides of **Equation 5.3** on the y axis and **Equation 4.41** on the x axis can be seen in **Figure 5.6** for all PADs tested. When grouping all devices together the m and Φ, were 0.718 and 0.4636R2 (R^2 = 0.71). When grouping PADs 3, 4, and 6 together the m and Φ, were 0.654 and 0.5409, respectively (R^2 = 0.89).

5.3.2 In Vitro Resistance Testing and Computational Model Validation

When pumping glycerol through the PAD, the resistance of the device increased in a linear manner as can be seen in **Figure 5.7**. The linear fit of the data yields **Equation 5.9**, and has a R^2 of 0.974.

$$R_{PAD_g} = (0.8758 * Q) + 2.3405 \quad (5.9)$$

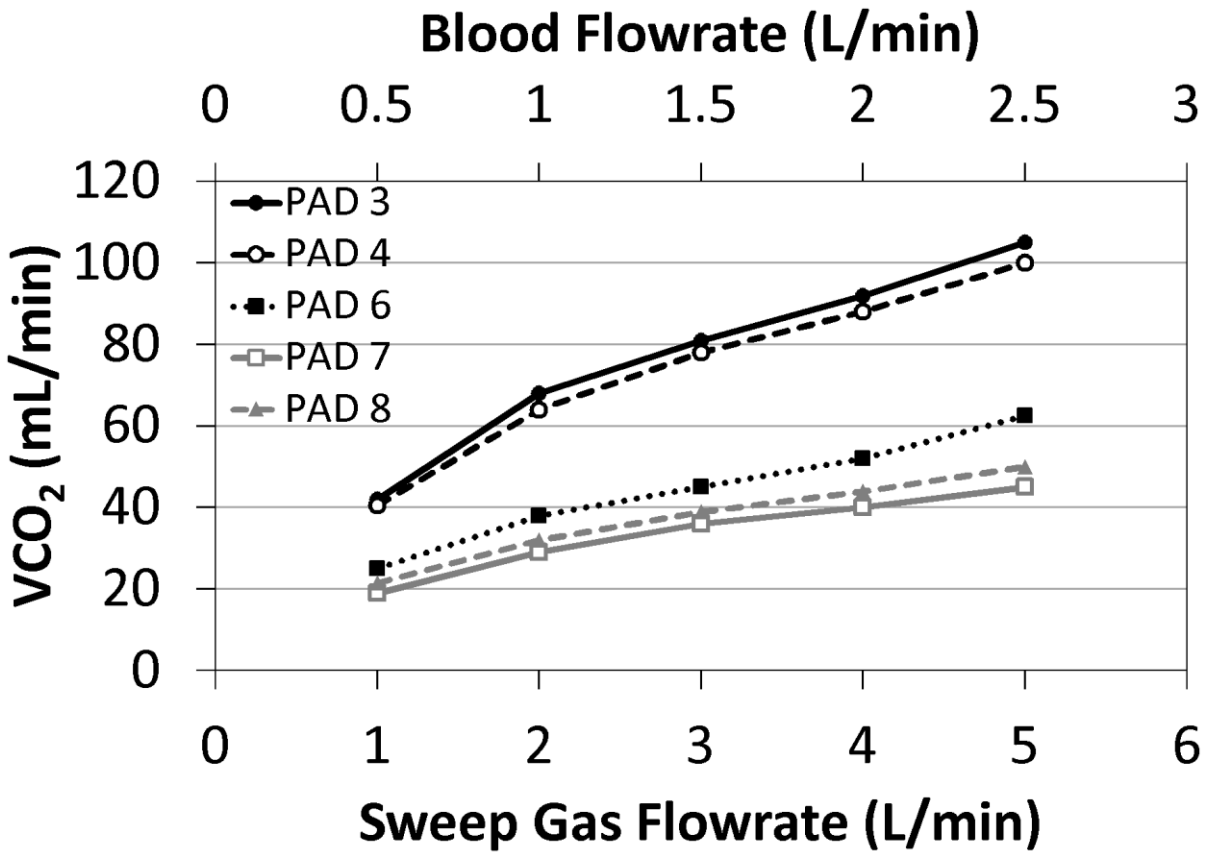

Figure 5.5: The carbon dioxide exchange as a function of sweep gas flowrate.

where R_{PADg} is the resistance of the PAD in mmHg/(L/min) using glycerol and Q is the glycerol flowrate in L. At 1.25 L/min, the *in vitro* testing of the PAD yielded a resistance of 3.650±0.004 mmHg/(L/min) while the computational simulations predicted a resistance of 1.498 mmHg/(L/min).

5.4 Discussion

5.4.1 In vitro Gas Exchange Testing

The prototype PADs did not meet performance goals in terms of oxygen exchange with the device saturating outlet blood to less than 95% at all blood flowrates above 0.5 L/min. Most notable was that PADs 7 and 8, that were prototyped in a single batch, performed significantly worse than the other three devices. Post experiment, gas resistance testing was performed to quantify the opposition to sweep gas flow. Comparison of gas resistance testing results is an indirect method

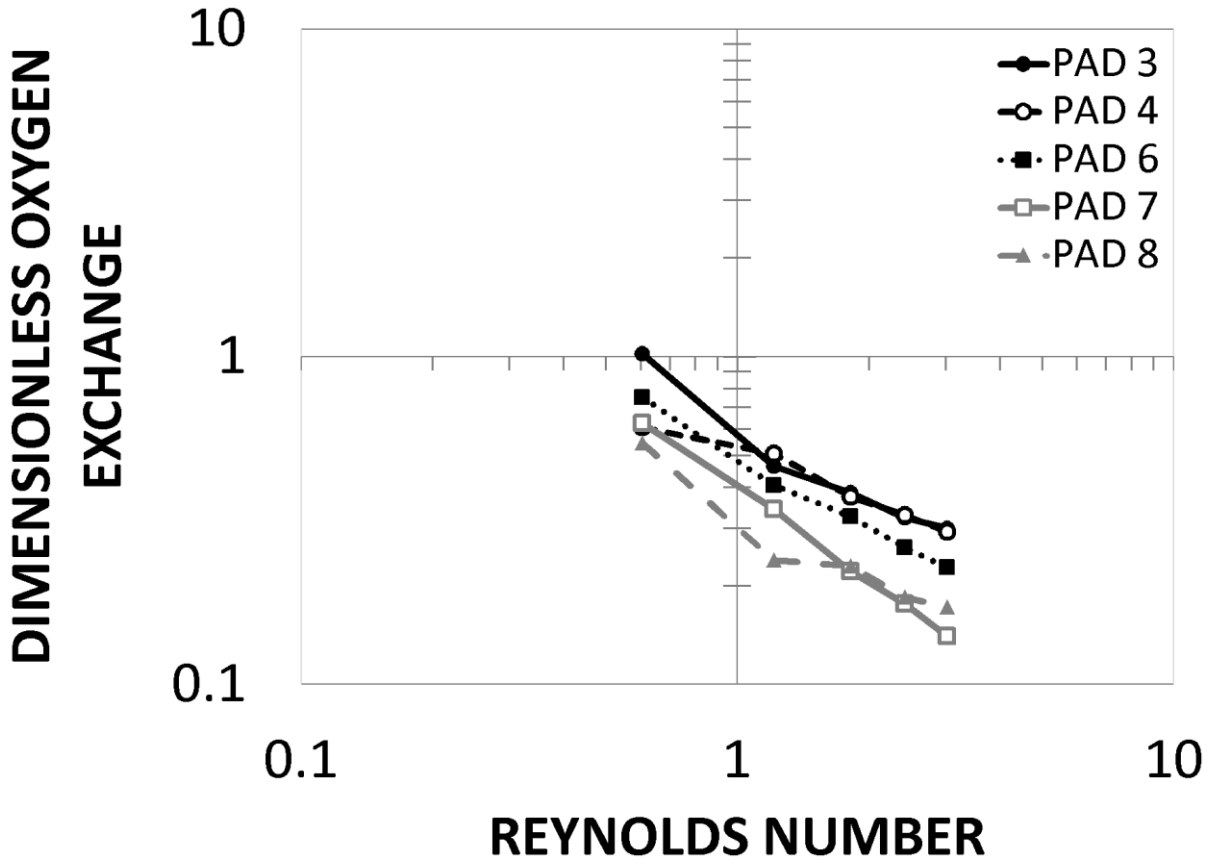

Figure 5.6: The dimensionless oxygen exchange as a function of Reynolds number.

for measuring the relative amount of unplugged fibers of a device in relation to other devices. In these tests, PADs 7 and 8 had an average gas flow resistance of 3.8 mmHg/(L/min)while PADs 3, 4, and 5 had an average resistance of 1.3 mmHg/(L/min) at a sweep gas flowrate of 2.5 L/min, indicating plugging of the lumen of a large portion of fibers, leading to poor gas exchange. This plugging may be the result of fiber ends being open rather than sealed shut during the potting process, which

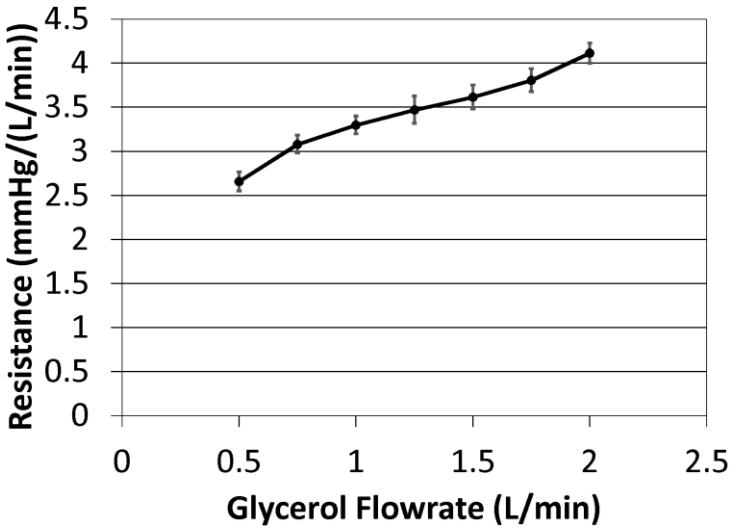

Figure 5.7: The resistance of the PAD as a function of glycerol flowrate.

would allow potting material to build up significantly on the inside of the fibers. Another compounding factor that could decrease gas exchange would be a device being potted too deeply, which covers up a portion of the gas exchange surface. However, potting depth for the PAD can only be checked with a destructive measurement. Overall, the PAD's fiber bundle will need to be redesigned for increased oxygen exchange using the new gas exchange constants derived from PAD's 3,4, and 6, and fabrication methods will need to be improved to prevent future plugging of the fibers.

In terms of carbon dioxide exchange, the devices with the lowest gas resistance (PADs 3 and 4) outperformed all other prototypes. In order to compare to the carbon dioxide exchange prediction predicted by the computational bundle modeling, the amount of carbon dioxide removed was compared at a blood flowrate of 1.25 L/min and gas flow rate of 2.5 L/min. At these flowrates the computational modeling predicted 57.6 mL/min carbon dioxide removal. Since the *in vitro* tests did not include this exact data point, the carbon dioxide exchange could be linearly interpolated between the 1 L/min blood flowrate-2 L/min gas flowrate and 2 L/min blood flowrate-3 L/min gas flowrate cases to yield a carbon dioxide exchange for a blood flowrate of 1.25 L/min and a gas flowrate of 2.5 L/min. PADs 3 and 4 outperformed the computational modeling predictions with carbon dioxide removal of 74.5 and 71 mL/min, respectively. PADs 6, 7, and 8 under performed with carbon dioxide removal of 41.5, 32.5, and 35.5 mL/min. A more in depth analysis of carbon dioxide transfer will be needed where blood flowrate is held constant at 1.25 L/min and the sweep gas flowrate is varied from 1 L/min up to 5 L/min. However, the future surface area increases needed to accomplish oxygen exchange goals should result in a PAD that will exceed performance goals for CO_2 at any reasonable gas flow resistance.

5.4.2 In Vitro Resistance Testing and Computational Model Validation

The *in vitro* resistance testing of the PAD resulted in a resistance of 3.650 mmHg/(L/min) with a glycerol flowrate of 1.25 L/min. This single module resistance was lower than the lowest gas exchanger resistance on the market, the 5-6 mmHg/(L/min) resistance of the Novalung.(7-9) When two modules are placed in parallel, the combined resistance of the PADs is 1.825 mmHg/(L/min). Although the single module resistance is low, it is more than twice the resistance predicted by the computational model, 1.498 mmHg/(L/min). The large discrepancy in resistance

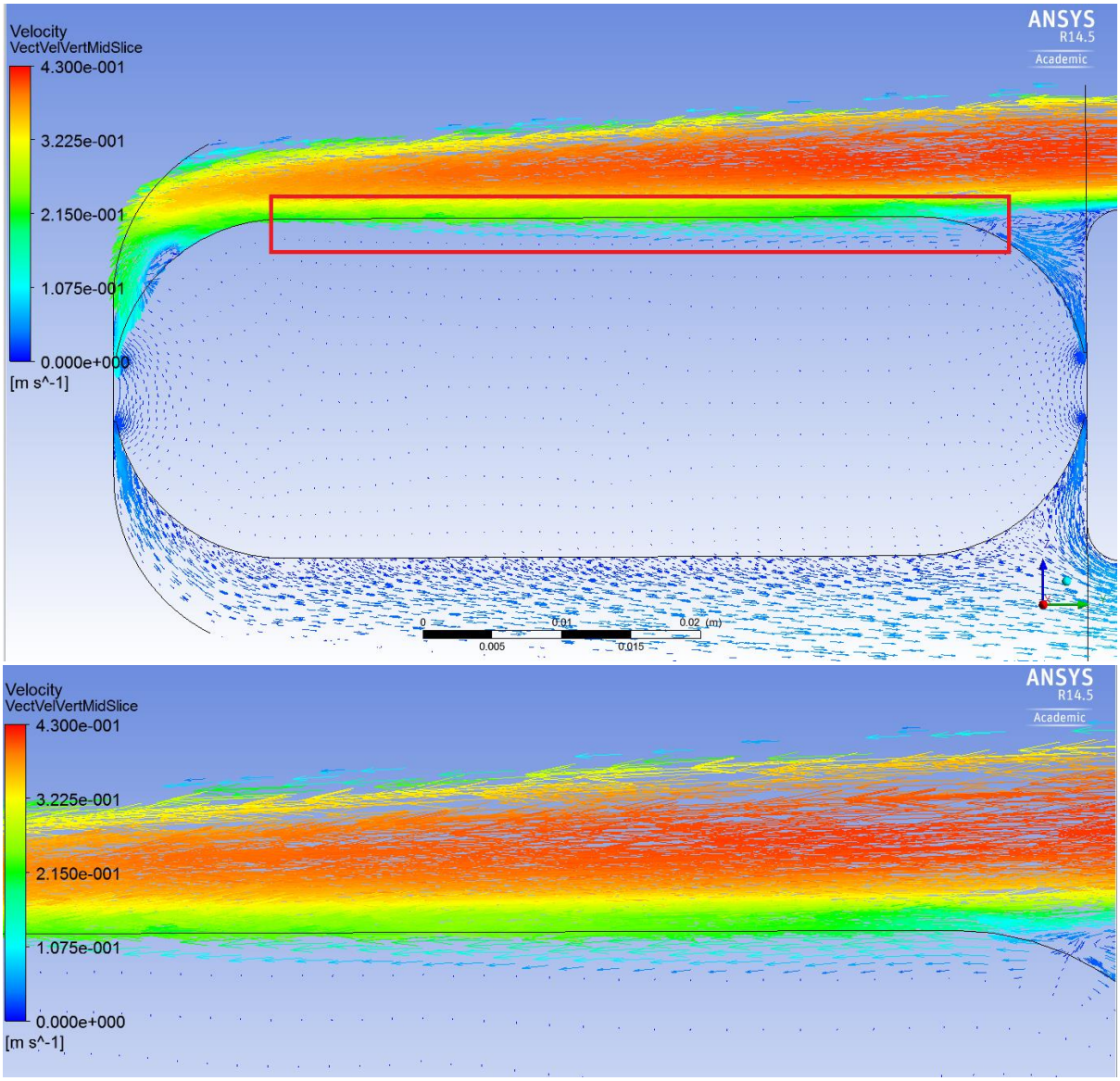

Figure 5.8: Velocity vector plots of the mid-slice. *Top:* Highlighting a region of fluid jet impact on the fiber bundle. *Bottom:* Zooming in on this highlighted area.

between the computational model and *in vitro* results is problematic, since the flow patterns predicted by the model are not validated. Therefore, the CFD simulations may not provide suitable insight into the possible regions of clot inducing blood stasis and recirculation within the PAD. An improved CFD model is needed to investigate areas of stasis and recirculation and to redesign the PAD for improved fluid flow patterns in the device.

The discrepancy between the CFD predictions and *in vitro* testing likely results from the jetting fluid directly impacting the fiber bundle as it flows through the inlet half of the device. In the CFD simulation, the jetting fluid impacts the fiber bundle and the jet continues to flow against a low resistance fiber bundle to the back of the device as a result of the homogenous Darcy porous media model.(**Figure 5.8**) This reduces the validity of the computational model in two manners: (1) as the jet flows over the top of the fiber bundle it will be flowing over the top of a rough surface formed by the radii of the individual fibers, resulting in minor losses not predicted by the computational model, and (2) the geometry of the layers of fiber in the fiber bundle creates a very low permeability path in the direction of the jetting in comparison to the permeability used in the computational model.

As can be seen in **Figure 5.9** of two layers of fiber mat, as the jet enters from the y-direction and flows over the top of the fiber bundle it encounters the radii of each individual fiber in the mat. These repeated radii will impart drag and minor losses into the flow that will

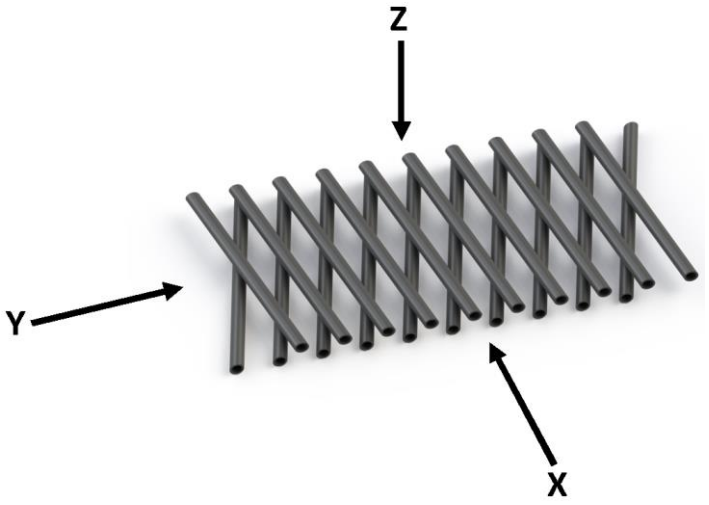

Figure 5.9: A two layer mat of fiber with orthogonal blood flow directions labeled.

not be captured by the porous media model used in these CFD simulations. Numerical data for a similar drag as a function of bundle porosity for similar fiber mats exists (5) and may be able to be integrated into the CFD model to more fully capture the interactions of the jetting fluid with the top of the fiber bundle.

The Darcy porous media model used in the CFD simulations models the fiber bundle as having a consistent permeability in three dimensions, as if the fiber bundle was a sponge with consistent pore size.(10) However, the fiber bundle is composed of a bank of fibers that has large geometric variation in three dimensions. An individual layer of fiber in orientated in an ordered fashion with a 15˚ offset. Layers are stacked in an alternating fashion to create a 30˚ offset between the fibers of alternating layers.(**Figure 5.9**) The orientation of the fiber arrays creates a permeability that varies in three dimensions depending on the flow direction in relation to the fiber bundle.

In the CFD modeling, the permeability was set according to the assumption that the flow through the fiber bundle is largely normal to the top face fiber bundle as can be seen in **Figure 5.9** as flow in the z-direction. However, in the inlet half of the device the direction of flow from the jet impacting the fiber bundle varies greatly from the normal direction (z-direction). (**Figure 5.8**) This jetting in the PAD will create flow that varies in all directions, so the fluid will experience very different permeabilities depending on the location in the x-y plane of the fiber bundle. As the flow progresses through the fiber bundle cases it will eventually normalize to the z-direction. However, until the point where the flow is normal to the fiber bundle top face, there will be error in the model.

An improved permeability model would vary the permeability in all three dimensions. The Ansys Fluent software used in CFD modeling has the capability for variation of permeability in

three directions. However, experimental derivation of permeability for a fiber bundle in three dimensions is not a simple process as fabrication and potting of a fiber bundle with flow coming purely from the x or y directions is difficult due to the potting process involved in the fabrication of a gas exchanger.

Overall, the resistance of the PAD is very low in comparison to commercially available gas exchangers, and when placed in a 2 module parallel configuration has a resistance approaching that of a healthy natural lung. However, this resistance did not meet the original design goal of having a single module resistance of 2.5 mmHg/(L/min). The resistance measured during *in vitro* experiments greatly exceeded the resistance predicted by the CFD analysis, necessitating an improvement of the computational model. Following computational model improvement, the PAD will need to be redesigned for improved gas exchange and coagulation avoiding blood flow patterns.

5.5 References

1. Cook KE, Perlman CE, Seipelt R, Backer CL, Mavroudis C, Mockros LF. Hemodynamic and gas transfer properties of a compliant thoracic artificial lung. ASAIO journal. 2005;51(4):404-11.
2. Vaslef SN, Mockros LF, Cook KE, Leonard RJ, Sung JC, Anderson RW. Computer-Assisted Design of an Implantable, Intrathoracic Artificial Lung. Artificial Organs. 1994;18(11):813-7. doi: 10.1111/j.1525-1594.1994.tb03328.x.
3. Vaslef SN, Mockros LF, Anderson RW, Leonard RJ. Use of a Mathematical Model to Predict Oxygen Transfer Rates in Hollow Fiber Membrane Oxygenators. ASAIO Journal. 1994;40(4):990-6.
4. Mockros L, Leonard R. Compact cross-flow tubular oxygenators. ASAIO Journal. 1985;31(1):628&hyhen.
5. Cook K. Design and testing of intrathoracic artificial lungs [master's thesis]. Northwestern University. 1996.
6. Vaslef SN. Analysis and design of an intravascular lung assist device1990.
7. Müller T, Lubnow M, Philipp A, Bein T, Jeron A, Luchner A, et al. Extracorporeal pumpless interventional lung assist in clinical practice: determinants of efficacy. European Respiratory Journal. 2009;33(3):551-8. doi: 10.1183/09031936.00123608.
8. Flörchinger B, Philipp A, Klose A, Hilker M, Kobuch R, Rupprecht L, et al. Pumpless Extracorporeal Lung Assist: A 10-Year Institutional Experience. The Annals of thoracic surgery. 2008;86(2):410-7.
9. Wiebe K, Poeling J, Arlt M, Philipp A, Camboni D, Hofmann S, et al. Thoracic Surgical Procedures Supported by a Pumpless Interventional Lung Assist. The Annals of Thoracic Surgery. 2010;89(6):1782-8. doi: http://dx.doi.org/10.1016/j.athoracsur.2010.03.012.
10. Khanafer KM, Cook K, Marafie A. The role of porous media in modeling fluid flow within hollow fiber membranes of the total artificial lung. Journal of porous media. 2012;15(2).

Chapter 6 Conclusion

6.1 Conclusions

This work focused on the design and testing of three extracorporeal gas exchangers for treatment of acute and chronic respiratory failure; the compliant thoracic artificial lung (cTAL), the compact cardiopulmonary support device (CCSD), and the pulmonary assist device (PAD). The cTAL was tested for long term biocompatibility and device function in a 14 day *in vivo* experiment. Computational simulations and *in vitro* studies were utilized to design individual components of the CCSD. Following component design, the entire CCSD system was tested *in vitro* to characterize its pumping abilities. The PAD bundle size was designed using numerical modeling of gas exchange and bundle resistance. The PAD housing was designed using computational fluid dynamics simulations. *In vitro* tests were performed to characterize the actual gas exchange capabilities and resistance of the PAD. After preforming these studies, it can be concluded that:

6.1.1 cTAL

1) The cTAL is able to maintain functioning for 14 days without major clot formation, despite a lack of anti-coagulant coatings. The resistance of the cTAL's did not significantly increase as a group over the course of the experiment, with only one device exhibiting an increase in resistance. However, this device had no visual signs of thrombus formation and resistance measurements may have been erroneous.

2) *In vivo* resistance of the cTAL in the 14 day experiments (0.99 mmHg/(L/min)) was twice that of previous *in vitro* and acute *in vivo* experiments (0.51 mmHg/(L/min)). This occurred as a result

device positioning on the side of the fiber creating less favorable hydrostatic pressure on the compliant housing of the device during 14 day *in vivo* testing. In turn, the housing collapsed in the upper regions of the device, creating altered flow patterns. This resistance is still very low in comparison to any other gas exchange device and can provide unloading of the right heart.

3) The cTAL caused very little dysfunction of the kidneys and liver. In the early post-operative time period there were changes in organ function markers due to surgical trauma, but they rebounded as the experiment progressed.

4) Hematologically, the cTAL consumes very little in terms of blood products. Initially, there is a large hemodilatory affect from the large prime volume of the device, but hemoglobin counts decrease very little over the remainder of the experiment and platelet counts rebound to pre-device attachment levels.

5) Excess clamping on the sides of the fiber bundle can induce stasis and subsequent clotting. Clot formation occurred at the fiber bundle of a device that utilized a holder with large clamping forces. In subsequent experiments this clot formation was eliminated by reducing clamping force.

6) The polypropylene fibers of the cTAL allowed plasma leakage after 1 week, but periodic increases in sweep gas flowrate was able to effectively clear the plasma.

6.1.2 CCSD

1) The individual components of the CCSD perform very well. The enclosure flexure only leads to 4.7 mL of stroke loss as it is cycled from -200 mmHg to 300 mmHg. Valves with a leaflet thickness of 0.060” and a diameter of 1.125” are able to perform with low levels of backflow at flowrates of 4 L/min.

2) The CCSD system is able to produce flowrates of 4 L/min. However, large magnitude negative pressures inside the enclosure induce gas leakage into the blood side of the device.

3) Negative enclosure pressures can be reduced by improved priming methods and a change in systolic time, but not to an extent that would alleviate risk of gas embolism in a patient.

6.1.3 PAD

1) Numerical modeling of the gas exchange and resistance of the fiber bundle predicted that a bundle frontal area of 35 cm^2 and a surface area of 0.4 m^2 would meet design goals.

2) CFD modeling predicted that resistance of the PAD will be 1.498 mmHg/(L/min) and 0.963 mmHg/(L/min) for 0.375 inch and 0.5 inch diameter inlet housings, respectively. Inlet manifold angle had very little effect on resistance. Thus, all housing designs were predicted to meet design goals. The 45 degree inlet manifold was chosen for in vitro testing due to its more compact size when compared to the 30 degree inlet manifold angle.

3) Large recirculations occurred in all housing designs as a result of fluid forming a jet as it flowed through the inlet manifold. The jetting fluid impacted the back of the housing and the fiber bundle. Thus, the housing of the PAD will need to be redesigned.

4) The tubing size required for the 0.5" inlet diameter PAD is a non-standard size in the medical field, and would require new pump interfaces. Thus the 0.375" inlet diameter was chosen for *in vitro* testing.

5) *In vitro* gas exchange testing yielded oxygen exchange performance well below design goals. However, two of the five PAD's that were tested had a manufacturing defect that result in plugging of the gas exchange fibers. When excluding the defective devices, the oxygen exchange of the PAD was below the design goals, but not to as a great extent.

6) *In vitro* resistance testing of the PAD yielded a resistance more than twice that predicted by the CFD simulations. As a result, the computational model was not able to be validated.

7) *In vitro* resistance exceeded the design goal by 46%. As a result, the PAD must be redesigned

to decrease resistance.

6.2 Limitations and Future Work

The CCSD was greatly limited by the magnitude of large pressures in the enclosure housing. These negative pressures resulted in gas being pulled from the gas side of the device to the blood side. In a patient, if the gas entered circulation it would lead to gas embolism and subsequent patient mortality and morbidity. This risk greatly outweighs any benefits of the CCSD system. Thus, the CCSD system should not be developed further. However, recent strides in ECMO pump technologies may allow for adoption of pulsatile flow in ECMO.

The 14 day in vivo cTAL experiments were largely limited by non-device complications that reduced animal numbers in the later stages of the experiment. One sheep was euthanized as a result of a bradycardic arrhythmia that progressively became more severe as experimental time increased. This arrhythmia was evident shortly after surgery and was likely the result of grafting directly onto the left atrium. In the future, the graft attachment will likely need to be improved to reduce complications.

From a device standpoint, the rapid prototyped connectors that connected the cTAL to the device failed catastrophically in two cases. In one case this resulted in the euthanization of an animal. In the other case the connector failed immediately after detaching the cTAL from the animal at the conclusion of the experiment. These connectors must be replaced with injection molded or machined polycarbonate connections prior to future long term *in vivo* studies. The large prime volume of the device led to initial hemodilution when the device was attached. Thus, the device will need to be decreased in size to reduce the prime volume of the device. This will be possible as the cTAL is overdesigned in terms of gas exchange performance. This re-design will also need to incorporate PDMS coated polypropylene gas exchange fibers to prevent future plasma

leakage issues. Despite no anti-coagulant coatings being applied to the cTAL and its circuitry, the cTAL remained relatively clot free for 14 days. In the future, anti-coagulant coatings should be applied to allow for an even greater device lifespan. Following anti-coagulant coating and prime volume reduction, the cTAL should be tested in two month *in vivo* biocompatibility studies to prove efficacy as a destination therapy device.

The PAD work was limited by the accuracy of the computational models used in its design. The CFD model was highly inaccurate in its prediction of the resistance of the device. This may be due in part to a fluid jet impacting the fiber bundle. The fiber bundle is not modeled in a way that takes into account minor losses from fluid moving over the top of the fiber radii on the top surface of the fiber bundle or the decreased permeability of the bundle in the direction of the jetting fluid flow. Future efforts will be needed to improve the validity of the computational modeling including the addition of directional permeability and minor losses on the top surface of the fiber bundle.

The *in vitro* gas exchange of the device was also lacking in comparison to the predictions of the numerical models. However, this was expected as the gas exchange constants used in the modeling were derived from past experiments that failed to challenge the tested gas exchangers. The new gas exchange constants derived from the current work should be used for future oxygen transfer modeling. *In vitro* gas exchange varied between devices due to a fabrication defect that resulted in plugging of the gas exchange fibers. Future fabrication techniques will need to improve the sealing of the fiber ends prior to potting, so as to avoid plugging during the potting process. Additionally, all future devices should be screened for a high gas resistance prior to ***in vitro*** and *in vivo* use to avoid gas exchange abnormalities.

From an overall device design standpoint, the housing and fiber bundle will need to be

redesigned to improve gas exchange, reduce resistance, and improve potential biocompatibility. The fiber bundle will need to be increased in path length and surface area to increase gas exchange capabilities. Concurrently, the frontal area must be increased to reduce the overall device resistance. Care will need to be taken to avoid designing a device too large for in home use. The housing will need to be redesigned to reduce the jetting that results in increased stasis regions, increased recirculation regions, and decreased computational model validity. As the recirculations are reduced, the PAD's clotting potential should be reduced, and there may be some gains in gas exchange and resistance performance. Following a redesign of the PAD, future in vivo studies will be needed to test the biocompatibility of the PAD and its ability to serve as a destination therapy device.

Appendix A: CCSD Valve Fabrication

A.1 Valve Dip Casting

1. Perform all dip casting in the dipping hood/glove box heated to 120°F with proper ventilation.

2. Clean the delrin valve mold with isopropyl alcohol.

3. Thread a section of threaded rod into the back of the mold to facilitate dipping and rotisserie attachment. (**Figure A.1**)

4. Slowly insert valve mold into a vat of Biospan polyurethane dissolved in cyclohexanone, making sure to angle the valve so that one corner of mold dips in first. (**Figure A.1**) This will help avoid air pockets forming in the leaflet cavities.

5. Slowly withdraw the valve mold, once again tilting it so that one corner is facing downward to avoid bubble formation.

6. Keep the valve in angled and allow Biospan to drip off of this corner for 30 seconds.

7. After 30 seconds, slowly rotate the valve so that biospan drips off of the next corner, and let drip for 30 seconds.

8. Rotate slowly to the last corner and let drip for 30 seconds.

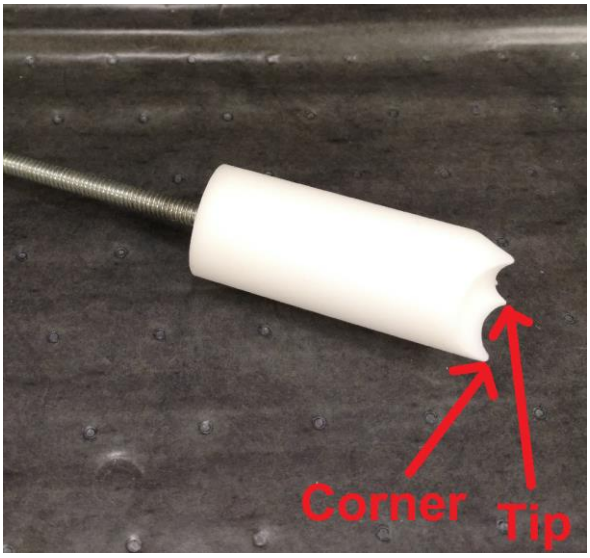

Figure A.1: A CCSD valve mold with attached threaded rod with the valve center tip and valve corner labeled.

9. Angle the valve so that the biospan drips off of the center point connecting all three valve leaflets. (**Figure A.1**)

10. Drip for a final 30 seconds.

11. Use a stainless steel dental pick to pop any bubbles that formed on the leaflet.

12. Angle/rotate the valve mold so that biospan fills in the void from the bubble after popping.

Figure A.2: A CCSD valve mold attached to the rotisserie.

13. Following bubble popping and filling, angle the mold so that its axis is horizontal.

14. Rotate the valve on its axis to evenly spread biospan over the valve leaflet faces.

15. While continuing to rotate the valve, attach it to the rotisserie. (**Figure A.2**)

16. Turn the rotisserie on to its slowest setting.

17. Allow the valve to dry for 2 hours before the next dip.

18. Turn off rotisserie and repeat the above dipping steps.

19. Repeat the procedure until the desired number of coats have been obtained.

20. After the last dip, allow the valve to dry over night.

21. Remove mold from the dipping hood and insert into the drying oven inside the fume hood, with the oven temperature set to $120^{\circ F}$.

A.2 Valve Demolding

1. Remove the valve mold from the oven.

2. Set the valve mold into a beaker of water for at least an hour.

3. Starting from the back edge, roll the valve biospan over onto itself to form a folded-over lip of biospan.

4. Pull this biospan lip towards the leaflets of the valve to remove the valve from the mold.

5. Immediately flip the valve right-side-out.

6. Rinse the valve with water and dry thoroughly.

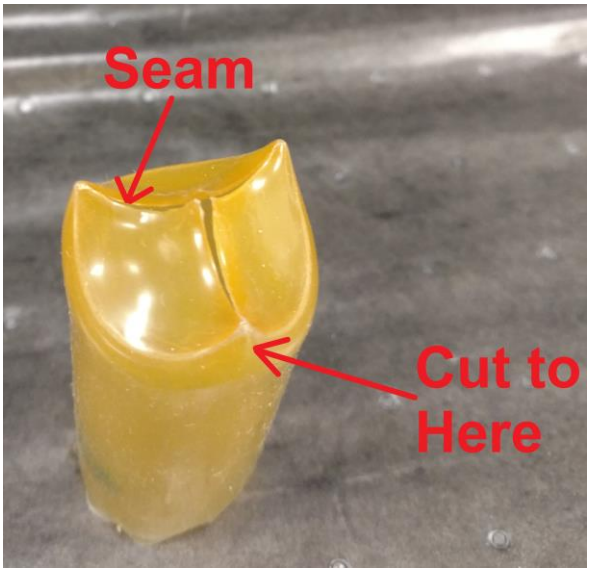

Figure A.3: A CCSD valve with leaflets cut free labeled with the cutting seam and the distance to cut past the valve corner.

A.3 Valve Finishing

1. Starting from the center leaflet joining tip, cut the seam between leaflets (3 in total). Once a seam has been cut, cut just slightly further beyond the valve corner. (**Figure A.3**)

2. Once all leaflets are feed from eachother, color the edges of the valves with a permanent marker to allow easy visualization of leaflet movements.

3. Cut the excess valve tubing off, so that valves are approximately 1 inch long (**Figure A.4**)

4. Sand the non-blood contacting surfaces of the valve with 220 grit sandpaper to ensure proper adhesion of polyurethane in the following steps.

5. Use BJB polyurethane to glue valves into an outer biospan tube for valve testing or the

Figure A.4: A cut to length CCSD valve with colored leaflet edges.

CCSD blood conduit for CCSD system testing. When inserting into blood inlet and outlet conduits, ensure that one valve opens towards the fiber bundle and the other opens away from the fiber bundle.

6. Use BJB polyurethane to glue a stiff plastic tube onto the outside of the biospan valve-tube assembly. This prevents valve collapse. (**Figure A.5**)

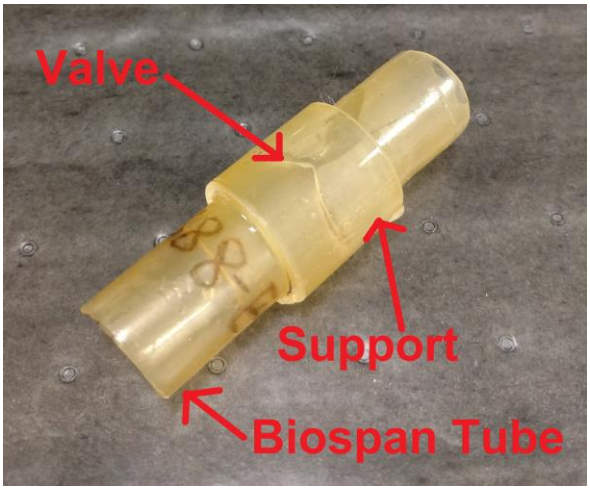

Figure A.5: A valve glued into a biospan tube with a rigid support tube.

A.4 References

1. Schewe-Mott RE. Thoracic Artificial Lung Design: University of Michigan; 2012.

Appendix B: Gas Exchanger Manufacture

The manufacture of the PAD, cTAL, and CCSD are very similar with the exception of the housing construction, type of material used as potting, and the addition of valves into the CCSD blood conduits. The PAD manufacturing process is the most evolved, so the entire manufacturing process will be described in the most detail for the PAD with notes that designate major differences with CCSD and cTAL construction. The construction of the cTAL has been described previously in detail.(1) The CCSD construction is identical to cTAL construction with the exception of the addition of valves into the blood conduits according to procedure outlined in **Appendix A**.

B.1 Fiber Bundle Rolling

1. Cut a properly sized core from a 3/32 inch thick sheet of acrylic with a laser cutter. (**Figure B.1**) *Note: Originally CCSD and cTAL cores were cut from polycarbonate sheet using a dremel tool. However the PAD method is an improvement and should be followed for future cTAL and CCSD manufacture*.

2. Sand all surfaces of the acrylic core that are embedded in the potting material using 320

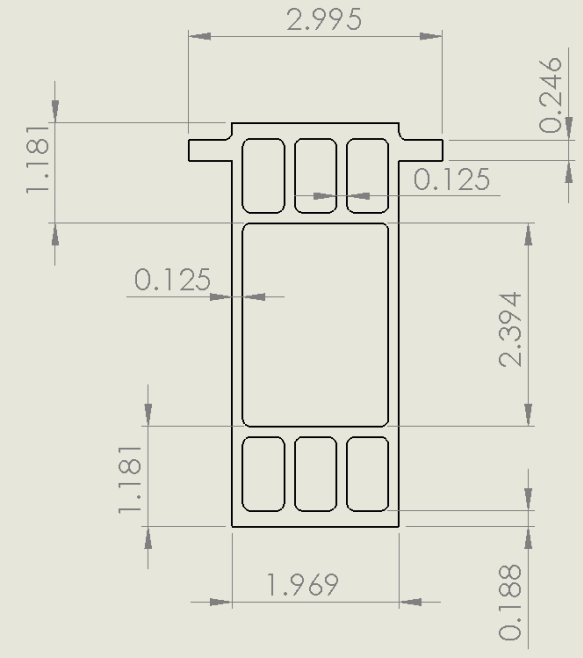

Figure B.1: A PAD core drawing with all dimensions labeled in inches.

grit sand paper, making sure to remove all sharp edges.

3. Wash cores thoroughly with water.

4. Lightly wipe the cores with a Kim-wipe that has isopropyl alcohol on it. Be careful to only use a small amount of alcohol on the Kim-wipe, as the alcohol will craze the acrylic core and weaken it.

5. Prime all sanded surfaces with Nusil MED-163 following manufacturer instructions. *Note: This step is specific to potting with PDMS rather than polyurethane.*

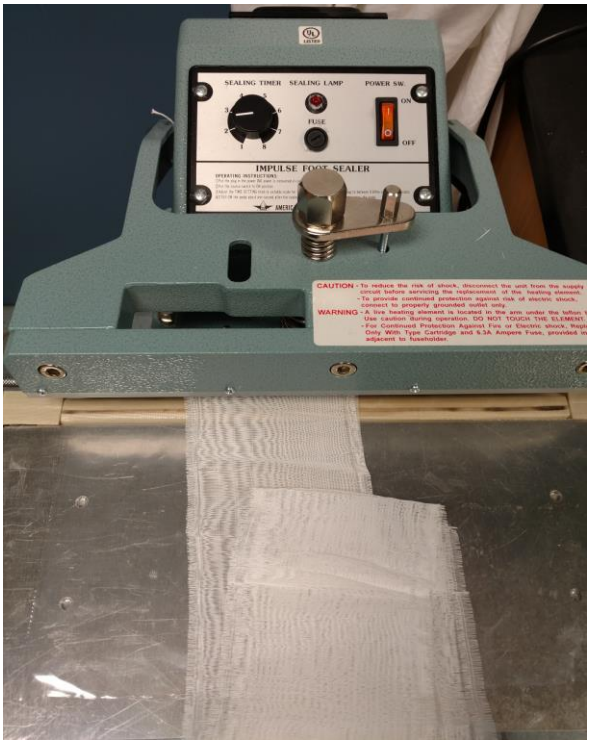

Figure B.2: Heat sealing across the width of a fiber mat.

6. Using a natural hair brush, apply a thin layer of PDMS to all surfaces in contact with the potting material. *Note: This step is specific to potting with PDMS rather than polyurethane.*

7. Allow the PDMS to cure in an oven for at least 2 hours prior to handling. *Note: This step is specific to potting with PDMS rather than polyurethane.*

8. Heat seal across the width of the fiber mat, and cut off the excess fiber mat. (**Figure B.2**)

9. Attach the fiber mat to the core using a small amount of PDMS on the core where the potting material will later contact. *Note: This step is specific to potting with PDMS rather than polyurethane. If potting with polyurethane, use polyurethane rather than PDMS for this step. In previous versions of the cTAL and CCSD, two sided tape was utilized. However, the tape served as a nidus for clot formation and should not be used for future CCSDs and cTALs.*

10. Place the fiber and core into the oven and allow it to cure for at least 4 hours prior to attempting to roll the fiber bundle.

11. Lay clean plastic out on the benchtop and unroll the length of fiber that is attached to the core onto the benchtop.

12. Measure out and mark the length of fiber that will result in the desired gas exchanger surface area. (140.893 inches of double layer fiber mat for the PAD) *Note: This bundle sizing step and future bundle sizing quality control steps were only performed for the PAD, but would result in more consistent fiber bundles for cTALs and CCSDs.*

13. Flip the core over 51 times to roll the fiber bundle. *Note: 58 times for the CCSD, 84 times for the cTAL*

14. Check that you are within one turn of the mark placed on the fiber that corresponds to the proper bundle surface area. *Note: This bundle sizing quality control step was only performed for the PAD, but would result in more consistent fiber bundles for cTALs and CCSDs.*

15. Measure the thickness of the fiber bundle using a caliper without crushing down on the fiber bundle. Use this measurement and core thickness to ensure that the spacing between layers of fiber is 5-20 micrometers. *Note: This bundle sizing quality control step was only performed using a caliper for the PAD, but would result in more consistent fiber bundles for cTALs and CCSDs.*

16. Measure the bundle width to ensure that the bundle is 20-40 micrometers oversized from the width of the housing. *Note: This bundle sizing quality control step was only performed for the PAD, but would result in more consistent fiber bundles for cTALs and CCSDs.*

17. If the fiber bundle is out of specification, re-roll the bundle until bundle sizing specifications are met.

18. Heat seal across the width of the fiber mat where it rolls over the side of the bundle at the end of the last flip.

19. Cut the fiber along this heat seal.

20. Apply a small amount of PDMS to the fiber bundle to connect this last flap of fiber to the fiber, while making sure to only apply PDMS to places that will be encapsulated during the potting process. *Note: This step is specific to potting with PDMS rather than polyurethane. If potting with polyurethane, use polyurethane rather than PDMS for this step. In previous versions of the cTAL and CCSD, two sided tape was utilized. However, the tape served as a nidus for clot formation and should not be used for future CCSDs and cTALs.*

21. Place the fiber bundle in the oven to allow the PDMS to cure for at least 2 hours before handling.

22. Apply PDMS to the ends of the fibers on the fiber bundle to connect the layers of fiber to eachother. *Note: This step is specific to potting with PDMS rather than polyurethane. If potting with polyurethane, heat seal the layers of fiber together with a hot plate.*

23. Place the fiber bundle in the oven to allow the PDMS to cure for at least 2 hours before handling.

B.2 PAD Housing Preparation

1. Sand all inside surfaces of the 3-D printed housing, surfaces coming on contact with potting material, and sealing faces between the two halves of the housing with 320 grit sand paper. (**Figure B.3**)

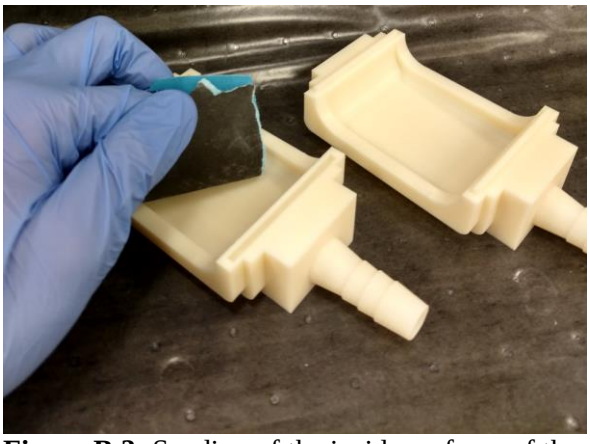

Figure B.3: Sanding of the inside surfaces of the PAD housing.

2. Wash the housing with water and dry in the oven.

3. Clean the housing with isopropyl alcohol.

4. Prime all sanded surfaces with the exception of potting contacting surfaces and the sealing faces between the two housing halves with Nusil MED-163 primer according to manufacturer instructions.

5. Prepare Nusil MED-6019 PDMS according to manufacturer instructions, and paint onto the primed surfaces of the housing.

6. Place housing into the oven and allow to cure overnight.

7. Prime all potting contacting surfaces with Nusil MED-163 primer according to manufacturer instructions.

8. Prepare Wacker Chemie Elastosil RT625 PDMS according to manufacturer instructions, and paint onto the newly primed surfaces of the housing.

9. Place housing into the oven and allow to cure overnight.

10. Prime the sealing faces between the two housing halves with Nusil MED-163 primer according to manufacturer instructions.

11. Prepare Wacker Chemie Elastosil RT625 PDMS according to manufacturer instructions, and paint onto the sealing faces of the housing, making sure to avoid excessive PDMS that could seap into the fiber bundle when the two halves of the housing are sandwiched together.

12. Insert fiber bundle into one half of the housing.

13. Carefully sandwich the two halves of the housing together to avoid PDMS flowing into the fiber bundle.

14. Clamp the fiber bundle lightly with C-clamps.

15. Place housing-fiber bundle assembly into the oven and allow to cure at least two hours.

B.3 Device Potting

Pot only according to current potting protocols, as the potting procedure is continuously improving and varies depending on equipment. These steps are only meant to serve as a basic potting outline and is not as detailed as current lab potting protocols. Only pot after being properly trained by current lab staff, and never pot alone.

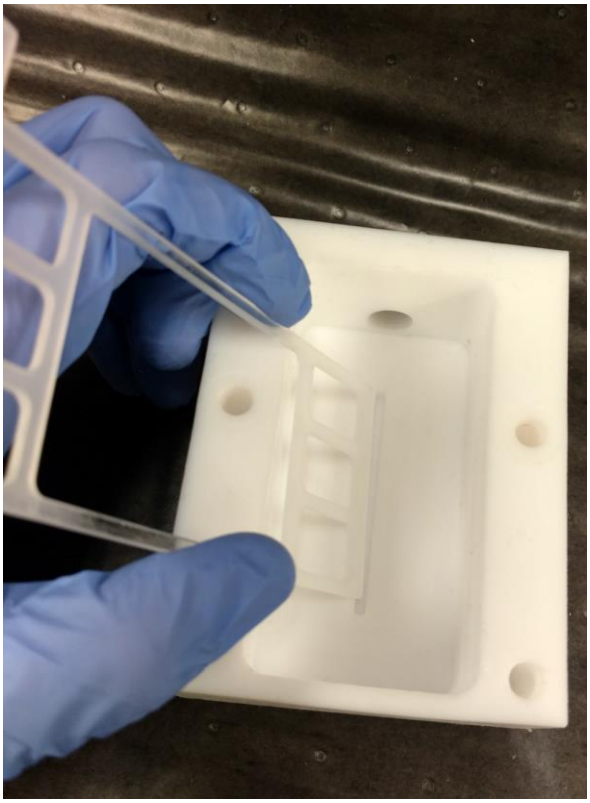

Figure B.4: A bare core being slid into the potting mold core slot.

1. Clean all Teflon potting molds thoroughly.

2. Secure the housing-fiber bundle assemblies in the potting fixture, and ensure that all bolts and nuts are properly tightened. Apply low strength thread-locker to the proper bolts that connect the Teflon mold to the aluminum fixture.

3. When inserting the housing fiber bundle assembly into the potting fixture ensure that the core of the fiber bundle slides into the slot in the Teflon mold. *Note: This is only done in the new mold design of the PAD, but future CCSD and cTAL molds should incorporate a core slot to properly secure the fiber bundle during potting.* (**Figure B.4**)

4. When inserting the housing fiber bundle assembly into the potting fixture ensure that you allow for a small overflow gap between the mold and the housing. *Note: This only applies to the solid housing PAD.* (**Figure B.5**)

5. Insert the potting fixtures into the centrifuge and secure to the centrifuge arm (one PAD on each end of the centrifuge arm, ensuring equal distance from the rotational axis). (**Figure B.6**)

6. Attach silicone tubing between the potting molds and the centrifuge potting boat.

7. Follow the "Potting Safety Checklist" to prepare the centrifuge. Also be prepared to hit the emergency stop button on the centrifuge. Operate the centrifuge according to current lab safety protocols.

8. Prepare the Wacker Chemie Elastosil RT625 PDMS according to manufacturer instructions and insert into the potting gun syringes. *Note: The previous CCSD and cTAL used polyurethane potting material rather than PDMS. Refer to previous polyurethane potting documents for detailed polyurethane preparation, centrifuge heating instructions, centrifuge speeds, and centrifugation timings.*

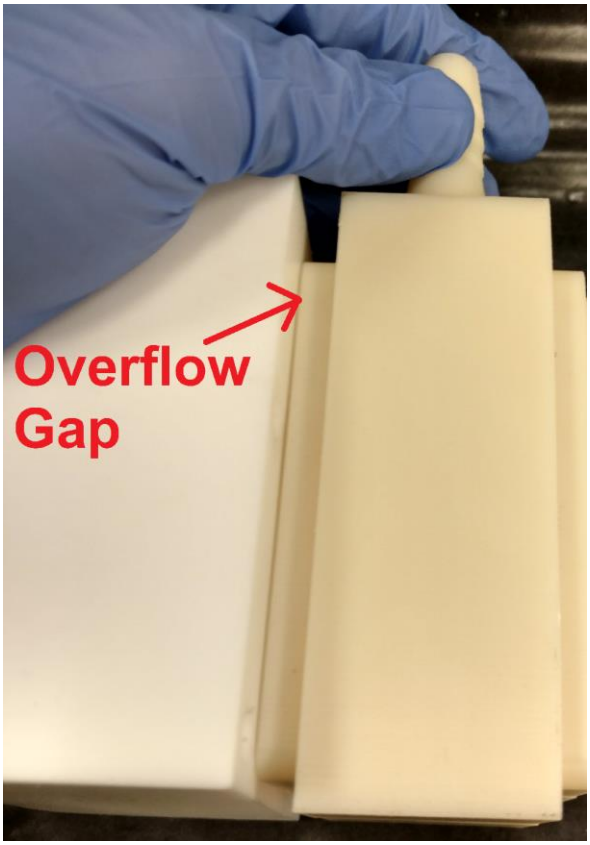

Figure B.5: A PAD housing inserted into a potting mold with the overflow gap labeled.

9. Turn on centrifuge and turn speed up to 707 rpms.

10. Slowly inject PDMS into the potting boat.

11. Turn on heat gun at highest settings.

12. Monitor centrifuge temperature.

13. Stay at this rotational speed until the time hits 24 minutes or the temperature reaches 120$^{\circ F}$ for at least 5 minutes, whichever occurs later.

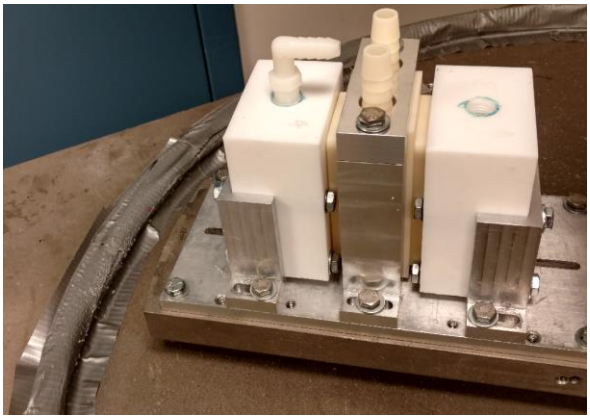

Figure B.6: The PAD potting fixture attached to the centrifuge arm.

14. Turn down the centrifuge speed to approximately 200 rpm until the total centrifuging time reaches 1 hour.

15. Monitor the temperature and ensure that it does not exceed $130^{\circ F}$.

16. At the end of the centrifuge cycle allow the molds to cool for 1 hour.

17. Flip the fixtures around to pot the second side of the PADs.

18. Clean out the potting boat, and remove all tubing and tubing connectors from the previously potted molds.

19. Attach new silicone tubing to the un-potted molds and repeat the above procedure to pot the second side of the PADs.

20. Upon completion of the second round of potting, remove the fixtures from the centrifuge and insert into the oven to post cure the PDMS potting for at least a day. *Note: This only applies to PDMS potting.*

21. De-mold the PADs and place back into the oven to post cure for at least 2 more days. *Note: This only applies to PDMS potting.*

B.4 Device Cutting

Follow all safety precautions and current lab safety protocols when cutting, since the cutting saw has the potential to severely injure you and others when used improperly. Cut only according to current cutting protocols, as the cutting procedure is continuously improving and varies depending on equipment. Only senior staff are permitted to cut devices, and they are never permitted to cut alone.

These steps are only meant to introduce the basic process with the purpose of describing the preparation of the PAD and give context to the discussions in the main dissertation body.

1. Mark the potting material 3/8 of an inch from the housing on both potted sides.

2. Plug/cover the blood inlet and outlet conduits.

3. Insert the PAD into the cutting fixture and secure properly.

4. Follow current lab cutting safety protocols.

5. Cut a thin slice of potting material away with the saw.

6. Repeat cuts until you cut away your marking.

7. Flip the device around and repeat the above procedure.

8. Remove from the PAD from the cutting fixture.

9. Inspect the last slice from each side of PAD by holding the slice up to the light to see if the lumen of the fibers are not plugged with potting material.

10. If plugging exists, cut further slices from the PAD and check again.

B.5 Sealing the PAD Housing

The 3-D printed PAD housing is very porous, so it must be sealed after cutting the potted sections in order to prevent gasses from passing into the blood side of the housing and to prevent liquids from passing outside of the housing.

1. Prepare a marine grade epoxy according to manufacturer instructions.

2. Using a tongue depressor paint the entire outside of the PAD housing with epoxy with exception of the faces that come in contact with blood tubing and the gas caps.

4. Allow the epoxy to dry in the fume hood according to manufacturer instructions.

5. Apply a very thin layer of silicone RTV gasket maker to the remaining external surfaces of the PAD, making sure to thoroughly smooth out the silicone and force it into cracks with a gloved finger.

6. Allow the silicone RTV to dry in the fume hood according to manufacturer instructions.

B.6 Leak Testing the Potted Section

1. Fill the PAD with deionized water.

2. Attach tubing to each blood conduit.

3. Attach a barbed tubing connector with leur lock to each tube.

4. Connect another section of tubing to the other end of barbed tubing connection.

5. Fill all tubes and connectors with deionized water and clamp the terminal tubing ends with tubing clamps.

6. Attach a pressure transducer to the leur lock on one barbed tubing connection, and attach a syringe filled with deionized water to the leur lock on the other barbed tubing connection.

7. Inject fluid with the syringe to pressurize the PAD to 40 mmHg.

8. Inspect the potted regions for leaks.

9. If there are leaks, mark them for patching with a fine tipped permanent marker.

10. Empty the PAD and dry the device with filtered air for at least 8 hours.

11. Prepare the Wacker Chemie Elastosil RT625 PDMS according to manufacturer instructions.

Note: The previous CCSD and cTAL used polyurethane potting material rather than PDMS.

12. Apply a small dot of PDMS to the marked leaks using a blunt applicator needle.

13. Place the PAD in the oven for at least one day to cure.

14. Repeat the above procedure until the device is leak free.

15. Log all leak testing and patching in lab leak testing binders.

B.8 PAD Gas Cap Attachment

1. Clean the gas caps with water if they are made from acrylic. Use isopropyl alcohol if they are manufactured from polycarbonate, as polycarbonate resists crazing by isopropyl alcohol.

2. Apply a thick layer of silicone RTV gasket maker to the PAD housing faces that interface with the gas caps.

3. Smooth this layer out with a gloved finger.

4. Slide the gas cap onto the PAD housing gas cap shoulders.

5. Apply a thick layer of silicone RTV bridging any gap between the PAD housing and gas cap.

6. Force the silicone RTV into any gaps using a gloved finger, and smooth the silicone RTV out.

7. Allow the silicone RTV to dry in the fume hood according to manufacturer instructions.

B.9 PAD Gas Cap Leak Testing

1. Attach tubing to the blood inlet and outlet conduits, and clamp these off with tubing clamps.

2. Attach tubing to the gas inlet and outlets on the gas caps.

3. Flow oxygen through the gas inlet at a rate of at least 3 L/min.

4. Submerge the PAD in a bucket of water while making sure that the gas outlet does not become submerged.

5. Inspect the seams between the gas caps and the housing for air leaks.

6. If there is a leak, mark it with a permanent marker for later patching.

7. Dry the device thoroughly before patching.

8. Force silicone RTV into any leaking areas with a glove finger.

9. Allow the silicone RTV to cure in the fume hood according to manufacturer instructions.

10. Repeat the above procedure until no leaks are present.

11. The PAD is not ready for *in vitro* testing. However, the blood contacting surfaces should be rinsed with deionized water for a day before *in vivo* use.

Appendix C: Graft Assembly Fabrication

C.1 Dacron Graft Preparation

Dacron grafts (**Figure C.1**) are typically coated with a gelatin coating during the manufacturing process. If this coating is not removed prior to graft insertion into the assembly tubing, the graft will separate from the tubing and cause a life threatening failure.

1. Prepare a 5% bleach solution.
2. Submerge grafts into bleach.
3. Use a toothbrush to scrub the gelatin off of the graft.
4. Rinse thoroughly with water and dry.
5. If there is discoloration or stiffness in the valve, repeat the above process with a bleach concentration stepped up 5% until grafts are clean.

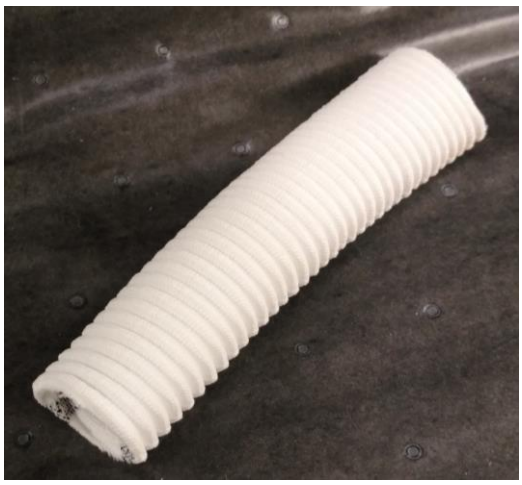

Figure C.1: A section of 18 mm Dacron graft material.

C.2 Tubing Preparation

The tubing that the grafts slide into will need to be expanded in diameter to accommodate graft insertion. If the tubes are under expanded, the graft will kink upon insertion and clot may form on the kink when used *in vivo*. If the tubes are over expanded, the graft-tubing connection will be weak and susceptible to separation.

1. Heat the smallest diameter aluminum expansion rod with a heat gun. (**Figure C.2**)

2. Inside of a fume hood, heat the final inch of an 8 inch long piece of Tygon R-3603 tubing with a heat gun.

Figure C.2: An aluminum expansion rod.

3. During heating rotate the tubing in order to allow for even softening and avoidance of tubing burning.

4. Once a small amount of smoke/vapor is emitted from the tubing, it is sufficiently heated.

5. Slide the tubing onto the taper of the expansion rod, allowing for at least ½ inch of the tubing to be expanded for graft insertion.

6. Wait for the rod and tubing to cool.

7. Invert the tubing and pour isopropyl alcohol into the tubing.

8. Over top of a sink push forwards, and then pull backwards on the tubing to free it from the expansion rod.

9. Carefully insert a bare graft into the expansion of the tubing.

10. If the graft inserts easily with little or no friction on the tubing, the tubing is expanded sufficiently.

11. If the tubing is not expanded in diameter enough, repeat the above steps with a larger diameter expansion rod.

C.3 Graft-Tubing Connection

1. Perform all steps in a fume hood with appropriate PPE.

2. Cut Tygon R-3603 tubing into small pieces.

3. Dissolve tubing in a glass jar using cyclohexanone (100 mL cyclohexanone to 12.5 g tubing)

4. Adjust concentration of cyclohexanone in the mixture until the mixture has the consistency of syrup.

5. Using a natural hair brush, paint the first inch of the graft with pvc-cyclohexanone mixture. The graft will absorb the mixture.

6. Paint the expansion section of the expanded tube lightly with pvc-cyclohexanone mixture.

7. Use a stainless steel weighing spatula to remove air bubbles between the graft and tubing.

8. Fill any spaces between the tubing and graft with pvc-cyclohexanone mixture.

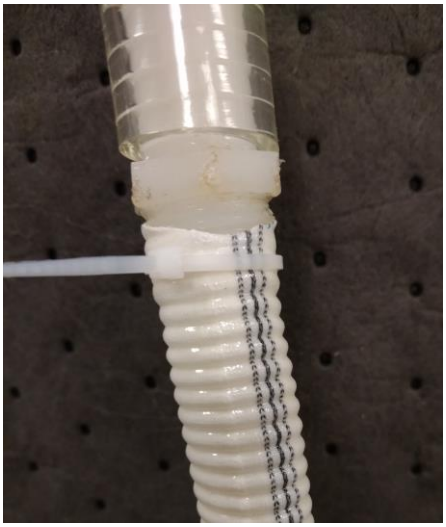

Figure C.3: An extension connector threaded onto a synthetic graft.

9. Stand the assembly vertically by inserting the unused end of the tubing on the coating base.

10. Let the assembly dry for a day to allow for cyclohexanone to evaporate off.

C.4 Graft Coating

1. Perform all steps in a fume hood while using appropriate PPE.

2. Thread the extension connector onto the graft material and zip tie in place. (**Figure C.3**)

3. Tie the extension connector to a supporting structure to allow for graft extension. The Graft should be extended just far enough to allow for coating between the graft ridges, but not extended so far as to limit graft flexibility. (**Figure C.4**)

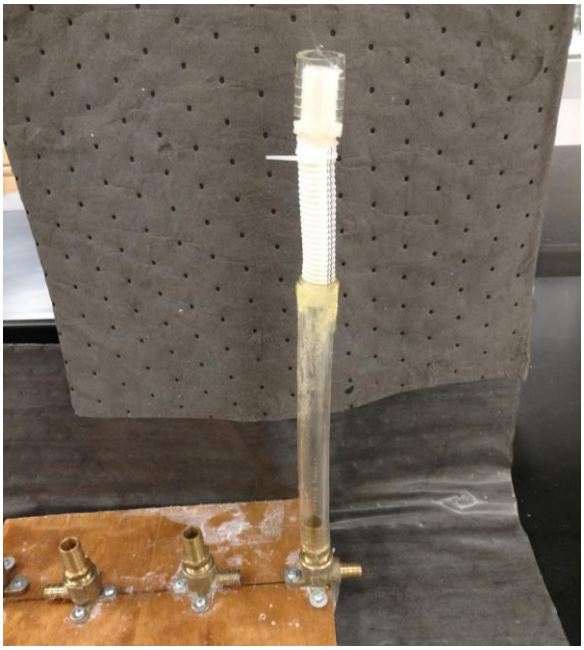

Figure C.4: Proper extension of a graft-tubing assembly demonstrated with a used assembly.

4. Paint the pvc-cyclohexanone mixture onto the graft material starting from the top and working to the bottom.

Figure C.5: A completed graft assembly with felt sutured on.

5. Wipe away any excess material that drips down the length of the tubing.

6. Allow the assembly to dry for at least two hours.

7. Apply additional coats until the desired graft stiffness is achieved. (typically 4-6 coats depending on pvc concentration)

8. Allow the grafts to dry at least one day.

C.5 Graft Finishing

1. Perform all steps in a fume hood with appropriate PPE.

2. Cut a rectangle of felt that is 5 inches long and with a width that corresponds to circumference of the tubing.

3. Pull the felt to flare out the last inch of the felt to allow for attachment on the expanded section of the tubing.

4. Paint pvc-cyclohexanone mixture onto the outside of the tubing that extends from the expansion section of the tubing to a distance 5 inches from the expansion end of the tubing.

5. Apply the felt onto the section of tubing that was coated with the pvc-cyclohexanone mixture.

6. Using a silk suture, suture the felt together on the tubing using a simple continuous suturing technique and tie off. (**Figure C.5**)

7. Allow to dry for at least three days. The longer it dries, the better.

8. Remove the graft-tubing assembly from the extension assembly and rinse thoroughly with water.

9. Dry the assembly fully.

10. Sterilize with ethylene oxide sterilization

Appendix D: Bundle Path Length Calculation

With an array of frontal and surface areas known the first step in modeling the fiber bundle was to calculate the height or path length of the fiber bundle. This was accomplished by first finding the surface area of a single fiber, then finding the surface area of a single layer of fiber, and then calculating how many layers are needed to achieve the desired surface area. The surface area of an individual fiber, SA_{if}, was calculated using **Equation D.1**

$$SA_{if} = \frac{\pi * \Phi_f * w}{\cos\theta} \tag{D.1}$$

where Φ_f is the diameter of a single fiber, w is the width if the fiber bundle, and θ is the distortion angle that the angled fiber of the fiber mat makes with the axis across the width of the fiber bundle as shown in **Figure 4.3**. The surface area of a single layer of fibers, SA_{layer}, was calculated using **Equation D.2**

$$SA_{layer} = L * spacing * SA_{if} \tag{D.2}$$

where L is the length of the fiber bundle and spacing is the density of fiber packing in the fiber mat expressed as the number of fibers per unit length. The surface area of the entire fiber bundle, SA, was calculated using **Equation D.3**

$$SA = no_{layers} * SA_{layer} \tag{D.3}$$

where no_{layers} is the number of layers of fiber mat that comprise the fiber bundle. Combining **Equations D.1-D.3** yields **Equation D.4**

$$SA = \frac{\pi * \Phi_f * w * L * spacing * no_{layers}}{\cos\theta} \tag{D.4}$$

Since the frontal area is equal to the width times the length **Equation D.4** can be further simplified into **Equation D.5**

$$SA = \frac{\pi * \Phi_f * FA * spacing * no_{layers}}{\cos\theta} \quad \text{(D.5)}$$

where FA is the frontal area of the fiber bundle through which blood flows. The pathlength or height of the fiber bundle, PL, can be found using **Equation D.6**

$$PL = no_{layers} * (\Phi_f + gap) \quad \text{(D.6)}$$

where gap is the space between layers of stacked fibers, which was modeled as 20 microns for these analyses. **Equations D.5** and **D.6** can be combined and solved for PL to yield **Equation D.7**

$$PL = \frac{(\Phi_f + gap) * SA * \cos\theta}{\pi * \Phi_f * FA * spacing} \quad \text{(D.7)}$$

Equation D.7 was solved for the array of frontal and surface areas to yield an array of pathlengths for future analyses.

Appendix E: Matlab Bundle Modeling Code

E.1 Main Matlab Bundle Modeling Program

```
%%Comprehensive Bundle Design Program V8.1
%%Setting up graph variables
clear all
gap=20e-6;
CO=input('Enter the device flowrate in L/min > ');%cardiac output L/min
CO=CO/(60*1000);%cardiac output m^3/sec
SA=(input('Enter the bundle surface area in m^2; \n minimum > '):input('step size >
'):input('maximum > '));%surface area m^2
FA=(input('Enter the bundle frontal area in cm^2; \n minimum > '):input('step size >
'):input('maximum > '));%frontal area cm^2
FA=FA/(100*100);%frontal area m^2
[SA,FA]=meshgrid(SA,FA);%%array form of surface area and frontal area
L_W_ratio=1;
%%Initializing variables-path length
%%Fiber Initialization
standard_fiber_input_question=input('Do you want to keep the standard fiber specs
(spacing=43fibers/in(porosity~0.75), fiber diameter 203 microns, crossing angle 30 degrees?
Enter "y" or "n" > ','s');
if strcmp(standard_fiber_input_question,'y')
```

```
        phif=203;%%fiber diameter microns
        theta=30;%%fibercrossing angle degrees
        spacing=43;%%fibers/inch
elseif strcmp(standard_fiber_input_question,'n')
    spacing=input('Enter the fiber spacing in fibers/inch (standard 43) > ');%%fiber diameter
    microns
    phif=input('Enter the fiber diameter in microns (standard 203) > ');%%fibercrossing angle
    degrees
    theta=input('Enter the fiber crossing angle in degrees (standard 30) > ');%%fibers/inch
end
theta=(theta/2);%% fiber angle with horzontal degrees
phif=phif/1000000;%%fiber diameter m
theta=(theta*pi)/180;%%fiber angle with horizontal radians
spacing=spacing/0.0254;%%fibers/m
%%Initializing variables-resistance
%%permiability calcs from hard shell paper 2012
standard_permiability_input_question=input('Do you want to keep the fiber bundle permiability
data from the 2012 hard shell paper? Enter "y" or "n" > ','s');
if strcmp(standard_permiability_input_question,'y')
    muexp=0.003;%%dynamic viscosity of blood from hard shell paper 2012 kg/(m*sec)
    Rbexp=0.29;%%bundle resistance from hardshell 2012 mmHg/(L/min)
    Rbexp=Rbexp*(60*1000*133.322368);%kg/(sec*m^4)
    Afexp=0.016;%bundle frontal area from hardshell 2012 m^2
```

```
        Lexp=0.038;%bundle path length from hardshell 2012 m
perm=(muexp*Lexp)/(Afexp*Rbexp);%permiability calculated from hard shell 2012 m^2
elseif strcmp(standard_permiability_input_question,'n');
        yes_standard_permiability_input_question=input('Do you want to enter a permiability or
        experimental data? Enter "p" for permiability or "e" for experimental data > ','s');
        if strcmp(yes_standard_permiability_input_question,'p')
                perm=input('Enter the fiber bundle permiability in kg/(m*sec) > ');
        elseif strcmp(yes_standard_permiability_input_question,'e')
                muexp=input('Enter the dynamic viscosity in kg/(m*sec)(standard 0.003) >
                ');%%dynamic viscosity of blood kg/(m*sec)
                Rbexp=input('Enter the fiber bundle resistance in mmHg/(L/min) (standard 0.29)
                > ');%%bundle resistance mmHg/(L/min)
                Rbexp=Rbexp*(60*1000*133.322368);%kg/(sec*m^4)
                Afexp=input('Enter the fiber fundle frontal are in cm^2 (standard 160 cm^2) >
                ');%bundle frontal area cm^2
                Afexp=Afexp/(100*100);%bundle frontal area m^2
                Lexp=input('Enter the bundle path length in cm (standard 3.8) > ');%bundle path
                length cm
                Lexp=Lexp/100;%bundle path length m
        perm=(muexp*Lexp)/(Afexp*Rbexp);%permiability m^2
        end
end
%%Initializing variables-gas exchange
```

```
%%User input data
standard_gas_exchange_question=input('Do you want to keep the standard bundle gas transfer
constants from the Cook 2005 paper, m=0.214 phi=0.82? Enter "y" or "n" > ','s');
if strcmp(standard_gas_exchange_question,'y')
        mb=0.214;%bundle gas transfer constant
        phib=0.82;%bundle gas transfer constant
elseif strcmp(standard_gas_exchange_question,'n')
        mb=input('Enter the bundle gas exchange constant m (standard 0.214) > ');%%user input
        gas exchange constant
        phib=input('Enter the bundle gas exchange constant phi (     standard 0.82) > ');%%user
        input gas exchange constant
end
por=1-(pi*phif*spacing/4);%porosity of the device as a fraction
standard_gas_exchange_question=input('Do you want to keep the standard bundle CO2 transfer
constant from the unpublished data from 2005 Cook paper unpublished data, k_CO2=4.61?
Enter "y" or "n" > ','s');
if strcmp(standard_gas_exchange_question,'y')
        k_CO2=4.61;%bundle gas transfer constant
elseif strcmp(standard_gas_exchange_question,'n')
        k_CO2=input('Enter the bundle CO2 exchange constant k (standard 4.61) > ');%%user
        input gas exchange constant
end
k_CO2=k_CO2/(60*1000*1000*133.322368);
```

```
standard_sweep_gas_question=input('Do you want to keep the standard partial pressure of
oxygen in the sweep gas from 760 mmHg?  Enter "y" or "n" > ','s');
if strcmp(standard_sweep_gas_question,'y')
        Pg=760;%pO2 of sweep gas mmHg
elseif strcmp(standard_sweep_gas_question,'n')
        Pg=input('Enter the sweep gas partial pressure of oxygen in mmHg > ');
end
Pg=Pg*133.322368;%kg/(m*sec^2)
standard_blood_condition_question=input('Do you want to keep the AAMI blood conditions and
assume equal inlet and outlet pH (inlet pH=outlet pH=7.40, fractional inlet oxygen saturation =
0.65, hemoglobin concentration=12 g/dL, fractional hematacrit=0.4, blood temp = 37 deg.
celsius) Enter "y" or "n" > ','s');
if strcmp(standard_blood_condition_question,'y')
        pHo=7.40;%pH of the blood at the outlet
        pHi=7.40;%pH of the blood at the inlet
        si=0.65;%venous saturation
        cHb=12;%hemoglobin concentration g/dL
        H=0.4;%fractional hematocrit
        T=37;% body temp in celsius
elseif strcmp(standard_blood_condition_question,'n')
        pHo=input('Enter the outlet pH (standard 7.40) > ');
        pHi=input('Enter the inlet pH (standard 7.40) > ');
        si=input('Enter the inlet oxygen saturation as a fraction (standard 0.65) > ');
```

```
        cHb=input('Enter the hemoglobin concentration in g/dL (standard 12) > ');
        H=input('Enter the hematacrit as a fraction (standard 0.4) > ');
        T=input('Enter the body temp in celsius (standard 37) > ');
end
cHb=cHb*10;%%hemoglobin concentration kg/L
mu=(2.205e-5)*exp(((1965/(273.15+T))+(2.31*H)));%dyn visc blood poise
mu=0.1*mu;%%dyn visc blood kg/(m*sec)
rho=(1.09*H)+(1.035*(1-H));%density of blood g/mL
rho=rho*1000;%density of blood kg/m^3
%%Blood constants for Humans
standard_blood_constants_question=input('Do you want to keep the standard blood constants for
humans? (aspect ratio of RBC,m, 0.283, hill equation parameter for blood,n, 2.7) Enter "y" or
"n" > ','s');
if strcmp(standard_blood_constants_question,'y')
        mrbc=0.283;%aspect ratio of RBC for humans
        nrbc=2.7;%Hill equation parameter for human blood
elseif strcmp(standard_blood_constants_question,'n')
        mrbc=input('Enter the aspect ratio of a RBC, m > ');
        nrbc=input('Enter the hill equation parameter for human blood,n > ');
end
%%Actual Coding
PLi=pathlength_solid_rect_V1_1(SA,FA,spacing,phif,theta,gap,L_W_ratio);
R_B_array=bundle_resistance_calc_darcy_v1_1(FA,PLi,perm,mu);
```

```
[VO2,so]=gas_exchange_v4_2(SA,FA,CO,PLi,phif,mb,phib,por,Pg,pHo,pHi,si,cHb,H,T,mrbc,nr
bc,mu,rho);
[V_CO2_1,V_CO2_2,Qg]=CO2_exchange_v1_2(SA,Pg,k_CO2);
FA=FA*100*100;
PLi=PLi*100;
sqrtFA=FA.^0.5;
sqrtFA_ratio_PLi=sqrtFA./PLi;
R_B_array=R_B_array/(133.322368*60*1000);
VO2=VO2*60*1000*1000;
V_CO2_1=V_CO2_1*60*1000*1000;
V_CO2_2=V_CO2_2*60*1000*1000;
Qg=Qg*60*1000;
so=so*100;
if size(SA(1,:))==1
        SA_labels=['Surface Area ',num2str(SA(1)),' m^2'];
else
        i=0;
        for g=SA(1,1):(SA(1,2)-SA(1,1)):SA(1,end)
        i=i+1;
                SA_labels{i}=['Surface Area ',num2str(SA(1,i)),' m^2'];
        end
end
figure
```

```
set(gcf,'name','Path_Length','numbertitle','off')
plot(FA,PLi,'LineWidth',3)
set(gca,'FontSize',20)
legend(SA_labels,'FontSize',16)
xlabel('Frontal area (cm^2)','FontSize',20)
ylabel('Bundle Path Length (cm)','FontSize',20)
title ('Bundle Path Length','FontSize',20)
figure
set(gcf,'name','Aspect_Ratio','numbertitle','off')
plot(FA,sqrtFA_ratio_PLi,'LineWidth',3)
set(gca,'FontSize',20)
legend(SA_labels,'FontSize',16)
xlabel('Frontal area (cm^2)','FontSize',20)
ylabel('Bundle Aspect Ratio ( (cm^2)^0^.^5 / cm )','FontSize',20)
title ('Bundle Aspect Ratio','FontSize',20)
figure
set(gcf,'name','Bundle_Resistance','numbertitle','off')
plot(FA,R_B_array,'LineWidth',3)
set(gca,'FontSize',20)
legend(SA_labels,'FontSize',16)
xlabel('Frontal area (cm^2)','FontSize',20)
ylabel('Bundle Resistance (mmHg/(L/min))','FontSize',20)
title ('Bundle Resistance','FontSize',20)
```

```
figure
set(gcf,'name','VO2','numbertitle','off')
plot(FA,VO2,'LineWidth',3)
set(gca,'FontSize',20)
legend(SA_labels,'FontSize',16)
xlabel('Frontal area (cm^2)','FontSize',20)
ylabel('VO2 (mL/min)','FontSize',20)
title ('Oxygen Exchange','FontSize',20)
figure
set(gcf,'name','Oxygen_Saturation','numbertitle','off')
plot(FA,so,'LineWidth',3)
set(gca,'FontSize',20)
legend(SA_labels,'FontSize',16)
xlabel('Frontal area (cm^2)','FontSize',20)
ylabel('Outlet Oxygen Saturation (%)','FontSize',20)
title ('Outlet Oxyhemoglobin Saturation','FontSize',20)
figure
set(gcf,'name','CO2 Exchange with 1 Device','numbertitle','off')
flat_V_CO2_1=V_CO2_1(:);
min_V_CO2_1=roundnum(min(flat_V_CO2_1),-1,10);
max_V_CO2_1=roundnum(max(flat_V_CO2_1),1,10);
plot(Qg(:,:,1),V_CO2_1(:,:,2),'LineWidth',3)
set(gca,'FontSize',20)
```

```
legend(SA_labels,'FontSize',16)
xlabel('Sweep Gas Flowrate (L/min)','FontSize',20)
ylabel('VCO2 (mL/min)','FontSize',20)
ylim([min_V_CO2_1 max_V_CO2_1])
title ('Carbon Dioxide Exchange with 1 Module','FontSize',20)
figure
set(gcf,'name','CO2 Exchange with 2 Devices','numbertitle','off')
flat_V_CO2_2=V_CO2_2(:);
min_V_CO2_2=roundnum(min(flat_V_CO2_2),-1,10);
max_V_CO2_2=roundnum(max(flat_V_CO2_2),1,10);
plot(Qg(:,:,1),V_CO2_2(:,:,2),'LineWidth',3)
set(gca,'FontSize',20)
legend(SA_labels,'FontSize',16)
xlabel('Sweep Gas Flowrate (L/min)','FontSize',20)
ylabel('VCO2 (mL/min)','FontSize',20)
ylim([min_V_CO2_2 max_V_CO2_2])
title ('Carbon Dioxide Exchange with 2 Modules','FontSize',20)
```

E.2 Path Length Subprogram

```
function PLi = pathlength_solid_rect_V1_1( SA,FA,spacing,phif,theta,gap,L_W_ratio)
%UNTITLED2 Summary of this function goes here
%   Detailed explanation goes here
PLi=(((phif+gap)*SA*cos(theta))./(FA*pi*phif*spacing));
End
```

E.3 Resistance Calculation Subprogram

```
function [ R_B_array ] = bundle_resistance_calc_darcy_v1_1( FA,PLi,perm,mu )
%bundle_resistance_calc_darcy calculates the Darcy fiber bundle resistance
%       This function calculates the estimated fiber bundle
        resistance using
%       the Darcy law porous media assumption coupled with previous prelininary
%       data.
%%      resistance
R_B_array=(mu.*PLi)./(FA.*perm);%kg/(sec*m^4)
end
```

E.4 Oxygen Exchange Calculation Subprogram

```
function [ VO2,so ] = gas_exchange_v4_2(
SA,FA,Qal,PLi,phif,mb,phib,por,Pg,pHo,pHi,si,cHb,H,T,mrbc,nrbc,mu,rho )
%UNTITLED6 Summary of this function goes here
%       Detailed explanation goes here
%%Calculated Values
kc=(4.658e-5)*(1.01)^(37-T);%solubility constant for cells mL o2/mL blood*mmHg
kc=kc/133.322368;%solubility constant for cells in L O2 *m*sec^2/L blood* kg
kp=(2.855e-5)*(1.01)^(37-T);%solubility constant for plasma mL o2/mL blood*mmHg
kp=kp/133.322368;%solubility constant for palsma in m^3 O2 *m*sec^2/m^3 blood* kg
k=(kc*H)+(kp*(1-H));%overall solubility constant m^3 o2*m*sec^2/m^3 blood*kg
p50=26.6*(10^((0.42*(7.4-((pHo+pHi)/2)))-(0.024*(37-T))));%p50 eq for humans mmHg
p50=p50*133.322368;%kg/(m*sec^2)
```

```
nu=mu/rho;%kinematic viscosity of blood m^2/sec

Dc=(0.76e-5)*((1.025^(T-25)));%diffusivity in cells cm^2/sec

Dc=Dc/(100*100);%diffusivity in cells m^2/sec

Dp=(1.62e-5)*((1.025^(T-25)));%diffusivity in plasma cm^2/sec

Dp=Dp/(100*100);%diffusivity in plasma m^2/sec

N=(kc*Dc)/(kp*Dp);%constant in calcuating D with Frick

beta=((N-1)/3)*(((2/(1+((N-1)*(mrbc/2))))+(1/(1+((N-1)*(1-mrbc))))));%con 4 Fick

chi=(1-(N*(1-beta)))/(N-1-beta);%con 4 Fick

G=H*((N-1)/(N+chi));%con 4 Fick

D=Dp*(kp/k)*((1+(chi*G))/(1-G));%diffusivity of O2 in blood using Fick m^2/sec

%%%%%%%%%%%%%%%%%%%%%%%%%%%%%%%%%%%%%%%%%%%%%%

%%%%%%%%%%%%%%%%%%%%%%%%%

%%Start of the actual coding

%%%%%%%%%%%%%%%%%%%%%%%%%%%%%%%%%%%%%%%%%%%%%%

%%%%%%%%%%%%%%%%%%%%%%%%%

%%gas exchange

pin=p50*((si/(1-si))^(1/nrbc));

Ls=0.0000005;

VO2=zeros(size(FA));

so=zeros(size(FA));

rcheck=size(FA,1);

ccheck=size(FA,2);

if size(SA(1,:))==1
```

```
c=1;
r=0;
FAi=FA;
for rows=1:1:rcheck
        r=r+1;
        if isnan(PLi(r,c))
                VO2(r,c)=nan;
                so(r,c)=nan;
        else
                P=pin;%kg/(m*sec^2)
                L=0;%m
                Af=FA(r,c);%m^2
                while L<PLi(r,c)
                        L=L+Ls;
                        lambda=(1.34*cHb*nrbc*((P/p50)^(nrbc-
                        1)))/(1000*k*p50*((1+((P/p50)^nrbc))^2));%%unitless, base units
                        for all variables, units of 1.34 mL O2 / g hb, the equations do the
                        unit conversions
                        dPdx=phib*((((1-por)*Af*nu)/(Qal*phif))^mb)*((4*(1-
                        por))/(por*phif))*((D/nu)^(2/3))*((Pg-
                        P)/((1+lambda)^(2/3)));%kg/((m^2)*(sec^2))
                        P=P+(Ls*dPdx);%kg/(m*sec^2)
                end
```

```
                po(r,c)=P;%kg/(m*sec^2)
                so(r,c)=((po(r,c)/p50)^nrbc)/(1+((po(r,c)/p50)^nrbc));
                VO2(r,c)=Qal*((k*(po(r,c)-pin))+((1.34*cHb*(so(r,c)-
                si))/(100*10)));%VO2 transferred m^3/sec
        end
        %r=r+1;
    end
    %c=c+1;
else
    c=1;
    for columns=1:1:ccheck
        r=1;
        FAi=FA;
        for rows=1:1:rcheck
            if isnan(PLi(r,c))
                VO2(r,c)=nan;
                so(r,c)=nan;
            else
                P=pin;%kg/(m*sec^2)
                L=0;%m
                Af=FA(r,c);%m^2
                while L<PLi(r,c)
                    L=L+Ls;
```

```
                    lambda=(1.34*cHb*nrbc*((P/p50)^(nrbc-
                    1)))/(1000*k*p50*((1+((P/p50)^nrbc))^2));%%unitless,
                    base units for all variables, units of 1.34 mL O2 / g hb, the
                    equations do the unit conversions
                    dPdx=phib*((((1-por)*Af*nu)/(Qal*phif))^mb)*((4*(1-
                    por))/(por*phif))*((D/nu)^(2/3))*((Pg-
                    P)/((1+lambda)^(2/3)));%kg/((m^2)*(sec^2))
                    P=P+(Ls*dPdx);%kg/(m*sec^2)
                end
                po(r,c)=P;%kg/(m*sec^2)
                so(r,c)=((po(r,c)/p50)^nrbc)/(1+((po(r,c)/p50)^nrbc));
                VO2(r,c)=Qal*((k*(po(r,c)-pin))+((1.34*cHb*(so(r,c)-
                si))/(100*10)));%VO2 transferred m^3/sec
            end
            r=r+1;
        end
        c=c+1;
    end
end
end
```

E.5 Carbon Dioxide Exchange Calculation Subprogram

```
function [ V_CO2_1,V_CO2_2,Qg ] = CO2_exchange_v1_2( SA,Pg,k_CO2 )
%bundle_resistance_calc_darcy calculates the Darcy fiber bundle resistance
```

```
%       This function calculates the estimated fiber bundle resistance using
%       the Darcy law porous media assumption coupled with previous prelininary
%       data.
P_CO2_blood=35:5:50;
P_CO2_blood=P_CO2_blood*133.322368;
Qg=0:0.01:10;
Qg=Qg/(60*1000);
SA=SA(1,:);
[SA,Qg,P_CO2_blood]=meshgrid(SA,Qg,P_CO2_blood);
V_CO2_1=(2*P_CO2_blood.*Qg*k_CO2.*SA)./((2*Qg)+(k_CO2*SA*Pg));
V_CO2_2=(2*P_CO2_blood*2.*Qg*k_CO2*2.*SA)./((2*2*Qg)+(k_CO2*2*SA*Pg));
end
```